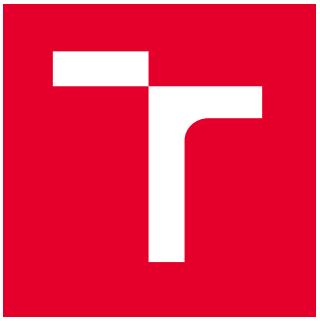

BRNO UNIVERSITY OF TECHNOLOGY

VYSOKÉ UČENÍ TECHNICKÉ V BRNĚ

CENTRAL EUROPEAN INSTITUTE OF TECHNOLOGY BUT

STŘEDOEVROPSKÝ TECHNOLOGICKÝ INSTITUT VUT

LOW-TEMPERATURE PLASTIC DEFORMATION OF BCC METALS WITH INTERNAL MAGNETIC ORDER

NÍZKOTEPLOTNÍ PLASTICKÁ DEFORMACE BCC KOVŮ S VNITŘNÍM MAGNETICKÝM USPOŘÁDÁNÍM

DOCTORAL THESIS
DIZERTAČNÍ PRÁCE

AUTHOR — Ing. Jakub Holzer
AUTOR PRÁCE

SUPERVISOR — doc. Ing. Roman Gröger, Ph.D. et Ph.D.
ŠKOLITEL

BRNO 2022

Abstract

While plastic deformation of body-centered cubic (bcc) metals at low temperatures is now well understood, the effect of internal magnetic order on mechanical properties and the effect of plastic deformation of internal magnetic order remain largely unexplained. The aim of this thesis is to elucidate the low-temperature plastic deformation of α-iron and chromium with focus on magnetism. It is investigated by slip-trace analysis of deformed specimens, electron backscattered diffraction, and transmission electron microscopy (TEM) where necessary. The internal magnetic order in chromium is explored by means of magnetic neutron diffraction at SINQ facility of the Paul Scherrer Institute in Switzerland. The vibrating sample magnetometry is utilized to look for changes in mass susceptibility in order to discriminate between different magnetic states. The anomalous slip was found in a deformed chromium specimen for the first time. The dislocation network responsible for the anomalous slip is characterized by the $\mathbf{g} \cdot \mathbf{b}$ analysis in TEM, where a network of $1/2\langle 111 \rangle$ intersecting screw dislocations and their $\langle 100 \rangle$ junctions were observed to form on low-stressed $\{110\}$ planes. Furthermore, twins produced by antitwinning shear were found in chromium, but not in α-Fe. This phenomenon is explained using atomistic simulations employing semi-empirical interatomic potentials. The magnetism in α-iron is studied by the vibrating sample magnetometry and the results are reconciled using the Jiles-Atherton model. The magnetic domains in α-Fe were imaged by the Kerr microscopy and the results show that twins can effectively block the movement of domain walls and nucleate new ones.

Keywords

α-Fe, chromium, low-temperature deformation, twinning, antitwinning, anomalous slip, internal magnetic order

Abstrakt

Přestože plastická deformace kovů s prostorově středěnou kubickou mřížkou za nízkých teplot je dnes dobře vysvětlena, vliv vnitřního magnetického uspořádání na mechanické vlastnosti a vliv plastické deformace na vnitřní magnetické uspořádání zůstávají z větší části nevysvětleny. Cílem této práce je popsat nízkoteplotní plastickou deformaci α-železa a chromu pomocí analýzy skluzových čar, elektronovou zpětně odraženou difrakcí a transmisní elektronovou mikroskopií (TEM). Vnitřní magnetické uspořádání chromu je zkoumáno pomocí magnetické neutronové difrakce v neutronovém centru na Institutu Paula Scherrera ve Švýcarsku. Vibrační magnetometrie je využita pro hledaní změn v hmotnostní susceptibilitě, aby byly rozeznány různé magnetické stavy. Anomální skluz byl poprvé pozorován v deformovaném vzorku chromu. Dislokační síť zodpovědná za anomální skluz je charakterizována pomocí $\mathbf{g}\cdot\mathbf{b}$ analýzy v TEM. Síť protínajících se $1/2\langle 111\rangle$ šroubových dislokací a jejich $\langle 100\rangle$ spoje se tvoří na nízkozatížených $\{110\}$ rovinách. Dvojčata vytvořená antidvojčatovým smykem byla pozorována v chromu, ale nikoliv v α-železe. Tento jev je vysvětlen pomocí atomárních simulací využívajících semiempirické interakční potenciály. Magnetické domény v α-železe byly studovány pomocí Kerrovy mikroskopie. Výsledky ukazují, že dvojčata mohou efektivně blokovat pohyb doménových stěn a nukleovat nové.

Klíčová slova

α-Fe, chrom, nízkoteplotní plastická deformace, dvojčatění, antidvojčatění, anomální skluz, vnitřní magnetické uspořádání

HOLZER, Jakub. Nízkoteplotní plastická deformace BCC kovů s vnitřním magnetickým uspořádáním. Brno, 2022. Dostupné také z: https://www.vutbr.cz/studenti/zav-prace/detail/144957. Dizertační práce. Vysoké učení technické v Brně, Středoevropský technologický institut VUT, Středoevropský technologický institut VUT. Vedoucí práce Roman Gröger.

Prohlašuji, že jsem dizertační práci Nízkoteplotní plastická deformace BCC kovů s vnitřním magnetickým uspořádáním vypracoval samostatně pod odborným vedením doc. Ing. Romana Grögera, Ph.D. et Ph.D. s použitím materiálů uvedených v seznamu literatury.

V Brně dne 29.07.2022

Ing. Jakub Holzer

Acknowledgment

Firstly, I would like to thank my supervisor Assoc. Prof. Roman Gröger, for his time and leadership during my Ph.D. study and his support in publication of the results in scientific journals and at conferences. I also want to express my gratitude to my supervisor for the simulations presented in this work, that help to explain many of the problems presented in the thesis. Secondly, I thank Prof. Tomáš Kruml for valuable discussions concerning the transmission electron microscopy presented in this work, to Dr. Zdeněk Chlup for his help with mechanical testing and to Dr. Oksana Zaharko for her leadership during my internship at the Paul Scherrer Institute and her invaluable help with the neutron scattering experiments. I would further like to thank Prof. Marek Niewczas from McMaster University for his measurements of the residual resistivity ratios, Dr. Michal Staňo for help with Kerr microscopy, Dr. Jiří Pospíšil for several attempts at the growth of single crystals of α-Fe, and Prof. Lejček for donation of one α-Fe single-crystalline specimen. Lastly, I would like to thank my family, my partner and colleagues for their support throughout my studies.

I would like to acknowledge the Ministry of Education, Youth and Sports of the Czech Republic, which funded my stay at the Paul Scherrer Institute in Switzerland through the International mobility of employees of IPM project, reg. num. CZ.02.2.69/0.0/0.0/$18_0$53/0016933. My gratitude is also due to Brno University of Technology which funded a part of this research through the Specific research project CEITEC-VUT-J-19-5955, and to the Ph.D. Talent project funded by Brno municipality.

Contents

1 Introduction

The low temperature plastic deformation of magnetic body-centered cubic (bcc) metals $\alpha-$Fe and Cr has received very little attention despite the fact that they are essential ingredients in dilute ferroalloys $Fe_{1-x}Cr_x$, which are model materials for the development of ferritic/martensitic steels with applications in the design of fusion reactors [1]. The mechanisms governing the plastic deformation of bcc metals are very different from those of close-packed metals such as Al, Cu, or Au [2]. Yet, the plastic behavior of the latter metals is still used as a paradigm for the understanding the deformation behavior of all crystalline materials. The experiments required to elucidate the deformation mechanisms are extremely challenging as they require single crystals of considerable size and very high purity, whose preparation is complicated, especially those of α-Fe. The preparation of iron single crystals is problematic due to the structural transition from the high-temperature ferritic body-centered cubic phase to the austenitic face-centered cubic (fcc) phase and again the low-temperature ferritic bcc phase, the latter of which remains stable to 0 K.
The situation with Cr is very different. Large enough single crystals of high purity have been available commercially for many years. However, they often contain internal defects such as holes and voids.

To the best of our knowledge, only two old experimental papers looking at some aspects of the low-temperature plastic behavior of pure Cr single crystals can be found in the literature [3, 4]. Greiner [3] reported wavy slip traces in chromium deformed at room temperature and suggested that it is caused by the operation of multiple slip systems. He also asserts, that the deformation mechanism is similar to that of α-Fe. Reid et al. [4] state that the slip is restricted to thin regions sheared by the $\{110\}\langle 111\rangle$ systems below 130 K and confirms Greiner's observation of the wavy slip above 195 K, which is explained as alternating slip on planes belonging to the $\langle 111\rangle$ zone. Furthermore, the twinning systems were found to be of the $\{112\}$ type.

The existing knowledge about the behavior of pure α-Fe owes much to detailed experiments by Aono et al. [5]. What α-Fe and Cr, together with other metals of groups 5 and 6, have in common is the non-closed-packed bcc structure in which the screw dislocations possess non-planar cores. Their movement under stress is very limited at low temperatures [6], which results in steel increase of the flow stress as the temperature is lowered. Unlike other bcc metals, Cr and α-iron are both metals with internal magnetic order. α-iron is a well-known ferromagnetic material. In contrast, the magnetic state of chromium is characterized by antiferromagnetic spin-density waves [7], which is a more complex magnetic state than that of other, simple antiferromagnets such as metal oxides MnO, FeO and NiO. The spin density

waves in chromium are incommensurate with the structural unit cell, whereby their wavelength is not an integer multiple of the lattice parameter.

The properties of magnetic materials are commonly described by the hysteresis curve, shown in Fig. 1.1, and parameters obtained from it. The hysteresis curve (or loop) is a graphical representation of the relationship of the magnetic flux density B (or magnetization M) and magnetizing field H. The hysteresis curves are often measured in the vibrating sample magnetometer by applying the magnetic field across the sample and measuring the magnetic moment induced in the specimen in the direction of the magnetizing field by vibrating the specimen near a set of measurement coils.

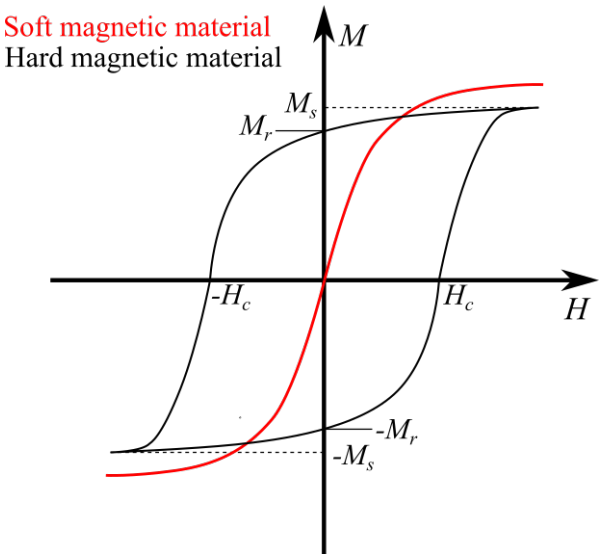

Figure 1.1: Schematic drawing of the typical hysteresis curve for magnetically soft and hard materials represented by the red and black curves, respectively.

The magnetic hysteresis arises in the material when an external magnetic field is applied and magnetic moments are aligned with the field. Upon removal of the magnetizing field, part of the magnetic order will remain. Once the material is magnetized, it will stay that way unless acted upon by external forces such as temperature or magnetizing field applied in the opposite direction. The hysteresis curve is characterized by several parameters, as shown in Fig. 1.1. The saturation magnetization in the positive direction M_s or in the negative direction $-M_s$ are estimated simply as maximum value of magnetization in saturation[1]. The remanence, alternatively remanent magnetization, M_r is the magnetization that remains in the material when the external magnetic field is removed. In the hysteresis curve, this value is found at the intersection of the vertical axis with the curve. Similarly, the magnetic coercivity, alternatively coercive field, H_c characterizes the ability of the material to retain its magnetization in demagnetizing fields. The value of coercivity is found at the intersection of the horizontal axis with the hysteresis loop. Magnetic materials are often characterized as magnetically soft or hard. Magnetically soft materials,

[1]Saturation is reached when the increasing magnetizing field no longer increases the magnetization. Microscopically this is achieved when all magnetic dipoles are aligned with the magnetizing field.

whose typical hysteresis loop is shown by the red curve in Fig. 1.1, have very low coercivity, low remanence, and small area enclosed by the curve. Due the low remanence, the material will practically demagnetize after the magnetizing field is turned off and the hysteresis losses are very small. On the other hand, magnetically hard materials have high coercivity, high remanence, and large area of the hysteresis loop, as shown by the black curve in Fig. 1.1. They will retain a large part of magnetization after the magnetizing field is removed and, therefore, they are used as permanent magnets.

The effects of the elastic deformation on the magnetic properties of materials have been known for a long time. The effect of residual stress, and generation of new pinning sites and their effect on magnetization curves were discussed in depth by Makar et al. [8]. They also argue that the residual stress left in the material after plastic deformation is not as important as the generation of new pinning sites, which arrest or hinder the movement of magnetic domains. They can be in the form of dislocations, dislocation clusters, interfaces (such as twin boundaries), or secondary phase particles [9]. The level of plastic deformation can be also correlated with the coercive field H_c. With increasing deformation, the coercive field increases in both single crystals and polycrystals. However, the initial value is larger in the case of polycrystals due to the presence of grain boundaries [10]. The effect of internal stress on magnetism and vice versa can be also explored by simulations and is often the only way to study magnetism at the smallest scales. Bienvenu et al. [11], for example, suggests that in chromium, the $1/2\langle 111\rangle$ dislocations shearing the crystal would produce magnetic faults. In order to remove this fault, another dislocation of the same type would have to be present, which creates a super-dislocation with the $\langle 111\rangle$ Burgers vector. This theoretical prediction has, however, not been experimentally proven.

1.1 Low-temperature plastic deformation of bcc metals

The plastic deformation of bcc metals is governed by the motion of $1/2\langle 111\rangle$ screw dislocations [12, 13]. Many atomistic simulations and Density Functional Theory (DFT) studies of bcc metals made in the past three decades have provided ample evidence that the cores of these dislocations are non-planar [14–19], which gives rise to phenomena that do not occur in close-packed structures. The motion of these dislocations was first studied using the Peierls-Nabarro (P-N) model, originating from isotropic elasticity theory, which was developed in 1940 by Peierls [20], and modified by Nabarro in 1947 [21] and Eshelby in 1949 [22]. Nowadays, modified P-N models are still frequently used, often with parameters derived from DFT calculations, and present a link between atomistic and continuum approaches of material modeling. The atomic structures of dislocation cores and their changes under stress were studied using a variety of interatomic potentials, first starting with pair potentials [20–22], then many-body potentials of central forces based mostly on the embedded atom method (EAM) [23–26], empirical potentials with directional bonds (MEAM) [27, 28] and, most recently, semi-empirical potentials (BOP - Bond Order

Potentials, MGPT - Model Generalized Pseudopotential Theory) based partially on description of bonds using methods based on first principles [29–32]. The embedded atom model first was described by Daw and Baskes in 1984 [23] and soon after expanded by by Holian et al. in 1991 [24] and Baskes again in 1999 [25]. It is used primarily for modeling materials with predominantly metallic bonds [28]. Nonetheless, the EAM method falls short when it comes to modeling covalent bonds.
The concept of bond order was first used by Tersoff to describe silicon in 1988 [29]. His description of atomic bonds takes into account not only the attractive and repulsive force of two atoms, but also the strength of the bond via the bond-order parameter [30] and is thus able to incorporate directional bonds [31]. It is worth mentioning the bond-order potentials that were formulated more recently for the bcc metals by Mrovec et al. for Mo [33], W [34] and for ferromagnetic iron [35] or by Lin et al. [36,37]. The Model Generalized Pseudopotential Theory was developed by Moriarty in 1988 [38]. Similarly to the BOP, the MGPT models the are partially based on quantum-mechanical description of bonds and were used for studies of dislocations in bcc metals [39]. The last frequently used method worth mentioning here is the DFT method which stems from the work of Hohenberg and Kohn [40] and later Kohn and Sham [41]. The biggest advantage of the DFT is its ability to predict material properties of unknown systems without experimentally obtained parameters. Nonetheless, even DFT uses many approximations [42] in comparison with the Hartree-Fock method [43], but its advantage is that DFT allows for simulations of larger systems. Ventelon et al. used DFT to investigate the Peierls potential of screw dislocations in W and Fe [44], dislocation core structure in α-Fe [17] and compared the results of DFT and empirical potentials calculation of the dislocation core structure [45]. Dezerald et al. [46] further studied by DFT the dislocation paths in bcc metals, and kink-pair activation enthalpies of screw dislocation in V, Nb, Ta, Mo, W and Fe [47]. Recently Casillas-Trujillo et al. [48] studied the dislocation core structure of paramagnetic bcc iron and Bienvenu et al. [11] focused on effect of magnetism on screw dislocations in bcc chromium.

A schematic representation of the spreading of the core of 1/2[111] screw dislocation on three {110} planes in the zone of [111] slip direction is shown in Fig. 1.2. Fig. 1.2(a) and 1.2(b) show by arrows the screw and edge component of the differential displacement maps, respectively.

The differently colored atoms in Fig. 1.2 belong to the three successive (111) atomic layers. The magnitude of the arrows represent the relative displacement of the two atoms in the direction perpendicular to the figure's plane (Fig. 1.2(a)) or parallel (Fig. 1.2(b)). If the arrow in Fig. 1.2(b) points from one atom to another, it represents bond stretching. On the other hand, if the arrow does not point from one atom to another, the bond is partially rotated and stretched, as visualized in the bottom part of Fig. 1.2(b). Moreover, a vector sum of the edge components on any path encircling the center of the dislocation is zero, while vector sum of screw components along any such path is the Burgers vector of the dislocation.

The plastic response of all bcc metals is characterized by steep increase of the flow stress (stress required to maintain plastic deformation) with decreasing temperature and increasing strain rate [2, 49]. The core spreading creates a significant Peierls barrier, which hinders the dislocation motion [50]. This is significant at low

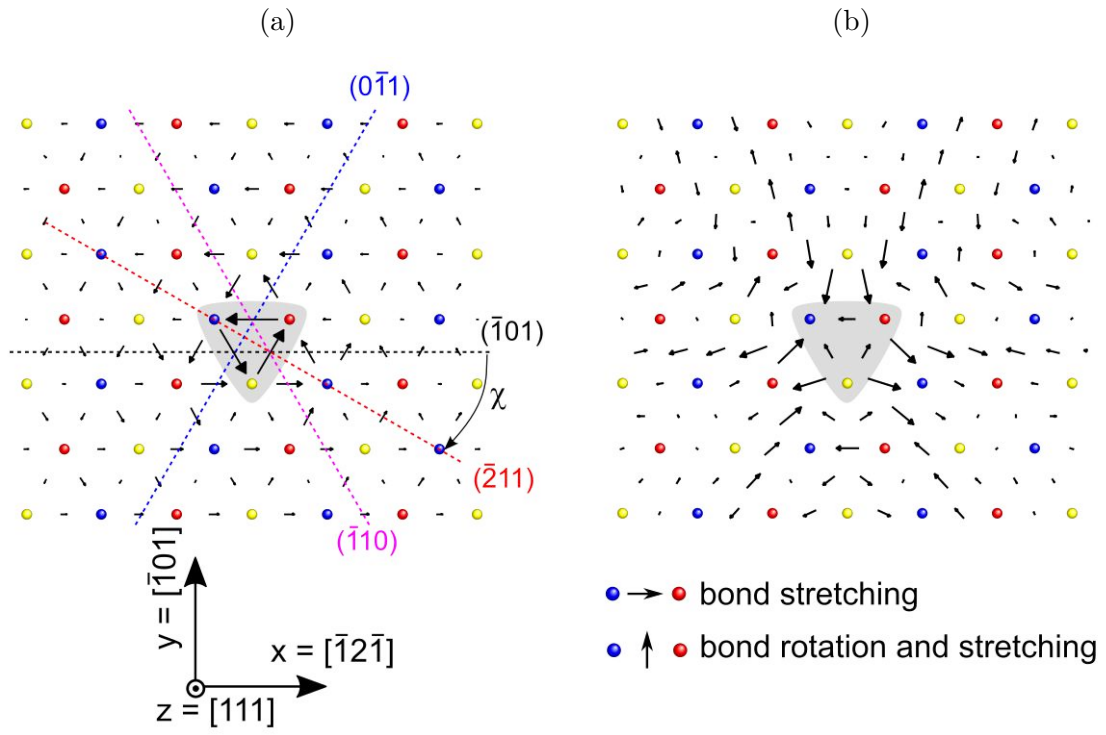

Figure 1.2: (a) screw component of the core spreading of a 1/2[111] screw dislocation. The arrows represent the relative displacement of a pair of atoms in the direction perpendicular to the plane of the figure. (b) edge component of the core spreading of 1/2[111] dislocation. The arrows here represent the relative displacement in the plane of the figure and are magnified 10x. The χ in (a) represents the angular deviation of the maximum resolved shear stress plane to the ($\bar{1}$01) plane.

temperatures, where high stresses are needed to move the dislocations. On the other hand, at high temperatures, the stress needed to move the dislocation is much lower.

The movement of the dislocation with the non-planar core cannot occur without the transformation of the core to a glissile configuration. The exact process of core transformation and movement is a subject of investigation [51]. Nonetheless, this process is thermally activated, which is why ductile-brittle transition is found in bcc metals[2]. Another remarkable feature of the bcc lattice is the twinning-antitwinning asymmetry of the shear stress parallel to the slip direction [52, 53]. In practice, the twinning-antitwinning asymmetry is manifested by a relatively low resistance to shearing the crystal on the {112} plane in the twinning direction and higher resistance to shear in the opposite, antitwinning, direction [54]. This asymmetry has its origin in different atomic arrangements when shearing the crystal in the two opposite directions [55]. Fig. 1.3 shows a schematic illustration of the bcc lattice sheared in the twinning and antitwinning sense.

[2]In practice, ductile-brittle transition is heavily influenced by the level of impurities in the material.

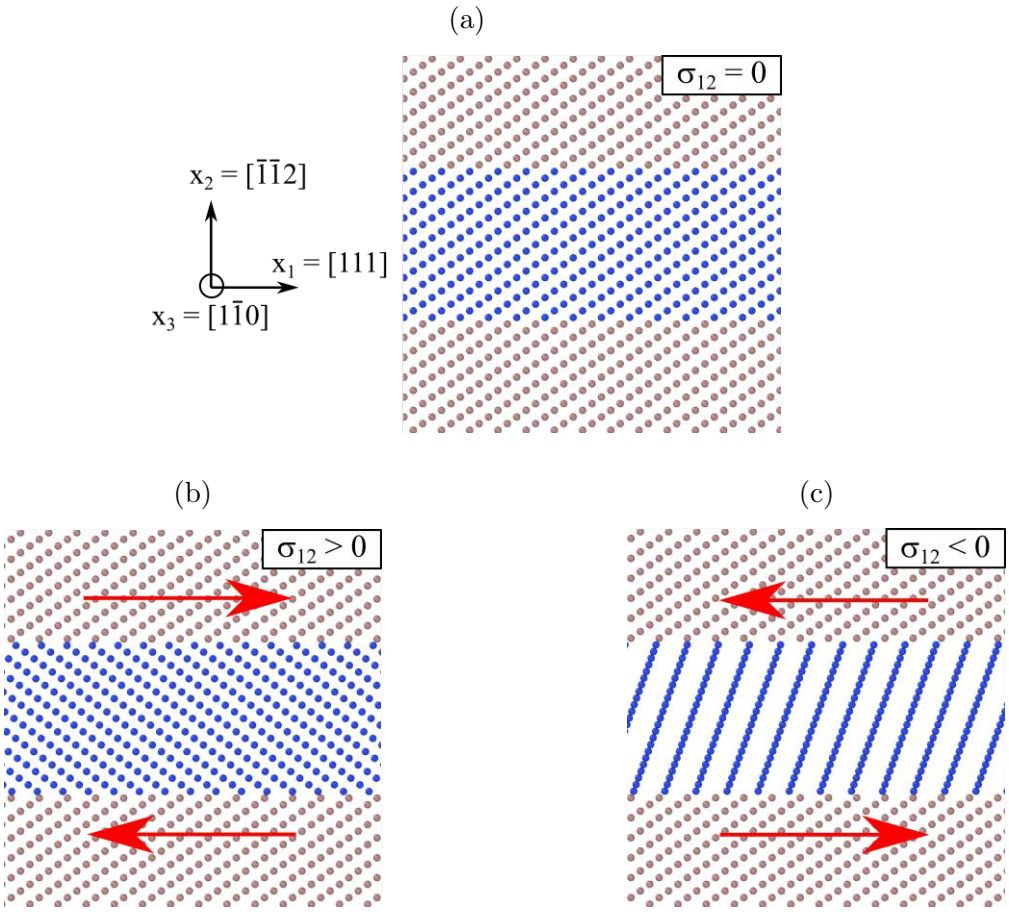

Figure 1.3: Illustration of the deformation of the perfect bcc lattice (a) in the twinning sense (b) and in the antitwinning sense (c).

Fig. 1.3 shows different lattice deformations when shearing the crystal in [111] or $[\bar{1}\bar{1}\bar{1}]$ directions along a {112} plane. Fig. 1.3(a) is the initial bcc lattice at zero applied shear. Fig. 1.3(b) shows the structure generated by shear applied in the twinning sense, which results in a twinned structure. The remaining Fig. 1.3(c) shows deformation caused by the shear of the same magnitude applied in the antitwinning sense that results in a structure different from the twin.

Using atomistic modeling, Ito and Vítek [56] found out that shear stress parallel to the slip direction, referred to as critical resolved shear stress (CRSS) is not symmetric with respect to the change of sign of the angle χ of the maximum resolved shear stress plane (MRSSP, the plane in the zone of the slip direction with the largest resolved shear stress parallel to the slip direction). This is represented in Fig. 1.4.

According to the Schmid law, the plastic deformation is initiated on the slip system for which the resolved shear stress parallel to the slip direction acting in this slip plane is the largest [57]. The relation between the uniaxial load represented by the stress σ, the orientation of the applied load, and the Schmid stress τ is:

$$\tau = m\sigma, \tag{1.1}$$

where $m = \cos\chi \cos\lambda$ is the Schmid factor. Here, χ is the orientation of the MRSSP,

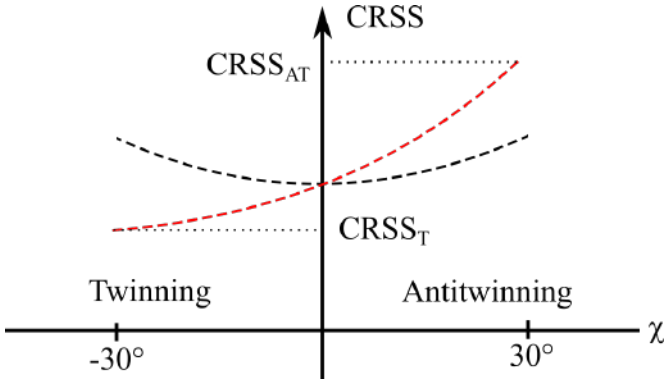

Figure 1.4: Schematic representation twinning-anitwinning asymmetry (red) for shear stress applied in various MRSSPs (angle χ) parallel to the slip direction. The black dashed curve follows the CRSS(0)/cosχ relationship and represents a hypothetical material without the twinning-antitwinning asymmetry.

as explained before, and λ the angle between the loading axis and the slip direction. The CRSS and the Schmid stress are related by $\tau = \text{CRSS} \cos\chi$.

Due to the crystal symmetry, the angle χ ranges from values from -30° to 30°, i.e. from $(\bar{1}\bar{1}2)$ plane to $(\bar{2}11)$ plane. Shearing the crystal in the $(\bar{1}\bar{1}2)$ plane parallel to the [111] direction produces a twin shown in Fig. 1.3(b). However, applying the shear of the same magnitude but opposite direction, i.e. $[\bar{1}\bar{1}\bar{1}]$, does not produce a twin; instead it results in the high-energy structure shown in Fig. 1.3(c). If one of the above {112} planes is sheared in the twinning sense, the other is sheared in the antitwinning sense and vice versa. Reversing the sense of shearing on the MRSSP thus swaps the character (twinning $\leftrightarrow$ antitwinning) on the neighboring {112} plane.

Furthermore, due to the dislocation core being extended into three planes, the dislocation glide is affected by stresses not belonging to the slip plane. These stresses are called non-Schmid stresses [56,58,59]. The asymmetry of the CRSS with respect to the orientation of the MRSSP and its variation with the shear stresses parallel to the slip direction cause the breakdown of the Schmid law in bcc metals.
The simulations also revealed that if the shear stress perpendicular to the slip plane of 1/2[111] dislocation is high enough, the dislocation may glide on planes with lover resolved shear stress than the most highly stressed plane. This unusual behavior is referred to as anomalous slip. While the previously mentioned phenomena are prevalent in bcc metals at low temperatures, anomalous slip has been reported only in Mo, V, W, Nb, Ta [58,60–74]. This proves that this behavior is not connected only to crystallography but also to details of the atomic bonding. The effect of non-glide stresses also plays an important role in the tension-compression asymmetry [75], where tension and compression stress-strain curves for single crystals with the same loading axis differ significantly. The non-planar character of the dislocation also allows for easier cross-slip of the dislocation into a {110} plane with lower resolved shear stress parallel to the slip direction. For the above-mentioned reasons, it is clear that the prediction of plastic behavior from the yield criteria based on the Schmid law cannot effectively describe the onset of plastic deformation in bcc metals [76]. A more appropriate form was proposed by Qin and Bassani [59] and parameterized

for Mo, W and Cr by Gröger et al. [77, 78]. and for α-Fe by Chen [76]. The yield criterion based solely on the Schmid law, in a simple way, would take the form of Eq. (1.2):

$$\tau^{\alpha}_{Schmid} \leq \tau^{*}_{cr}. \tag{1.2}$$

In this equation, τ^{α}_{Schmid} represents the Schmid stress acting in the slip system α and drives the dislocation in the glide plane. When it reaches the the critical value of stress on the slip system α, the dislocation glide will begin. This yield criterion doesn't account for non-glide stresses. The generalized version of (1.2) yield criterion takes the form:

$$\tau^{\alpha *} = \tau^{\alpha}_{Schmid} + a_1\tau^{\alpha}_{1} + a_2\tau^{\alpha}_{2} + a_3\tau^{\alpha}_{3} \leq \tau^{*}_{cr}. \tag{1.3}$$

The three terms containing a_1, a_2 and a_3 represent the stresses that modify the structure of the dislocation core (so-called non-glide stresses). The term τ^{α}_{1} is the stress acting parallel to the slip direction but applied in a different $\{110\}$ plane. This term introduces the twinning-antitwinning asymmetry of the critical resolved shear stress. The τ^{α}_{2} and τ^{α}_{3} are shear stresses perpendicular to the slip direction (they do not affect the Peach-Koehler force acting on the dislocation). The coefficients (a_1, a_2, a_3 and τ^{*}_{cr}) represent adjustable parameters determined by atomistic calculations [77]. The form (1.3) describes accurately the onset of plastic deformation in non-magnetic materials and magnetic materials (α-Fe [76]), where the changes of magnetism do not affect yielding. In general, the presence of internal magnetic order requires further generalization of the yield criterion described by (1.3). In the case of bcc metals, only chromium and α-iron show internal magnetic order. We suggest that the extended form of the yield criterion for magnetic materials takes the form:

$$\tau^{\alpha *} = \tau^{\alpha}_{Schmid} + a_1(\mathbf{M})\tau^{\alpha}_{1} + a_2(\mathbf{M})\tau^{\alpha}_{2} + a_3(\mathbf{M})\tau^{\alpha}_{3} \leq \tau^{*}_{cr}(\mathbf{M}), \tag{1.4}$$

where the $\mathbf{M}$ broadly represents the internal magnetic state of the material. These yield criteria are essential for the simulation of the behavior of the materials. Buchheit et al. [79] used the yield criterion published by Gröger and Vítek [77] and implemented it to polycrystalline plasticity model. Cereceda et al. [80] developed a temperature-dependent yield criterion for tungsten single crystal based solely on the atomistic simulations. A single crystal yield criterion for chromium was recently developed by Gröger and Vítek [78] based on atomistic modeling of isolated 1/2[111] screw dislocation. Generally, these yield criteria and fracture criteria are used extensively in applied research, and industry [81–85].

The glide of $1/2\langle 111\rangle$ screw dislocations in bcc metals have been also studied from the 1950s by quantum mechanics, and it was hypothesized that their movement could happen due to the quantum tunneling of the dislocation through the potential barrier [86]. Mott [87] was the first to outline the theory, however, did so without a knowledge of the exact atomic positions around the dislocation. Weertman in 1958 proposed a theory for low-temperature dislocation creep employing also the quantum effects [88]. In the later years, the theory was further expanded and studied [89–92]. The dislocation core has been studied thoroughly using DFT by Frederiksen and Jacobsen [16]. Ventelon et al. compared DFT with the empirical potentials in [45] and investigated the Peierls potential of the screw dislocation in Fe and W

in [44]. Proville studied in 2012 the quantum effects on thermally activated glide of dislocations in α-iron and suggested that quantum effects strongly affect the critical stress to move the dislocation at temperatures below the Debye temperature [93]. Other relevant DFT studies concerning dislocation slip in bcc metals have been published by Dezerald et al, Rodney et al. and Marichal et al. [19, 46, 94].

1.2 Crystal and magnetic structure of α-Fe

The ground state crystal structure of α-iron is the bcc structure. Iron undergoes two phase transformations between the absolute zero temperature and the melting point of 1811 K. The high-temperature allotrope, δ-iron exists from melting point to 1667 K, and crystallizes in the bcc crystal structure. Upon further cooling, the δ-iron changes into γ-iron, which is accompanied by a change in the crystal structure to a face-centered cubic structure. The γ-iron allotrope is stable down to 1185 K when it changes to α-iron with the bcc structure, which is stable down to 0 K. Occasionally, the β-iron allotrope is mentioned and defined as the non-magnetic version α-iron above the Curie temperature of 1043 K even though no change in the crystal structure takes place.

Under ambient conditions, α-iron is ferromagnetic. The ferromagnetism originates from four unpaired $3d$-electrons, whose dipolar interaction gives rise to long-range order and formation of magnetic domains [95]. The parallel orientation of spins stems from exchange interaction which favors parallel alignment of spins on nearest neighbor atoms. Within the domain, the magnetization has a well-defined direction. The macroscopic sample is usually unmagnetized, because of the presence of many domains with random orientations of magnetizations. The internal magnetic structure of solids can be manipulated by external magnetic field.

The internal magnetic state of crystals is affected by magnetocrystalline anisotropy, which has been studied extensively in the past [96, 97]. Magnetocrystalline anisotropy is a phenomenon where more energy is necessary to magnetize the crystal in certain crystallographic orientations than in others. The direction of spins in α-iron is usually in the $\langle 100 \rangle$ direction, which is the so-called easy axis of magnetization as it requires the least energy to reach this state. However, α-iron can also be magnetized along $\langle 110 \rangle$ and $\langle 111 \rangle$, which are called the medium and hard axis of magnetization, respectively. The magnetization curves for each direction are shown schematically in Fig. 1.5.

The magnetic anisotropy for cubic materials can be expressed by Ref. [98, pp. 198–202]:

$$E_{crys} = K_1(\alpha_1^2\alpha_2^2 + \alpha_2^2\alpha_3^2 + \alpha_3^2\alpha_1^2) + K_2(\alpha_1^2\alpha_2^2\alpha_3^2) \tag{1.5}$$

where K_1, K_2 are material and temperature dependent constants and α_1, α_2 and α_3 are the directional cosines of the angles between the the orientation of spins and a particular crystal axis. The K_1 and K_2 constants for α-iron are 4.8 $\times 10^4$ J/m^3 and ± 0.5 $\times 10^4$ J/m^3 Ref. [98, p. 227]. A 3D shape visualization of the magnetic anisotropy energy density of α-iron at room temperature is shown in Fig.

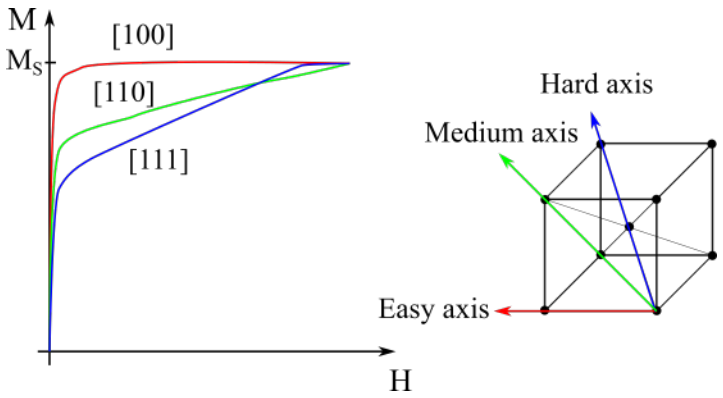

Figure 1.5: Schematic representation of magnetization curves for easy (red, ⟨100⟩ directions), medium (green, ⟨110⟩ directions) and hard (blue, ⟨111⟩ directions) axes of magnetization. Image modified from [98, p. 199].

1.6(a). Fig 1.6(b) shows the magnetic anisotropy energy density in the stereographic projection.

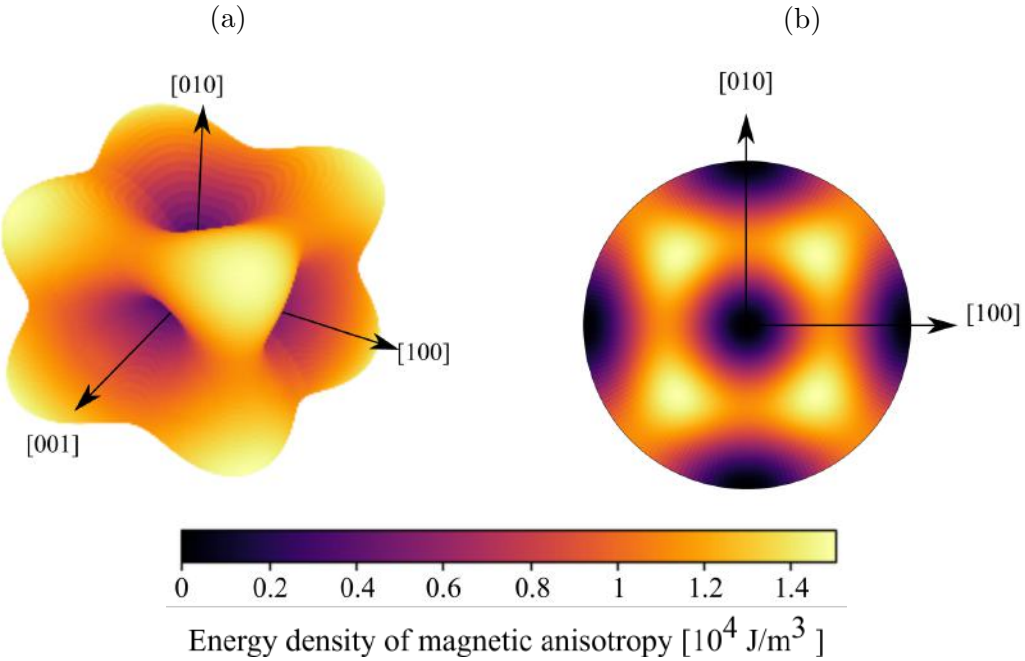

Figure 1.6: (a) 3D visualization and (b) stereographic projection of a magnetic anisotropy energy density of α-iron single crystal at ambient temperature. The graphs correspond to anisotropic coefficients $K_1 = 4.8 \times 10^4$ J/m^3, $K_2 = 0$ J/m^3.

1.3 Crystal and magnetic structure of Cr

Chromium crystallizes in the bcc structure and keeps the same crystal structure until the melting point of 2180 K. Chromium is also the only element of the 6$^{\text{th}}$ group with internal magnetic order. Its unpaired $4s$ and $3d$ spins condense into incommensurate Spin Density Waves (SDW) with wavevectors $\mathbf{Q}$ parallel to ⟨100⟩ directions

and wavelengths between 21 units cells at 78 K and 28 unit cells at 311 K [99]. The observed magnetic behavior is a consequence of sinusoidal polarization of the d-band electron magnetic moments [100]. The magnetic state is, however, dependent on form of chromium. It has been shown that powder chromium exhibits simple antiferromagnetism even at temperatures higher than the Néel temperature of a single crystal [101]. Annealed single-crystalline Cr exhibits two first-order magnetic phase transitions at 123 and 311 K. In the temperature range from 0 to 123 K, the stable magnetic phase is represented by longitudinal SDWs (LSDW) in which the orientations of all magnetic spins $\mathbf{S}$ are parallel to the wavevector $\mathbf{Q}$. The first atomic neighbors in bcc Cr favor antiferromagnetic coupling, which results in two SDWs that are mutually phase-shifted by one-half of their wavelength, as shown in Fig. 1.7(a). Between 123 and 311 K the stable phase is composed of transversal SDWs (TSDW), where all spins $\mathbf{S}$ are perpendicular to the wavevector $\mathbf{Q}$ [7,102,103]. This structure is shown in Fig. 1.7(b) and is again represented by two opposite SDWs with antiferromagnetic coupling between the first nearest neighbors. Above the Néel temperature of 311 K, Cr becomes a paramagnet. The two first-order phase transitions at 123 K and 311 K cause singularities in the measurements of susceptibility [104], and lead to non-negligible changes of elastic constants [105, 106].
The temperature at which the character of SDWs changes is often referred to as the spin-flip temperature T_{SF}. Moreover, the shortest lattice vectors of the bcc structure, and thus the Burgers vectors of dislocations, are of the $1/2\langle 111\rangle$ type, but the shortest separation between identical spins in parallel SDWs is of the $\langle 100\rangle$ type. On the other hand, the $\langle 100\rangle$ dislocations would give rise to about 1.3 times larger stored elastic energy per unit dislocation length as compared to $1/2\langle 111\rangle$ dislocations, if Cr is treated as an elastically isotropic material. The presence of dislocations with $1/2\langle 111\rangle$ Burgers vectors, predicted by elasticity, thus results in local frustration of the internal magnetic order. The magnetic structure of Cr around dislocations in modeled by Bienvenu et al. [11] using the density functional theory. The authors suggest that simple antiferromagnetism is a good approximation of the SDW ground state observed experimentally. They further state, that $\langle 100\rangle$ dislocations are stable in chromium and shearing the crystal by $1/2\langle 111\rangle$ dislocation on $\{110\}$, $\{112\}$ and $\{113\}$ plane introduces a magnetic fault. They further argue, that due to the magnetic order a necessity for the second $1/2\langle 111\rangle$ dislocation that follows the original dislocation arises, thus creating a superdislocation of the $\langle 111\rangle$ type.

The experimental study of magnetic defects in antiferromagnetic materials is a challenging problem. However, there are at least three techniques capable of delivering some information about the magnetic order around defects. Probing the chromium single crystal by coherent X-rays can reveal magnetic defects embedded a short distance under the surface in bulk chromium [107]. Probably the most useful technique to determine magnetic changes in materials is neutron scattering. However, the neutron diffraction cannot focus on individual defects but rather observes the whole crystal. This fact is often advantageous since it allows us to study the changes in a more statistical way. So far, no neutron diffraction experiment was utilized to look for changes in magnetic ordering due to plastic deformation, but rather to precisely describe the antiferromagnetic states and features in chromium [108]. The third technique is spin-polarized scanning tunneling microscopy [109], which

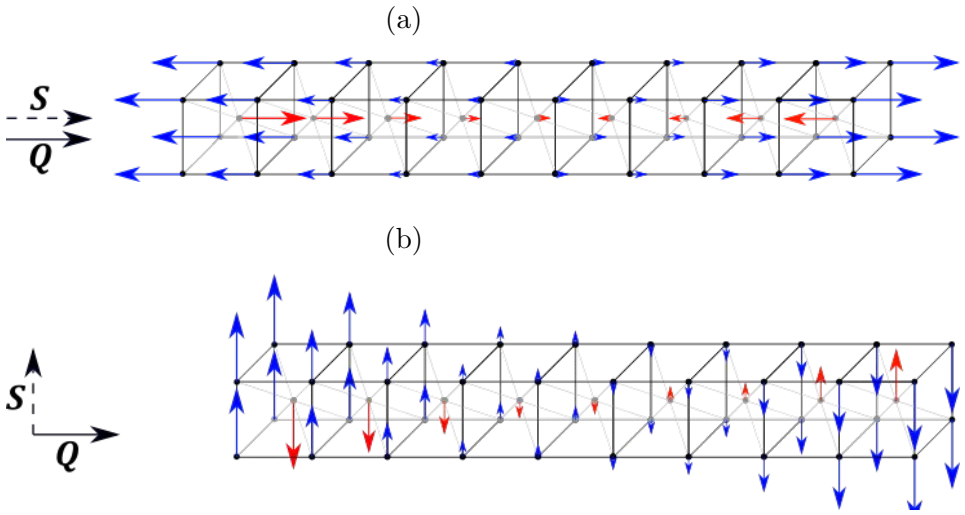

Figure 1.7: Orientation of spins **S** relative to the wavevector **Q** in (a) longitudinal spin density wave, (b) transversal spin density wave.

is a scanning probe microscopy technique capable of delivering information about magnetism in the material as well as topography. An extremely sharp tip coated with magnetic material scans the surface while the tip is biased against the specimen. The electron current can tunnel through the gap between the tip and the specimen. The electrons with spins aligned parallel to the magnetization of the tip have higher chance of tunneling and thus creating current.

1.4 Low-temperature deformation of α-Fe

The first study concerning the deformation of the iron crystals was done in 1926 by Taylor and Elam [13] who proposed a deformation model based on the distortion of a bundle of hexagonal rods in order to explain wavy nature of the slip lines. This concept precedes the invention of the concept of dislocations almost by a decade. Another major work was done by Steijn & Brick [110] on single crystals of iron with small amounts of titanium intended to serve as a deoxidizer, produced by strain anneal method. The specimens were prestrained to approx. 3 % and annealed, starting at 723 K with the temperature increasing every 24 hours by 60 K until 1163 K. After reaching the highest temperature, the specimens were further annealed for three days, and cooled in furnace. The annealing was done in purified helium. The authors report that the specimens tested in tension at 90 K fractured by cleavage without any slip lines or striations visible, except one sample that showed slip on the (110) plane. The specimens tested in compression showed less distinct slip lines compared to the specimens tested at room temperature (RT), and twinning was identified by loud crunching sounds during the straining. The authors conclude that slip occurred on the planes in the $\langle 111 \rangle$ zone. At low temperatures, the slip tends to shift towards $\{110\}$ planes. However, the authors suggest that slip takes place also on high-index planes. Soon after, Allen et al. [111] published a study on

iron single crystals prepared by the strain anneal technique with a purity of 99.96 % Fe deformed in the temperature range from 20 to 373 K. The authors report that all tensile tests at temperatures higher than 77 K (149, 199, 293, and 373 K) resulted in ductile deformation and all samples had a 100% reduction in the area regardless of their orientation. The largest variation of the deformation mechanism occurred at 77 K, which included the cleavage, slip and twinning. The dependence of the slip mechanism on the orientation of the loading axis for 77 and 20 K is shown in Fig. 1.8(a) and 1.8(b) respectively. At 77 K, the slip is dominant for orientations from the center of the stereographic triangle towards the $[011] - [\bar{1}11]$ edge, whereas the cleavage dominates for the loading directions from the [001] corner to the center. Twinning is confined to the region with loading directions along the $[012] - [\bar{1}12]$ line and a small area near the [011] pole. This observation agrees with the finding of Harding [112], who did the tensile tests at 77 K with a strain rate of $10^{-3}\,s^{-1}$ on iron single crystals with 276 wt. ppm impurities (C+N+O+H concentration of interstitial impurities is approx. 41.4 wt. ppm). Biggs et al. [113] also reported the same behavior at 90 K for strain rates of $10^{-4}\,s^{-1}$ on single crystals with 4400 wt. ppm of impurities (from which it was 600 wt. ppm. of C).

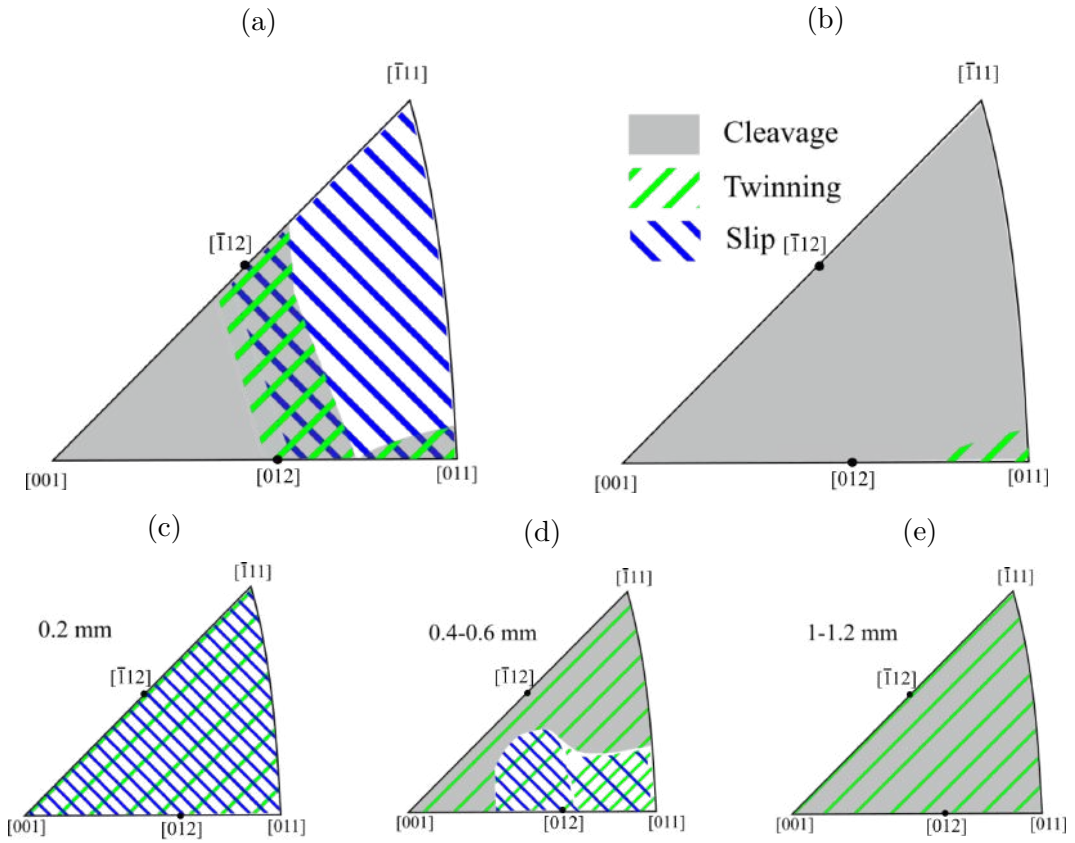

Figure 1.8: The distribution of dominant deformation mechanism in α-Fe single crystals in tension at (a) 77 and (b) 20 K according to [111] and in compression at 77 K as described by Altshuler et al. [114] and Aono et al. [5] for single crystals with the diameters of (c) 0.2 mm, (d) 0.4-0.6 mm and (e) 1-1.2 mm.

In contrast, the deformation mechanism at 20 K is cleavage, except again of a

very small area around [011] pole (see Ref. [111]). The authors conclude that slip traces were observed on the {110}, {112} and {123} planes. They were straight in the early stages of the deformation, and became wavy in the later stages.
The authors argue that the high critical stresses for slip and twinning at 77 K for orientation that favor multiple slip is possibly caused by dislocation locks or pinning of dislocations to the obstacles, which consequently leads to the increased propensity to cleavage. Further research of Keh in 1965 [115] focused on work hardening in iron single crystals at room temperature. He suggests that the slip occurs on planes that contain the ⟨111⟩ vectors (which are {110}, {112} and {123} planes), however from the electron micrographs shown in his work, we can assume that at least majority, if not all of the slip, occurs on {110} planes. The author further confirms that the waviness of the slip traces is the result of the zig-zag motion of $1/2\langle 111\rangle$ screw dislocations on two {110} slip planes and concludes that the initial work hardening rate in iron crystals depends on a number of operational slip systems (the more slip systems, the greater the work hardening) and on the ratio of the density of dislocations in primary and secondary slip systems. A comprehensive study of the plastic deformation of α-iron was done by Altshuler and Christian in 1967 [114]. They performed compression tests from 2 to 293 K on both single-crystalline and polycrystalline specimens and focused primarily on the temperature and strain rate sensitivity of the plastic deformation. The authors report that polycrystalline specimens with grain sizes ranging from 13 µm in the center of the specimens to 40 µm along the $[011]-[\bar{1}11]$ edge have similar mechanical properties with single crystals, and both deform by slip on {110} planes. Furthermore, the large temperature and strain rate sensitivity is not caused by the residual interstitial impurities and the authors lean to the explanation of lattice friction in terms of the Peierls-Nabarro force. Aono et al. [5] performed tension tests on iron single crystals at 4.2 K prepared from different source materials and reported the deformation mechanism based on the diameter of the cylindrical single crystals and their orientation. Their findings are summarized in Fig. 1.8(c), 1.8(d) and 1.8(e) for diameters of 0.2, 0.4-0.6 and 1-1.2 mm, respectively. The average concentration of interstitial impurities is 45 wt. ppm (C + N + O) and 890 wt. ppm (substitutional elements) in Altshuler's specimens and 37 wt. ppm (C + N + O) and 157 wt. ppm (substitutional elements) in Aono's specimens. In the case of large single crystals, the predominant deformation mechanism is pure cleavage or cleavage mixed with twinning. The twinning can be found in most orientations for single crystals with the diameters between 0.4 and 0.6 mm. However close to the $[\bar{1}11]$ corner of the stereographic triangle, the cleavage starts to dominate. Twinning is most dominant around the [011] corner, accompanied by slip, which is visualized by the increased density of the hatching in Fig. 1.8(d). In the center of the stereographic triangle, the slip is dominant but accompanied by twinning. The slip with less pronounced twinning is also the dominant mechanism for single crystals with the diameters of 0.2 mm regardless of the orientation of the loading axis. These findings partially agree with those of Keh in the case of the small crystals. However, they give contradictory predictions for the larger crystals. It is important to emphasize that prestrain suppresses the nucleation of twins (Aono et al. [5]).

Franciosi et al. [116] examined non-pre-strained iron single crystals at room tem-

perature in-situ by the SEM and AFM methods. Their results showed that if the slip occurs on {110} planes, the slip traces are long and straight. However, if the slip traces are macroscopically wavy, they are composed of short segments of traces that match {110} planes and most likely propagate by composite slip and cross-slip. They reported that the purity of their samples was 86 wt. ppm (of interstitial impurities C+N) and 1317 wt. ppm of substitutional impurities while strain rate was 10^{-5} s^{-1}. Kimura [117] performed tensile tests of coarse-grained iron specimens at temperatures between 4.2 K and 273 K with a purity of more than 99.999% and less than 0.5 wt. ppm of carbon, strained at 8×10^{-5} s^{-1}. He reports that coarse-grained specimens had purity expressed as residual resistivity ratio (RRR, measured between 4.2 and 273 K) between 3800 and 5000. The specimens strained at 4.2 K with the RRR of 3800 fractured by ductile fracture with a reduction of the area by 100 %, while the specimen with the RRR of 5000 fractured by cleavage. Kimura suggests that the fracture of pure specimen could be caused by intrinsic low temperature brittleness of iron but advocates that low temperature brittleness of iron is caused predominantly by impurities. The crystallographic orientation of the grains, where the cleavage was manifested, is not mentioned. The deformation mechanism of most of the specimens was slip. However, some if his stress-strain curves exhibit stress drops that may be associated with twinning. Kranzlein et al. [118] prepared a single crystal of α-Fe by employing the strain anneal technique and tested them in tension from 77 K to the room temperature. The approximate amount of impurities was 33.2 wt. ppm (C + N + O + H) and up to 143 wt. ppm of substitutional elements. The strain rate was approximately 3×10^{-4} s^{-1}. Kranzlein et al. further states that the deformation mode of iron single crystals at 77 K depends on the orientation of the crystal. The cleavage dominates for loading directions close to the [001] pole, slip is mostly dominant along [011]–[$\bar{1}$11] edge, and twinning accompanied by the cleavage is observed at the center of the stereographic triangle. Yabe et al. [119] further discusses the simple shear and plane strain compression tests on single-crystalline α-iron specimen with respect to the orientation of the loading axis.

1.5 Low-temperature deformation of Cr

The early studies of Cr made in the late 1960s and 1970s focused primarily on its magnetic properties [102, 120]. The first studies of plastic behavior done on single crystals by Greiner [3] provided some insight into the high-temperature deformation behavior and fracture of Cr. Marcinkowski et al. [121] studied low-temperature deformation of polycrystalline chromium in tension and discussed the effect of grain size and strain rate on the yield and flow stress and compared the results with the Hall-Petch equation. Marcinkowski further uses one of the first models for nucleation of twins in bcc metals, where the 1/2[111] screw dislocation dissociates into a pair of 1/3[112] and 1/6[11$\bar{1}$] partial dislocations [121]. According to the model, the latter dislocation is highly mobile even at low temperatures. The strain rate used in the study is 8.28×10^{-5} s^{-1}, but the purity is not mentioned. Marcinkowski further states that twins originate in the {112} planes with a twinning direction of $\langle 111 \rangle$. The yield stress is unaffected by the change in the magnetic order and twinning is the dominant deformation mechanism below 123 K. The first in-situ straining ex-

periments on Cr (99.98 % with 27 ppm of C + H + N + O impurities) at 300 K by Reid and Gilbert [122] revealed that cross-slip events were not compatible with the glide of conventional $1/2\langle 111\rangle$ dislocations, but it could be explained by the motion of $\langle 100\rangle$-type dislocations. Reid, Gilbert and Hahn [123] subsequently tested Cr single crystals of similar purity in tension between 77 and 300 K and observed slip on {110} planes, twinning on {112} planes, and cleavage on {100} planes. In many cases, the slip was rather homogeneous, which complicated the identification of operational slip systems by the slip trace analysis. Sameljuk et al. [124] found a similar behavior when observing cleavage along {100} planes in tension at 198 K. However, no detailed analysis of the internal structure of twins was presented except that their orientation agrees closely with the traces of {112} planes. The level of impurities in the material used was 75.1 wt. ppm (substitutional) and 110 wt. ppm (C + O + N interstitial). The velocity of deformation used was 1 mm/min. Recently, attention was paid to dislocation nucleation at higher temperatures studied by nanoindentation. Wu and Nieh [125] described the pop-in behavior that occurs during nano-indentation and suggested that dislocations required to accommodate the plastic deformation during the indentation are nucleated heterogeneously with the main contribution from interstitials. Choi et al. [126] discussed the phenomenon of thermally-activated plasticity by examining the temperature-dependent mechanical behavior of high-purity chromium using high-temperature nanoindentation.
The mechanism of plastic deformation depended sensitively on crystal purity, whereby even a small concentration of interstitial impurities in the order of tens of wt. ppm was sufficient to make the material brittle at room temperature [127]. Recent studies done on chromium focus on explaining deformation mechanisms at high temperatures by employing the relatively non-destructive technique, such as nanoindentation. However, more in-depth research involving the analysis of slip traces and surface misorientations is still lacking.

1.6 Neutron diffraction

In principle, neutron diffraction is similar to X-ray or electron diffraction in principle. However, due to different interaction of these particles/waves with matter, the reason for their use differs. While electron sources are easily obtained and relatively cheap, the penetration depth is very small (depending on the energy of the incident electron and the material). The electron, as a particle, carries both spin and electric charge and can be, therefore, influenced by electric and magnetic fields. However, the scattering due to the electric field (electrostatic interaction with the atomic electron cloud) is much stronger. Therefore, the only obtainable information about the magnetic properties of the material results from the induced magnetic fields reaching out of the specimen, which influence the electrons [128] by the Lorentz force. This can be used in Lorentz microscopy [129], which can visualize magnetic domains in specific orientations. These studies are made using unpolarized electrons. If one can differentiate the polarization of the electrons, the magnetic domains can be visualized, and the direction of magnetization measured [130, 131]. Polarized X-ray diffraction has been shown to be a complementary technique to neutron diffraction [132]. However, the penetration depth is small compared to the latter, and thus

the information comes from the surface of the specimen. The neutrons do not carry an electric charge and, unlike the electrons or X-rays, scatter from atomic nuclei and not from the electron clouds surrounding the nuclei. Furthermore, the neutron carries a spin and is, therefore, sensitive to the unpaired electrons which make up the magnetism in solids [133]. Due to the interaction with atomic nuclei and not the electron clouds around them, neutrons scatter very weakly, and neutron sources thus produce lower flux compared to the other techniques. The weak interaction of neutrons leads to one of the most significant advantages of neutron scattering - the scattering happens in the whole specimen and is not constrained to the surfaces or very small volumes as the X-ray or electron diffraction. However, the operation of a neutron facility is very costly and, therefore, this technique is concentrated to a few places around the world.

There are only two methods of effective neutron creation. First uses the nuclear reactor, similar to those operated in the nuclear power plants. The second option is a spallation source which requires an accelerated beam of protons with the energy around 1 GeV created by the cyclotron or linear accelerator. These protons hit a target (commonly a large steel tube filled with mercury, tantalum, lead, tungsten, or other heavy metal [134]). The nuclei in the target are excited by the impact and release neutrons upon deexcitation [135]. The spallation process is more expensive than nuclear fission, however, it is also more efficient. Other advantages of the spallation source are the ability to create a neutron pulse by pulsing the incident proton beam (neutron flux created by fission is constant), and the spallation neutrons cannot trigger further spallation to produce more neutrons [136]. This makes the spallation source safer as no chain reaction can occur.

Because neutrons are chargeless, it makes them very hard to focus compared to electrons or X-ray photons as no lenses effective to neutrons exist, but the use of mirrors is needed. Furthermore, neutrons scattering lengths differ widely among the elements and isotopes and are independent of the atomic number. For example hydrogen, virtually undetectable with electrons or X-rays, can be easily distinguished by neutrons [137]. Nonetheless, using neutrons as particles for imaging is still a relatively new method, and the resolution of neutron microscopes are far behind the electron microscopes [137]. The following list offers neutron scattering facilities with spallation or reactor sources around the world [138–163]:

- Spallation sources: KENS (Japan), J-Parc (Japan), JAERI (Japan), ISIS (United Kingdom), SINQ (Switzerland), ORNL (USA), LANSCE (USA).

- Reactor sources: KUR-RI (Japan), ISSP (Japan), KAERI (South Korea), OPAL (Australia), ILL (France), GeNF (Germany), BENSC (Germany), FRM II (Germany), TUDelft (Netherlands), BNC (Hungary), FLNP (Russia), PNPI (Russia), NPI Řež (Czech Republic), JEEP II (Norway), ORNL (USA), MNR (Canada), NCNR (USA), CRL (Canada), CARR (China), CMRR (China).

The Swiss spallation neutron source, SINQ, is a large-scale facility operated by the Paul Scherrer Institute, one of the federal research centers in Switzerland. The SINQ delivers a continuous thermal neutron flux of 10^{14} $cm^{-2}s^{-1}$ to a wide range of instruments or, alternatively, slows them down by deuterium moderator to make the

neutrons more useful for other types of experiments. The single crystal diffractometer Zebra is one of the instruments of the SINQ that uses a monochromatic flux of thermal neutrons to study the materials. The Zebra diffractometer is equipped to use the neutrons with the 1.18 Å or 2.32 Å wavelengths. A wide range of additional instruments such as furnaces, cryogenics, an apparatus to create a magnetic field, and others are available. A linear (1D) or areal (2D) detector can be utilized to measure the the diffraction spectra [164]. We have used this facility for all neutron scattering measurements done in this work.

1.6.1 Expected neutron reflections in bcc lattice

The visibility of nuclear diffraction peaks is dependent on the crystal structure. In some cases, certain diffractions are not allowed due to destructive interference. This restriction comes from the structure factor for the bcc lattice [165, p. 259]:

$$F = f\{1 + e^{\pi i(h+k+l)}\} \tag{1.6}$$

where h, k and l are indices in reciprocal space. The structure factor in Eq. (1.6) can be expanded into:

$$F = f\{1 + \cos[\pi(h+k+l)] + i\sin[\pi(h+k+l)]\}. \tag{1.7}$$

In this form, one can more clearly see the effect of the h, k and l indices. Since they are always integers, the sine part will be always zero and the cosine part will oscillate between 1 and -1 for odd and even sum of h,k,l, respectively. Thus, for $h + k + l =$ odd, the structure factor $F = 0$ and for $h + k + l =$ even, the structure factor $F = 2f$. The structure factor is used for computations of the complex amplitude of the diffracted beam. In cases, where the structure factor is zero, the amplitude of the diffracted beam will be also zero. Diffraction in bcc lattices is thus allowed only from the planes for which the sum of h, k and l is even (i.e. 110, 200, 211 etc.).

In reality, reflection from planes with odd sum of the indices cancel each other out, as the diffraction from successive plane will come with exactly the opposite phase than that of the previous plane, as shown in Fig. 1.9. The phase change arises from a different relative position of atoms in the {100} and {200} planes.

The diffraction peaks may occur also due to the internal magnetic order of the material. Here, we briefly discuss the effect of different magnetic orders, namely disordered paramagnetic state, ferromagnetic state, antiferromagnetic state, and antiferromagnetic spin-density waves.

The diffraction techniques can only detect structures that repeat with certain frequency. **Paramagnetic** state does not have an order to the direction of the spins and thus no diffraction peaks are visible.

In case of **ferromagnetism**, all spins are oriented in one direction and since they originate from the atoms, they repeat with the same frequency as the crystal lattice. Therefore, the magnetic diffraction peaks are placed on the nuclear diffraction peaks and their intensities are superimposed. As the magnetic and structural lattices are identical, forbidden reflections are also applicable for magnetic scattering. Moreover, the intensity of reflections will decrease with increasing temperature

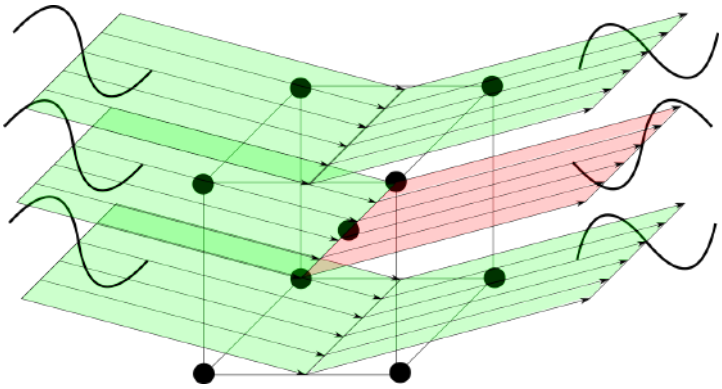

Figure 1.9: Schematic representation of diffraction from {100} and {200} planes in the bcc structure. The sinusoidal curves represent the amplitude of the scattered wave.

as the ferromagnetic order becomes more disordered. The contribution of magnetic scattering will be zero for temperatures above the Curie temperature [166].

Antiferromagnetism produces magnetic peaks at positions where nuclear reflection are forbidden. For example, chromium can exist in antiferromagnetic state and magnetic neutron scattering will reveal a single peak corresponding to a 100 reflection (Ref. [101]). This can be explained by imagining the antiferromagnetic cell as two simple cubic cells shifted by $1/2\langle 111\rangle$ vector from each other. This creates two simple cubic cells, one with spins oriented in one direction and the second with spins oriented in the opposite direction. Moreover, since simple cubic lattice has no forbidden reflections, one can expect to see magnetic reflection peaks resulting from antiferromagnetic structure at places where the nuclear reflections are forbidden. However, in come cases the magnetic cell is larger than the structural unit cell, such as in NiO. In this particular case, the magnetic diffraction occurs from a magnetic cell that is twice as large as chemical cell. Therefore, magnetic and nuclear peaks will correspond to two different lattices [167, 168].

An **incommensurate spin-density wave** with antiferromagnetic coupling along $\langle 100\rangle$, found in annealed chromium, has a temperature-dependent wavelength λ of approx. 21 unit cells at 78 K to approx. 28 unit cells at 311 K [7]. This is manifested by two diffraction peaks spaced by $\pm 1/\lambda$ from the forbidden $\langle 100\rangle$ nuclear reflections in reciprocal space. A more detailed explanation of reflections expected in chromium with SDW is in Section 1.7.

1.7 Manipulation of magnetic states

The magnetic domains present in the ferromagnetic materials represent regions with different magnetization and are separated by domain walls to minimize its internal energy [169]. The first observation of the magnetic domain walls was done by Williams, Bozorth, and Shockley in 1949 [170]. In a magnetically soft material, which is not being acted upon by external magnetizing field or stress, the macroscopic contribution of the magnetic domains to creation of the external magnetic field is canceled out by the opposite orientation of the magnetic domains, as shown

in Fig. 1.10(a). Therefore, its contribution to the external magnetic field is negligible. One can see in this figure that the vector sum of the magnetization is zero. If the external magnetizing field **H** is imposed, shown in Fig. 1.10(b), the magnetic domain with the same orientation will grow the most, while the one opposite to the external magnetic filed **H** will shrink. If the magnetizing field **H** is increased even more, the magnetization of the domains will start to rotate to align itself with the field, as shown in Fig. 1.10(c). The saturation is reached when the preferred magnetic domains reach their maximum size and are rotated "as much as they can". The growth of the domains in Fig. 1.10(b) is represented by the straight part of the magnetization curve in Fig. 1.1 and the rotation of the domains starts when the magnetization curve deviates from the straight line.

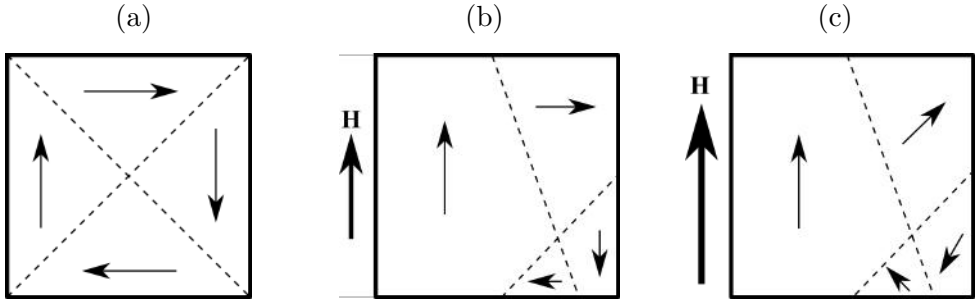

Figure 1.10: A schematic representation of domains in feromagnetic materials when acted upon by external magnetic field **H**. The arrows inside the pictures represent the direction of domain's magnetization and the bold arrow on the side demonstrates direction and magnitude of the external magnetizing field: (a) no external magnetic field, (b) small external magnetic field and, (c) large external magnetic field.

The second external process that influences the magnetization of the material is the magnetostrictive effect. The magnetostriction is a property of ferromagnetic materials that changes the dimensions of the specimen in response to the magnetic field. It is an effect caused mainly by the spin-orbit coupling. The atoms in ferromagnetic materials can be though of as magnetic dipoles due to the nonspherical nature of the electron distribution around the nuclei [98, p. 257]. If these oval dipoles are aligned so that their minor axes are aligned and the spins are parallel, pointing in the same direction, the repulsive forces between them are minimized. On the other hand, if they are aligned by their major axes, they produce a repulsive force which is relaxed by the change in the lattice parameter as they try to get further apart and this is manifested by strain. It should be noted, that the magnetostrictive effect is very small and the changes to the dimensions (strains) are in the order of 10^{-5} [171].
An opposite effect that causes changes to the magnetization in relation to the applied stress is called an inverse magnetostriction and the process is exactly opposite. The stretching of the crystal lattice caused by the stress rotates the dipoles into the direction with minimal energy. A schematic example of inverse magnetostriction effect is shown in Fig. 1.11. The initial state of the sample is identical with that shown in Fig. 1.10(a). The applied stress in the horizontal direction in Fig. 1.11(a) will favor the domains with magnetization to be aligned with stress. Upon increasing the magnitude of stress, shown in Fig. 1.11(b), the domains with magnetization

perpendicular to stress will vanish and if the stress is increased again, Fig. 1.11(c), the specimen will be saturated as only one domain remains.

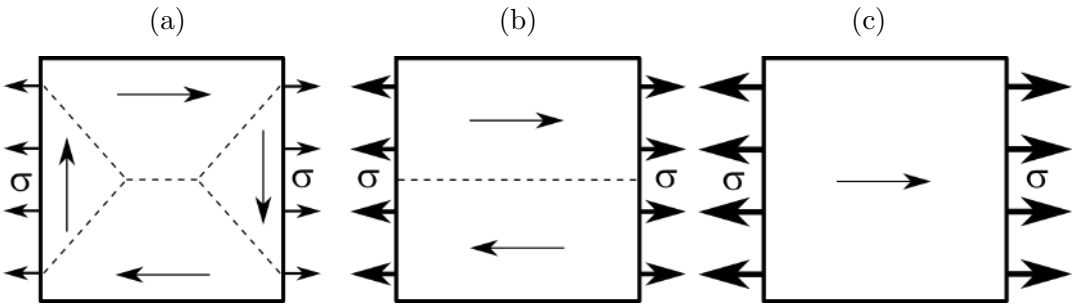

Figure 1.11: A schematic representation of domains in feromagnetic materials with positive magnetostriction under tensile stress $\boldsymbol{\sigma}$. The arrows inside the pictures represent the direction of domain's magnetization and the bold arrows on the sides demonstrate direction and magnitude of the stress. The initial state is similar to that shown in Fig. 1.10(a). Magnetic domains under (a) low tensile stress, (b) medium tensile stress, and (c) large tensile stress. The picture was adapted from [98, p. 263].

When chromium is heated above the Néel temperature, the magnetic order will naturally break apart, and the material will become paramagnetic. If it is cooled below Néel temperature *without an external magnetic field*, the magnetic order will become antiferromagnetic with SDW, which will be oriented randomly along $\langle 100 \rangle$ directions, and several domains will be created. This state is described as Triple-**Q** state, which is characterized by the wavevector **Q** parallel to all three $\langle 100 \rangle$ directions. To visualize a magnetic state of chromium, we will use reciprocal space diagrams as described by Bastow and Street [172]. These diagrams display the positions of measured or predicted satellite reflections in the form of balls in the neighborhoods of $\langle 100 \rangle$ reflections on axes correlating with the crystal directions. The nuclear reflections from the $\langle 100 \rangle$ planes are not shown in the diagrams since they are forbidden reflections[3]. Furthermore, only all positive (+,+,+) octant of the reciprocal space is shown and measured since the other seven octants are mirrored reflections of each other. The peak splitting notation is often simplified by assigning the reciprocal value of the wavelength as δ and, for example, the splitting of the peak in the neighborhood of [100] reflection in the direction of [010] would be noted as $[1, \pm\delta, 0]$. Throughout this work, we mark the reflections by square brackets and wavectors by round brackets, same as Bastow and Street [172].

The reciprocal space diagrams of neutron diffraction from chromium that has been cooled down without any perturbations[4] are shown in Fig. 1.12. The SDWs in such material will be oriented randomly along $\langle 100 \rangle$ and create domains similar to those observed in ferromagnetic materials. The high-temperature TSDW produces satellite reflections in all $\langle 100 \rangle$ directions in the neighborhoods of all $\langle 100 \rangle$ reflections as shown in Fig. 1.12(b). The random orientation of the spin density waves remain

[3]Forbidden reflections in bcc lattice are those whose sum of the Miller indices *h, k, l* is odd. The structure factor would thus be zero implying destructive interference.

[4]In this case we mean mainly cooling under elastic stress or magnetic field.

even below the spin-flip temperature, but the "on-axis" reflections in longitudinal spin density wave modification disappear. This is caused by the fact that there is no magnetic scattering from a magnetic moment that is parallel to the scattering vector [108]. The theoretical explanation is that the scattering vector **q** is the dot product of unit vector in the direction of magnetic moment and unit vector normal to the diffracting plane, which in this configuration equals zero. Further explanation can be found in chapter 6.5.2. of [173].

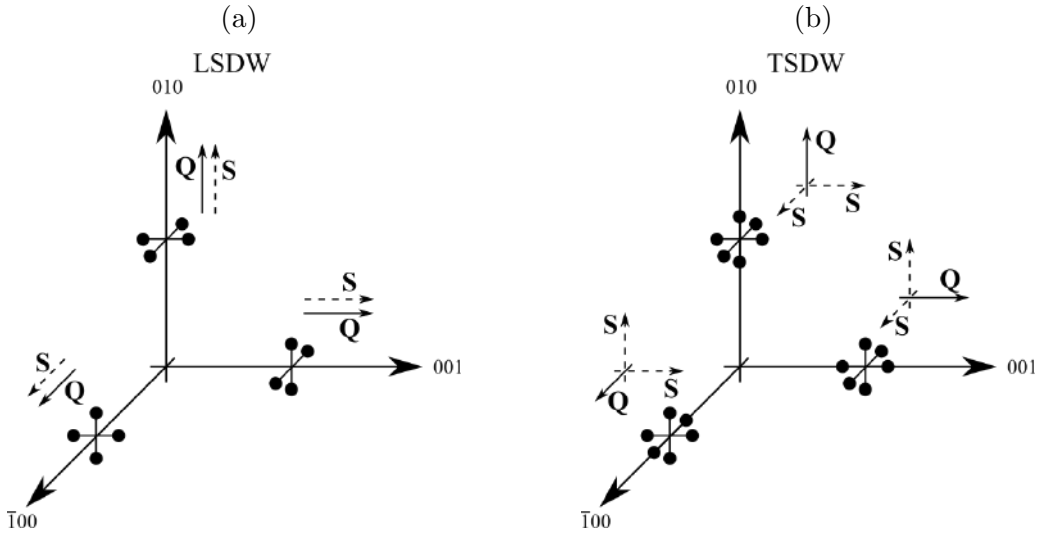

Figure 1.12: Reciprocal space diagrams representing the magnetic diffraction peaks in neutron diffraction spectra of unmodified chromium in: (a) LSDW state, (b) TSDW state.

One of the possible ways of creating a single-**Q** state, the state when the wavevector **Q** is oriented in one particular ⟨100⟩ direction throughout the specimen, is so-called field cooling. When a chromium single crystal is cooled from above the Néel temperature down to a few K in a strong magnetic field, the wavevector **Q** will possess the same orientation as the direction of the magnetic field [174, 175]. The reported values necessary to turn a chromium crystal into a single-**Q** state are between 12 to 65 kOe (1.2 to 6.5 T) depending on the amount of crystal defects present [176]. After heating the crystal with a single-**Q** state in the LSDW regime above the spin-flip temperature T_{SF}, the single domain will split into several domains with different $\boldsymbol{\eta}$. These $\boldsymbol{\eta}$ domains are sub-domains of the **Q** domains but differ in the geometrical orientation of the spins. The hypothetical oval-shaped crystal in the TSDW state in Fig. 1.13 is split into three single-**Q** domains by full lines, and each single-**Q** domain is split into two possible $\boldsymbol{\eta}$ domains which have the same **Q** but different orientations of the spins. The direction of the **Q** vector is represented by the full arrows, whereas dashed arrows represent the direction of spins.

Ando et al. [176] further hypothesize that magnetic domains are created in such a way that the internal strain is relaxed by magnetostriction. Werner et al. [177] state that once the single-**Q** state is achieved, it is extremely stable and cannot be switched to another direction below T_{SF}, certainly not by the same field as used for its creation (2.7 T in Werner's study). A specimen in the triple-**Q** state below T_{SF}

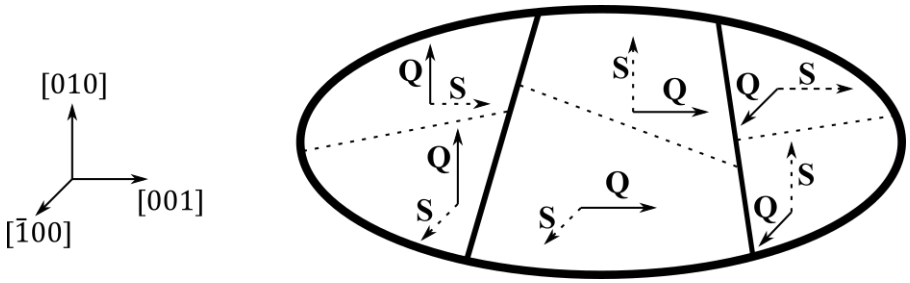

Figure 1.13: Schematic representation of possible orientations of different **Q** domains (separated by full line and different $\boldsymbol{\eta}$ sub-domains within separated by the dashed lines.

is, however, prone to switching of the orientation of **Q** by relatively low magnetic fields (1.2 T).

The reciprocal space diagram of field-cooled chromium along the [010] direction in the TSDW state is shown in Fig. 1.14(b). The field-cooling favors the growth of domains with the wavevector **Q** parallel to the magnetic field, and in doing so, only the SDWs with wavevectors $(0, 1\pm\delta, 0)$ are allowed to exist. According to Bastow and Street [172], the on-axis reflection is stronger than the other two off-axis reflections, which are marked in Fig. 1.14(a) by the larger circles. The reciprocal space diagram of the field-cooled chromium along [010] in the LSDW state is shown in Fig. 1.14(a). In this case, the on-axis reflection disappears due to the magnetic moment being parallel to the scattering vector, and only the two off-axis reflections are present. The reflections anticipated after field cooling are also listed in Table 1.1.

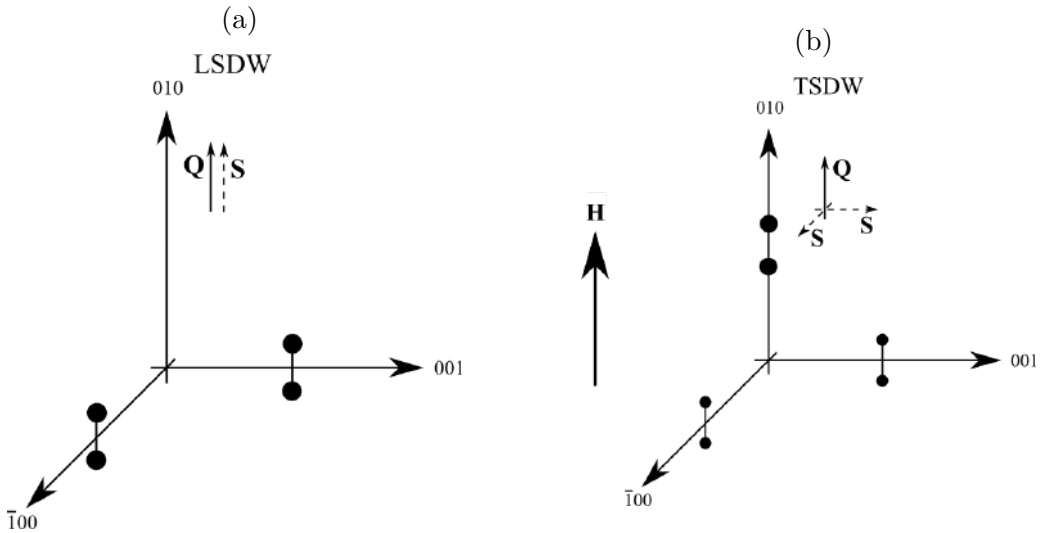

Figure 1.14: Reciprocal space diagrams of magnetic neutron diffraction peaks of the field-cooled chromium with the direction of the magnetic field along the [010] direction. (a) LSDW state, (b) TSDW state.

The second process that manipulates chromium's magnetic state is stress cooling. If chromium single crystal is compressed in a $\langle 100 \rangle$ direction and cooled through the Néel temperature under zero magnetic field, the growth of magnetic domains with

the wavevector parallel to the direction of the applied stress will be suppressed. The produced magnetic structure will thus be complementary to the one produced by field cooling [172]. The only spin density waves with vectors of $(\pm\delta, 0, 1)$ or $(1, 0, \pm\delta)$ will remain if the stress direction is along the [010] direction.

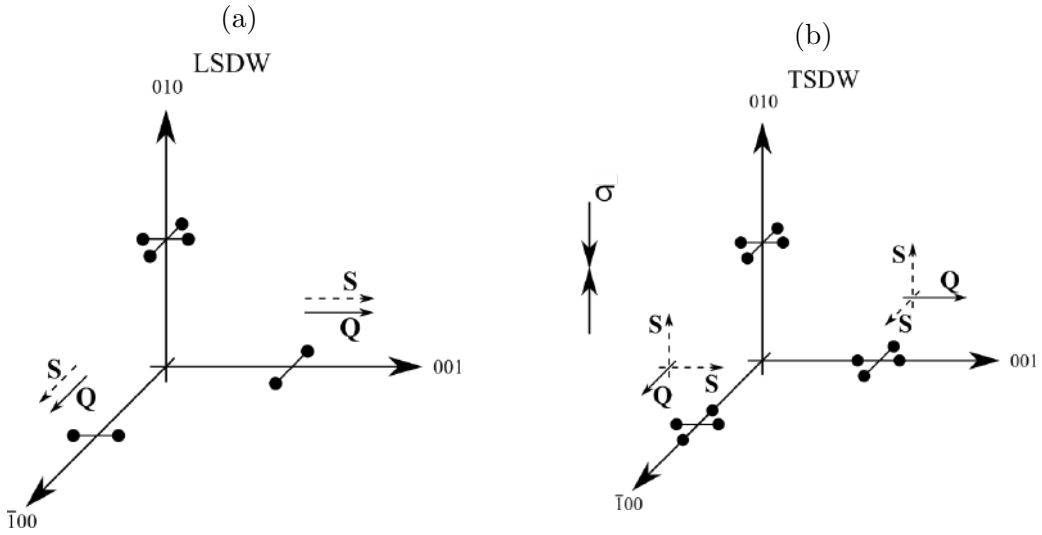

Figure 1.15: Reciprocal space diagrams of magnetic neutron diffraction peaks for stress-cooled chromium. The direction of applied compressive stress is along [010]. (a) LSDW state, (b) TSDW state.

The list of all reflections measured on the unmodified chromium, field-cooled with magnetic field along [010] direction, and stress-cooled with applied stress along [010] direction are presented in Table 1.1. Only reflections for the first octant are listed, however, the list would be the same for all other octants, i.e. $(1, \pm\delta, 0)$ behaves the same as $(-1, \pm\delta, 0)$.

Table 1.1: A list of reflections measured in the unmodified, field-cooled and stress-cooled chromium. The direction of magnetic field and applied stress is along [010] direction.

	Unmodified Cr		**Field-cooled Cr**		**Stress-cooled Cr**	
Reflectiom	**TSDW**	**LSDW**	**TSDW**	**LSDW**	**TSDW**	**LSDW**
$[1 \pm \delta, 0\ 0]$	✓	✗	✗	✗	✓	✗
$[1, \pm\delta, 0]$	✓	✓	✓	✓	✗	✗
$[1, 0, \pm\delta]$	✓	✓	✗	✗	✓	✓
$[\pm\delta, 1, 0]$	✓	✓	✗	✗	✓	✓
$[0, 1 \pm \delta, 0]$	✓	✓	✓	✗	✗	✗
$[0, 1, \pm\delta]$	✓	✗	✗	✗	✓	✓
$[\pm\delta, 0, 1]$	✓	✓	✗	✗	✓	✓
$[0, \pm\delta, 1]$	✓	✓	✓	✓	✗	✗
$[0, 0, 1 \pm \delta]$	✓	✗	✗	✗	✓	✗

1.8 Kerr microscopy

The magneto-optical Kerr effect (MOKE) was first hypothesized by Kerr in 1877, who was inspired by Faraday's hypothesis that light is an electromagnetic wave in nature and by Fresnel's and Malus's experiments with polarization and reflection [178]. The observation of magnetic domains by magneto-optics is possible due the weak dependence of optical constants on magnetization of the specimen [179, p. 24]. The magneto-optical Kerr effect describes the interaction of plane-polarized light with opaque object, which induce rotation of the polarization plane after reflection. Often, other effects are present that can cause elliptical polarization rather than simple rotation, but some can be negated by addition of compensator to the optical axis [180]. Schematic construction of the Kerr microscope is shown in Fig. 1.16. The incident light, K_{in}, coming from the light source on the right is linearly polarized by the polarizer, passes through the beam splitter and objective. The polarization plane is indicated by the red arrows in the inset of Fig. 1.16. The polarization plane is changed based on the direction of magnetization of the domain (indicated by the white arrows), from which it scatters, as shown schematically by the rotation of the red arrows in the inset. The gray arrows indicate the orientation of the polarization plane if no change occurred. Subsequently, the reflected light K_{ref} passes through the objective, beam splitter and analyzer, which allows only certain polarization directions to pass, as indicated by different intensity peaks along the reflection lines. Camera is then used to capture the images. Important part of the Kerr microscope is also an electromagnet, which is used to alter the magnetization of the specimen.

Depending on the orientation of the polarization plane, the angle and direction of incident light, three cases of Kerr effects are distinguished. Polar effect, shown in Fig. 1.17(a), where the axis of incoming, K_{in}, and reflected, K_{ref}, light, as well as magnetization are all parallel. In this case, only the contrast of domains with magnetization perpendicular to the surface will be visible, shown in Fig. 1.17(a) by differently shaded domains with magnetization vector going out-of-plane and in-plane of the specimen surface. The rotation of the polarization plane for both domains is shown in the lower two insets. However, in this case the orientation of polarization plane is not important and is set arbitrarily. The longitudinal parallel effect, shown in Fig. 1.17(b) takes place when the magnetization vector and the vectors of incident and reflected light[5] lie in the polarization plane. In this configuration, only domains with the magnetization direction parallel to the sample surface that lie in the plane of incidence will be detectable. Note that the two domains with magnetization perpendicular to the surface also show a variation in contrast, albeit smaller than the domains with magnetization direction in the incidence plane. This is caused by the polar effect described previously, whose magnitude is dependent on the incidence angle and is strongest for the 0° incidence. A similar situation is present in the case of longitudinal transverse effect, where the magnetization direction lies in the incidence plane, but polarization is perpendicular to it as shown in Fig. 1.17(c). Again, only domains with the magnetization direction in the incidence plane cause the rotation of the polarization plane. The change of the polarization direction caused by the longitudinal perpendicular effect is shown under the 3D fig-

[5]The plane created by the incoming and reflecting plane is also called the plane of incidence.

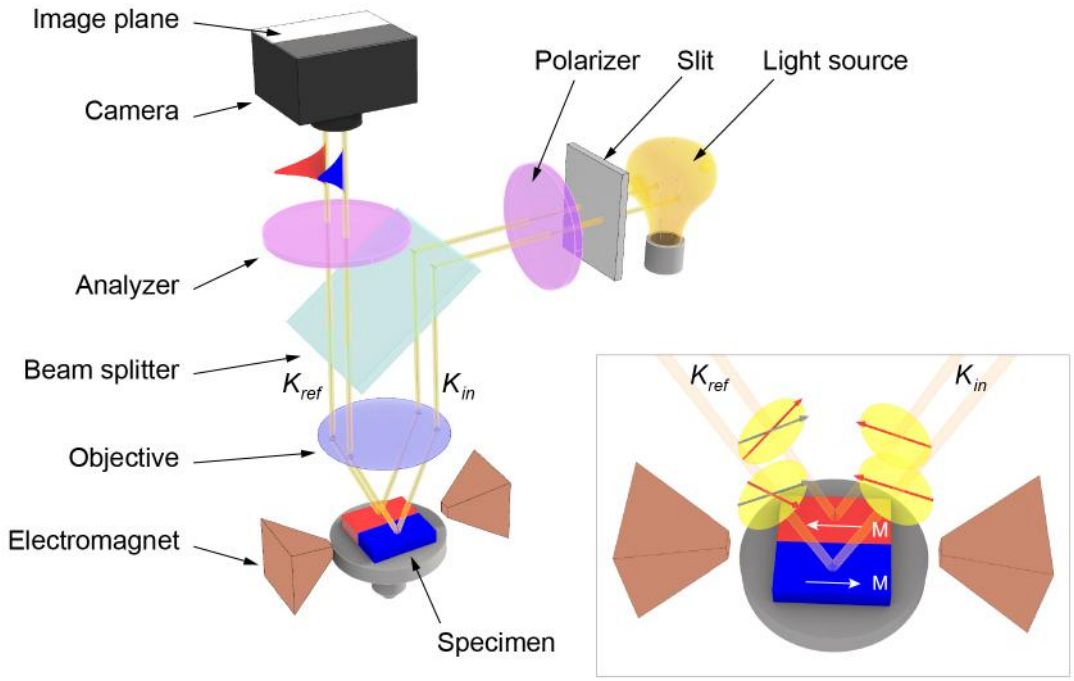

Figure 1.16: Schematic representation of the Kerr microscope setup and principle. The blue and green areas of the specimen represent the differently magnetized part of the specimen. Red arrows represent the polarization direction of the light.

ures in Fig. 1.17. The coordinate system showing the rotation of the polarization has the third axis along the K_{in} or K_{ref} direction. Contrary to the polar effect, the longitudinal effect is more pronounced with increasing incident angle [181].
The transverse effect, not shown in Fig. 1.17, takes place when the polarization and incidence plane are identical and magnetization direction is perpendicular to them. However, in this case, there is no change in the orientation of the polarization plane, but there is a change in the amplitude. Nonetheless, the amplitude change causes little effect on the contrast [179, p. 27].

Based on the described effects, one is only able to fully measure the domains magnetized in one direction. In order to visualize domains magnetized along the z direction in Fig. 1.17, one has to rotate the specimen or the incidence plane. In the former case, the rotation would expose expose the specimen to different magnetizing field, unless magnet can be rotated. Moreover, the contrast in not readily visible upon the first illumination, but is produced as subtraction of image taken when the specimen is magnetically saturated from the image taken at a certain magnetizing field. Further information can be found in a recent review paper by McCord [181], that deals with the underlying physics as well and recent advances in Kerr microscopy.

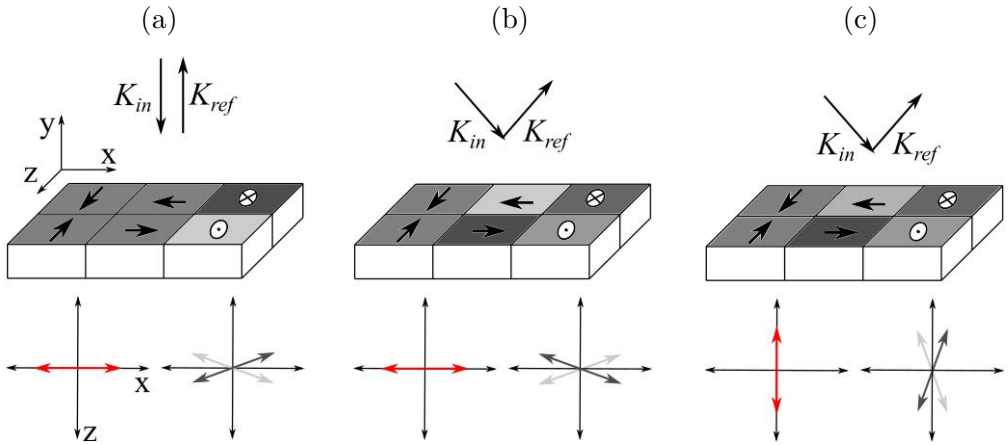

Figure 1.17: Different mutual configurations of incoming light, polarization and magnetization direction and its effect on domain contrast. The arrows in the specimen represent the direction of magnetization, red arrow the plane of polarization and lighter and darker gray arrow the changed polarization plane from equally colored regions. (a) polar configuration, (b) parallel longitudinal configuration and (c) perpendicular longitudinal configuration. Figures adapted from [180].

List of symbols

Symbol	Meaning	Equation
Latin symbols		
a_1, a_2, a_3	Stress modifiers	(1.3, 1.4)
B	Magnetic flux density	
E_{crys}	Magnetic anisotropy	(1.5)
F	Structure factor	(1.6, 1.7)
h, k, l	Plane indices	(1.6, 1.7)
H	Magnetizing field	
H_c	Coercive field/force	
K_1, K_2	Material and temperature dependent constants	(1.5)
K_{in}	Incident light direction	
K_{ref}	Reflected light direction	
m	Schmid factor	(1.1)
$\mathbf{M}$	Representation of internal magnetic state	(1.4)
M	Magnetization	
M_s	Saturation magnetization	
M_r	Remanent magnetization	
$\mathbf{Q}$	Wavevector	
Greek symbols		
$\alpha_1, \alpha_2, \alpha_3$	Directional cosines	(1.5)
δ	Reciprocal value of wavelength	
λ	Wavelenght	
σ	Stress	(1.1)
σ_{12}	Stress component	
τ	Schmid stress	(1.1)
τ^*_{cr}	Stress coefficient	(1.1, 1.3, 1.4)
χ	Angle of the MRSSP	

2 Objectives

The main objective of this thesis is to elucidate the low-temperature plastic deformation of α-Fe and Cr. The secondary objective is to study the magnetic properties of the materials before and after the deformation. In particular, we want to show how plastic deformation, by dislocation glide and/or twinning internal magnetic order, but also how the internal magnetic order affects the movement of dislocations. The main tasks are:

- Utilize sufficiently pure samples and characterize their purity before testing.
- Carry out a series of compression experiments on chromium in as-received, i.e. Triple-**Q**, state, perform the slip-trace analysis, describe the deformation mechanism and compare our findings with other bcc metals. Furthermore, transmission electron microscopy is to be used in order to search for dislocation junctions of $\langle 100 \rangle$ type, which could shed light onto the existence or non-existence of anomalous slip in α-Fe and Cr.
- Perform a series of magnetic experiments and measurements to prepare the Single-**Q** state and check the magnetic state of these samples.
- Perform neutron diffraction experiments on deformed and undeformed chromium specimens with the same orientation of the loading axis but different orientations of wavevectors in the Single-**Q** state to elucidate the effects of deformation on internal magnetic order.
- Due to poor commercial availability of α-Fe single crystals with sufficient purity, we develop a process to grow polycrystalline α-Fe with sufficiently large grains.
- A slip-trace analysis will be performed on the α-Fe polycrystals deformed at 77 K and the effect of deformation on magnetic properties will be studied by vibrating sample magnetometry. Kerr microscopy will be utilized to look for changes caused by the deformation.
- The results will be compared with concurrent atomistic simulations that are being done in our group to better understand the experimental results.

3 Materials and methods

This chapter describes in detail the materials used in this work as well as the methods used to prepare the specimens for the tests and measurements. Attention is paid mainly to the chemical composition and internal defects of acquired single crystals and microstructure of polycrystalline specimens. Experimental conditions used for specimen surface preparation are described in detail.

3.1 Origin and chemical composition of used materials

3.1.1 Chromium specimens

Three single crystals of Cr were acquired, the first one from MaTecK Germany (from now on denoted as Cr-1), the second and the third from Accumet Materials, Co. (denoted Cr-2 and Cr-3). The chemical composition was measured by the inductively coupled plasma mass spectrometry (ICP-MS) at the Transport Research Center in Brno (Centrum dopravního výzkumu, v. v. i.). The results of the chemical composition of these single crystals are summarized in Table 3.1. The chemical composition of the Cr-3 specimen was not measured, but we believe it is comparable to that of Cr-2 since they were acquired from the same manufacturer. The chemical composition was measured from 0.0171 g (Cr-1) and 0.0188 g (Cr-2) pieces that were prepared by grinding and dissolved shortly in hydrochloric acid to remove any contamination on the surface. Subsequently, the pieces were dissolved in 7 ml of superclean hydrochloric acid (Analytika, Praha) in a microwave digestion system in PTFE vials at 200 °C and 35 bar. The dissolved specimens were diluted 100× and 1000× by ultraclean water (Merck). The measurements were done by the Calibration curve method using externally added inert standards. A collision/reaction cell was employed with He, H_2 and O_2 gases to get rid of possible interferences.

Chemical purity was also measured via the residual resistivity ratio (RRR) method [182, 183]. The value of RRR is represented by the ratio between electrical resistance of the sample at room temperature (300 K) and at the liquid helium temperature (4.2 K), written as:

$$\mathrm{RRR} = \frac{\rho(300K)}{\rho(4.2K)}. \tag{3.1}$$

Thin wires with dimensions of approximately $1 \times 1 \times 10$ mm were prepared by grinding, polishing and electrolytic polishing in the solution of 20% H_2SO_4, 65%

Table 3.1: Chemical composition of acquired chromium single crystals measured by the ICP-MS method. Elements above the detection limit are in bold. Concentrations are in weight ppm or ppb.

Element	**Cr-1 [ppm]**	**Cr-2 [ppm]**	**Element**	**Cr-1 [ppb]**	**Cr-2 [ppb]**
Na	≤ 0.439	≤ 0.439	Ni	≤ 39.4	≤ 39.4
Mg	≤ 3.08	≤ 3.08	Cu	≤ 266	≤ 266
Al	≤ 3.37	≤ 3.37	Ti	≤ 42.3	≤ 42.3
Si	≤ 5.66	≤ 5.66	**Zn**	≤ 10.3	**14.3**
K	≤ 2.77	≤ 2.77	As	≤ 3.50	≤ 3.50
Ca	≤ 3.03	≤ 3.03	Se	≤ 34.9	≤ 34.9
P	≤ 0.77	≤ 0.77	Mo	≤ 11.0	≤ 11.0
S	≤ 1.71	≤ 1.71	Cd	≤ 2.61	≤ 2.61
V	≤ 2.93	≤ 2.93	Sn	≤ 31.17	≤ 31.17
Cr	**Bal.**	**Bal.**	Sb	≤ 28.07	≤ 28.07
Mn	≤ 0.282	≤ 0.282	Ba	≤ 127	≤ 127
Fe	≤ 1.23	≤ 1.23	Tl	≤ 29.4	≤ 29.4
			Pb	≤ 7.07	≤ 7.07
			U	≤ 1.52	≤ 1.52
			Co	≤ 2.68	≤ 2.68

H_3PO_4 and 15% distilled water (in vol. %). The source chemicals were 96% H_2SO_4 and 85% H_3PO_4. This solution was first reported by Ponto and Landolt [184]. The electrolysis was done at 1.8 V, room temperature, and for 15 minutes using a platinum electrode, while the electrolyte was heavily stirred during the process. The resistivity curves, measured by Prof. Marek Niewczas (McMaster University) are shown in Fig. 3.1.

The measurements were only done down to 15 K. Therefore, we had to extrapolate down to 4.2 K by the modified Bloch's equation [185]:

$$\rho = \rho_0 + \alpha T^5. \tag{3.2}$$

The coefficients ρ_0 and α were obtained by fitting and are summarized in Table 3.2, together with RRR values and coefficients of determinations R^2, representing the goodness of the fit. Higher values of RRR signalized higher chemical purity and vice versa.

Table 3.2: Values of the fitting parameters ρ_0, α, RRR values, and coefficients of determination.

	ρ_0 [Ωm]	α [ΩmK^{-5}]	R^2 [-]	RRR [-]
Cr-1	7.9096×10^{-6}	4.8244×10^{-13}	0.99681	135.6
Cr-2	8.4856×10^{-6}	1.9093×10^{-13}	0.98006	128.5

The slightly higher value of ρ_0 of Cr-2 specimen in Table 3.2 correlates with lower purity of the specimen shown in Table 3.1. Nonetheless, the chemical purity

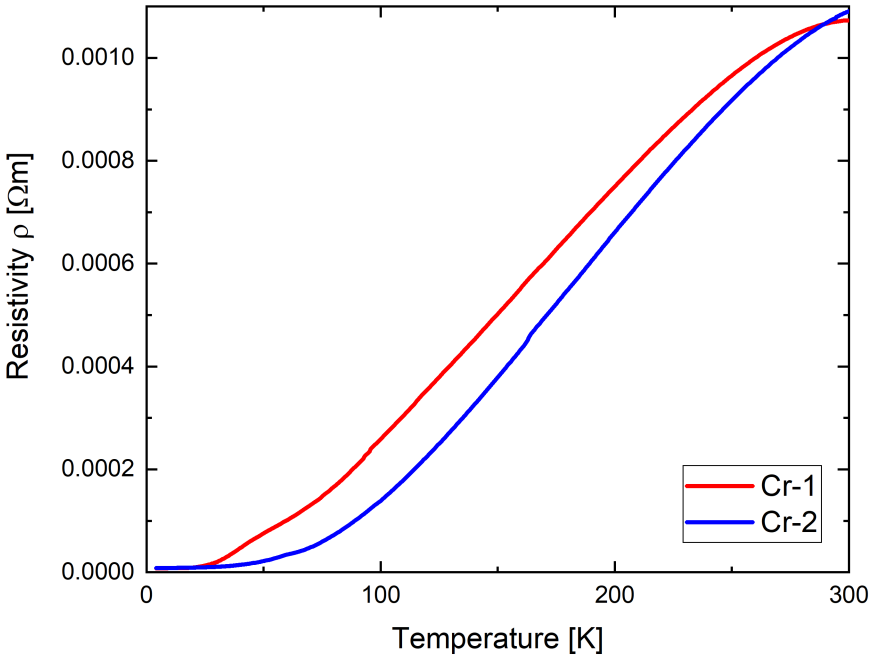

Figure 3.1: Measured resistivity curves for Cr-1 and Cr-2 specimens. The RRR values are 135.6 and 128.5 for Cr-1 and Cr-2, respectively.

of both specimens is mostly below the detection limit of the technique, the lower RRR value of Cr-2 suggests lower purity.

While the specimens acquired from MaTecK were cylindrical, those from the Accumet Materials were in the shape resembling an ovoid. After extraction of the first few specimens from the source crystal provided by Accumet Materials, we have noticed possible voids that were too large to be caused by grinding.
The computed tomography (CT) technique was used to map the materials's defects. The CT scans were performed and reconstructed in CEITEC at the CT-LAB (Brno, Czech Republic) on the General Electric Phoenix v|tome|x L240 machine. The CT reconstruction of the Cr-2 specimen has revealed a number of voids spanning almost the whole length of the specimen. The void space (colored black) is shown on a vertical cross-section in the left part of Figure 3.2(a). The right part of Fig. 3.2(a) shows a 3D reconstruction of the Cr-2 specimen, where the internal voids are colored red. Due to the extreme amount of defects present in the crystal, the Cr-2 specimen was not used for any mechanical tests. The second crystal from Accumet Materials, Cr-3, also contained a lot of cavities. However, these cavities were smaller in size and number compared to Cr-2. The horizontal and vertical cross-section of the Cr-3 specimen is shown in the top and bottom of Fig. 3.2(b), respectively. The red circles highlight smaller cavities, which would be hardly visible at this magnification. Despite the presence of voids, we have decided to extract the specimens from this crystal by electro-erosive machining, but all the specimens were later rechecked by CT to make sure that no significant voids were present. The compression specimens

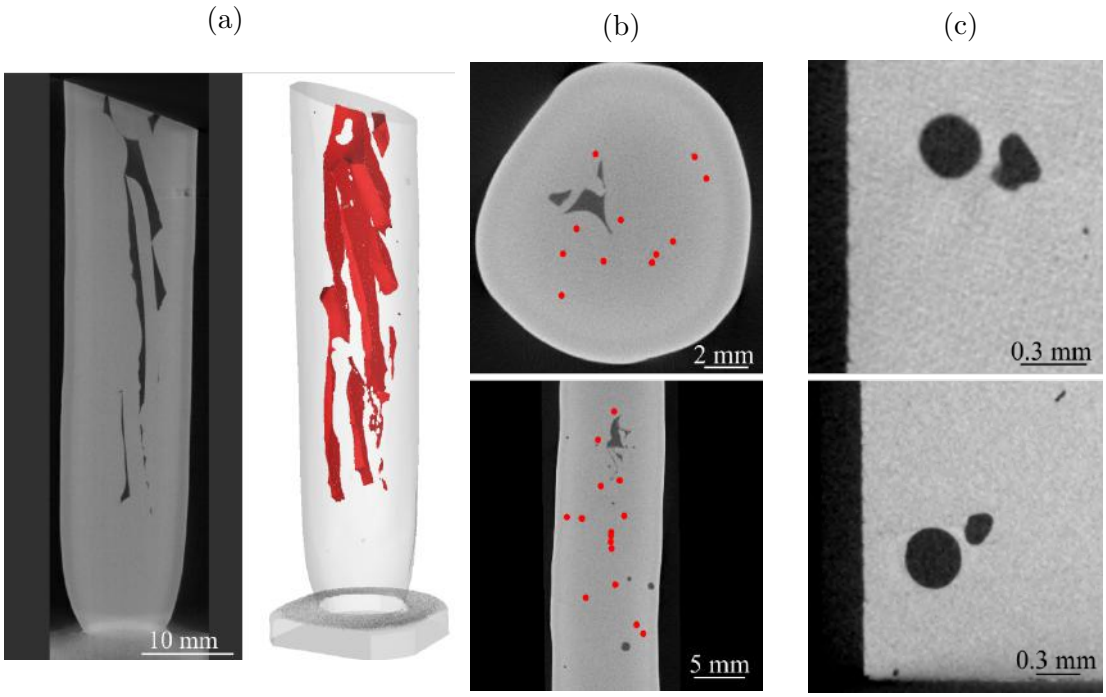

Figure 3.2: Computed tomography reconstructions: (a) The Cr-2 specimen (left picture vertical cross-section, right picture 3D reconstruction with voids filled red), (b) The Cr-3 specimen (top picture horizontal cross-section, bottom picture vertical cross-section, red dots mark smaller voids), (c) a compression specimen cut from Cr-3 (top vertical cross-section of selected part of the specimen, bottom vertical cross-section perpendicular to the one on the top image showing the same area).

with large voids, such as those shown in Fig. 3.2(c), were excluded from further testing. The top and bottom of Fig. 3.2(c) are perpendicular cross-sections showing the same void.

While the process of growth of the Cr-2 and Cr-3 crystals was not disclosed by manufacturers, the elements of 5^{th} and 6^{th} groups can be grown into single crystals directly from the melt since they do not undergo an allotropic transformation. However, due to their chemical reactivity and often high melting points, vacuum or inert gas environment is required. Most such single crystals are prepared by some variation of the zone melting technique. The floating zone is typically maintained by halogen lamps, laser, electron beam, or high-frequency induction. This method also purifies the crystal by vacuum extraction, and zone purification [186, 187].
The circular voids are most likely caused by excess gas that is expelled during the solidification. From this reason, it is advisable to use inert gas instead of vacuum. The origin of the larger plate-shaped defects can be explained if the Bridgman [188] or the Bridgman–Stockbarger method [189]. The Bridgman–Stockbarger method is based on heating a polycrystalline specimen above its melting point and slowly passing it through a sharp temperature gradient. The specimen is usually contained in a capsule for the duration of the growth. When the melt passes the temperature gradient, which is on one side above the liquidus temperature and on the other side below it, the melt crystallizes on the provided single-crystalline seed. The differ-

ence between the two mentioned methods is that the Bridgman method pulls the specimen out of the furnace. In contrast, Bridgman-Stockbarger pulls it into another furnace heated below the liquidus temperature. If the outer layer solidifies too fast, it will push the excess gas to the center and may prohibit the influx of new melt from reaching the void space.

3.1.2 Iron specimens

The iron single crystals were challenging to acquire. The difficulty of growing iron single crystals lies in the allotropic transformation at 912 °C and 1394 °C. Most of the single crystals are grown from the liquid phase, for example, by Czochralski or Bridgman method, especially in the semiconductor industry. Smaller single crystals primarily for research purposes are often grown by the floating zone method [190], where only one part of the thin cylindrical specimen is heated, usually above the liquidus temperature. The melted part, referred to as the zone, moves slowly through the specimen, which is facilitated by pulling or pushing the specimen along its long axis. The melted material in the zone is held together by the liquid's surface tension. The seed with the desired crystallographic orientation is inserted, and the atoms in the zone preferentially grow in accordance with the crystal orientation of the seed.

Despite the two allotropic transformations, we have attempted to grow an iron single crystal by this method after discussion with experts at the Department of Condensed Matter Physics of the Faculty of Mathematics and Physics, Charles University in Prague. The growth was attempted by the mentioned method in both optical and laser furnaces. All prepared specimens resulted in a coarse-grained microstructure with grains elongated along the axis of the rod, an thus along the zone's movement. The cross-sections of the specimens comprised of a few grains. However, the single-crystalline state was not achieved. The iron single crystal had the shape of a cylinder with the length of 40 mm and the diameter of 4 mm.

Due to the lack of large single-crystalline iron, its high price tag, and failure to create them via the floating zone method, we have attempted to create the single crystals also by strain anneal technique. This method is based on the deformation of the polycrystalline material to a critical level of strain and subsequently annealing at a temperature below 912 °C to induce recrystallization. This is usually achieved by pulling the specimen from the furnace through a cooler, which is able to induce temperature gradients of 200°C/cm [191]. The dislocations created during the straining provide the internal strain that drives the grain growth during recrystallization. It is of vital importance not to cross the $\alpha - \gamma$ transition temperature, otherwise, the growing grains would most likely transform to polycrystalline γ-Fe or during cooling back to polycrystalline α-Fe, in both cases with many small grains. Since we do not have a furnace with the temperature gradient and chamber with flowing dry hydrogen necessary to create a full single crystal, we have resorted to creating polycrystals with extremely large grains. The source material was acquired from Blyth Metals Ltd, UK, but the material is originally electrolytic iron from Japan. Chemical composition of this material is shown in Table 3.3. Carbon and nitrogen were measured by the infrared absorption method after combustion according to ČSN EN ISO 15350 at accredited laboratory TÜV NORD Czech s.r.o. and

its supplier Vítkovice Testing Centre s.r.o. The rest of the elements were measured by the ICP-MS method at Transport Research Center in Brno by the same process described above.

Table 3.3: Chemical composition of polycrystalline electrolytic iron. Elements above the detection limit are in bold. Concentrations are in weight ppm.

Element	**Concentration [ppm]**	**Element**	**Concentration [ppm]**
Na	≤ 3.38	As	≤ 0.064
Mg	≤ 16.6	Se	≤ 1.94
Al	**7.3**	**Mo**	**0.483**
Si	≤ 1.44	Cd	≤ 0.01
K	≤ 9.92	Sn	≤ 0.099
Ca	≤ 10.7	Sb	≤ 0.019
P	≤ 0.929	Te	≤ 0.008
S	≤ 8.11	Tl	≤ 0.054
V	≤ 0.029	Ba	≤ 0.051
Cr	**1.39**	Pb	≤ 0.029
Mn	≤ 0.198	U	≤ 0.002
Fe	**Bal.**	**C**	**0.0027**
Co	≤ 0.004	**N**	**0.0011**
Zn	≤ 01.29		

The single crystal specimen was given to by Prof. Lejček, most likely from older stock of Prof. Šesták, for which we are very grateful. The chemical composition measured by the ICP-MS method of the α-Fe single crystal specimen is summarized in Table 3.4.

Table 3.4: Chemical composition of single-crystalline iron. Elements above detection limit are in bold. Concentrations are in weight ppm.

Element	**Concentration [ppm]**	**Element**	**Concentration [ppm]**
Na	≤ 6.8	**As**	**0.799**
Mg	≤ 2.07	**Cu**	**47.6**
Al	**5.2**	Mo	≤ 0.044
Si	**8.46**	Cd	≤ 0.012
K	≤ 6.94	**Sn**	**0.689**
Ca	≤ 23.8	Sb	≤ 0.003
P	≤ 14.7	Ti	≤ 0.027
S	≤ 6.65	Tl	≤ 0.029
V	≤ 0.03	Ba	≤ 0.006
Cr	≤ 0.120	**Pb**	**1.17**
Mn	2.02	U	≤ 0.009
Fe	**Bal.**	Zn	≤ 0.045
Co	≤ 0.009	Se	≤ 0.079

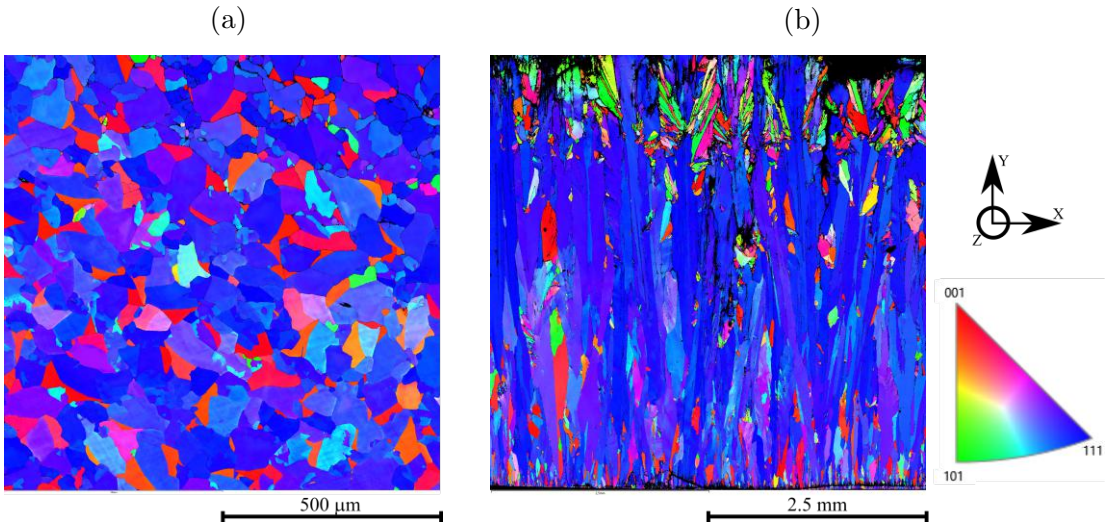

Figure 3.3: Inverse pole figure maps acquired by EBSD: (a) IPF Z map from the surface of the flake, (b) IPF Y map from the cross-section.

Strain annealing of α-Fe specimens

The electrolytically produced iron is in the form of thin flakes with thickness usually between two to eight mm and various shapes, usually about a size of the thumb. Due to the nature of electrolytic growth, the flakes are made up of columnar grains with strong $\langle 111 \rangle$ texture in the direction of growth.

In order to increase the grain size and remove the texture, we have utilized a method of repeated cold work and annealing as described by Kadečková & Šesták [191]. A cuboidal specimen with dimensions approximately $4 \times 4 \times 12$ mm was cut from the electrolytic flakes, carefully grinded, and polished, and the remaining deformed layer was removed by Nital (10% HNO_3 solution in ethanol). As the first step, three specimens were deformed by approximately 5 % in the two directions perpendicular to the long axis of the specimen and enclosed in a quartz tube under vacuum (the quartz tube was flushed with argon and evacuated several times).
The specimens were placed in a furnace set at 870 °C for six, eight, and ten hours to determine the optimal annealing time. The average equivalent circle diameter[1] rose from 164.5 µm to 248.3, 270.3, and 269.3 µm respectively. The grain size achieved after 8 hours of annealing is almost identical to the one after 10 hours. Therefore, for further experiments, we have chosen 8 hours as the ideal annealing time. The next set of three specimens was deformed, enclosed in the quartz tube, and annealed for 8 hours. The first specimen of the set was prepared by two cycles of this process, the second by three cycles and the third by four cycles. The average equivalent circle diameter increased to 365.5 µm after two cycles, 406 µm after three cycles, and to 542.4 µm after four cycles. The increase of the grain sizes was not homogeneous. Instead, some grains grew very fast while leaving islands of small grains scattered throughout the specimen. The grain size distribution computed from electron back scattered diffraction (EBSD) map on the electrolytic iron before any strain annealing is shown in Fig. 3.4(a) and after four cycles of strain annealing in Fig. 3.4(b). Side A

[1]Diameter of a circle with the same area as the grain.

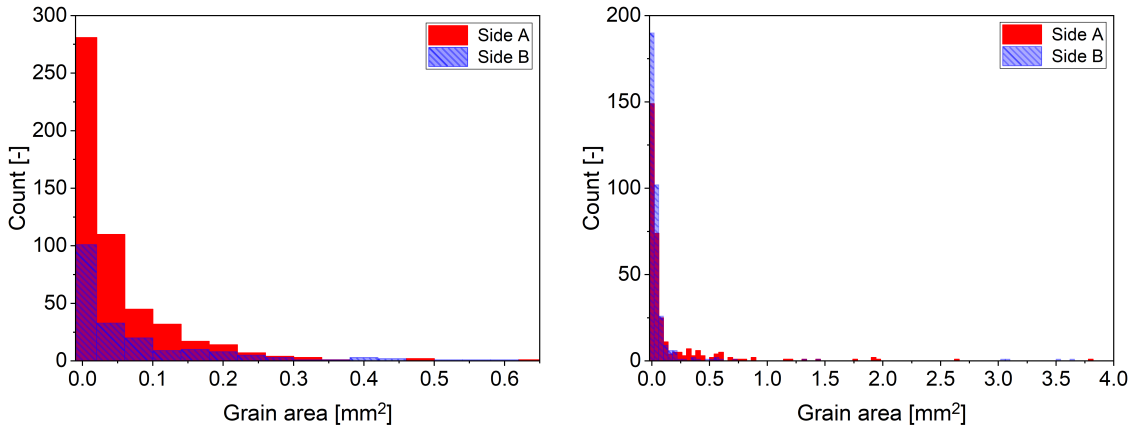

Figure 3.4: Grain size distribution of electrolytic iron: (a) after one cycle of strain annealing, (b) after four cycles of strain annealing. In both cases, the bar width is 0.04 mm.

represents the initial surface of the flake, as depicted in Fig. 3.3(a), side B represents the cross-section of the flake, as shown in Fig. 3.3(b).

The strain annealing increased the size of the largest grains by at least an order of magnitude. From the histograms in Fig. 3.4(a) and 3.4(b), it is evident that the number of small grains is reduced slightly while the larger grains start to emerge. The largest grain after one cycle of strain annealing reached 0.63 mm^2, while after four cycles, the largest grain was almost 4 mm^2. The histogram of the grain size distribution fails to represent the grain growth properly since the number of large grains is low and seems almost nonexistent when compared to the hundreds of smaller grains. In order to better describe the grain size, we have written a Python script that implements the intercept method as described by the ASTM E112 standard. The intercept method consists of drawing a random line on a micrograph of the specimen's microstructure and counting how many times the line intercepts the grain boundary. The ratio of the line length L to the number of intercepts N is the average grain size (0.5 intercepts are considered for each end of the line). Of course, the greater the number of randomly placed lines, the closer the result is to reality. Thanks to the automation, we are not only able to calculate the average grain size, i.e., the average L/N ratio of all lines, but we can also store the lengths of segments between individual intercepts. The micrographs used in this method were created from the EBSD data, where only the grain boundaries were kept in the picture. For each micrograph, 15 000 random lines were drawn and evaluated.

The histogram in Fig. 3.5(a) suggests that most line segments (distances of two successive line intercepts with grain boundaries) are around 0.2 mm long, while the largest segments reach about 1 mm in length. The side B, which initially contains a strong columnar grain structure, shows more line segments with lengths from 0.6 mm and above. After four cycles of strain annealing, shown in Fig. 3.5(b), one can observe a transition to multi-modal distribution, where side A shows a local

(a) (b)

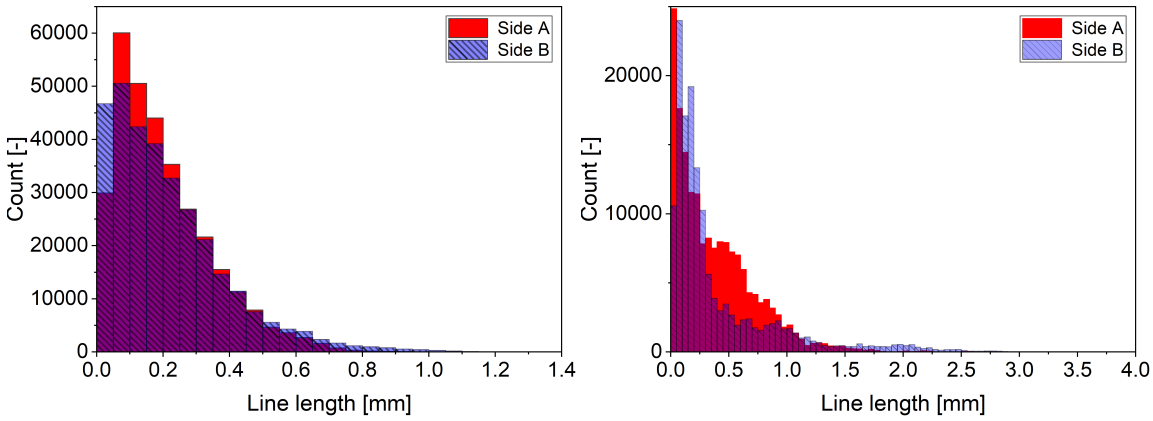

Figure 3.5: The distribution of line lengths from the intercept method used on specimen after: (a) one cycle of strain annealing, (b) four cycles of strain annealing.

peak around 0.5 mm, which is not present on side B. However, side B shows more line segments with the length of 2 mm. A small number of segments are close to 4 mm long, which means that some of the grains are almost 4 mm in certain directions. Furthermore, we can characterize the change in the aspect ratio of the grains. The fitted ellipse aspect ratio (FEAR) can be calculated from the EBSD data by fitting an ellipse around each of its grains are observing the change in the ratio of the long and short axis. In the initial state, the average FEAR of the grains in Fig. 3.3(a) is 2.05, while those in Fig. 3.3(b) have average FEAR of 4.46. The first cycle of the strain annealing slightly reduced the FEAR of the less elongated grains on side A to 1.82, but in the case of the elongated grains on side B, the FEAR parameter was reduced to 2.1. The other three cycles of the strain annealing were not as effective in reducing the elongation. The FEAR was 1.92 and 1.83 for sides A and B, respectively.

Furthermore, we have attempted to characterize the average volume of the grain. Smith and Guttman [192] proposed a method to calculate the average volume per particle V_p from the two-dimensional sections as:

$$V_p = \frac{4}{\pi}\left(\frac{N}{L}\right)\left(\frac{A}{M}\right)^2, \tag{3.3}$$

where the N/L is the reciprocal result of the intercept method, A the area of the measurement region, and M the number of grains in the area A. The number of grains was calculated from the EBSD measurement. Eq. (3.3) is valid for grains or particles of constant shape and size, which is not our case. While it can lead to imprecise results, the general trend should be correct. The average volume of the grain after one cycle of strain annealing is $V_p = 0.00156$ and 0.00492 mm^3 for sides A and B, respectively. The four cycles of strain annealing increased the average grain size to $V_p = 0.05038$ and 0.06962 mm^3. If we combine the average grain sizes

from both sides, their average volume almost doubles from $V_p = 0.0342$ mm^3 to 0.06 mm^3 during the three extra cycles of strain annealing. The findings described are discussed in more detail in our submitted publication [193].

3.2 Preparation of compression specimens

The specimens for compression testing were cut from the source single crystal by electro-erosive machining. Before the cutting, the source crystal orientation was determined by electron back-scattered diffraction measurement, and rotations needed to cut the specimens were calculated. The source crystal was then placed on a goniometer and oriented as precisely as possible for further cutting. The electro-erosive machining was used to cut out specimens with required orientation and dimensions slightly bigger than those required in order to leave enough material for subsequent grinding. The excess material is necessary as the electro-erosive machining leaves the surface with many cracks, depicted in Fig. 3.6, which need to be removed.

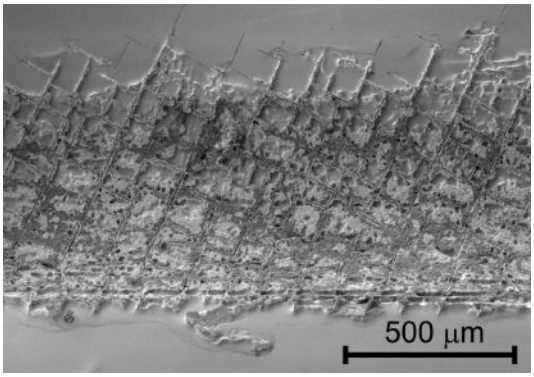

Figure 3.6: Cracks left on the surface by electro-erosive cutting. The depicted area is a radius where the grinding was not done properly. The top and bottom show well prepared surfaces produced by electrolytic polishing.

The dimensions of the compression specimens were $2.5 \times 2.5 \times (8 - 12)$ mm. The length depended on crystal orientation and is was long as the geometry allowed. Due to the cracks, the specimens' width and depth dimensions were reduced to 2×2 mm. After the initial grinding, all sides of the specimen were grinded by a set of abrasive papers with decreasing grit size down to the P2000 paper. Subsequently, the sides were polished with 3 µm and 1 µm diamond paste. Chromium specimens were electropolished under the same conditions that were described in the previous chapter about RRR measurements, while α-Fe specimens were electropolished in solution containing 94 % of acetic acid and 6 % of perchloric acid at room temperature with voltage of 30 V for 20 to 30 s. A corner was cut off to ensure that the orientation was kept at all times during the experiment and characterization. The model of the specimen is shown in Fig. 3.7(a) and schematic representation on slip systems in the single-crystalline specimen after the compression test in Fig. 3.7(b).

After the specimens were prepared, an EBSD measurement was used to orient the sample and to determine the orientation of the loading axis of the specimen.

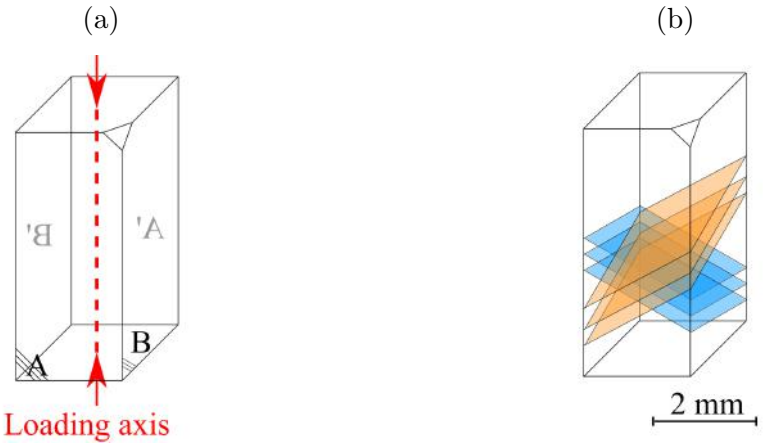

Figure 3.7: (a) model of the compression specimen with the designation of the sides (A, B, A', B'), (b) slip systems in the specimen after the test and their trace marks on the surface on the right.

The measurements were done in scanning electron microscope Tescan LYRA 3 XMU FEG/SEMxFIB equipped initially with Oxford Instruments Nordlys, and with more recent studies done using Symmetry EBSD camera and Aztec software. After completing the compression test, EBSD analysis was performed for the second time to evaluate the rotation in the loading axis during straining.

The specimens were tested on the Instron 8862 100 kN machine equipped with a custom-made cooler to hold the liquid nitrogen around the specimen. Some specimens were predeformed at room temperature. To increase the mobile dislocation density an thus to prevent brittle fracture. The specimen was placed in the compression cell and pre-loaded to 200 N. Liquid nitrogen was poured into the cooler and continuously refilled during the experiment. Before the test began, the machine and the sample were let to stabilize for at least 30 minutes. Due to the cooler and specimen being submerged in the liquid nitrogen, it is not possible to measure the deformation with extensometers. Therefore, we rely on the stress-strain relationship measurement by the testing machine. The cross-head speed is set to 30 µm/min, which causes the plastic strain rate of about 10^{-5} s^{-1}. Because the measurement was done without the extensometer, it is necessary to perform corrections. These were done after the test based on true plastic strain computed from dimensions of the specimen before and after the deformation, and the elastic modulus calculated for each orientation.

3.3 Preparation of samples for TEM, VSM and Kerr microscopy

The TEM foils in this study were prepared by carefully thinning the material to approximately 100 µm by grinding and polishing in an in-house made holder.
It allowed for careful adjustment of thickness and preventing inhomogeneous thinning and thus reducing the possibility of creating the wedge-like shape of the specimen, which would create problems with electrolytic thinning. After reaching the

desired thickness, a foil with the diameter of 3 mm was punched out from the plate with a disc punch machine. The electrolytic polishing was performed on TenuPol 5 from Struers with an electrolyte consisting of 950 ml of acetic acid and 50 ml of perchloric acid. The electrolyte was used at 12 °C and 80 V until obtaining a hole with an electron transparent rim.

The lamellae were prepared on Thermo Scientific Helios 5 Dual Beam or Tescan LYRA 3 XMU FEG/SEMxFIB by standard lift-out techniques using gallium focused ion beam (FIB). An approximately 1.5 µm thick protective layer of amorphous platinum or tungsten was deposited using a gas injection system (GIS). The GIS delivers a precursor containing one of the mentioned elements, which are broken down by the ion (or electron) beam and deposited onto the surface, thus creating the protective layer. Trenches were milled on both sides of the future lamella, and the lamella was undercut by the ion beam leaving just a small bridge to the surrounding material that holds the lamella in place. Subsequently, the needle of a micromanipulator was connected to the lamella by the deposition from GIS, and the bridge was milled away by FIB. After lifting the lamella out from the material, it was welded onto a special copper or molybdenum TEM grid and thinned by FIB with decreasing beam energy and current in steps until the electron transparency was achieved.

The specimens used in magnetic measurements were carefully cut from the source material and grinded to avoid deformation in the material. In all cases, the specimens were electropolished to remove any deformation left after the grinding.
The specimens were glued onto the holder of the vibrating sample magnetometer (VSM) machine with Varnish glue. The iron specimens were magnetized mainly in the LakeShore 7400 series VSM because of its ease of use at room temperature. The Physical Property Measurement System (PPMS) with EverCool 2 from Quantum Design was used for precise measurements at low temperature. Thanks to its operational temperatures between 2 and 400 K, it was used also for the magnetization of the chromium specimens and for more precise measurement on the α-Fe specimens. In cases where the magnetization or measurement in a certain direction was necessary, we have first used EBSD measurement to determine the orientation. Custom 3D-printed holders were designed to achieve the desired orientation and keep the specimen stable during the measurement, shown in Fig. 4.11(c).

ZEISS Axio Imager A2m microscope modified by Evico Magnetics GmbH at CEITEC Nano was used to image the magnetic domains in α-iron. The specimens, previously grinded and polished to 3 µm diamond paste, were prepared by the electropolishing technique on LectruPol-2 machine (Struers) using A3 electrolyte at room temperature and 30 V for 5-15 seconds. Moreover, the specimens were clamped in aluminum holder to minimize movement during magnetization.

List of symbols

Symbol	Meaning	Equation
Latin symbols		
A	Area	(3.3)
L	Line length	(3.3)
M	Number of grains in measured area	(3.3)
N	Number of intercepts	(3.3)
R^2	Coefficient of determination	
T	Temperature	(3.2)
V_p	Average particle volume	(3.3)
Greek symbols		
α	Fitted parameter	(3.2)
ρ	Electrical resistivity	(3.1)
ρ_0	Electrical resistivity at 0 K	(3.2)

4 Characterizations of magnetic states

This chapter deals with the measurements of magnetic properties of chromium and α-Fe. We use Vibrating Sample Magnetometry (VSM) measurements and neutron magnetic scattering to elucidate the changes of magnetic moments in the specimens before and after plastic deformation.

4.1 VSM measurements on polycrystalline α-Fe

A specimen with dimensions approximately 2.9 × 3 × 0.51 mm was prepared from one of the samples after 4 cycles of strain annealing and the hysteresis curve was measured by applying magnetic field along its shortest and longest axis. The specimen was deformed in compression to $\epsilon_{pl} = 0.1$ and 0.24 in the direction of the shortest axis, and the magnetic measurement was performed after each deformation step on the PPMS machine in the VSM mode. The resulting hysteresis loops are shown in Fig. 4.1.

The probing field was applied perpendicular to the deformation axis. Since the deformation of the specimen changed its size, we have corrected the measured curves using the demagnetizing factor [194, pp. 35–38]

$$H \simeq H' - NM, \tag{4.1}$$

where H is the magnetic field in the specimen, H' the external (applied) field, N the demagnetizing factor, and M the magnetization. In general, the demagnetizing factor is a 3 × 3 tensor, but it can be simplified for symmetrical objects such as cuboids, cylinders and ovals [195–198]. For our purposes, we have considered the demagnetization factor N_H approximation for rectangular prisms published by Aharoni [199]. For a magnetic field applied along the z axis, it is defined as

$$\begin{aligned} \pi N_H = {} & \psi_{ef} \ln \epsilon_e + \psi_{eg} \ln \epsilon_f + \frac{f}{2g} \ln \theta_{ef} + \frac{e}{2g} \ln \theta_{fe} + \frac{g}{2e} \ln \theta_{fg} + \frac{g}{2f} \ln \theta_{ag} \\ & + 2 \arctan \frac{ef}{g\rho} + \omega_3 + \omega_2 \rho + \frac{g}{ef}(\sqrt{\eta_{ef}} + \sqrt{\eta_{fg}}) - \frac{\eta_{ef}^{3/2} + \eta_{fg}^{3/2} + \eta_{eg}^{3/2}}{3efg}, \end{aligned} \tag{4.2}$$

where g is the length of the specimen in the direction of the magnetic field, and e, f the two perpendicular dimensions. The substitutions in Eq. (4.2) are: $\psi_{xy} = (x^2 - y^2)/2xy$, $\epsilon_x = (\sqrt{e^2 + f^2 + g^2} - x)/(\sqrt{e^2 + f^2 + g^2} + x)$, $\theta_{xy} = (\sqrt{x^2 + y^2} + x)/(\sqrt{x^2 + y^2} - x)$, $\omega_x = (e^x + f^x - 2g^x)/3efg$, $\eta_{xy} = x^2 + y^2$ and $\rho = \sqrt{e^2 + f^2 + g^2}$.

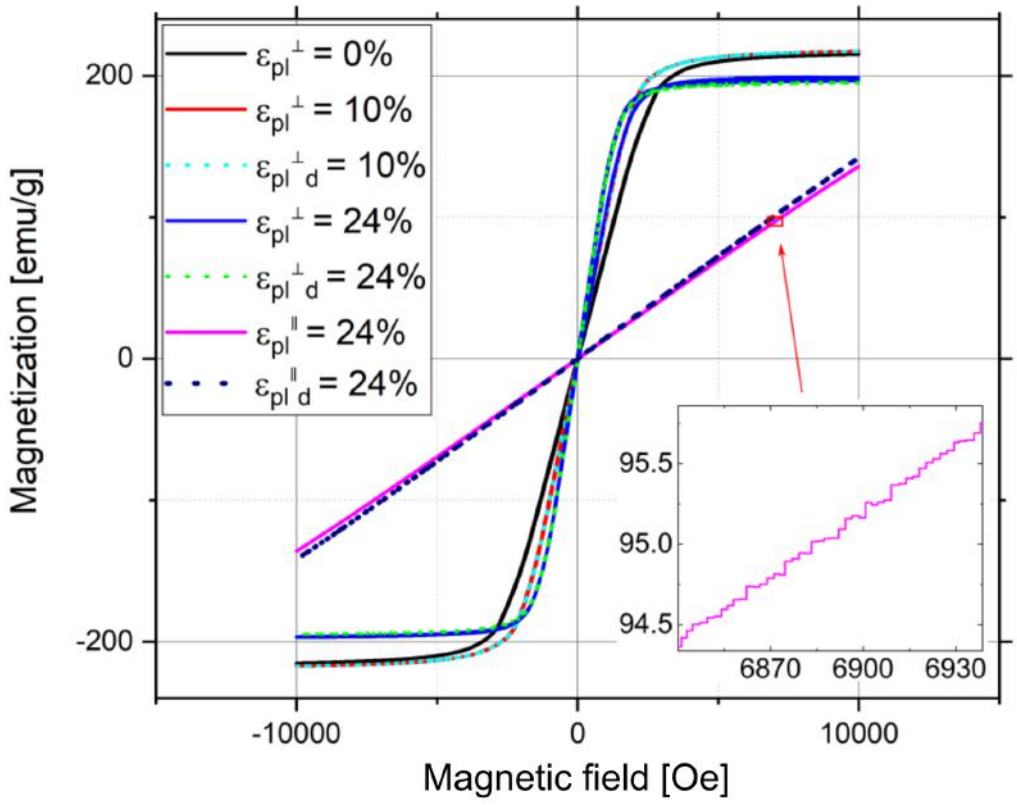

Figure 4.1: Hysteresis loop of polycrystalline α-iron specimen measured perpendicularly and parallel to the applied strain at RT. Measurements done perpendicularly to the applied field are marked by $\perp$, while those measured in parallel direction are marked by $\parallel$. Furthermore, dotted lines were measured after demagnetization and are marked by the subscript *d*. The inset shows enlarged part of the hysteresis curve of the specimen deformed to 24% which was measured with probing field along the direction of the deformation axis direction. The increments of the magnetic field during the measurement are 2 Oersteds.

The hysteresis loop measured on the deformed specimen in Fig. 4.1 increases its slope with increasing deformation. It is important to emphasize that the probing magnetic field was perpendicular to the deformation axis. Usually, with increasing deformation the slope of the curve tend to decrease, as is evident in the magenta and dark blue curves, which were measured with probing field along the deformation axis. We attribute the increase of slope of the curves measured perpendicularly to the rotation of crystal axis to more easily magnetizable direction. Furthermore, the inset in Fig. 4.1 shows an enlargement of small part of the curve measured at deformed specimen with probing field along the deformation axis. Unlike other curves, this one shown steps on the curve, which we attribute to the Barkhausen effect. The steps are caused by domain wall pinning on lattice defects [200]. However, acoustic emission measurements were not done. The hysteresis loops measured

on the specimen deformed to $\epsilon_{pl} = 0.24$ with probing field parallel to the loading axis (magenta and dark blue curves) do not reach the saturation. We attribute this to heavy deformation that prevents the growth of the magnetic domains.

4.1.1 Jiles-Atherton model

In order to link the magnetic properties of samples' to materials' parameters, we have fitted our data to the Jiles-Atherton (JA) model [201], which was modified to include magnetic anisotropy [202, 203]. The JA-model considers the domain wall motion by describing interplay between energy losses and changes of magnetization. The elementary idea of the model is that the bulk magnetization M is a sum of reversible magnetization M_r and irreversible magnetization M_{ir} [204]. The reversible magnetization M_r is attributed to the reversible bowing of the domain walls, whereas the irreversible magnetization M_{ir} arises from domain wall pinning at crystal defects and inclusions [205]. Within this model [201], the equation for anhysteretic[1] *isotropic* magnetization is

$$M_{an}^{iso} = M_s \left[\coth \frac{H_e}{a} - \frac{a}{H_e} \right] \tag{4.3}$$

where the equation in the bracket is the Langevin function. Here, H_e is the effective magnetizing field defined as

$$H_e = H + \alpha M, \tag{4.4}$$

where α is the Bloch interdomain coupling coefficient. The parameter a in Eq. (4.3) determines the slope of the anhysteretic curve at the beginning of the magnetization (in the limit of zero H_e) and is expressed as:

$$a = \frac{\bar{N} k_B T}{\mu_0 M_s}, \tag{4.5}$$

where $\bar{N}$ is average domain density present in the material, k_B the Boltzmann constant, T the temperature in Kelvins, μ_0 the magnetic permeability of free space, and M_s the saturation magnetization.

The anhysteretic *anisotropic* magnetization is described in [203, 206] as:

$$M_{an}^{aniso} = M_s \left[\frac{\int_0^\pi e^{E_1+E_2} \sin\theta \cos\theta d\theta}{\int_0^\pi e^{E_1+E_2} \sin\theta d\theta} \right], \tag{4.6}$$

where θ is the angle between the direction of the atomic magnetic moment and the direction of the magnetizing field. The terms E_1 and E_2 are further described as:

$$E_1 = \frac{H_e}{a} \cos\theta - \frac{K_{an}}{M_s \mu_0 a} \sin^2(\psi - \theta) \tag{4.7}$$

and

[1] Anhysteretic magnetization is an ideal magnetization without losses resulting from domain wall displacements in cyclic magnetic fields.

$$E_2 = \frac{H_e}{a}\cos\theta - \frac{K_{an}}{M_s\mu_0 a}\sin^2(\psi+\theta), \tag{4.8}$$

where ψ is the angle between the magnetizing field and the easy axis of magnetization and K_{an} the average energy density dependent on the uniaxial anisotropy, which can be for cubic single crystals computed by Eq. (1.5)[2]. Of course, this equation is for single-crystalline material. For polycrystals K_{an} is the average value taken across all grains for the given direction of the magnetic field. It should be noted that the average energy density depends on stress in the material and can be expressed as [98, pp. 262]:

$$K_{an}(\sigma) = \frac{3}{2}\lambda\sigma\sin^2\beta, \tag{4.9}$$

where λ is magnetostriction, σ the uniaxial stress, and β the angle between the direction of stress and magnetization. Furthermore, the relationship between the reversible magnetization M_r, anhysteretic magnetization M_{ah} and irreversible magnetization M_{ir} is given by

$$M_r = c(M_{ah} - M_{ir}), \tag{4.10}$$

where c describes the magnetization reversibility [207]. Finally, the magnetic hysteresis loop of the specimen can be calculated from the following differential equation [201, 208]:

$$\frac{dM}{dH} = \frac{\delta_M}{1+c}\frac{M_{ah}-M}{\delta k - \alpha(M_{ah}-M)} + \frac{c}{1+c}\frac{dM_{ah}}{dH}. \tag{4.11}$$

Here, k describes average energy required to break the magnetic domain walls free of the pinning site. The parameters δ and δ_M are introduced to keep the mathematical model within physical boundaries. The rules for their values are as follows:

$$\delta = \begin{cases} 1 & \frac{dH}{dt} \geq 0 \\ -1 & \frac{dH}{dt} < 0 \end{cases} \tag{4.12}$$

and

$$\delta_M = \begin{cases} 0 & (\frac{dH}{dt} < 0 \ \wedge \ M_{an} - M > 0) \vee (\frac{dH}{dt} \geq 0 \ \wedge \ M_{ah} < 0) \\ 1 & \text{otherwise.} \end{cases} \tag{4.13}$$

The δ parameter ensures that the domain wall pinning opposes the changes in magnetization, and δ_M maintains that the incremental susceptibility is always positive. Table 4.1 shows the units of the parameters used in the JA model.
The model fits only the parameters shown in Table 4.2.

We have fitted the experimentally measured curves in Fig. 4.1 to the anisotropic Jiles-Atherton model described by Eq. (4.11). All of the fits consider the easy axis

[2] In this case, we use the K_{an} instead E_{crys}, same as the literature concerning the Jiles-Atherton model does.

Table 4.1: List of the parameters and their units used in the Jiles-Atherton model.

Parameter	Units	Equation
M_s	A/m	(4.3, 4.6, 4.7, 4.8)
a	A/m	(4.3, 4.7, 4.8)
α	-	(4.4, 4.11)
N	-	(4.4)
T	K	(4.4)
k_B	$\mathrm{m^2\ kg\ s^{-2}\ K^{-1}}$	(4.4)
μ_0	H/m	(4.4)
K_{an}	$\mathrm{J/m^3}$	(4.7, 4.8)
θ	deg	(4.6, 4.7, 4.8)
ψ	rad	(4.7, 4.8)
λ	μm/m	(4.9)
σ	Pa	(4.9)
β	deg	(4.9)
c	-	(4.10, 4.11)
k	A/m	(4.10,4.11)

of magnetization to be perpendicular to the magnetizing field. We have attempted to use also the isotropic model, however, we were unsuccessful in optimizing the fit. Furthermore, the magnetic field was fitted in T and kA/m, otherwise the optimization was also unsuccessful. The initial parameters were estimated based on the recommendations in Ref. [209] as:

$$\begin{gathered} M_s \in M_{tip} \cdot \langle 1, 1.2 \rangle \\ k \in H_c \cdot \langle 0.2, 5 \rangle \\ c \in \langle 0; 1 \rangle \\ a \in H_c \cdot \langle 0.5, 5 \rangle \\ \alpha \approx H_{tip}/M_{tip}, \end{gathered}$$

where H_{tip} and M_{tip} are the coordinates of the positive saturation point, and H_c the coercivity. The fit was done in the MATLAB code written by Prof. Szewczyk [208], also available online at [210].

The results are summarized in Table 4.2. In many cases, we have arrived at slightly different results when starting the optimization with different initial conditions. The results in Table 4.2 are shown as averages and standard deviations of the fits. In the case of the specimen deformed to $\epsilon_{pl} = 0.24$ and measured with the probing field parallel to the deformation axis, the model did not fit the measured data exactly and showed best fit that reached saturation.

Table 4.2 shows decrease in the average energy density K_{an} with the amount of applied strain, which could be caused by rotation of grains during the deformation. The Bloch interdomain coupling constant a, magnetization reversibility c, and saturation magnetization M_s also decrease. The only parameter that increases is k, which describes the average energy to break the domain walls free from the pinning

sites, which agrees with the deformation in both cases, regardless the orientation of the probing field to the deformation axis.

Table 4.2: Results of the fit of experimental data to the JA model.

Constant	$\epsilon_{pl}^{\perp} = 0$	$\epsilon_{pl}^{\perp} = 0.1$	$\epsilon_{pl}^{\perp} = 0.24$	$\epsilon_{pl}^{\parallel} = 0.24$
a [A/m]	5.89 ± 0.39	6.08 ± 0.75	4.00 ± 0.85	0.65 ± 0.37
k [A/m]	7.88 ± 0.28	8.43 ± 0.77	10.67 ± 0.45	9.2 ± 0.9
c [-]	0.37 ± 0.77	0.20 ± 0.11	0.09 ± 0.01	0.10 ± 0.03
M_s [10^6 A/m]	1.73 ± 0.03	1.73 ± 0.01	1.56 ± 0.01	0.96 ± 0.04
α [10^{-5}]	1.12 ± 0.15	0.16 ± 0.1	1.32 ± 0.26	2.04 ± 0.45
K_{an} [10^2 J/m^3]	2.68 ± 0.03	1.92 ± 0.02	1.41 ± 0.06	4.31 ± 0.11
ψ [rad]	$\pi/2$	$\pi/2$	$\pi/2$	$\pi/2$

To understand the changes of the parameters entering the Jiles-Atherton model, we draw the hysteresis curves with different choices of parameters as shown in Fig. 4.2. The change in saturation magnetization, M_s, shown in Fig. 4.2(a) logically causes the curve to reach different magnetization values, but also affects the initial slope of the curve. The change of the Bloch interdomain coupling parameter a, Fig. 4.2(b), causes most notable changes in the curvature "knee" of the curve and seems to influence the growth of of the domains, as well as smaller changes to the saturation magnetization. It should be noted that we used $a = 100$ A/m to exaggerate these changes. Fig. 4.2(c) shows the changes of the hysteresis curves upon varying the parameter α. When high values were used, the model did not produce the typical hysteresis curves. Still, the α parameter causes very little change to the hysteresis curve. On the contrary, the parameter k which describes the difficulty of breaking the domain walls free of the pinning sites, shown in Fig. 4.2(d), causes major changes to the hysteresis curves in regions from zero magnetization to full saturation. However, it does not influence the shape of the curves when leaving the saturation magnetization. Similarly to the parameter α, the magnetization reversibility c does not influence the shape of the curve much when changed, which is shown in Fig. 4.2(e). The change in the K_{an} parameter describing the anisotropic average energy density, shown in Fig. 4.2(f) has smaller, but opposite effect than the parameter a. Lastly, the change of the angle between the easy axis of magnetization and the orientation of the magnetizing field, ψ, shown in Fig. 4.2(g), influences the ease of magnetization and behaves similarly to the parameter a. However, the former does not cause such a sharp "knee". From the analysis of the changes caused by the parameters used in the Jiles-Atherton model, we can assume that, in some cases, the parameters in the fit can balance each other out, and changes of some parameters have very little impact on the shape of the hysteresis curves.

(a)

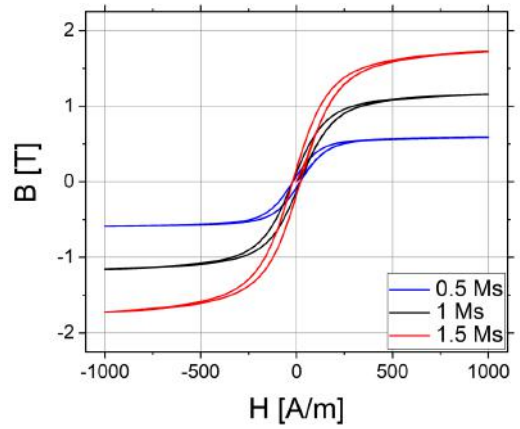
B [T]
H [A/m]
0.5 Ms
1 Ms
1.5 Ms

(b)

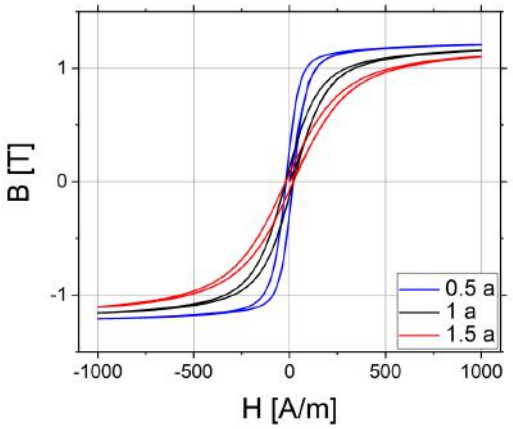
B [T]
H [A/m]
0.5 a
1 a
1.5 a

(c)

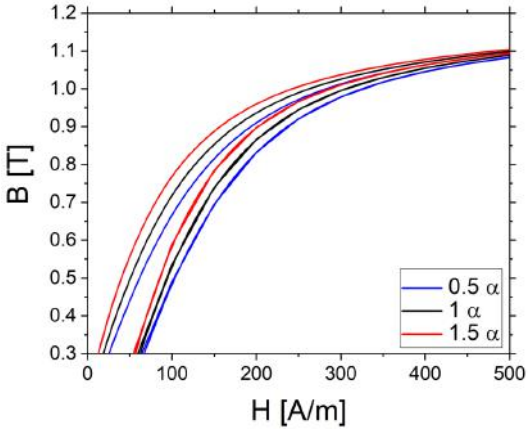
B [T]
H [A/m]
0.5 α
1 α
1.5 α

(d)

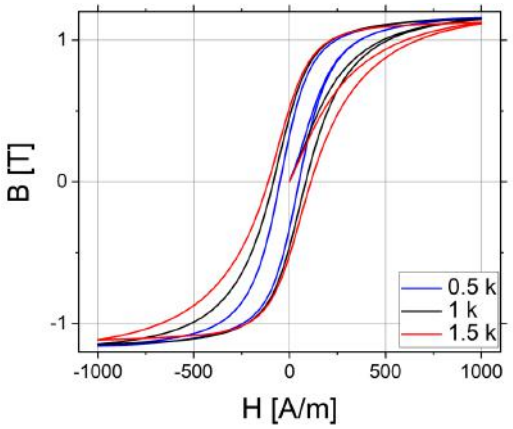
B [T]
H [A/m]
0.5 k
1 k
1.5 k

(e)

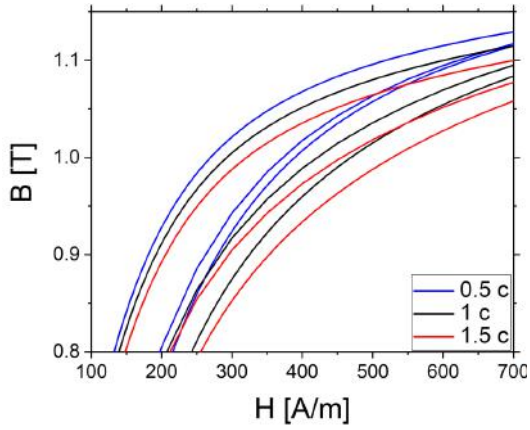
B [T]
H [A/m]
0.5 c
1 c
1.5 c

(f)

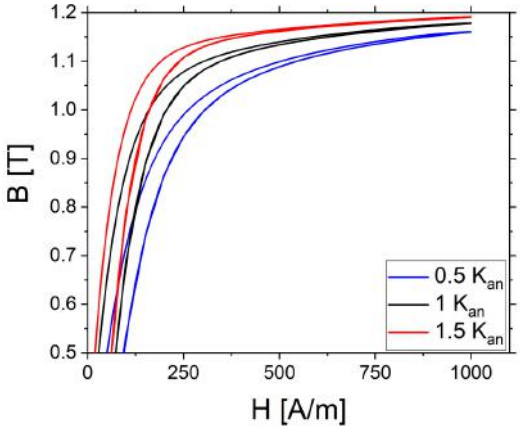
B [T]
H [A/m]
0.5 K_an
1 K_an
1.5 K_an

(g)

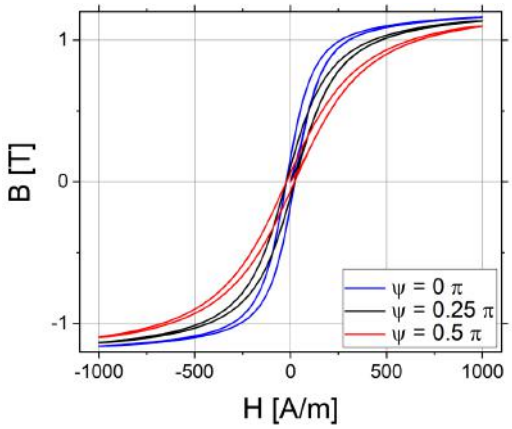

Figure 4.2: Variation of the magnetization curves due to changes in one parameter. Reference parameters are: $M_s = 1 \times 10^6$A/m, $a = 100$ A/m, $\alpha = 5 \times 10^{-5}$, $k = 20$ A/m, $c = 0.8$, $K_{an} = 400$ J/m^3, $\psi = 0$. In each picture, only one parameter is varied from 0.5 to 1.5 times its initial value while the others are fixed to the reference value: (a) M_s, (b) a, (c) α, (d) k, (e) c, (f) K_{an}, and (g) ψ varied from 0 to $\pi/2$.

4.2 Magnetic domains in iron specimens

The magnetic domains were observed by employing the Kerr microscope as described in Section 1.8. An example of magnetic domains in single-crystalline specimen is shown in Fig. 4.3. Here, one small grain can be seen in the upper right corner. This solitary grain was the only imperfection found in the single crystal and was used for easier orientation. In this case, the direction of the magnetizing field is vertical and illumination is also vertical, which allows us to image magnetic domains with magnetization vectors in the vertical direction. Fig. 4.3(a) shows the domains at zero applied field, Fig. 4.3(b) and 4.3(c) at -0.1 T and 0.1 T of, respectively. The color coding in the images is artificial to increase the visibility of the domains (false colors). Since the movement of domains is not significant, we also subtract the unmagnetized state image from the image showing the magnetized state. Fig. 4.3(d) shows difference between the -0.1 T state and the unmagnetized state. Similarly, Fig. 4.3(e) shows the difference between 0.1 T and unmagnetized state. The plots are achieved by subtraction of the unmagnetized state image from the image showing the magnetized states. Thus the contrast variation in these images does not represent the domains, but their growth (dark) or withdrawal (bright) in certain directions. In all Figures in this section, the direction of illumination $\boldsymbol{K}$ and direction of magnetic field $\boldsymbol{H}$ is shown by the arrows in top image of each figure. Furthermore, orientation of crystal directions best matching the shape of magnetic domains is shown. This orientation was revealed by EBSD measurements. The magnetic domains in Fig. 4.3 roughly follow the $\langle 100 \rangle$ direction in the crystal, visualized by the arrows in Fig. 4.3(a). The $\langle 100 \rangle$ directions in α-Fe are also easy axes of magnetization. The domains in this figure for either long rectangular domains (marked

A) or smaller loops containing domains with both magnetization direction (marked B). These loops are located in the upper left region of the images. Some domains appear as series of separated islands in a certain direction. However, also the domain best visible in Fig. 4.3(b) in the lower right corner shows serrations in its structure, which seems similar in size to the smaller separated islands . Lastly, the small grain in the top right corner contains domains with similar size to its surroundings.

Fig. 4.4 shows magnetic domains in Fe-mono-1 single crystal specimen, which was deformed by approx. 6% at room temperature. Compared to Fig. 4.3, which shows the specimen in the undeformed state, the magnetic domains seem to be of approximately the same size and they still follow the basic $\langle 100 \rangle$ crystal direction. Other magnetic domains (not shown here) look similar to those photographed on the undeformed specimen. Even though two different places are shown, the homogeneous deformation does not seem to cause any distinct change in the domain size. The domains here are reminiscent of of trees with branches sticking out of the trunk. We have not found any similar magnetic domain structures in the literature. These structures were not observed in the undeformed specimen. However, the whole surface was not studied and thus we cannot prove that these structures are a result of plastic deformation.

The Fe-mono-2 specimen was predeformed at room temperature to 1.7% and than to 2.5% at 77 K. The magnetic domains are shown in Fig. 4.5. These domains, contrary to previous measurements, seem to be bounded by $\langle 110 \rangle$ crystal directions instead of $\langle 100 \rangle$. The domains are also smaller, but repeat more frequently. Similar domain structure was observed by Bozorth [211], who call this a maze structure. However, Bozorth report that the domains are bounded along $\langle 100 \rangle$ directions. McKeehan and Elmore [212] also observed similar maze-like domains. In their case, the domains form a proper maze structure, whereas our magnetic domain structure seems to overlap. This can be caused by a different method of observation, as they used used magnetic powder to image the domains and we used Kerr microscopy. Secondly, in our case, the crystal surface is not perfectly along a $\{100\}$ crystal plane, which may cause distortion to the domain appearance. Large domains bounded by the $\langle 100 \rangle$ direction were observed on this specimen (not showed), similar to those shown in Fig. 4.3.

Fig. 4.6 shows magnetic domains in polycrystalline specimen Fe-poly-1, which was predeformed at room temperature to 0.9% and further deformed at 77 K to 2.5%. This polycrystalline specimen also deformed by twinning.

Fig. 4.7(a) shows an EBSD IPF Z map of the same area shown in Fig. 4.6 with identified twinning systems. Fig. 4.7(b) is the Kerr micrograph of the identical area showing crystal directions along which change in the magnetic domains occur. The magnetization can change along the (001) or (010) planes. As mentioned in Section 1.2, the easy axis of magnetization in α-iron is along the $\langle 100 \rangle$ crystal directions. In Fig. 4.7(b), the twins can block the magnetic domains from continuing further to the matrix. However, in some cases the magnetic domain continues uninterrupted, as can be seen around the middle part of the left-most $(\bar{2}11)[\bar{1}\bar{1}\bar{1}]$ twin (marked A), where the darker domain continues through the twin. At other places however, the domain is stopped at the twin-matrix boundary and a different domain emerges on the other side (marked B). A similar phenomenon is evident at the

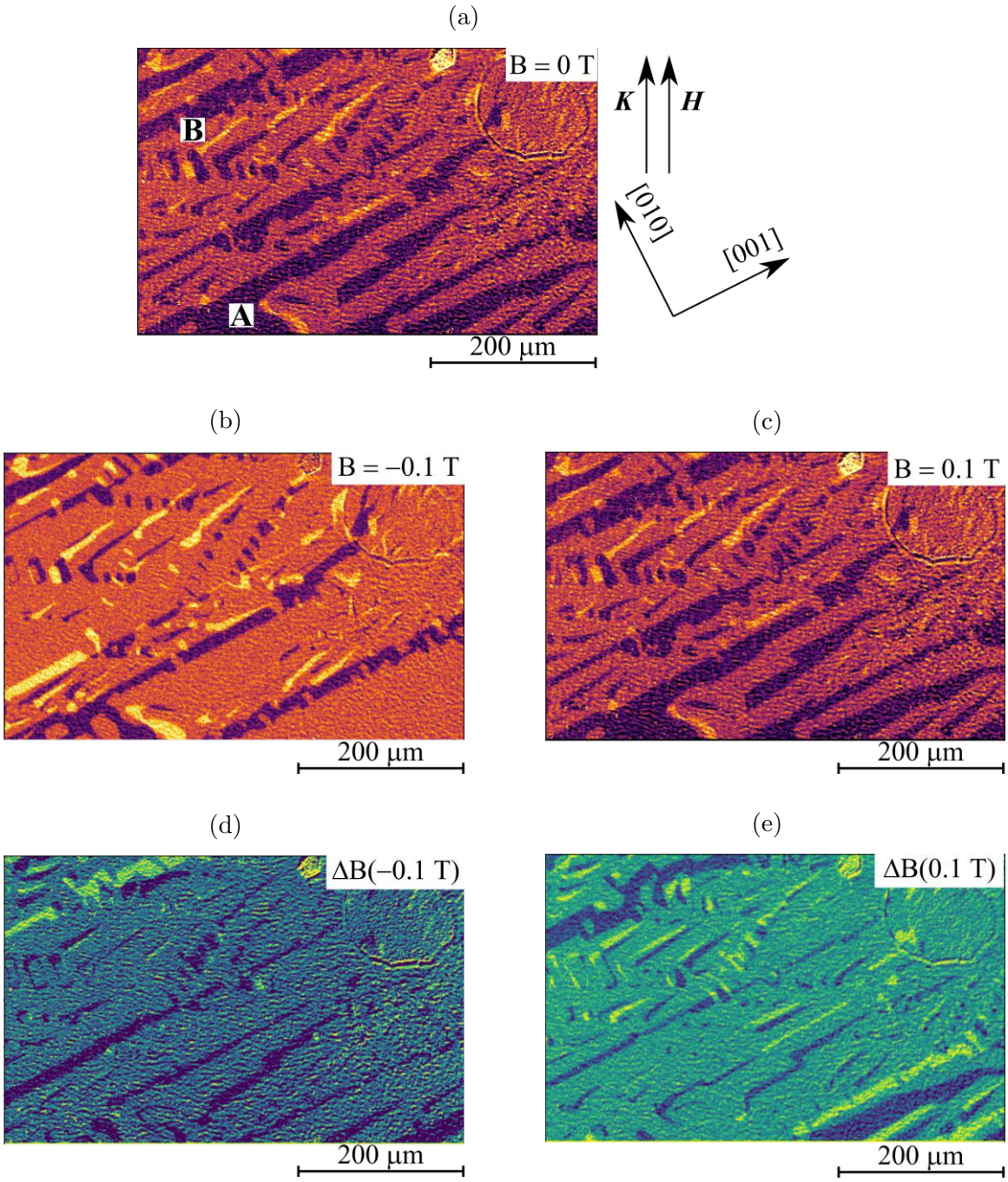

Figure 4.3: Magnetic domains measured by Kerr microscopy on α-iron Fe-mono-1 specimen before deformation in different magnetizing fields. Illumination $\boldsymbol{K}$ is vertical, thus only domains with vertical magnetization vectors are visible. The direction of magnetic field $\boldsymbol{H}$ is also vertical. (a) Unmagnetized state, (b) magnetized at -0.1 T, (c) magnetized at 0.1 T. Domain change between (d) -0.1 T and unmagnetized state and (e) 0.1 T and unmagnetized state.

left $(\bar{1}21)[11\bar{1}]$ twin. Needle-like domains form on $(321)[1\bar{1}\bar{1}]$ twins along the trace of $(0\bar{1}1)$ plane. A larger, but similarly looking domains also emerge spontaneously from the matrix, but form along (001) plane. The twins seem to have a large influ-

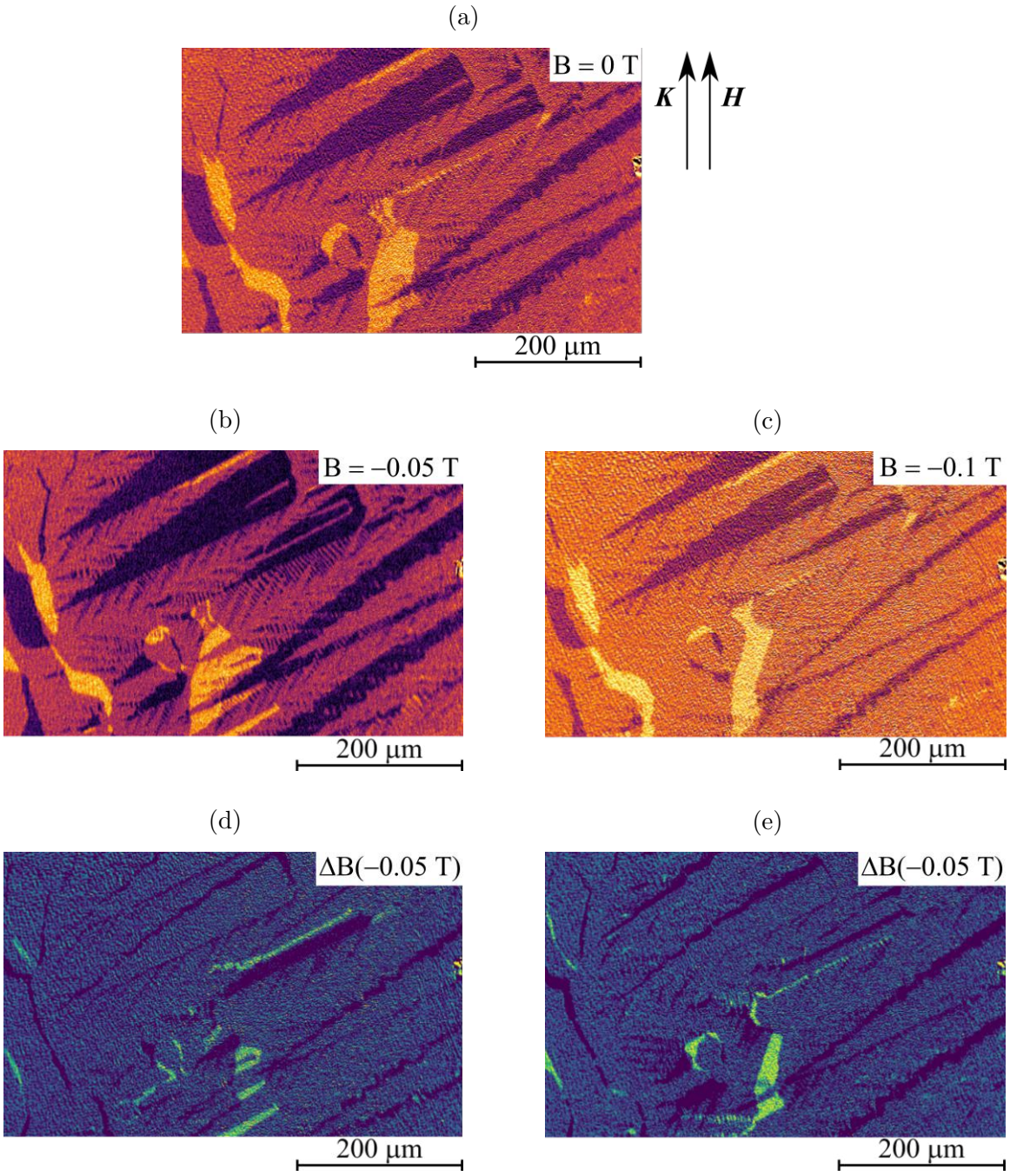

Figure 4.4: Magnetic domains measured by Kerr microscopy at α-iron Fe-mono-1 deformed specimen in different magnetizing fields. Illumination $\boldsymbol{K}$ is vertical, thus only domains with vertical magnetization vectors are visible. Magnetic field direction $\boldsymbol{H}$ is also vertical. (a) 0 T, (b) -0.05 T, (c) -0.1 T. Domain change between (d) -0.05 T and unmagnetized state and (e) -0.05 T and -0.1 T state. Background taken at 0.1 T.

ence on the magnetic domains that follow the the (001) and (010) directions. The smaller domains in the bottom right corner in Fig. 4.7(b) seem to be unaffected by the presence of the $(\bar{1}21)[11\bar{1}]$ twin. A similarly looking domains were reported

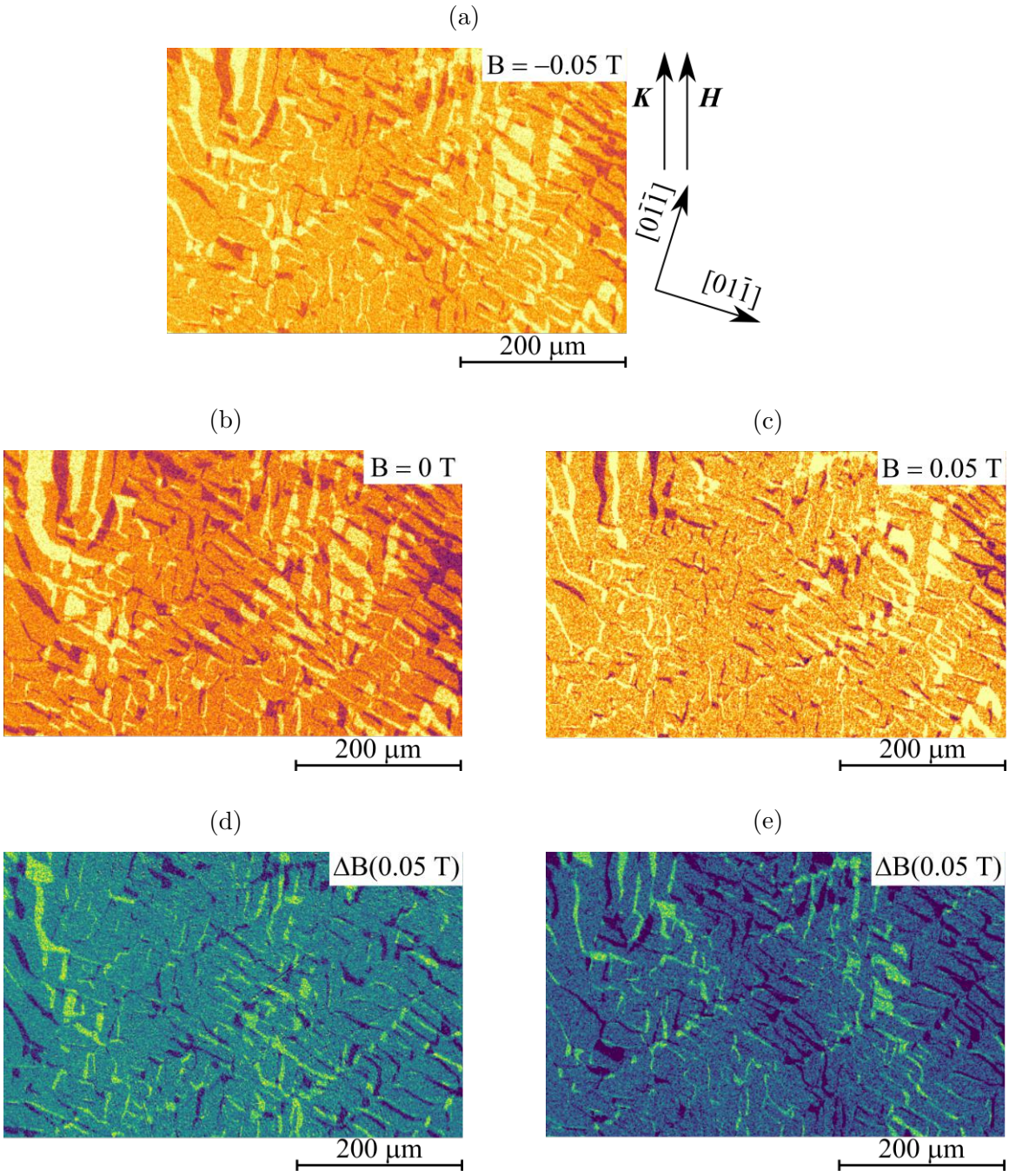

Figure 4.5: Magnetic domains measured by Kerr microscopy at α-iron Fe-mono-2 specimen in different magnetizing fields. Illumination $\boldsymbol{K}$ is vertical, thus only domains with vertical magnetization vectors are visible. Magnetic field direction $\boldsymbol{H}$ is also vertical. (a) -0.05 T, (b) 0 T, (c) 0.05 T. Domain change between (d) -0.05 T and unmagnetized state and (e) 0.05 T and unmagnetized state. Background taken at -0.1 T.

by Street and Hall [213] in iron with 3.5% of silicon. Due to different technique used to image the domain (colloidal Fe_2O_3 particles in soap water), it is difficult to compare the domain structures directly. Nonetheless, they report the needle-like

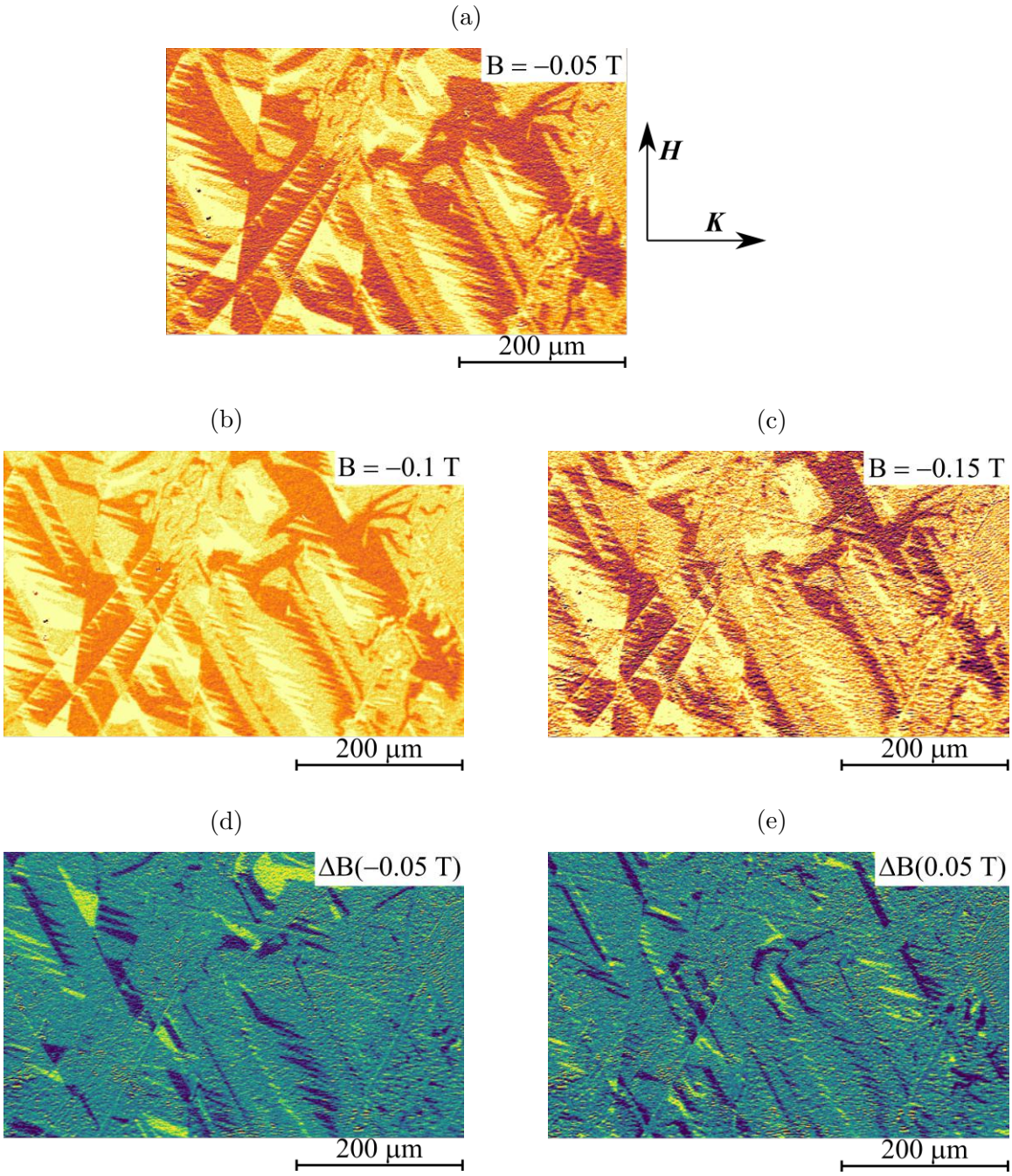

Figure 4.6: Magnetic domains measured by Kerr microscopy at α-iron Fe-poly-1 deformed specimen in different magnetizing fields. Illumination $\boldsymbol{K}$ is horizontal, thus only domains with horizontal magnetization vectors are visible. Magnetic field direction $\boldsymbol{H}$ is vertical. (a) -0.05 T, (b) -0.1 T, (c) -0.15 T. Domain change between (d) -0.05 T and -0.1 T and (e) -0.15 T and -0.1 T. Background taken at 0.1 T.

domains in $\langle 100 \rangle$ directions. They further argue that if the twin is sufficiently thin, the magnetic flux might not be contained on one side of the twin, but overlap to the other side. This qualitatively agrees with our results, as the thinner twins seem to nucleate the needle-like domains, but the thicker twins, such as $(\bar{1}21)[11\bar{1}]$ twin

in Fig. 4.7 seem to stop the magnetic domains without nucleating new ones on the other side. Furthermore, similar domains were observed by Hug [214] also in iron with 3.5% of silicon, who calls them "spikes". Hug reports these domains in undeformed specimens, originating from a grain boundary. He also shows that the domains often continue unchanged through a grain boundary, or create the spikes with reverse magnetization.

(a)

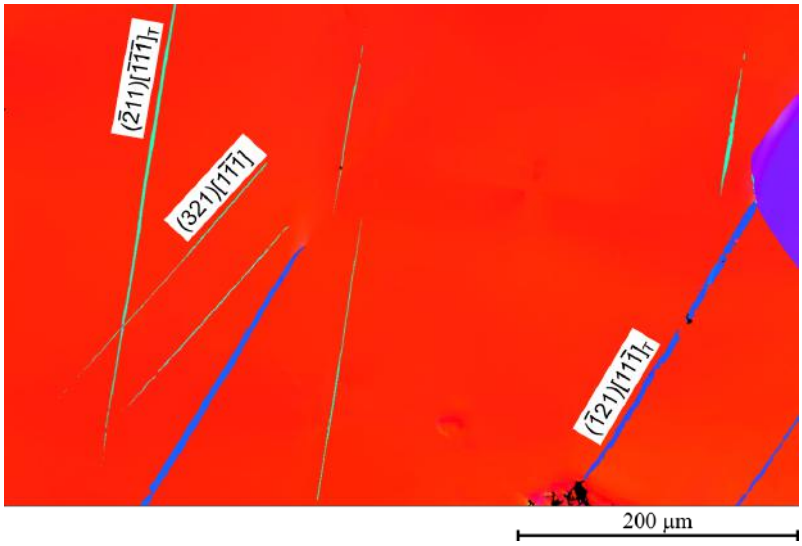

(b)

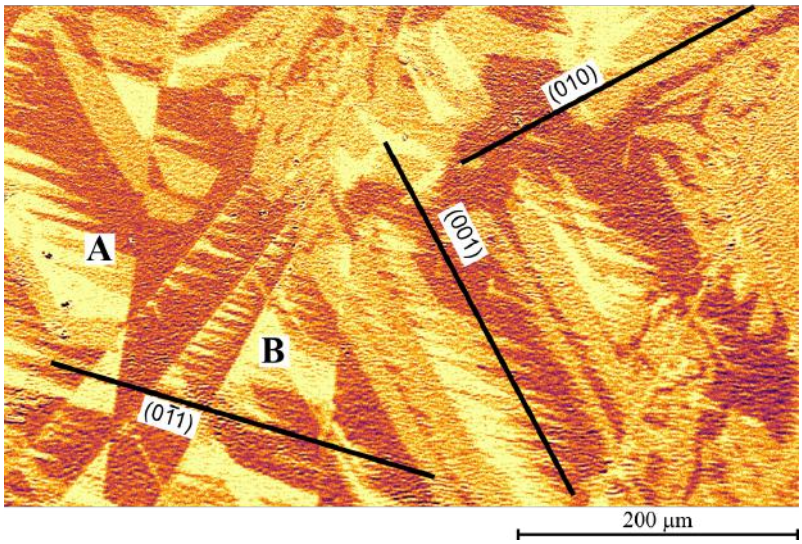

Figure 4.7: (a) EBSD IPF Z map showing twins and their labels in deformed Fe-poly-1 specimen, (b) Kerr micrograph of the same area as in (a) showing the magnetic domains and corresponding directions. Illumination and direction of the magnetic field is the same as in Fig. 4.6(a). The legend to the (a) is same as in Fig. 3.3(b). The subscripts in the labels of twinning systems in (a) mean that the system is sheared in the twinning sense.

4.3 VSM measurements on Cr single crystals

Single crystal Cr specimens were fabricated in the form of a cube of 3 mm edge length with sides perpendicular to ⟨100⟩ crystal directions. The sample preparation was identical to the process described previously. The PPMS 9T vibrating sample magnetometer system was used to characterize the magnetic states of specimens. The magnetic susceptibility was measured from 4 K to 298 K on heating cooling. The probing field used was 1 T. Measurements were also performed at lower fields (0.1 T and 0.01 T) but they proved to be too noisy. After the cooling and heating cycle, the specimen was rotated and measured again in all three ⟨100⟩ directions. The measurement on the as-received specimen is shown in Fig. 4.8. Differently colored lines represent different orientations, full lines represent heating (the specimen was heated from 4 K to 295 K), dashed lines represent cooling back down to 4 K. Vertical dashed-dotted line represents the spin-flip temperature, T_{SF}, at 123 K, where the magnetic state changes from TSDW at higher temperatures to LSDW at lower temperatures.

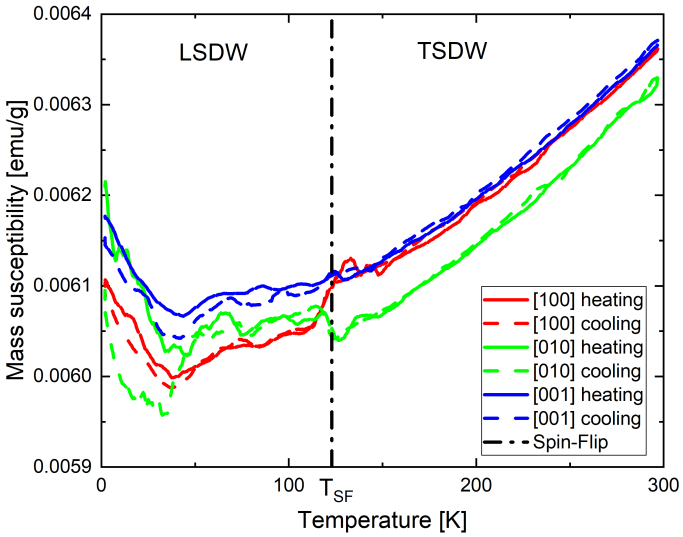

Figure 4.8: Mass susceptibility measurements on chromium specimens in the initially magnetically isotropic (triple-**Q**) state.

A similar methodology was used to turn the specimens into a single-**Q** state. The 3 mm cube specimen was heated above the Néel temperature and subsequently cooled down to 4 K in the field of 5 T. The results of mass susceptibility measurements on the same specimen as in Fig. 4.8 but in the single-**Q** state are shown in Fig. 4.9, where the direction of the magnetizing field is along the [100] direction.

The most notable changes between the two states occur around T_{SF} at 123 K. The almost gradual change of susceptibility around the spin-flip temperature in triple-**Q** state (Fig. 4.8) becomes abrupt in the single-**Q** state (Fig. 4.9). This observation suggests that spins suddenly align in longitudinal or transversal direc-

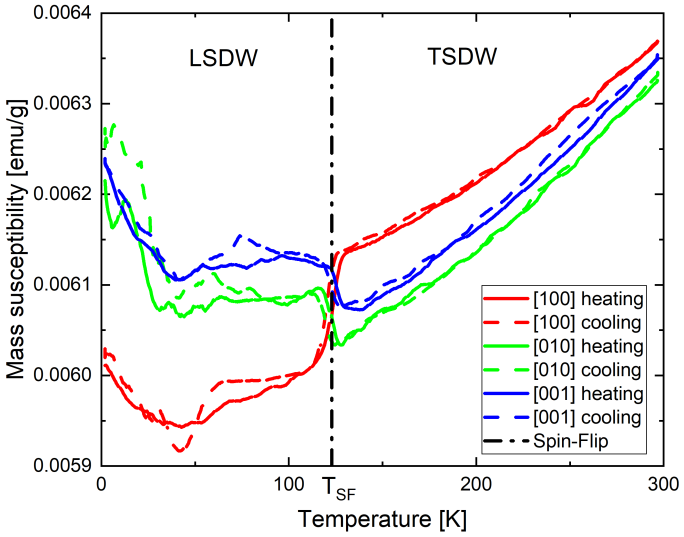

Figure 4.9: Mass susceptibility measurements on chromium specimens in the single-**Q** state.

tions and this phenomenon is detected during both hearing and cooling. In the ideal case, all curves in Fig. 4.8 should lie on top of each other. However, this is not the case. The differences are most likely caused by partial magnetization by the probing field. In the case of the single-**Q** state in Fig. 4.9, the green and blue lines should be on top of each other. This misalignment can be caused by two factors: (i) the orientation of the specimen is not exactly [100], or (ii) the magnetization in the direction of the magnetizing field is not 100%. Even with the mentioned facts, this method seems to be suitable for determining the magnetic state of the chromium single crystals. Fig. 4.10 offers explanation of the susceptibility curves in Fig. 4.9. In the real experiment, the specimen was rotated while the probing magnetic field **H** stayed fixed. It is important to keep in mind that the specimen was cooled down from above the Néel temperature in the field of 5 T to 4 K. The direction of the magnetic field, in relation to all pictures in Fig. 4.10 is horizontal and the direction of the crystal axes is identical to the diagrams shown in Section 1.7. The colors of the cubes in Fig. 4.10 correspond to the colors of the curves in Figs. 4.8 and 4.9. The vectors **S**, **H**, and **Q** represent the direction of spins, probing magnetic field and wavevector respectively. The pictures in the upper and lower rows in Fig. 4.10 represent the TSDW and LSDW state respectively. Following is the explanation of the meaning of the curves in Fig. 4.9 using the illustrations in Fig. 4.10.

- *Red curve in the [100] direction*
  The value of magnetic susceptibility is lower for the red curve in Fig. 4.9 below the spin flip temperature. This suggests that spins **S** are aligned with the probing field **H**. The sample was magnetized in the same direction as the magnetic field. Therefore, the wavevector **Q** is also in the same direction, as visualized in Fig. 4.10(d). When the specimen is heated above the spin flip

temperature, the orientation of the spin **S** changes, creating the transversal phase, visualized in Fig. 4.10(a). Here the spins can be oriented in two directions, both perpendicular to **Q** and the specimen is in the double $\boldsymbol{\eta}$ state described in Fig. 1.13. Now, the probing field **H** is perpendicular to the spins **S** and, therefore, the susceptibility increases. Because there are two possibilities for spin directions, both of them perpendicular to the probing field **H**, the values of susceptibility are higher than for the green and blue curves in Fig. 4.9.

- *Green curve in the [010] direction*
  The values of susceptibility are high in the region below the spin-flip temperature in Fig. 4.9 suggesting that the spins **S** are perpendicular to the probing filed **H** as shown in Fig. 4.10(e). Upon heating above the spin-flip temperature, the phase changes from longitudinal phase, where spins **S** and wavevector **Q** are parallel, to the transversal spin density wave phase where the spins **S** are perpendicular to the wavevector **Q**. Again, there are two possibilities for directions of the perpendicular spins, as shown in Fig. 4.10(b). Now at least one set of spins is parallel; therefore, the value of the susceptibility is lower compared to the red curve above.

- *Blue curve in the [001] direction*
  At low temperatures below the spin-flip temperature, the susceptibility value is high because of the orientation of the spins **S** and probing field **H** in Fig. 4.10(f). The reason is identical to that in the previous explanation for the green curve. Very similarly, when the temperature increases and spins flip, depicted in Fig. 4.10(c), one set of spins **S** is perpendicular to the probing field **H** which explains the decrease of susceptibility values around the spin-flip temperature.

In the TSDW phase, the values of the susceptibility increase with increasing temperature due to the increasingly strong effects of the temperature on the instability of the internal magnetic order. Furthermore, the rise in the susceptibility values for the red curve when switching from the LSDW phase to the TSDW phase is roughly double the decrease for the other two curves. This can be explained by the reorientation of spins, which are all in the same direction at low temperatures (Fig. 4.10(d)), and flipping into perpendicular directions at high temperatures (Fig. 4.10(a)). In the case of the blue and green curves, only half of the spins theoretically reorient by the probing filed **H**, which results in a smaller step at the spin-flip temperature.

Similar results were reported in chromium by Pepper et al. [215]. This behavior is, however, not unique to chromium and was reported also for other materials [216–219]. The susceptibility seems to decrease below the spin-flip temperature in case when the spins are parallel to the magnetic field (red curve in Fig. 4.9). This phenomenon is explained by Kittel [220, p. 321-345]: "When the external field is perpendicular to the spontaneously induced magnetic moment, the magnetic susceptibility is almost independent of temperature, while in the parallel case, the susceptibility decreases when the temperature is lowered because the force making magnetic moments antiparallel becomes stronger and stronger, which leads to

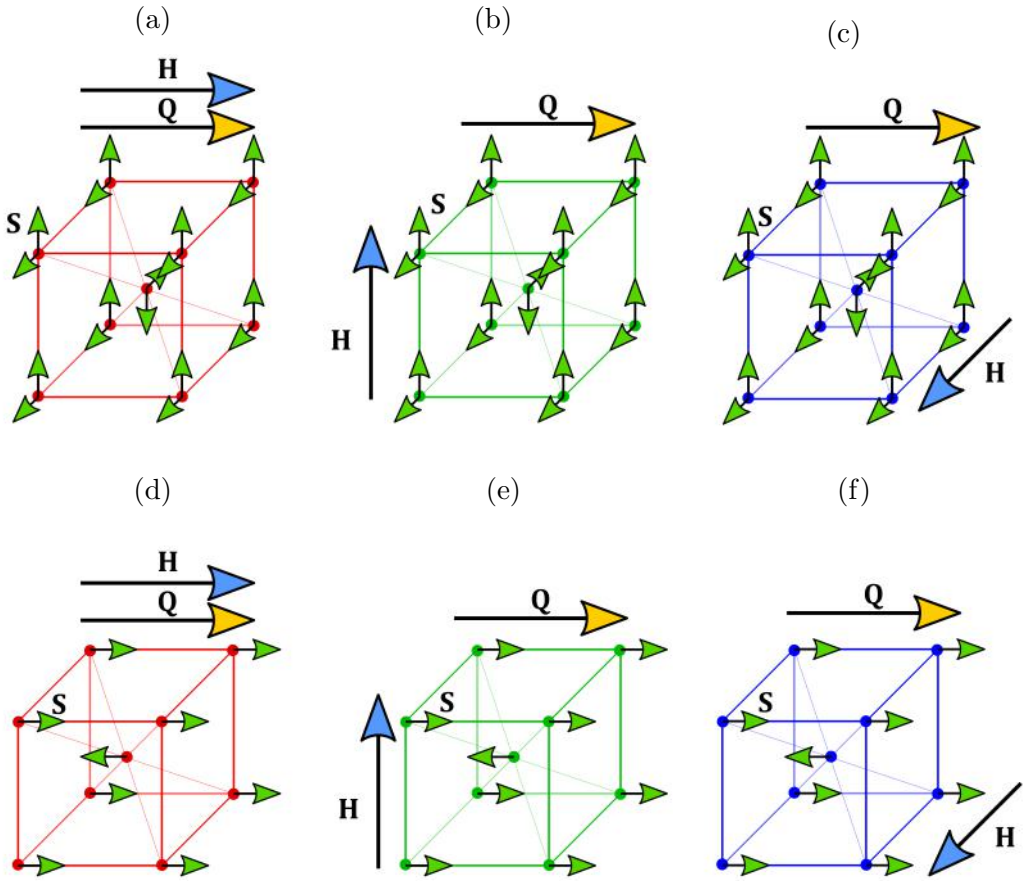

Figure 4.10: Orientations of the spins **S** (green arrows), directions of the probing field **H** (blue arrows), and the wavevectors **Q** (yellow arrows) for all six possible configurations. These are used to interpret the three curves above and below the spin-flip temperature in Fig. 4.9.

that the material being harder and harder to be magnetized by the external field". This explanation holds for the LSDW state, where the susceptibility decreases until approximately 50 K and both perpendicular susceptibilities stagnate. We do not currently have an explanation for the increase of the susceptibility below 50 K. However, it may be caused by the way the sample is attached to the VSM holder, in particular by freezing the air trapped by the glue that holds the specimen. This assertion is supported by the fact that the freezing point of oxygen and nitrogen are 54 and 63 K, respectively.

4.4 Neutron diffraction study of Cr single crystals

The specimens used in the following neutron diffraction studies were cut from the Cr-3 source crystal (Accumet Materials, Co.) by electroerosive machining and checked with CT to rule out any hidden defects in the specimens. The specimens that have passed have been prepared by grinding, polishing, and electropolishing as

explained in Section 3.1.1. All specimens in this section, except one cube-shaped specimen with a 3 mm edge length, have been cut in the same orientation. The loading axis is along the $[\bar{1}25]$ crystallographic direction, shown in Fig. 4.11(a), in which the slip on low-stressed $(0\bar{1}1)$ planes was observed. The cube specimen, measured in Section 4.3 by VSM, has $\langle 100 \rangle$ crystal directions along the edges of the cube. Because the presence of magnetism that breaks the crystal symmetry, the elementary area of the stereographic projection is not the standard $[001]-[011]-[\bar{1}11]$ triangle, but the triangle is formed by the axes [001], [010] and $[\bar{1}00]$, as shown in Fig. 4.11(a). Fig. 4.11(b) shows a visualization of the chromium single-crystalline specimen where the arrows represent the $\langle 100 \rangle$ directions with different color coding. The [001] direction is red, the [010] direction is green, and the $[\bar{1}00]$ direction is blue. In order to hold the specimen fixed in the desired orientation while doing the VSM measurements, we have made special holders using 3D printing. A visualization of such holder is shown in Fig. 4.11(c), in which the sample is oriented in [010] direction with the magnetic field applied along the long axis of the specimen holder.

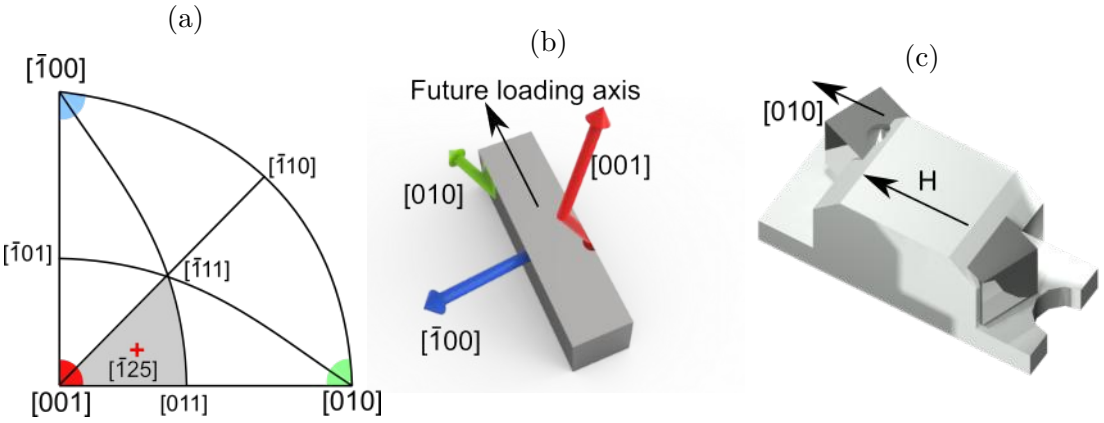

Figure 4.11: Orientation of the specimens used for magnetic neutron scattering experiments: (a) position of the $[\bar{1}25]$ loading axis in the extended stereographic projection with color-coded $\langle 100 \rangle$ directions, (b) visualization of the $\langle 100 \rangle$ directions in relation to the specimen with same color coding as in (a), (c) example of the 3D printed holder with inserted specimen oriented with [010] direction parallel with the magnetic field. The red, green, and blue colors represent the directions of the wavevectors of SDWs.

The specimen holder with the inserted specimen was glued to the holder of the PPMS VSM machine and magnetized by the field-cooling method described in Section 1.7. The specimen was heated to 340 K, which is about 30 K above the Néel temperature, in order to ensure proper demagnetization. After a short stay at 340 K, the magnetic field was switched to 5 T. The specimen was cooled to 4 K, after which the magnetic field was switched off. After re-heating, the specimen was taken out of the machine at approx. 280 K[3], quickly removed from the holder and kept in the freezer at 243 K to preserve the magnetic state. The schematic representation of the field-cooling process is shown in Fig. 4.12. A total of seven specimens were

[3]The machine does not allow opening the chamber below 273 K.

prepared in this way. Three pairs with the orientation of the loading axis along the [$\bar{1}$25] direction, each pair magnetized in [001], [010] and [$\bar{1}$00] directions. One specimen of cubic shape was oriented with the three ⟨111⟩ directions along the edges (the same specimen was used in Section 4.3).

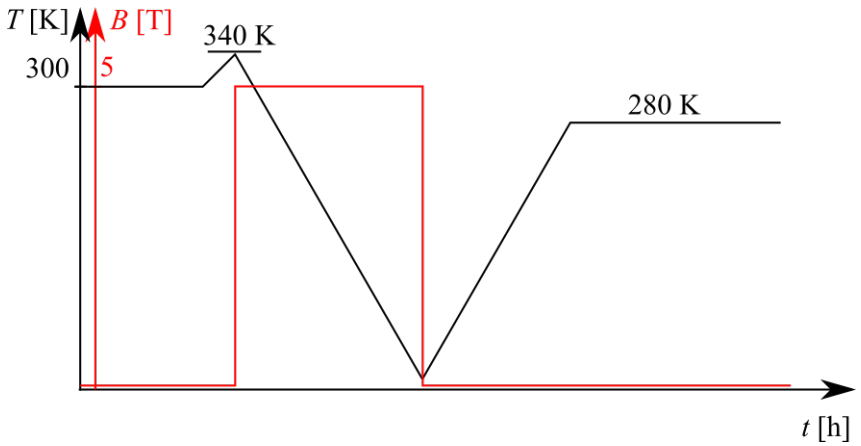

Figure 4.12: Schematic explanation of the magnetization by the field-cooling method. The black line represents the change of the temperature in Kelvins over time and the red line represents the magnitude of magnetic field in Tesla.

All specimens except the cube were predeformed at room temperature. The specimens were still cold when taken out of the freezer just before the deformation and they were kept in frozen cooling pads. The deformation was done using the Instron 8862 machine with maximum force of 100 kN. Due to the lack of space and time constrains, the predeformation was done without an extensometer with the crosshead speed of 50 µm per minute. The role of this predeformation is to create dislocations in the specimen and thus prevent the brittle fracture. The extent of predeformation was calculated after the deformation from the knowledge of the sizes of the sample before and after the experiment. As the extensometer is not present during the experiment, one has to guess the amount of the deformation from the crosshead displacement, which leads to inconsistent results. The desired predeformation was between 0.5 and 1 %, which was achieved. The specimens PSI 1, PSI 4, and PSI 9, previously field-cooled in [$\bar{1}$00], [010] and [001] directions, respectively, were put back into the freezer immediately after the measurement of deformation. Using these specimens we shall be able to capture the magnetic state before the low-temperature deformation of their conjugate samples (second specimen magnetized in the same way in this case). The specimens PSI 6, PSI 3, and PSI 10, field-cooled in [$\bar{1}$00], [010] and [001] directions, respectively, were left in the machine after predeformation, unloaded and the cryostat was immediately filled with liquid nitrogen. After 30 minutes of cooling, while nitrogen was continuously replenished, the low-temperature deformation was performed with the same crosshead speed as in the case of predeformation. After the deformation, the frozen specimen was taken out from the cryostat and returned into the freezer. The low-temperature deformation was done only to 2-3 % of plastic strain to prevent brittle fracture and disintegration of the specimen. The precise values of predeformation strain, low-temperature deformation strain, and yield stress reached during the low-temperature deformation

are summarized in Table 4.3. The Euler angles of the specimens expressed in the Bunge notation[4] (in degrees) are: PSI 4 (110.2°, 30.4°, 1.8°); PSI 10 (114.1°, 28.0°, 88.3°); PSI 9 (113.3°, 25.3°, 86.6°); PSI 3 (117.2°, 27.8°, 83.1°); PSI 1 (112.5°, 30.5°, 89.7°) and PSI 6 (111.8°, 31.1°, 0.4°).

The engineering stress-strain curves of the specimens deformed at 77 K are shown in Fig. 4.13. The colors of the curves correspond to the directions of wavevectors of SDWs shown in the stereographic projection in Fig. 4.11(a)[5]. Each of the loading axes of the three specimens deformed at 77 K is slightly different (although very close to the $[\bar{1}25]$ direction), and the same misorientation for PSI 6 and PSI 10 is coincidental. If we were to take the angle between the $[\bar{1}25]$ direction and the three {100} directions precisely, we would get 79.5°, 24.1°, and 69.6° for the [001], [010] and the $[\bar{1}00]$ directions respectively.

The engineering stress-strain curves in Fig. 4.13 show significant differences in the yield stress. Since the PSI 3, PSI 6, and PSI 10 specimens were prepared from the same source crystal, they have similar levels of predeformation ($\epsilon = 0.51$, 1, and 0.7, respectively). Their loading axis is almost identical and thus we assume that the differences in the yield stress must be caused due to the misorientation of the wavevector and the loading axis. The influence of the slightly different loading axis and slight difference in predeformation seem minute due to the almost exact match of the PSI 6 and PSI 10 stress-strain curves.

While we cannot describe the concrete process responsible for the almost 200 MPa difference in the yield stress (estimated by the 0.2 % offset strain), it cannot be reconciled by a slight difference in the predeformation or minute variation of the loading axis. Furthermore, a very small difference exists in the strain hardening of the specimens. While the samples PSI 6 and PSI 10 both showed very slight strain hardening, the sample PSI 3 showed very slight strain softening after approx. 2% of plastic strain.

Table 4.3: The summary of predeformation strain, strain generated by low temperature deformation at 77 K and the estimated yield stress at low temperatures for the six PSI specimens.

Magnetization direction	**[001]**		**[010]**		**$[\bar{1}00]$**	
Specimen	**PSI 4**	**PSI 10**	**PSI 9**	**PSI 3**	**PSI 1**	**PSI 6**
Predeformation [%]	0.51	0.7	0.48	0.51	0.68	1
Deformation at 77 K [%]	-	2.74	-	2.88	-	2.46
Yield stress [MPa]	-	989	-	1168	-	920

The specimens were transported from the IPM to the Paul Scherrer Institute, in a sealed polystyrene box filled with cooling pads frozen to -30 °C. Immediately

[4]The Bunge notation define the rotation of the coordinate system of the specimen into the coordinate system of the crystal. This is done by sequential rotation around the $z - x' - z'$ axes by the three angles [221].

[5]The loading direction is shown in the standard [001]-[011]-$[\bar{1}11]$ standard streographic triangle in Fig. 4.11(a) with the three orientations of wavevectors **Q** demonstrated in the enlarged part of the [001]-[010]-$[\bar{1}00]$ region shown.

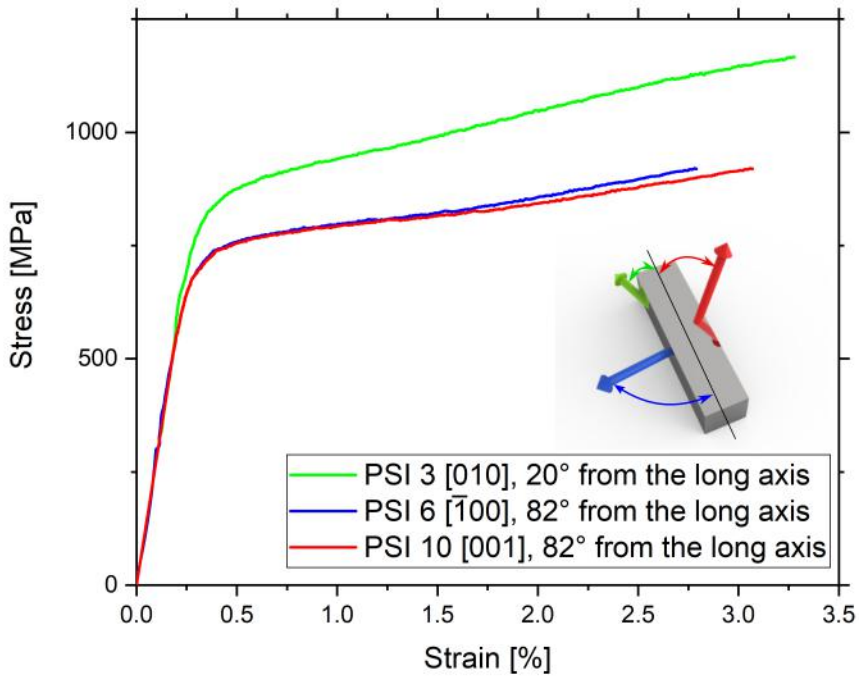

Figure 4.13: Engineering stress-strain curves for specimens PSI 3, PSI 6, and PSI 10 at 77 K. The angle represents the angle between the supposed direction of the wavevector (colored arrows) and the long axis of the specimen, which is identical to the loading axis as depicted by the inset.

after the arrival, the specimens were kept in the freezer in the SINQ facility until the experiment. In order to mount the specimen in the ZEBRA diffractometer, the specimens were placed onto a thin L-shaped aluminum sheet and tied with a thin aluminum or copper wire so they could not move during the tilting of the diffractometer's goniometer. The specimen holder was subsequently attached to the motorized goniometer and cooled with nitrogen vapor. Afterward, the holder with the specimen was enclosed in the aluminum chamber, and the closed-cycle helium refrigeration system was switched on to keep the specimen from reaching the Néel temperature. During the cooling, the orientation of the specimen to the diffractometer coordinate system was established. This process involves finding specific reflections (the approximate position of the individual crystal direction was known thanks to the previous EBSD analysis) and creating the so-called UB-Matrix [222]. Once the UB Matrix was established for the first specimen, similar matrices for other specimens were found quickly due to a very similar orientation. The orientation is established with a 1D He-3 detector tube, but most of the measurements were done using 2D He-3 area detector equipped with the oscillating radial collimator[6].
The 2D detector measures slices of the three-dimensional space, and thus a spa-

[6]The purpose of the oscillating radial collimator is to suppress the diffraction peaks from the specimen environment, such as the sample holder, cryostat, furnace, etc.

tial distribution of the reflection can be recorded. The recorded data can then be translated into the reciprocal space.

An example of this is shown in Fig. 4.14. In particular, Fig. 4.14(a) and 4.14(c) show [020] nuclear reflections measured at 250 K in the neighborhood of [010] magnetic reflection at 70 K respectively. The coordinate system used to visualize these reflections represents the detector space, where the X and Y are pixel positions of the detector, therefore representing the detector screen, and Z denotes individual frames taken during acquisition in ascending order. The measured neutron intensity at each voxel[7] is represented as a ball, whose transparency depends on the neutron intensity. The voxels with zero intensity are completely transparent and thus invisible, while the voxel with the highest intensity is completely opaque. The 3D reconstruction shown in Fig. 4.14(c) shows satellite reflections around the [010] reflection in reciprocal space (five oval-shaped objects roughly between Y = 100 and 150) and powder reflection from the specimen environment (a wall-shaped object near Y = 180). These datasets can be transformed into the reciprocal space with the knowledge of the neutron wavelength, UB-Matrix, specimen detector distance, and instrumental angles. The reflections in Fig. 4.14(a) and 4.14(c) are shown in Fig. 4.14(b) and 4.14(d) respectively in the reciprocal space. This representation advantageously shows the slice of the reciprocal space measured. It should be noted that for visualization purposes, only voxels with counts two and higher are shown in Fig. 4.14(c) and 4.14(d). The magnetic reflections are generally weaker than the nuclear ones. A summary of neutron diffraction reflections expected in bcc lattice is presented in Section 1.6.1.

Nonetheless, the 2D detector suffers from poorer resolution and lower efficiency compared to the 1D detector. It is mainly used to find the positions in the reciprocal space rather than to measure the precise shapes of the reflections. It is often beneficial and easier to understand the measurement when the data are projected onto one plane instead of the 3D visualization. This process is employed to visualize the data measured with the 2D detector in Fig. 4.15. Fig. 4.15(a) shows the projection of the [200] reflection on the XY plane at 70 K (specimen PSI 1), and Fig. 4.15(b) shows the same projection of exactly the same reflection but obtained on the specimen PSI 6. The [200] nuclear reflections of PSI 1 are slightly elongated, which is caused by the predeformation. A more distinct elongation of the PSI 6 [200] reflection in Fig. 4.15(b) is again caused by deformation, but in this case, both the predeformation and subsequent deformation at 77 K. Both figures are plotted with the same scale. The slightly brighter band to the right of the reflection is again the powder diffraction of the holder or the aluminum chamber in which the specimen is enclosed. The band is not visible in Fig. 4.15(a) due to the higher intensity of the reflection. Fig. 4.15(c) shows an integrated intensity over the ω angle of the PSI 1 and PSI 6 [200] nuclear peaks, where ω represents the rotation of the specimen according to the 4-cycle geometry with the detector fixed in place [223]. For each frame of the 3D dataset, the intensity of the reflection can be summed, and the result plotted in relation to one of the instrumental parameters. The deformation causes the peak to lose intensity while increasing its width. The intensity decreased

[7] A voxel represents a value on the grid in three-dimensional space just as pixel represents a value on a grid in the two-dimensional space.

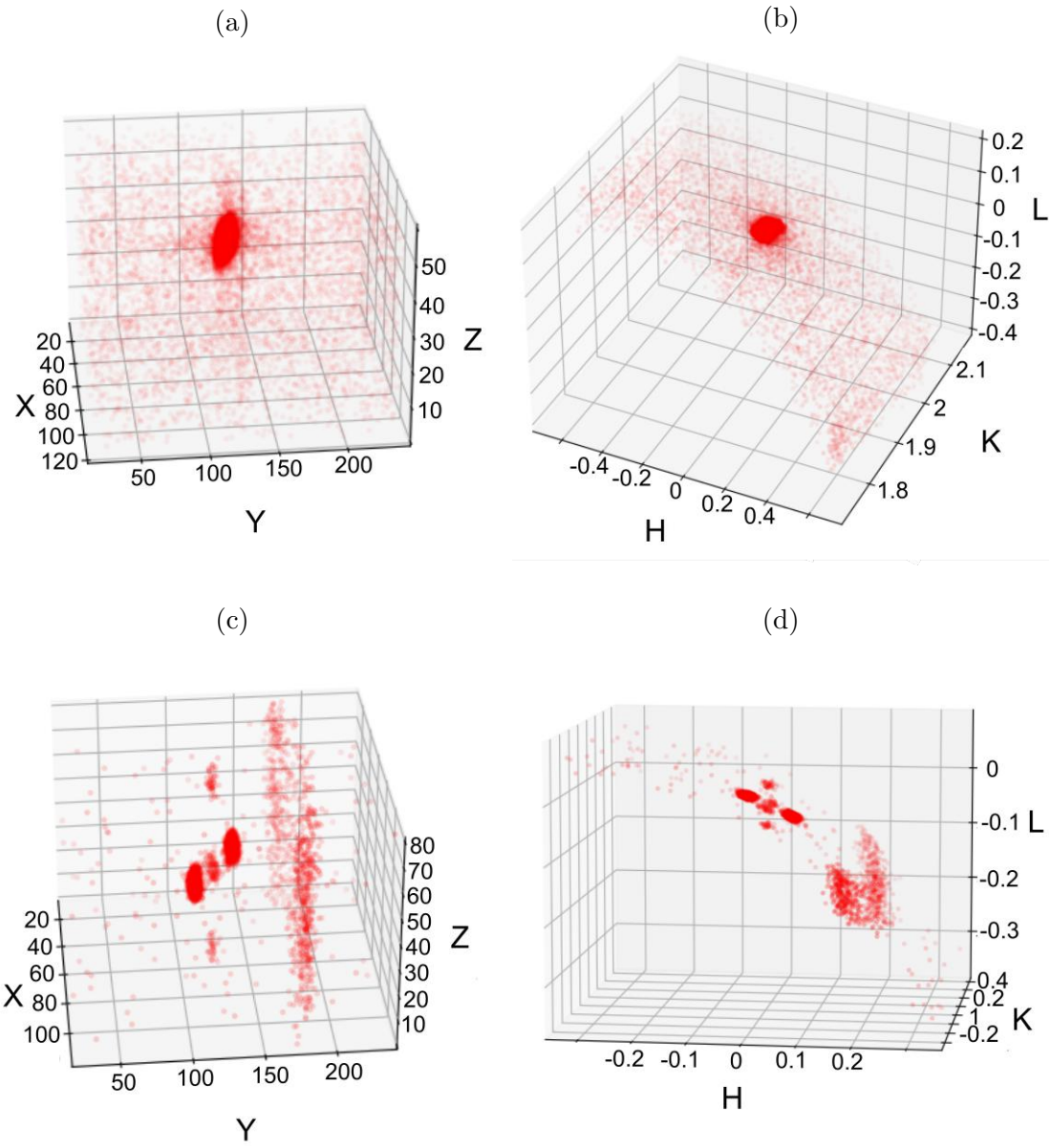

Figure 4.14: 3D reconstruction of the reflection measured with the 2D detector: (a) [020] nuclear reflection in the detector space, (b) [020] reflection in the reciprocal space, (c) neighborhood of [010] reflection in the detector space, (d) neighborhood of [010] reflection in the reciprocal space.

from 7191 a.u. to 2420 a.u. at the same time, the Full Width at Half Maximum (FWHM) increased from 0.46° to 1.43° (fitted as Gaussian peak).

The shape of the elongated nuclear peak is also transferred to the magnetic reflections. As an example, we show the neighborhood of the [001] magnetic reflection[8] of the only predeformed specimen PSI 9 (Fig. 4.16(a)), and the specimen PSI 3

[8]The [001] reflection is not visible because it is not an allowed nuclear reflection in the bcc lattice

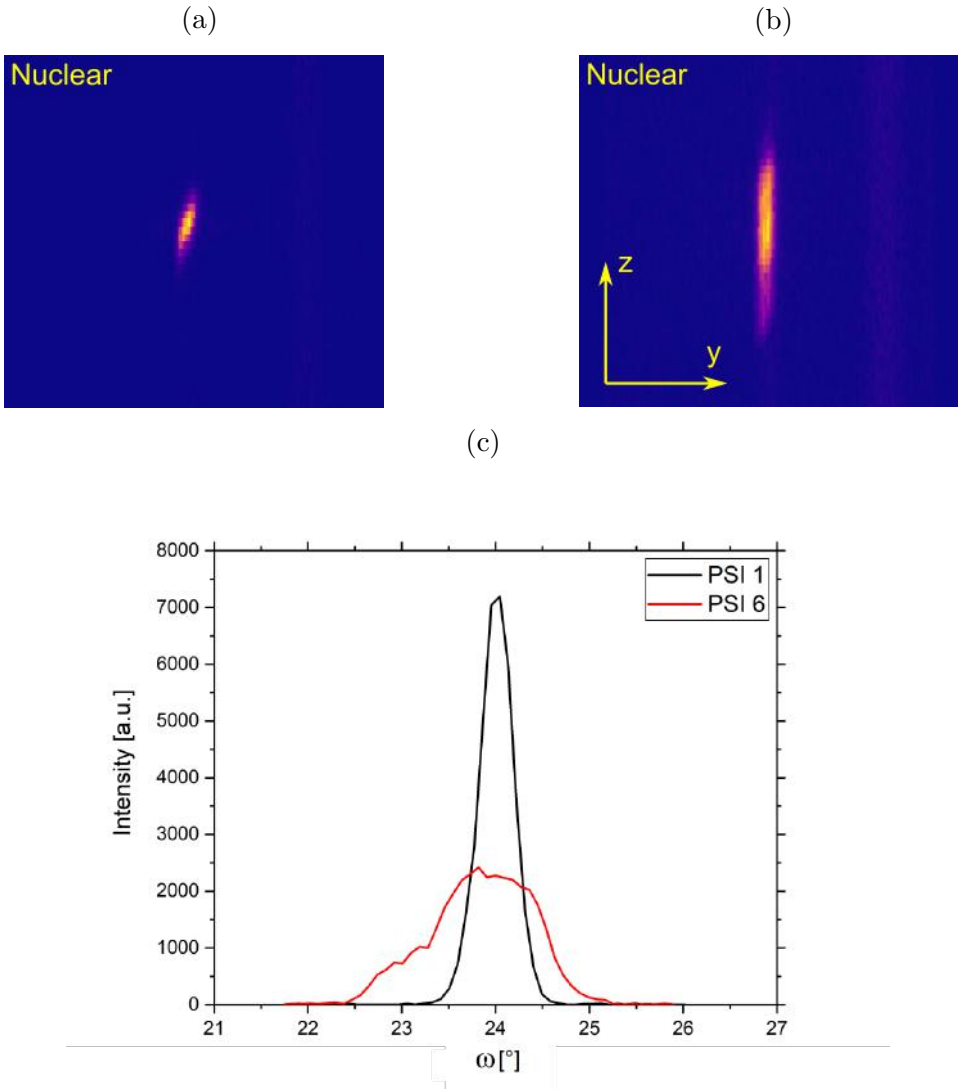

Figure 4.15: The [200] nuclear reflection at 70 K measured on the samples (a) PSI 1 and (b) PSI 6. The panel (c) shows an integrated intensity of the samples PSI 1 and PSI 6 around the [200] nuclear peak along the sample rotation ω.

(Fig. 4.16(b)) also deformed at 77 K. The magnetic reflections were measured at 150 K, at which the specimens were in the TSDW state. Fig. 4.16(a) shows $[\pm\delta, 0, 1]$ and $[0, 0, 1\pm\delta]$ reflections from two spin density waves, namely the $(1\pm\delta, 0, 0)$ and $(0, 0, 1\pm\delta)$ fundamental SDWs. One can also see that the $[\pm\delta, 0, 1]$ peak has a stronger reflected intensity compared to the latter, which means that this wave is dominant. Due to the deformation, the individual reflections shown in Fig. 4.16(b) overlap and appear as one. Nevertheless, from the projection in different directions (not shown), they can be clearly distinguished. The $[0, \pm\delta, 1]$ reflection is the only one in the [001] neighborhood and is the result of the deformation at 77 K. The powder diffraction rings (vertical streaks on the right side of both figures) are also more pronounced due to the lower intensity of the magnetic reflections.

The cubic specimen was the only one magnetized and not deformed to assess the magnetic state after field cooling without the interference of the deformation.

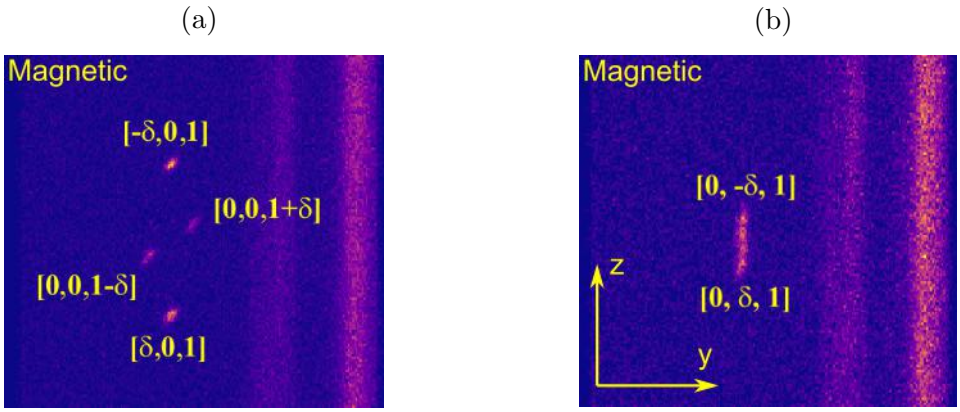

Figure 4.16: Example of the YZ projection of neighborhood of the [001] magnetic reflection from the 2D detector at 150 K: (a) PSI 9, (b) PSI 3.

Unfortunately, the specimen was a bi-crystal which was found during the neutron scattering experiment. As a result, some of the nuclear and subsequently magnetic reflections are split and represent the two slightly misoriented parts of the crystal. This is visualized in Fig. 4.17. Fig. 4.17(a) shows a projection of the [002] nuclear peak at 250 K, which is split into two unequally sized reflections, and Fig. 4.17(c) shows the projection of the [020] nuclear reflection under the same condition. The latter reflection does not show the splitting, which suggests that the crystal has a single orientation in this direction throughout the volume. The [200] nuclear reflection (not shown in the figures) is split similarly to Fig. 4.17(a). The magnetic reflections representing wavevectors that are split in the $[0, \pm\delta, 1]$ direction due to the inherent nature of the spin density wave seem to carry the information of the [020] nuclear reflection, which does not show the splitting due to the bi-crystallinity. This is represented in Fig. 4.17(b) that shows the neighborhood of the [001] reflection at 70 K. The $[\pm\delta, 0, 1]$ magnetic reflections show the same splitting as the [200] nuclear reflection, while the $[0, \pm\delta, 1]$ satellites have no counterpart around the [020] reflection. The same behavior is observed for the reflection in Fig. 4.17(d). Furthermore, the reflections in Fig. 4.17(d) measured at 150 K, show much higher intensity of the $[0, 1 \pm \delta, 0]$ magnetic reflection, which is caused by the field cooling. This means that the specimen is not fully in the single-**Q** state, only the wavevector created by the field cooling is dominant in the specimen.

To describe the magnetic states of the specimens, we have explored the neighborhoods of the [001], [010], and $[\bar{1}00]$ magnetic reflections in all specimens. We will describe the magnetic state by the reciprocal space diagrams of neutron diffraction as described in Section 1.7. Together with the measured data, represented by the black circles, we also show theoretical results of the field and stress cooling, represented by the blue and red circles, respectively. An example of such diagram is shown in Fig. 4.19. The magnetic state of the 3 mm cube specimen is described by the reciprocal space diagram shown in Fig. 4.18. This diagram for the TSDW state measured at 150 K is shown in Fig. 4.18(a). While all SDWs are present, the intensities of the reflections in Fig. 4.17(b) and 4.17(d), suggest that the fundamental $(0, 1\pm\delta, 0)$ SDW is dominant. This is also represented by larger circles in these diagrams. This state is further transferred to the LSDW phase in Fig. 4.18(b),

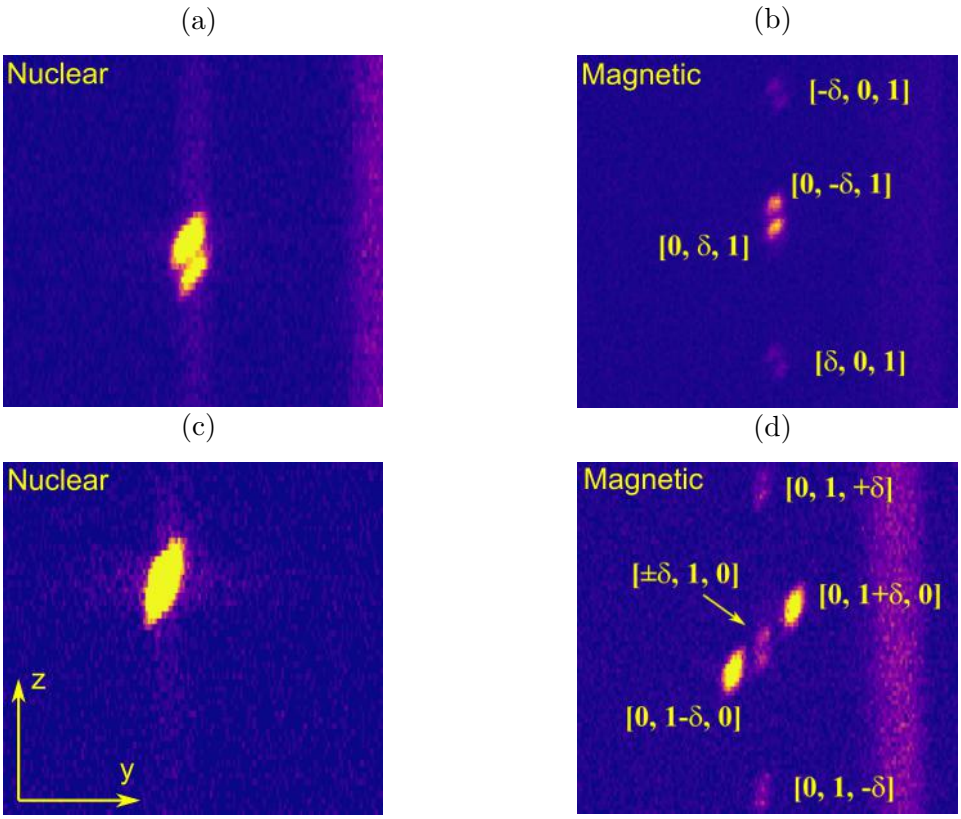

Figure 4.17: YZ projections of the nuclear and magnetic reflections of the 3 mm cube specimen: (a) [002] nuclear reflection measured at 250 K (b) neighborhood of the [001] magnetic reflection measured at 70 K, (c) [020] nuclear reflection measured at 250 K, (d) neighborhood of [010] magnetic reflection measured at 150 K.

where the same fundamental spin density wave is also dominant. Note that the on-axis reflections are not present in the LSDW state. They do not contribute to the magnetic scattering, because these reflections are parallel to the scattering vector.

4.4.1 Neutron diffraction experiments on specimens PSI 4 and PSI 10 with Q=[001]

The reciprocal space diagrams of the neutron scattering of the PSI 4 specimens measured at 150 and 70 K are shown in Fig. 4.19(a) and 4.19(b), respectively. The PSI 4 specimen was magnetized along the [001] axis and predeformed at RT to strain of 0.51%. The resulting magnetic state is most comparable to the state resulting from the stress cooling in the [010] direction closest to which the specimen was predeformed. It should be noted that the [010] direction is approximately 20° from the actual loading axis. However, the most intense reflections at 150 K (Fig. 4.19(a)) are $[1\pm\delta, 0, 0]$, $[\pm\delta, 0, 1]$ and $[\pm\delta, 1, 0]$ which all belong to the fundamental $(1\pm\delta, 0, 0)$ SDW. The less intense reflections are from the $(0, 0, 1\pm\delta)$ fundamental SDW. This distribution of reflections agree well with the stress cooling, as the SDWs parallel to the stress direction is not present. In the LSDW state, shown in Fig. 4.19(b), the $(1\pm\delta, 0, 0)$ fundamental SDW is also dominant. However, the $(0, 0, 1\pm\delta)$ reflection

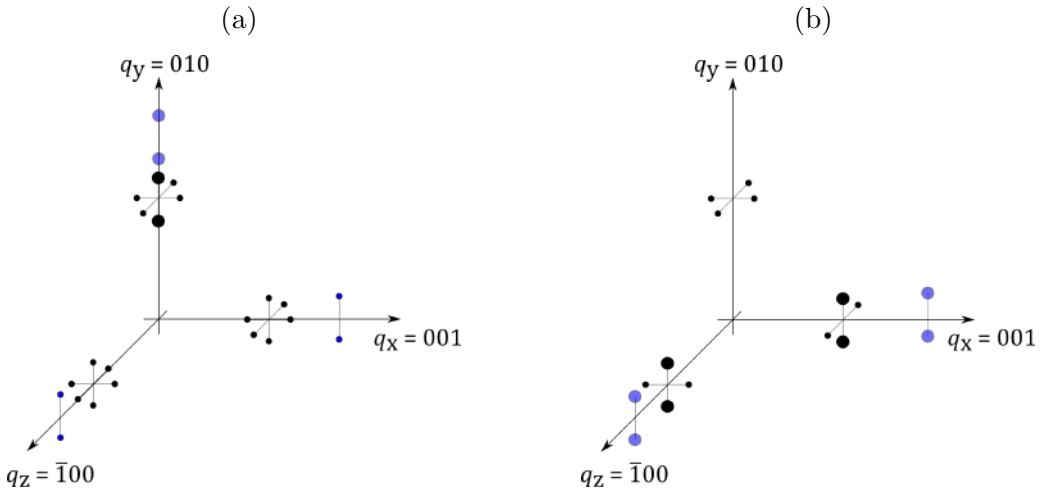

Figure 4.18: Reciprocal space diagrams of neutron diffraction of the 3 mm cube specimen described in Section 4.3: (a) TSDW state at 150 K, (b) LSDW state at 70 K. Black circles represent experimental data and blue circles the field-cooled state described in Section 1.7.

has transformed into the $(0, 1\pm\delta, 0)$ SDW, which is not in accordance with the stress cooling prediction.

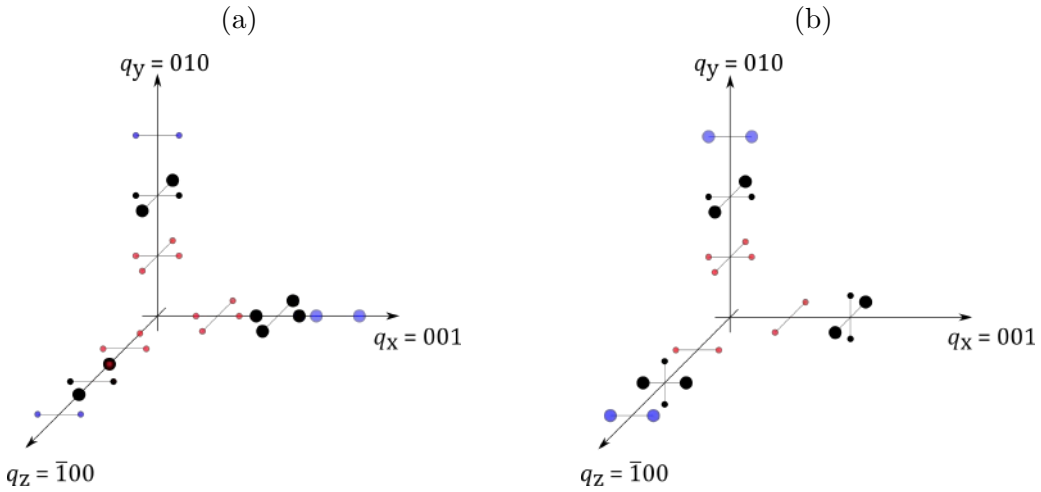

Figure 4.19: Reciprocal space diagrams of the neutron diffraction on the PSI 4 specimen: (a) TSDW state at 150 K, (b) LSDW state at 70 K. Black circles represent experimental data, blue and red circles the theoretical field-cooled and stress-cooled state, respectively, as described in Section 1.7.

The reciprocal space diagram of neutron diffraction of the specimen PSI 10, which was magnetized along the [001] crystal axis, predeformed at RT to 0.7 % and deformed at 77 K by another 2.74 % in the direction closest to the [010] crystal direction for the TSDW and LSDW state is shown in Fig. 4.20(a) and 4.20(b) respectively. The TSDW state measured at 150 K is characterized by the $[1, \pm\delta, 0]$, $[0, 1\pm\delta, 0]$ and $[0, \pm\delta, 1]$ magnetic reflections, representing the fundamental $(0, 1\pm\delta, 0)$ SDW, which would be created by the field cooling in the [010] direction. The same

SDW persists in the LSDW state measured at 70 K, and is represented by the $[1, \pm\delta, 0]$ and $[0, \pm\delta, 1]$ reflections. The resulting magnetic state is thus a single-**Q** state with the fundamental $(0, 1 \pm \delta, 0)$ spin density wave. This wave must have been caused by the plastic deformation, as field-cooling would result into a different configuration.

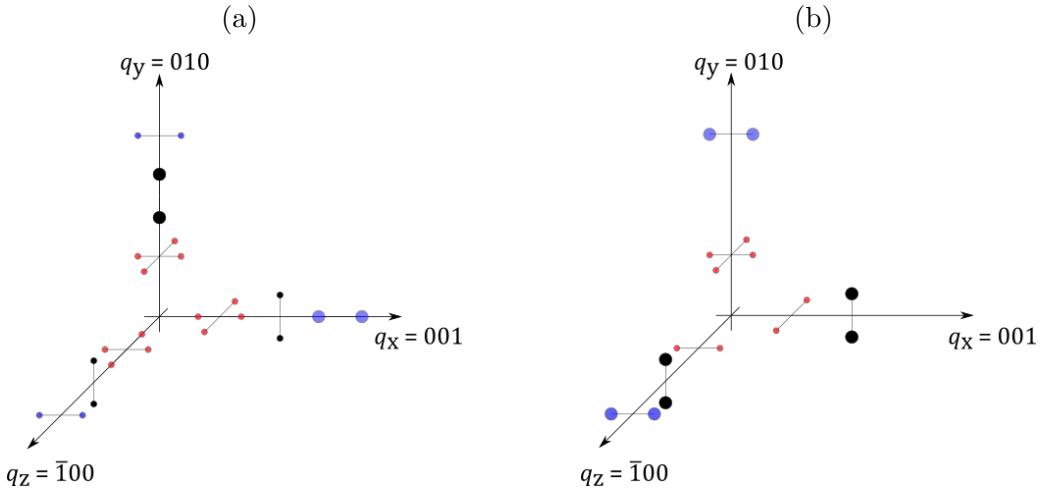

Figure 4.20: Reciprocal space diagrams of neutron diffraction of the PSI 10 specimen: (a) TSDW state at 150 K, (b) LSDW state at 70 K. Black circles represent experimental data, blue and red circles the field-cooled and stress-cooled state, respectively, as described in Section 1.7.

4.4.2 Neutron diffraction experiments on specimens PSI 3 and PSI 9 with Q=[010]

The PSI 9 specimen was magnetized along the [010] crystal axis direction and predeformed at RT to 0.48%. The magnetic state in the TSDW region at 150 K is shown in Fig. 4.21(a) and is represented by the $(1 \pm \delta, 0, 0)$ and $(0, 0, 1 \pm \delta)$ fundamental SDW that would agree with the state prepared by the stress cooling. The LSDW state measured at 70 K is shown in Fig. 4.21(b) from which we observe that the characters of the SDWs are unchanged.

The PSI 3 specimen was magnetized by the field cooling method with the wavevector along the [010] direction. Afterward, it was predeformed at room temperature and further deformed at 77 K in the direction closest to the [010] direction. The resulting magnetic states are described by the reciprocal space diagrams in Fig. 4.22(a) and 4.22(b) for the TSDW and LSDW state, respectively. Both states are characterized by the $(0, 1 \pm \delta, 0)$ fundamental spin density wave, which agrees with the magnetic state created by the field cooling along the [010] crystal direction. Again, the resulting state is the single-**Q** state.

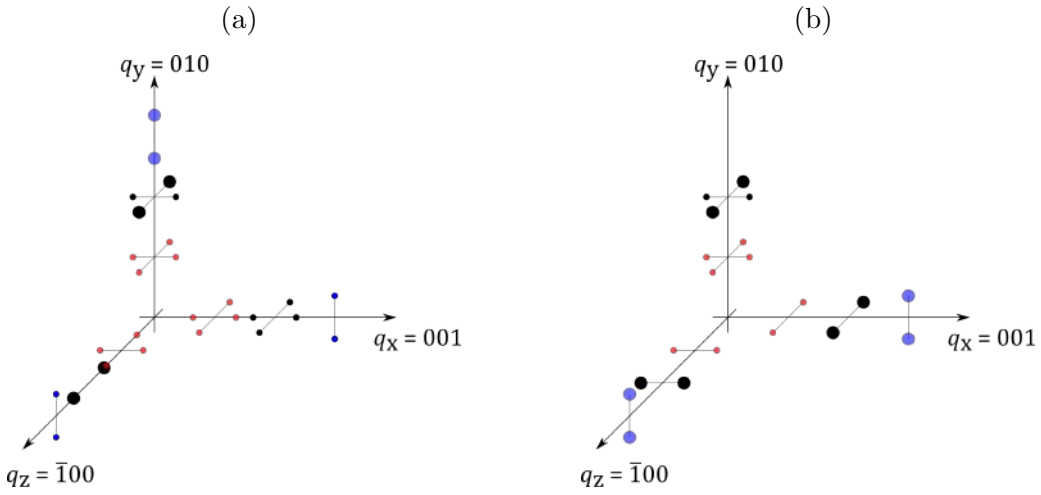

Figure 4.21: Reciprocal space diagrams of neutron diffraction of the PSI 9 specimen: (a) TSDW state at 150 K, (b) LSDW state at 70 K. Black circles represent experimental data, blue and red circles the field-cooled and stress-cooled state respectively, as described in Section 1.7.

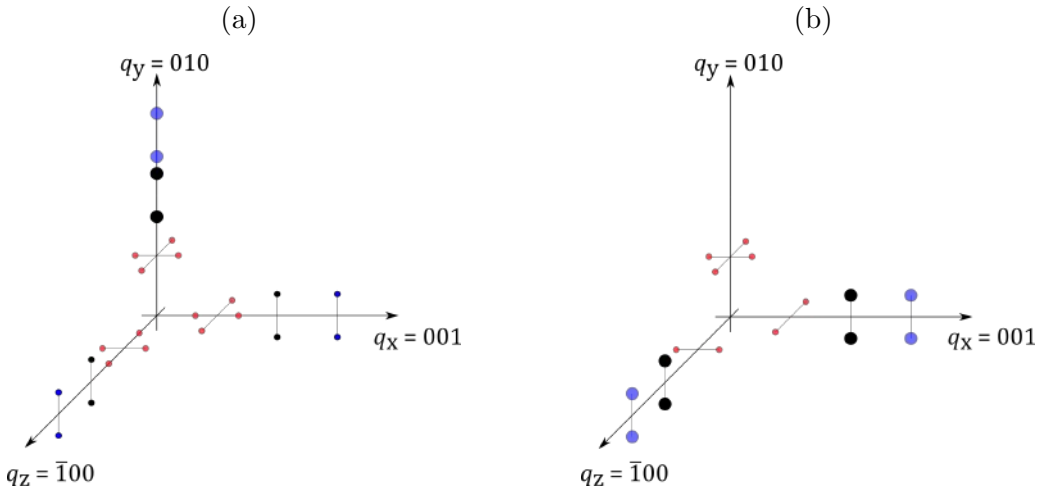

Figure 4.22: Reciprocal space diagrams of neutron diffraction of PSI 3 specimen: (a) TSDW state at 150 K, (b) LSDW state at 70 K. Black circles represent experimental data, blue and red circles the field cooled and stress cooled state respectively, as described in Section 1.7.

4.4.3 Neutron diffraction experiments on specimens PSI 1 and PSI 6 with Q=[$\bar{1}$00]

The PSI 1 specimen was magnetized along the [$\bar{1}$00] direction and predeformed at RT to 0.68%. The magnetic state in the TSDW regime at 150 K is shown in Fig. 4.23(a). Based on the $[1\pm\delta, 0, 0]$, $[\pm\delta, 1, 0]$ and $[\pm\delta, 0, 1]$ reflections, the majority of the volume is characterized by the $(1 \pm \delta, 0, 0)$ SDW, which would agree with the filed-cooled specimen. However, there is a very weak $[0, 0, 1 \pm \delta]$ reflection that is not accompanied by other reflections as would be expected for this SDW. A possible explanation of this behavior is that the this already weak reflection is the strongest

reflection of the $(0, 0, 1 \pm \delta)$ spin density wave and thus the remaining two $[1, 0, \pm\delta]$ and $[0, 1, \pm\delta]$ reflections which are even weaker have intensities comparable to the background. A similar situation is in the LSDW state shown in Fig. 4.23(b), where the magnetic state is characterized by the $(1 \pm \delta, 0, 0)$ spin density wave, represented by the $[\pm\delta, 0, 1]$ and $[\pm\delta, 1, 0]$ reflections. The remaining weaker reflection, $[1, 0, \pm\delta]$ would correspond to the $(0, 0, 1\pm\delta)$ SDW. However the $[0, 1, \pm\delta]$ reflection is missing. Since the visible weak reflection is alone in the [100] neighborhood, it is easier to resolve than reflection with another reflection close by, for example in the [010] neighborhood. Therefore, we believe that there is $[0, \pm\delta, 1]$ reflection, but it is overshadowed by the $[\pm\delta, 1, 0]$ reflection.

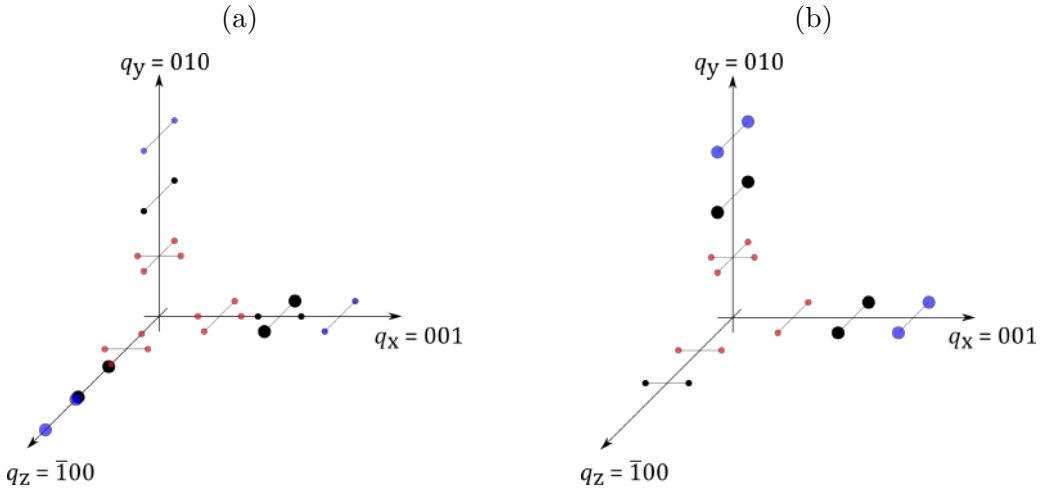

Figure 4.23: Reciprocal space diagrams of neutron diffraction of the PSI 1 specimen: (a) TSDW state at 150 K, (b) LSDW state at 70 K. Black circles represent experimental data, blue and red circles the field-cooled and stress-cooled state respectively, as described in Section 1.7.

The PSI 6 specimen was field-cooled in the $[\bar{1}00]$ direction, predeformed at the room temperature to 1 % of strain, and further deformed at 77 K by 2.46 % in the [010] crystal direction. The magnetic state is the same as in the other samples deformed at 77 K - PSI3 and PSI10 . It is characterized by the $(0, 1 \pm \delta, 0)$ fundamental spin density wave in both TSDW and LSDW states shown in Fig. 4.24(a) and 4.24(b), respectively.

The process of the field-cooling has been proven to work. The final magnetic state was not fully single-**Q**, but the spin density wave that was supposed to be produced by the field cooling was dominant. The predeformation seems to favor the $(1 \pm \delta, 0, 0)$ fundamental spin density wave. However, the magnetic state of predeformed specimens is not the same, because the initial magnetic state is broken by the deformation at room temperature. On the other hand, the deformation at 77 K always creates the $(0, 1\pm\delta, 0)$ single-**Q** state regardless of initial magnetic state.

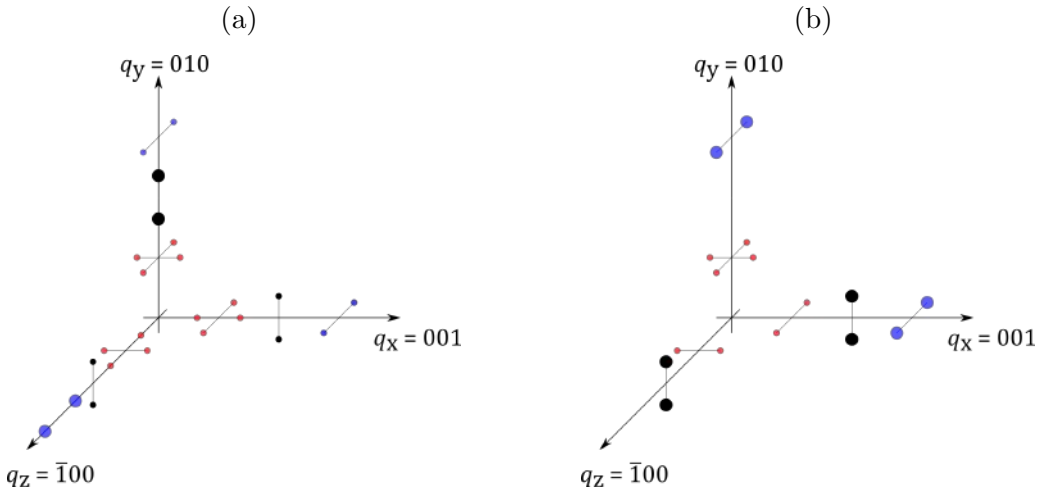

Figure 4.24: Reciprocal space diagrams of neutron diffraction of the PSI 6 specimen: (a) TSDW state at 150 K, (b) LSDW state at 70 K. Black circles represent experimental data, blue and red circles the field-cooled and stress-cooled state respectively, as described in Section 1.7.

4.4.4 Change in the spin-flip temperature due to plastic deformation

We have measured the temperature dependence of several magnetic reflections to demonstrate the change in the spin-flip temperature T_{SF}. The evolution of the intensity of the magnetic $[0, 1 \pm \delta, 0]$ reflection of the PSI 6 specimen on temperature is shown in Fig. 4.25. The intensity is computed as the sum of pixels contributing to the diffraction. The ω axis represents the rotation of the crystal and is proportional to the X coordinate of the detector space shown in Fig. 4.14. In this particular case, the magnetic reflection is not present in the LSDW state and originates at the spin-flip temperature. The measurements suggest that the spin-flip temperature is no longer sharp, but broadens over a finite temperature range. From the graph in Fig. 4.25, one can see a slight increase in intensity of the 110 K (teal color) followed by a sharper increase at 120 K (light green color), which is still below T_{SF} at normal conditions. At 130 K, the intensity reaches its maximum, and a slight drop in intensity can be observed upon further heating.

To illustrate the temperature evolution of the reflection intensity, we show the YZ projection of the $[0, 1 \pm \delta, 0]$ magnetic reflections at 100, 110, 120 and 130 K in Fig. 4.26(a), 4.26(b), 4.26(c) and 4.26(d), respectively. Even at 100 K, a very slight intensity increase can be observed in the places where the reflections appear at higher temperatures. In Fig. 4.25, the intensity in each frame is summed and expressed as the intensity at the ω angle. More precisely, we sum pixels in a box enclosing the reflection, not the whole frame. This is why we observe two separate peaks in Fig. 4.26, but see one in Fig. 4.25. The powder diffraction band is equally strong in all images, but gets relatively weaker as the magnetic diffraction becomes stronger with increasing temperature.

Furthermore, we can calculate the integrated intensity of the reflection for each temperature. This is a sum of all voxels contributing to the reflection and can be

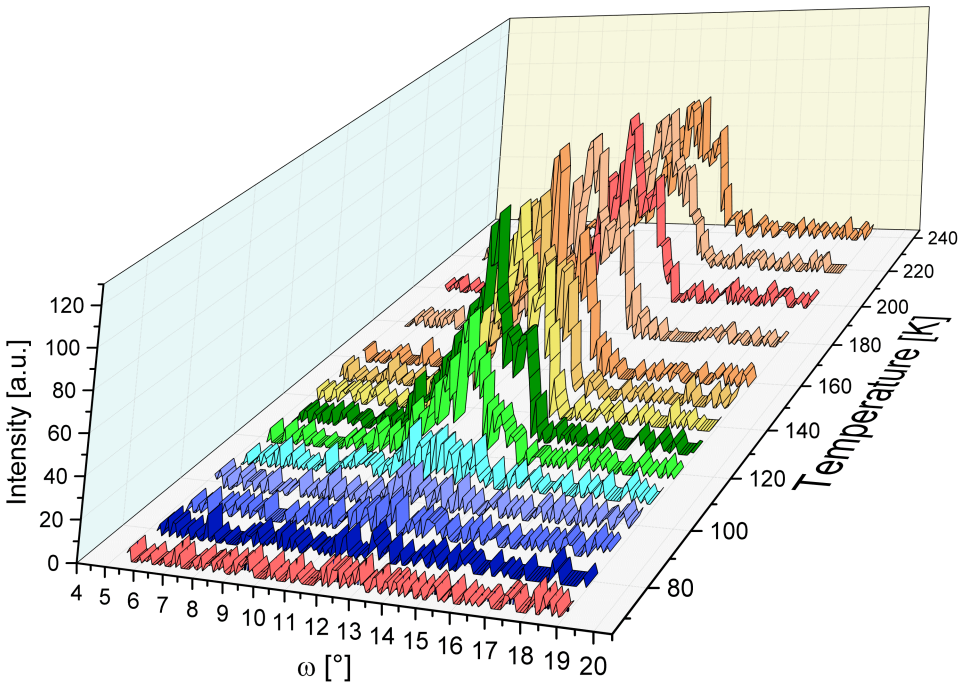

Figure 4.25: Evolution of the $[0, 1 \pm \delta, 0]$ magnetic reflection of the PSI 6 specimen with temperature. ω is a rotation of the specimen.

thus calculated as the numerical integral along each ribbon shown in Fig. 4.25. From the change of the integrated intensity on temperature, we can attempt to evaluate the changes in the spin-flip temperature. We have done this for the temperature range from 70 to 150 K on all six specimens and results are plotted in Fig. 4.27. The integrated intensities come from all reflections in the [010] neighborhood. The specimen predeformed at the room temperature does not have a consistent magnetic state. Therefore, the curves representing the temperature dependence of the integrated intensity, shown in Fig. 4.27(a), differ. The deformed specimens at 77 K have a more consistent magnetic state. They do not show any magnetic reflection in the LSDW phase, and the $[0, 1 \pm \delta, 0]$ reflections appear above the T_{SF}. The corresponding graph representing the integrated intensity vs. the temperature is shown in Fig. 4.27(b). Although, the individual specimens show different reflections, the variations of integrated intensities with temperature reveal similarities in magnetic behavior of samples PSI 1 and PSI 4. All the curves shown in Fig. 4.27 are corrected, such that they start or end at approximately zero intensity.

In order to describe these changes, we fitted the curves by the cumulative distribution function of the normal distribution:

$$I = I_0 + A \int_{-x}^{x} \frac{1}{\sqrt{2\pi}} e^{-\frac{(t-\mu)^2}{2\sigma^2}} \mathrm{d}t, \tag{4.14}$$

where I is the integrated intensity, I_0 the offset, A the amplitude, and μ, σ the mean and standard deviation of the distribution, respectively.

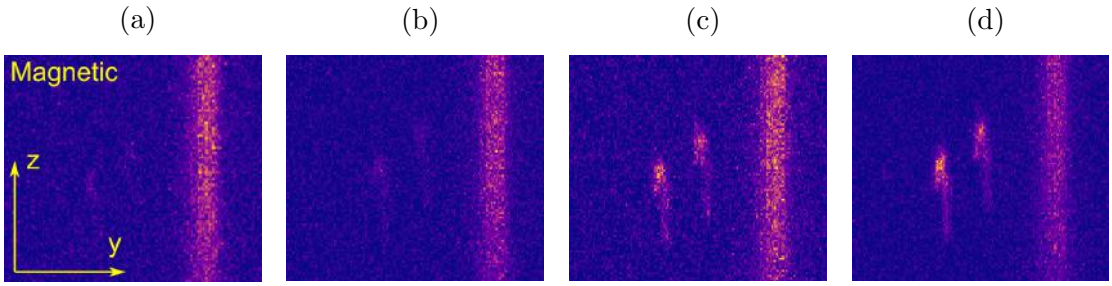

Figure 4.26: The YZ projection of the $[0, 1 \pm \delta, 0]$ magnetic reflection of the PSI 6 specimen (left peak is $[0, 1 - \delta, 0]$, right peak is $[0, 1 + \delta, 0]$) at: (a) 100 K, (b) 110 K, (c) 120 K, (d) 130 K. The vertical band appearing in figures is caused by powder diffraction from specimen holder or cryostat.

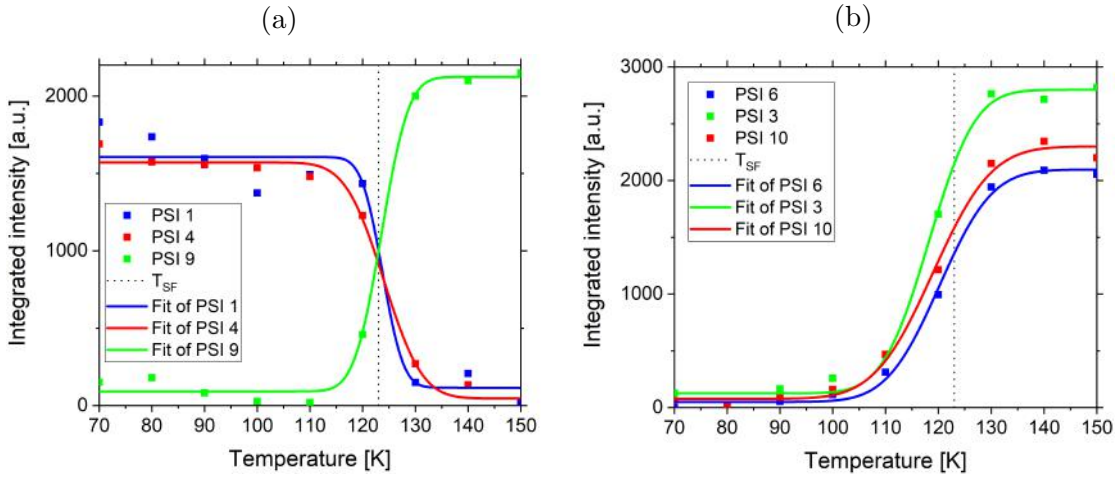

Figure 4.27: Temperature dependence of the integrated intensity of magnetic reflections in the [010] neighborhood.

From the results of the fit, we can then estimate the mean value (i.e. spin-flip temperature), and the standard deviation, which represents the temperature range into which the T_{SF} broadens. While the data are not sampled densely enough, we believe the results are consistent and represent the changes in the spin-flip temperature, even though burdened by experimental error and undersampling. The mean and standard deviation of the values obtained from the fit of Eq. (4.14) to the data in Fig. 4.27 are summarized in Table 4.4. The specimens in the table are ordered according to their cumulative strain (predeformation at RT and deformation at 77 K). The spin-flip temperature of the predeformed specimens is very close to the theoretical value of 123 K, while the spin-flip temperature of the more heavily deformed specimens is shifted approximately 4 K down to 119 K. An increase of the standard deviation is also observed in the case of the more deformed specimens. This was measured on specimens in the single-**Q** state. However, we believe that similar results would be achieved on specimens in triple-**Q** state.

Table 4.4: The PSI specimens ordered according to their cumulative plastic strain (in parenthesis), mean value of spin-flip temperature, and standard deviation acquired from the fit of the cumulative distribution function using Eq. (4.14).

Specimen (Strain)	**Mean T_{SF} [K]**	**Standard deviation [K]**
PSI 9 (0.48%)	123.7 ± 0.6	4.0 ± 0.5
PSI 4 (0.51%)	124.2 ± 1.0	5.7 ± 1.0
PSI 1 (0.68%)	123.7 ± 3.8	3.1 ± 2.6
PSI 3 (3.39%)	118.2 ± 0.8	6.9 ± 1.1
PSI 10 (3.44%)	119.0 ± 0.8	4.0 ± 0.5
PSI 6 (3.46%)	120.2 ± 0.6	7.9 ± 0.9

List of symbols

Symbol	Meaning	Equation
Latin symbols		
a	Initial slope of hysteresis curve	(4.3, 4.5, 4.7, 4.8)
A	Amplitude	(4.14)
c	Magnetization reversibility	(4.10, 4.11)
e, f, g	Dimensions of rectangular specimen	(4.2)
H	Magnetic filed	(4.1)
H'	External magnetic field	(4.1)
H_e	Effective magnetizing field	(4.3,4.4)
I	Integrated intensity	(4.14)
I_0	Intensity offset	(4.14)
k_B	Boltzmann constant	(4.5)
k	Average energy required to break the dislocation free of the pinning site	(4.11)
K	Direction of illumination	
K_{an}	Average energy density	(4.7, 4.8,4.9)
N	Demagnetizing factor	(4.1)
N_H	Demagnetizing factor for rectangular prism	(4.2)
$\bar{N}$	Average domain density	(4.5)
M	Magnetization	(4.1, 4.4)
M_{ah}	Anhysteretic magnetization	(4.10, 4.11
M_{an}^{iso}	Anhysteretic isotropic magnetization	(4.3)
M_{an}^{aniso}	Anhysteretic anisotropic magnetization	(4.6)
M_{ir}	Irreversible magnetization	(4.10)
M_r	Reversible magnetization	(4.10)
M_s	Saturation magnetization	(4.5,4.3,4.7, 4.8)
$\mathbf{Q}$	Wavevector	
q_x, q_y, q_z	Directions in reciprocal space	
$\mathbf{S}$	Spin direction	
T	Temperature	(4.5)
T_{SF}	Spin-flip temperature	
Greek symbols		
α	Bloch interdomain coupling coefficient	(4.4)
β	Angle between the direction of stress and magnetization	(4.9)
δ	Distance of reflection from a lattice point	
δ	Parameter	(4.11, 4.12)
δ_M	Parameter	(4.11, 4.13)
ϵ_{pl}	Plastic deformation	
θ	Angle between the magnetic moment and the magnetizing field	(4.6,4.7, 4.8)
λ	Magnetostrictive strain	(4.9)
μ	Mean value	(4.14)

μ_0	Magnetic permeability of free space	(4.5)
σ	Stress	(4.9)
σ	Standard deviation	(4.14)
ψ	Angle between magnetizing field and easy axis of magnetization	(4.7, 4.8)
ω	Specimen rotation	

5 Deformation mechanisms in Cr

This section of the thesis deals with uniaxial compression tests performed single-crystalline chromium. We use transmission electron microscopy to explore the possibility of anomalous slip in chromium. The results of these experiments are accompanied by atomistic simulations done by other members of our group. Furthermore, the presence of twins on the {112} planes sheared in the twinnning and antitwinning sense is investigated.

5.1 Compression test on Cr single crystals

A series of compression tests were carried out at 77 K on chromium single crystal specimens in the magnetically isotropic state to investigate how the slip morphology changes with the orientation of the applied load during the first 2-4% of the plastic deformation. The specimens were carefully photographed from all sides before and after the test. If necessary, scanning electron microscopy was used to characterize the surface after deformation. The loading axis on all figures showed here is always vertical unless otherwise specified. All specimens in this section come from the Cr-1 source crystal. An example of Specimen 8* before and after the deformation photographed using an Olympus GX51 light microscope is shown in Fig. 5.1(a) and 5.1(b).

Eight specimens were compressed in five different loading directions. The stereographic triangle in Fig. 5.2 shows the directions of individual loading axes before (white circles) and after deformation (black circles). To ease the reference to the individual loading axes, we divide this triangle into three separate parts. The asterisk (*) after the specimen number means that the predeformation has been applied at room temperature in the same direction as subsequent deformation at 77 K. The red region of the steregraphic triangle, which represents loading directions close to the [001] axis, contains the specimens 5 and 6*. For these loading directions, many slip systems are operational according to the Schmid law, which suggests that plastic deformation will proceed by homogeneous slip. The green part contains the specimens 3, 4*, and 7* compressed in the direction close to the center of the stereographic triangle. Two slip systems, $(\bar{1}01)[\bar{1}\bar{1}\bar{1}]$ and $(\bar{1}0\bar{1})[\bar{1}11]$, are expected to dominate the plastic deformation according to the Schmid law. These orientations are also ideal to test the occurrence of anomalous slip on low-stressed $(0\bar{1}1)$ planes. The blue part contains the specimens 1, 2*, and 8* that are compressed close to the [011]-$[\bar{1}11]$ edge of the stereographic triangle, which is prone to cross-slip and fracture. The amount of lattice rotation corresponds to the distance between the loading axis be-

(a)

(b)

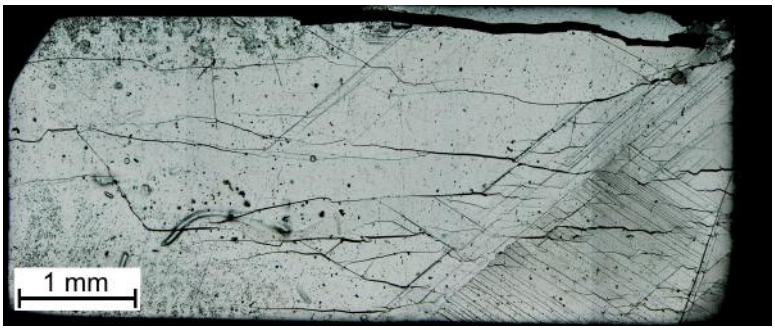

Figure 5.1: Side A of specimen 8*: (a) before deformation, (b) after deformation

fore deformation (here in the z-axis) and after deformation and thus to the length of the curved segments in Fig. 5.2 connecting the empty and filled circles. The misorientations of all loading axes caused by plastic deformation are summarized in Table 5.1.

Table 5.1: Summary of the misorientations of loading axes in individual samples.

Spec.	**Misorientation in x-axis [deg]**	**Misorientation in y-axis [deg]**	**Misorientation in z-axis [deg]**	**Misorientation total [deg]**
1	1.8	2.0	2.0	1.5
2*	5.0	1.8	4.8	2.1
3	4.4	4.4	0.5	3.7
4*	2.5	2.3	2.3	2.2
5	0.6	1.1	1.0	0.8
6*	3.7	3.9	1.5	3.3
7*	3.1	2.0	3.6	2.5
8*	0.9	1.1	0.6	0.8

Under compression, the loading axis rotates toward the pole that corresponds to the normal of the plane that carries the largest plastic strain. If the specimen deforms by single slip, the direction of lattice rotation allows unambiguous identification of the governing slip system. However, in the case of multiple slip, i.e.,

whenever two or more systems provide significant contributions to the plastic strain, the loading direction rotates toward the pole that is a weighted vector sum of the slip plane normals of the governing slip systems. In principle, these weights can be estimated by counting the number of slip traces corresponding to respective slip systems observed on a representative surface area. However, this analysis cannot be made when slip bands form. The orientations of loading axes before/after deformation and the accumulated (total) plastic strain are summarized in Table 5.2. The source single crystal used in this work was UHV-annealed, and thus the initial dislocation network is expected to be dominated by immobile dislocation tangles that act as the concentrators of stresses. Upon loading the specimens 1, 3, 5 at 77 K, these stresses may be relieved by nucleating twin embryos or microcracks, which then leads to preferential plastic deformation by twinning or to brittle fracture. On the other hand, predefoming the specimens 2*, 4*, 6*, 7*, and 8* at room temperature generates mobile dislocation networks that are expected to allow for a dislocation-controlled slip at 77 K.

Table 5.2: Summary of the orientations of the loading axes before and after deformation, accumulated plastic strain ϵ_{pl}^{pre} after predeformation at room temperature, and the total plastic strain ϵ_{pl} after compression at 77 K. The specimens marked with asterisks were predeformed at room temperature prior to their testing at 77 K.

Specimen	**Initial orientation**	**Orientation after deformation**	$R_{p0.2}$ [MPa]	ϵ_{pl}^{pre}[%]	ϵ_{pl}[%]
1	$[\bar{6}\ 11\ 15]$	$[\bar{3}\ 5\ 7]$	1075	0	2.2
2*	$[\bar{2}\ 4\ 5]$	$[\bar{5}\ 9\ 11]$	1132	1.5	2.5
3	$[\bar{7}\ 13\ 28]$	$[\bar{8}\ 11\ 25]$	857	0	4.1
4*	$[\bar{7}\ 13\ 29$	$[\bar{7}\ 11\ 27]$	971	0.9	2.3
5	$[\bar{3}\ 4\ 24]$	$[\bar{6}\ 7\ 44]$	876	0	3.1
6*	$[\bar{4}\ 7\ 44]$	$[\bar{5}\ 6\ 60]$	953	1.5	3.6
7*	$[\bar{1}\ 6\ 13]$	$[\bar{1}\ 7\ 17]$	779	0.5	2.6
8*	$[\bar{1}\ 6\ 8]$	$[\bar{3}\ 20\ 26]$	1157	1	2.3

The stress-strain curves of all specimens are shown in Fig. 5.3. The specimens compressed in the directions corresponding to the blue region (i.e., close to the [011]-$[\bar{1}11]$ edge of the triangle) exhibit a variable amount of smooth hardening followed by a sudden load drop after which the experiment was terminated. When reaching the maximum stress, the specimens 1, 2*, and 8* unload rapidly while generating appreciable plastic deformation corresponding to the almost straight part of their stress-strain curves. Comparing the response of specimens 2* and 8* with that of specimen 1 suggests that predeformation leads to a significant amount of parabolic hardening and a postponement of the moment when the strain burst occurs. The specimens compressed in the directions corresponding to the green region (i.e., close to the center of the stereographic triangle) again display initial parabolic hardening. However, this is followed by the region of easy glide, where the stress-strain curve is nearly linear. The predeformed specimens 4* and 7* continue to deform in this way until the termination of the experiment. In the case of specimen 3, the plastic

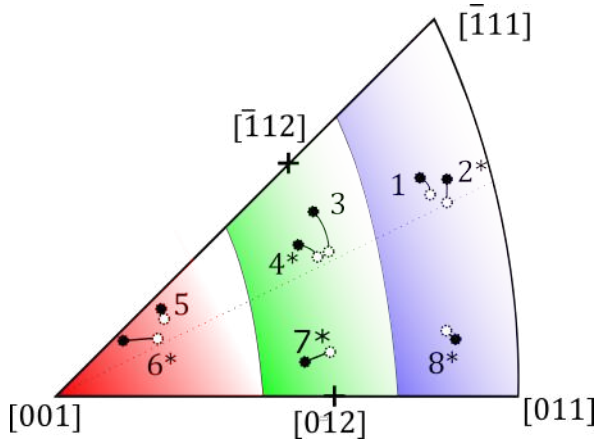

Figure 5.2: Directions of loading axes of specimens before (white circle) and after the test (black circles). The asterisks denote that the specimen was predeformed at room temperature.

deformation eventually exhibits a sudden load drop similar to the response of the specimens 1, 2*, and 8* at small strains. The specimens compressed in the directions corresponding to the red region (i.e., close to the [001] corner of the triangle) do not exhibit any strain burst irrespective of whether or not they were predeformed. However, predeformation leads to strain localization later during the plastic deformation and thus the formation of discrete and easily identifiable slip traces.

Following are detailed slip trace analyses of all specimens tested here. The Schmid law will be used to predict the activity of individual slip and twinning systems and compare these predictions with direct observations using the Nomarski light microscopy and SEM, including the technique of electron backscatter diffraction (EBSD) to quantify local misorientations of the crystal lattice. Surface markings generally have different visibilities depending on the orientation of the loading axis and the face of the specimen under observation (i.e., A, B, A', B' in Fig. 3.7). Therefore, we have always made the slip trace analysis on at least two perpendicular faces of the specimen. The visibility of slip markings on a particular face is represented by the quantity $|\,\hat{\boldsymbol{n}}\cdot\boldsymbol{b}\,|$, where $\hat{\boldsymbol{n}}$ is the unit normal of the face under observation, and $\boldsymbol{b}$ the Burgers vector of the dislocations in a given system. The same visibility analysis is also used to assess the relative visibility of regions with large misorientations, such as twinned regions, even though twinning dislocations have only fractional Burgers vectors. In the following light and electron micrographs, the orientations of loading axes are always vertical.

5.1.1 Specimens oriented close to the [001] axis

Specimens 5 and 6* have deformed homogeneously, and their plastic distortion was visible even by naked a eye. However, distinct slip markings could not be identified by either light microscopy or scanning electron microscopy. We can acquire indirect information about operative slip systems from the rotation of the crystal lattice in Fig. 5.2 by EBSD. Light microscopy and EBSD analysis on both specimens did not show any misoriented deformation bands, we assume that the plastic deformation

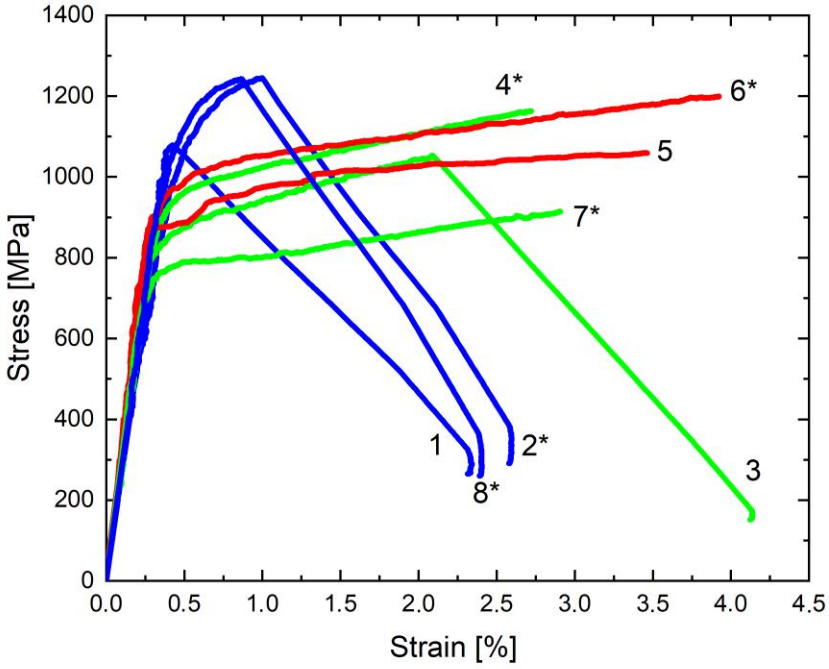

Figure 5.3: Stress-strain curves of the specimens corrected for the compliance of the testing machine. The color coding corresponds to that of the three regions shown in Figure 5.2.

in both specimens is a result of homogeneous dislocation slip. Based on the Schmid law, specimen 5, which was not predeformed, is expected to deform on the $(\bar{1}01)$ plane. On the other hand, specimen 6*, whose initial loading axis is similar to that of specimen 5, rotates toward the $[0\bar{1}1]$ pole. To reconcile both observations, the five most operative slip systems are shown in Table 5.3. The primary slip is expected to take place on the $(\bar{1}01)[\bar{1}\bar{1}\bar{1}]$ and $(\bar{1}0\bar{1})[\bar{1}11]$ systems with the highest Schmid factors. This assumption agrees well with the lattice rotation of specimen 5 but not with the lattice rotation of sample 6*. In the latter case, the rotation towards the $[0\bar{1}1]$ pole indicates that most of the plastic strain is due to the operation of $(0\bar{1}1)[1\bar{1}\bar{1}]$ and/or $(0\bar{1}1)[\bar{1}\bar{1}\bar{1}]$ systems. The Schmid factors of these systems are only 10-20% lower than that of the most stressed $(\bar{1}01)[\bar{1}\bar{1}\bar{1}]$ system and, therefore, the $(0\bar{1}1)$ slip does not constitute the anomalous slip.

5.1.2 Specimens with center-triangle orientations

Specimens in the green part of the stereographic triangle in Fig. 5.2 show intermediate deformation behavior compared to the specimens in the red and blue areas. Specimen 3, the only one without predeformation in the green area, fractured along the loading axis during the deformation. The measurement of the orientation of this crystal after deformation in Table 5.2 might be burdened by higher experimental uncertainty. A majority of slip markings on specimen 3 agree with the traces

Table 5.3: The five most operative slip systems for compression in the [$\bar{5}$ 6 60] direction (final orientation of the specimen 6*) as predicted from the Schmid law. Here, SF is the Schmid factor, and $|\,\hat{\boldsymbol{n}}\cdot\boldsymbol{b}\,|$ the visibility of surface markings on the two side faces of the specimen. Similar predictions apply for specimen 5 compressed in the red part of the stereographic triangle in Fig. 5.2.

Slip sys.	**SF**	$\lvert\,\hat{\boldsymbol{n}}\cdot\boldsymbol{b}\,\rvert_A$	$\lvert\,\hat{\boldsymbol{n}}\cdot\boldsymbol{b}\,\rvert_B$
$(\bar{1}01)[\bar{1}\bar{1}\bar{1}]$	0.442	0.61	0.66
$(\bar{1}0\bar{1})[\bar{1}11]$	0.435	0.71	0.48
$(0\bar{1}\bar{1})[\bar{1}\bar{1}1]$	0.434	0.53	0.57
$(0\bar{1}1)[1\bar{1}\bar{1}]$	0.428	0.71	0.48
$(0\bar{1}1)[\bar{1}\bar{1}\bar{1}]$	0.367	0.61	0.66

of $(\bar{1}21)$ and $(\bar{2}11)$ planes shown in Fig. 5.4(a) and 5.4(b). For the $(\bar{2}11)$ traces in Fig. 5.4(a) and 5.4(b), the EBSD analysis in Fig. 5.4(e) reveals three regions with different orientations, which are characterized by the Euler angles expressed in Bunge notation: matrix (152°, 36.2°, 17.5°), red region (288.7°, 41.8°, 71.5°), green region (165.7°, 31.8°, 20.7°). The smallest calculated misorientation between the red region relative to the same directions in the matrix are 36°, 45° and 58° for the x, y and z axes, respectively. Such large misorientations for the x and z axes cannot be attributed to dislocation glide, and thus it is likely that the red region represents a deformation twin. According to Table 5.4, we expect that the red traces originates from twinning on the most highly stressed $(\bar{2}11)[\bar{1}\bar{1}\bar{1}]$ system that is sheared in the twinning sense. Because this sample was not predeformed, the external load is concentrated at immobile dislocation junctions from which twins can be easily nucleated. The presence of twinning in specimen 3 is confirmed by the observation of a large load drop in Fig. 5.3 after which the test was terminated.

A similar analysis was done for the samples in the green region in Fig. 5.4(e) and the misorientation angles of 16°, 17°and 5° for the x, y and z axes, respectively. These rotations are much smaller, suggesting that the sample's deformation in the green region do not contain twins. Instead, we assume that the accumulated plastic strain in these samples was generated by the glide of dislocations. The internal morphology of the surface markings along the $(\bar{1}21)$ plane is shown in Fig. 5.4(c) and 5.4(d), which comprises two sets of alternating slip traces. The EBSD map obtained from this band in Fig. 5.4(f) shows that the blue band has Euler angles of (318.9°, 46.5°, 38°), whereas those of the surrounding matrix are (44.2°, 18.8°, 13.6°). From this, we can compute the smallest misorientation in x, y and z axes to be 57°, 25°and 56° respectively. Owing to the large misorientations in x and z axes, we consider that the $(\bar{1}21)$ traves arise from twinning on the $(\bar{1}21)[11\bar{1}]$ system sheared in the twinning sense. From the Euler angles of the band, we can further determine what {110} slip traces match accurately with the observations in Fig. 5.4(c) and 5.4(d). These slip traces correspond to the $(011)[1\bar{1}\bar{1}]$ system (SF=0.216) and to the $(110)[11\bar{1}]$ system (SF=0.263). The internal slip within the twinned regions that is shown in Fig. 5.4(c) and 5.4(d) was observed previously by McHargue [224] and Gröger et al. [225] on bcc Nb and associated with composite slip on the average

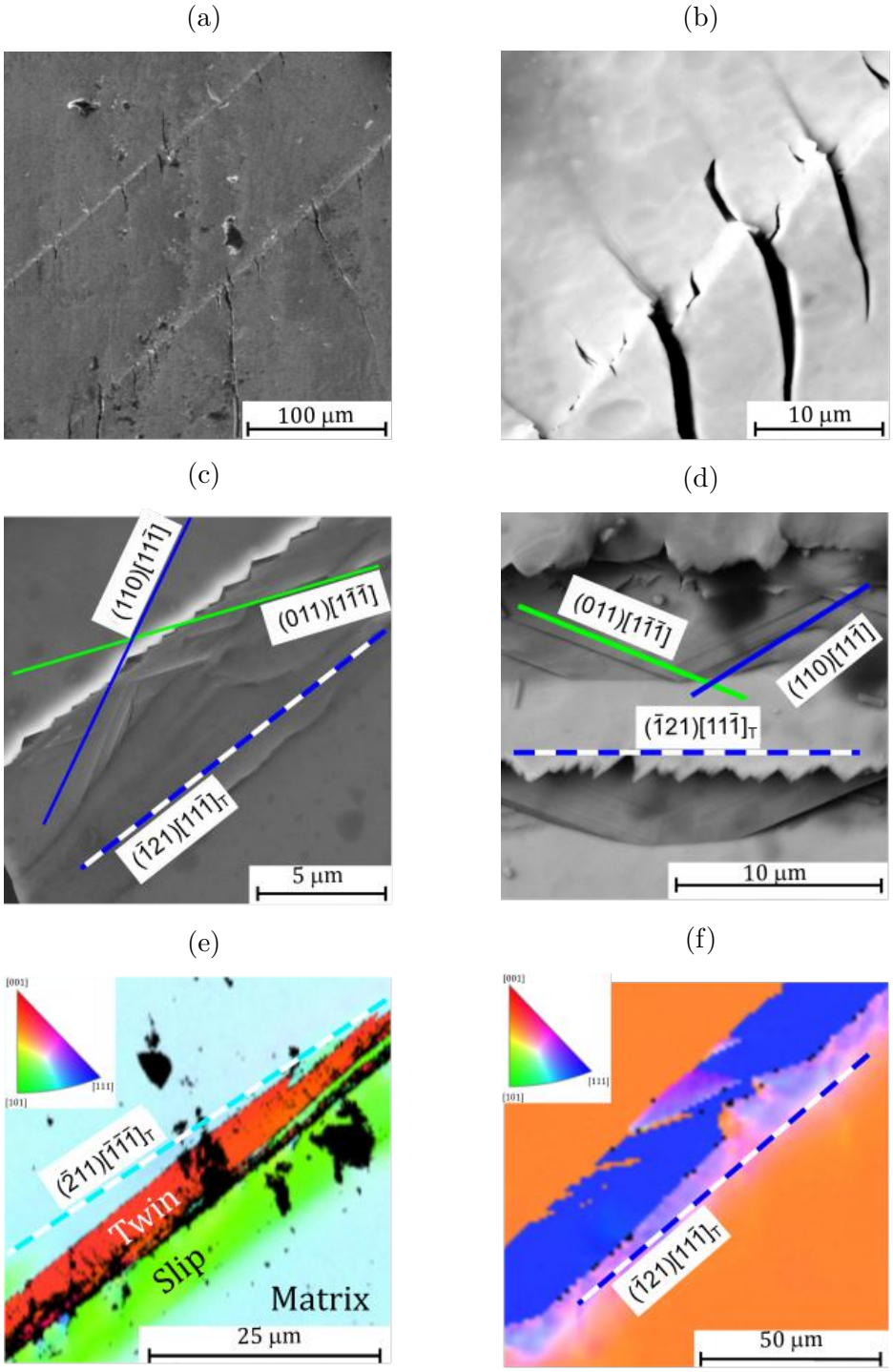

Figure 5.4: Surface morphology of specimen 3 after deformation: (a) an SEM micrograph from face A, (b) enlargement of the surface trace from (a) in backscattered electrons showing cracks originating from twin, (c) and (d) deformation bands corresponding to the $(\bar{1}21)[11\bar{1}]$ system on the face A and B, respectively, (e) EBSD IPF Y of the side B showing large misorientations along the trace of the $(\bar{2}11)[\bar{1}\bar{1}\bar{1}]$ system on the side A shown on (b), and (f) EBSD IPF Z map of surface markings on the face A along the trace of the $(\bar{1}21)[11\bar{1}]$ system shown in (c).

{112} plane. In the present case, we observe similar structures, but the internal slip seems to arise due to the glide of $1/2\langle 111\rangle$ dislocations on different {110} planes.

Table 5.4: The five most operative slip and twinning systems for compression in the [$\bar{7}$ 13 29] direction (initial orientation of the specimen 4*) as predicted by the Schmid law. The meaning of the symbols is the same as in the captions of Table 5.3. The subscripts T and AT distinguish the {112} planes sheared in the twinning and antitwinning sense, respectively.

Slip sys.	**SF**	$\lvert \hat{\boldsymbol{n}} \cdot \boldsymbol{b} \rvert_A$	$\lvert \hat{\boldsymbol{n}} \cdot \boldsymbol{b} \rvert_B$	**Twin sys.**	**SF**	$\lvert \hat{\boldsymbol{n}} \cdot \boldsymbol{b} \rvert_A$	$\lvert \hat{\boldsymbol{n}} \cdot \boldsymbol{b} \rvert_B$
$(\bar{1}01)[\bar{1}\bar{1}\bar{1}]$	0.486	0.62	0.75	$(\bar{2}11)[\bar{1}\bar{1}\bar{1}]_T$	0.436	0.62	0.75
$(\bar{1}0\bar{1})[\bar{1}11]$	0.416	0.87	0.37	$(1\bar{1}2)[1\bar{1}\bar{1}]_{AT}$	0.414	0.87	0.37
$(0\bar{1}\bar{1})[\bar{1}\bar{1}1]$	0.372	0.41	0.56	$(\bar{1}\bar{1}1)[\bar{1}\bar{1}\bar{1}]_{AT}$	0.405	0.62	0.75
$(0\bar{1}1)[1\bar{1}\bar{1}]$	0.302	0.87	0.37	$(112)[11\bar{1}]_{AT}$	0.328	0.41	0.56
$(\bar{1}10)[\bar{1}\bar{1}\bar{1}]$	0.270	0.62	0.75	$(\bar{1}21)[11\bar{1}]_T$	0.317	0.41	0.56

Fig. 5.4(f) shows, apart from the $(\bar{1}21)[11\bar{1}]$ twin sheared in the twinning sense, a localized surface deformation along the lower border of the twin, that was observed on the face B of the specimen 3. The large misorientation between the outskirts of this twin and the surrounding matrix suggest a presence of slip, similarly to the twin in Fig. 5.4(e).

The specimen 7*, which was slightly predeformed at room temperature, was deformed by homogeneous slip, similarly to the specimens compressed in the red region of the triangle in Fig. 5.2. The only hint of which systems were operational comes again from the rotation of the crystal lattice, which is toward the $[1\bar{1}2]$ pole. Such deformation could originate from two different mechanisms. If the surface of the crystal exhibits large misorientations, the plastic deformation may be again due to twinning on the $(1\bar{1}2)[\bar{1}\bar{1}\bar{1}]$ system. The second possible mechanism is a simultaneous operation the $(\bar{1}0\bar{1})[\bar{1}11]$ and $(0\bar{1}1)[1\bar{1}\bar{1}]$ systems, which are the second and the fourth most operative slip systems in Table 5.4, respectively. The ensuing composite slip of $1/2[1\bar{1}\bar{1}]$ screw dislocations on these two {110} planes would give rise to average slip trace along the $(1\bar{1}2)$ planes as observed.

Specimen 4* shows an entirely different slip morphology compared to Specimen 3 (not predeformed), even though both have a very similar orientation of the loading axis. In particular, the traces of the most highly stressed $(\bar{1}01)[\bar{1}\bar{1}\bar{1}]$ and $(\bar{1}0\bar{1})[\bar{1}11]$ systems were not observed, and most of the plastic strain occurred during the operation of low-stressed systems. On the side A', a single broad slip band corresponding to the operation of the $(0\bar{1}\bar{1})[\bar{1}\bar{1}1]$ system was observed as shown in Fig. 5.5(a). On the side B of this specimen, all observed discrete slip markings agreed with the traces of $(0\bar{1}1)$ planes as shown in Fig. 5.5(b). According to Table 5.4, these are expected to originate due to the operation of the $(01\bar{1})[111]$ and/or $(0\bar{1}1)[1\bar{1}\bar{1}]$ systems with similar Schmid factors. These two slip systems operate on the same plane, therefore, they differ only in the direction of the slip, making them indistinguishable solely from slip trace analysis. Therefore, we expect that both $1/2[111]$ and $1/2[\bar{1}11]$ screw dislocations may be equally mobile for this orientation of the

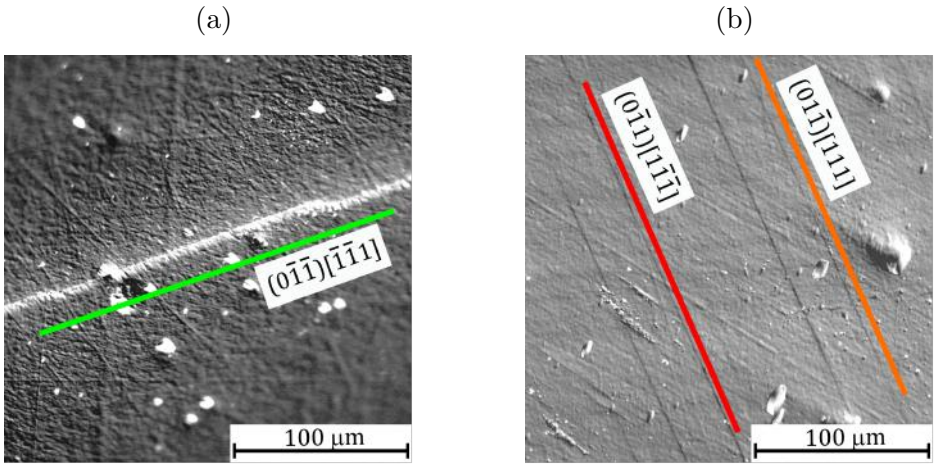

Figure 5.5: Slip morphology observed on the specimen 4*: (a) slip traces of $(0\bar{1}\bar{1})[\bar{1}\bar{1}1]$ system on the side B, (b) slip traces of $(01\bar{1})[111]$ and/or $(0\bar{1}1)[1\bar{1}\bar{1}]$ systems on the side A' that constitute the anomalous slip.

applied load. However, the Schmid factors of both these systems are much smaller than that of the most highly stressed system, and thus the dominant slip on the $(0\bar{1}1)$ plane cannot be explained by the Schmid law. This so-called anomalous slip has been observed frequently in the 5th group metals (Nb, Ta, V), but its origin is still not properly understood [69]. Our observations suggest that predeforming the specimens in the green part of the stereographic triangle in Figure 5.2 at room temperature and their subsequent deformation at 77 K in the same direction results in anomalous slip on the $(0\bar{1}1)$ plane. Without pre-straining, the plastic deformation results in the formation of twins, sometimes twinning on {112} planes (specimens 3, 7*), or even fracture (specimen 3).

5.1.3 Specimens with orientation close to the [011]-[$\bar{1}$11] edge

The specimen tested in compression in the directions corresponding to the blue region of the stereographic triangle in Fig. 5.2 exhibit considerably different response to loading as well as deformation markings compared to the specimens in the other two regions. Most macroscopic markings on the surface of the specimen 1, shown in Fig. 5.6(a), are parallel to the traces of $(\bar{2}11)$ planes and traverse the entire thickness of the specimen. We assume that they are composed of short alternating traces on $(\bar{1}01)$ and $(\bar{1}10)$ atomic planes, which arise due to the operation of the slip systems $(\bar{1}01)[\bar{1}\bar{1}\bar{1}]$ and $(\bar{1}10)[\bar{1}\bar{1}\bar{1}]$ with the highest Schmid factors according to Table 5.5. The simultaneous operation of these slip systems results in composite slip on the average $(\bar{2}11)$ plane.

The face A of specimen 1 exhibits interesting surface features that correspond to thin lamellae elongated in the direction of the trace of the $(\bar{1}\bar{1}2)$ atomic plane. These are visible only on the EBSD IPF X map shown in Fig. 5.7(a), but no contrast is generally found by light microscopy techniques, even using the Nomarski differential interference contrast, which is sensitive to topology or in SEM when imaging the surface with secondary electrons. Similarly, as in Fig. 5.4(f), the interior of the

Table 5.5: The five most operative slip and twinning systems for compression in the $[\bar{2}45]$ direction (initial orientation of the specimen 2) as predicted by the Schmid law. The meaning of the symbols is the same as in the caption of Table 5.3, with T/AT explained in Table 5.4.

Slip sys.	**SF**	$\mid \hat{\boldsymbol{n}} \cdot \boldsymbol{b} \mid_A$	$\mid \hat{\boldsymbol{n}} \cdot \boldsymbol{b} \mid_B$	**Twin sys.**	**SF**	$\mid \hat{\boldsymbol{n}} \cdot \boldsymbol{b} \mid_A$	$\mid \hat{\boldsymbol{n}} \cdot \boldsymbol{b} \mid_B$
$(\bar{1}01)[\bar{1}\bar{1}\bar{1}]$	0.445	0.60	0.80	$(\bar{2}11)[\bar{1}\bar{1}\bar{1}]_T$	0.477	0.60	0.80
$(\bar{1}10)[\bar{1}\bar{1}\bar{1}]$	0.381	0.60	0.80	$(\bar{1}\bar{1}2)[\bar{1}\bar{1}\bar{1}]_{AT}$	0.293	0.60	0.80
$(\bar{1}0\bar{1})[\bar{1}11]$	0.299	0.95	0.31	$(211)[1\bar{1}\bar{1}]_T$	0.288	0.95	0.31
$(0\bar{1}\bar{1})[\bar{1}\bar{1}1]$	0.245	0.26	0.55	$(\bar{1}21)[11\bar{1}]_T$	0.236	0.26	0.55
$(110)[1\bar{1}\bar{1}]$	0.200	0.95	0.31	$(1\bar{1}2)[1\bar{1}\bar{1}]_{AT}$	0.230	0.95	0.31

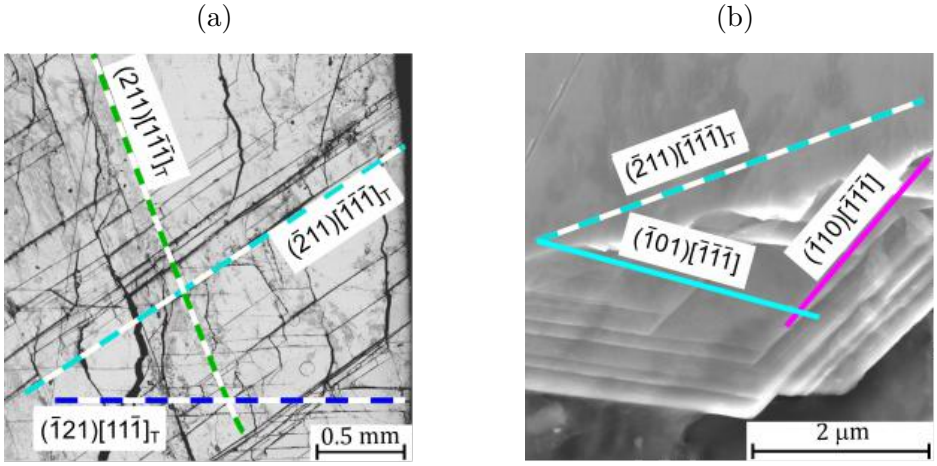

Figure 5.6: Surface morphology of the specimen 1 after deformation: (a) the side B deformed by $(\bar{1}21)[11\bar{1}]$,$(211)[1\bar{1}\bar{1}]$ and $(\bar{2}11)[\bar{1}\bar{1}\bar{1}]$ slip systems (b) scanning electron micrograph on side A showing the composite slip formed by the operation of the $(\bar{1}10)[\bar{1}\bar{1}\bar{1}]$ and $(\bar{1}10)[\bar{1}\bar{1}\bar{1}]$ slip systems that result in a trace along the $(\bar{2}11)$ plane on side A.

lamella exhibits large misorientation compared to the surrounding matrix. In this case, Figure 5.7(b) shows that the crystal inside these islands is rotated in the zone of the y axis, i.e., in the plane perpendicular to the loading axis. Such large rotations imply that these features are not produced by slip. The Euler angles expressed in Bunge notation of the misoriented regions are (141.6°, 43.8°, 24.6°), while those of the matrix are (225.3°,28°,5.5°). The smallest misorientation angles obtained using all symmetry operations of the cubic lattice obtained from these two Euler angles are 57.9°, 17.6° and 57.9° for the x, y and z axes, respectively. According to Table 5.5, the system $(\bar{1}\bar{1}2)[\bar{1}\bar{1}\bar{1}]$ is sheared in the antitwinning sense, which was predicted before to lead to high-energy stacking faults and not twins. These lamellae comprise highly misoriented regions whose character will later (Section 7) be investigated by diffraction in TEM.

Specimen 2* has a similar initial orientation as specimen 1, but the former underwent predeformation at room temperature. According to Fig. 5.2, the loading

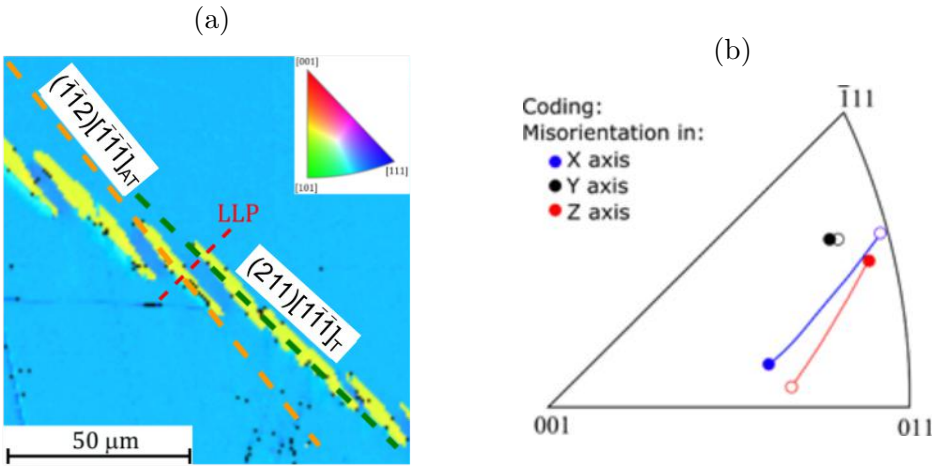

Figure 5.7: (a) EBSD IPF X map taken from the side A of specimen 1 showing thin lamellae with large misorientations along the trace of the $(\bar{1}\bar{1}2)$ plane sheared in the antitwinning sense (orange dashed line) and (211) plane sheared in the twinning sense (green dashed line). The red dashed line marks the lamella lift-out position (LLP). (b) misorintation of the lamellae relative to the matrix.

direction of the specimen 2* rotates closer to the $[\bar{1}10]$ pole, which is a manifestation of larger relative contribution of the $(\bar{1}10)[\bar{1}\bar{1}\bar{1}]$ slip system to the total plastic strain. The Schmid factor of this system, as well as its visibility on all side faces of the specimen, are comparable with those of the $(\bar{1}01)[\bar{1}\bar{1}\bar{1}]$ system with the highest Schmid factor. Similarly as for the loading directions in the red region in Fig. 5.2, it seems that predeformation suppresses the expected $(\bar{1}01)$ slip and promotes the operation of one of the conjugate slip systems with lower Schmid factors. Specimen 8* exhibits similar surface features as specimen 1, including the presence of cleavage. Most surface markings correspond to operation of the systems $(\bar{2}11)[\bar{1}\bar{1}\bar{1}]$ and $(1\bar{1}2)[1\bar{1}\bar{1}]$, as shown in Fig. 5.8(a) and 5.8(c). The former is the most highly stressed system in Table 5.5 that is sheared in the twinning sense, which suggests that the corresponding surface markings are caused by deformation twinning. The twin lamellae span the entire thickness of the specimen. This is confirmed by the EBSD analysis in Figure 5.8(b) that reveals large misorientations of the twin lamellae with the surrounding crystal. The internal structure of these twins, shown in Fig. 5.8(d), demonstrates that their interiors are again formed by slip traces corresponding to the operation of the $(\bar{1}01)[\bar{1}\bar{1}\bar{1}]$ and $(\bar{1}10)[\bar{1}\bar{1}\bar{1}]$ slip systems with two highest Schmid factors. Due to the observed sharp terminations of these slip traces in Fig. 5.8(d), we believe that the primary deformation has occurred by twin formation on the $(\bar{2}11)$ plane, and subsequent nucleation of slip within these twins. However, a different deformation mechanism is associated with the $(1\bar{1}2)[1\bar{1}\bar{1}]$ system above. According to Table 5.5, this system is sheared in the antitwinning sense, whose operation theoretically cannot produce twins. Nevertheless, the EBSD analysis in Fig. 5.8(b) reveals the presence of large lattice rotations. The character of these domains will be explored later in Section 7. The point of intersection of the $(\bar{2}11)[\bar{1}\bar{1}\bar{1}]$ twin with the lamella on the $(1\bar{1}2)$ plane coincides with the crack (black regions in Fig. 5.8(b)) and, therefore, we believe that the intersection of the two

types of lamellae result in the initiation of fracture. This is phenomenon has been observed in other specimens as well.

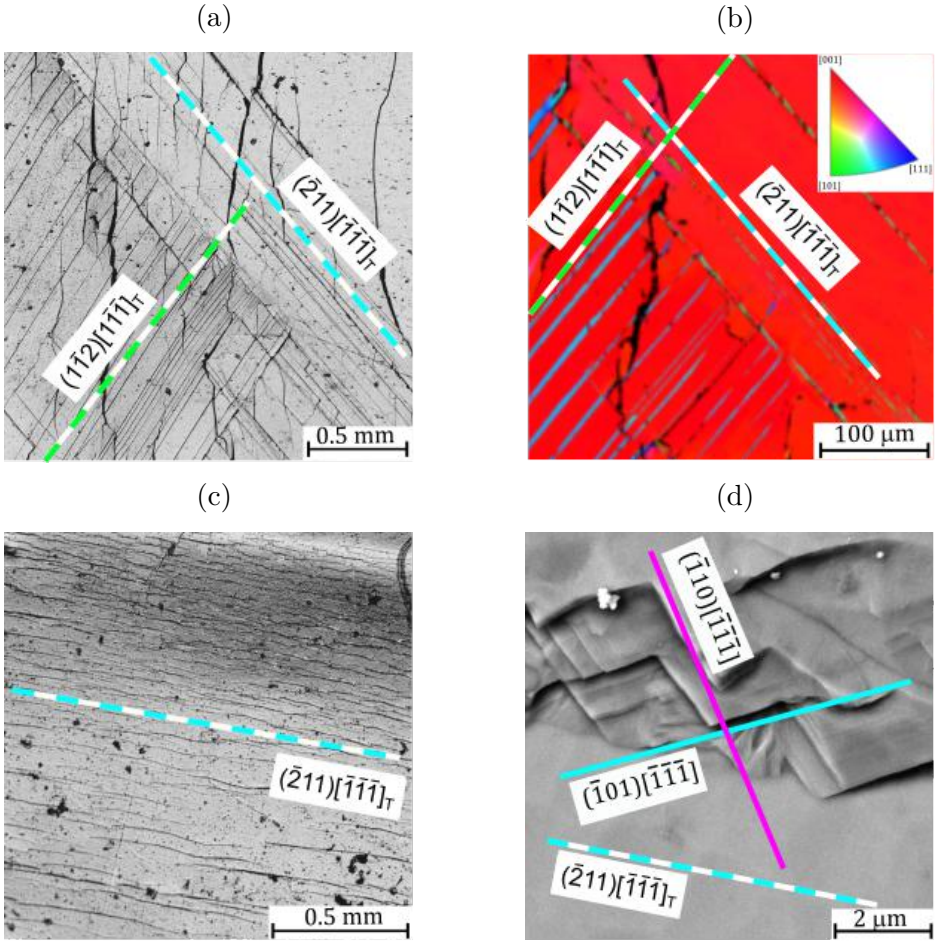

Figure 5.8: Surface markings on the specimen 8* after deformation: (a) face A, (b) EBSD IPF X map of face A. (c) Traces of $(\bar{2}11)[\bar{1}\bar{1}\bar{1}]$ system on the face B' (d) detail of the $(\bar{2}11)[\bar{1}\bar{1}\bar{1}]$ system on the face B' revealing a composite slip on the $(\bar{1}01)[\bar{1}\bar{1}\bar{1}]$ and $(\bar{1}10)[\bar{1}\bar{1}\bar{1}]$ systems.

The mechanism of plastic deformation of high-purity Cr single crystals at low-temperatures depends on the orientation of the applied load as well as on whether the sample was predeformed at room temperature or not. According to Fig. 5.9, the compression samples with loading axis close to [001] show homogeneous slip on those slip systems with the highest Schmid factors. In this region, predeformation does not change the mechanism of plastic deformation. Similar behavior is observed for the sample 7* predeformed at room temperature and subsequently compressed at liquid nitrogen temperature between the center-triangle orientation and the [001]-[011] edge. However, the sample 3 that was not predeformed at room temperature deformed at 77 K by a combination of composite slip and twinning. The sample 4* with the loading direction close to the center of the stereographic triangle exhibited anomalous slip on the $(0\bar{1}1)$ plane. For loading directions close to the $[011] - [\bar{1}11]$ edge of the stereographic triangle, the crystals deformed predominantly by twinning

on {112}⟨111⟩ systems, irrespective of preceding predeformation at room temperature. The rotation of the loading axis, as well as the observed type of deformation is shown in Fig. 5.9. They agree well with the model proposed by Hamelin et al. [226] for combined slip on {110}⟨111⟩ and {112}⟨111⟩ systems. The red area shows the orientation for which the anomalous slip was observed. The blue-white cross in the red area shows the loading axis used in the atomistic simulations of anomalous slip described later in Section 5.2.2.

All of the twin systems found and characterized in chromium specimens are of the {112} type. The results show that cracks originate at the intersections of twin lamellae and propagate along {100} planes. This agrees with the findings of Sameljuk et al. [124]. The surface morphology shown in Fig. 5.8(c) is similar to the wavy slip reported by Greiner [3] in 1950 on the specimens deformed at room temperature. However, there is no mentioning of any particular slip system in the Greiner's paper. Our results further match those reported by Reid et al. [4] who report twinning on {112} planes and slip on {110} planes. There is no visible internal structure of the misoriented regions caused by antitwinning shear in Fig. 5.7(a), which agrees with the previous work by of Gröger et al. on single-crystalline niobium [225].

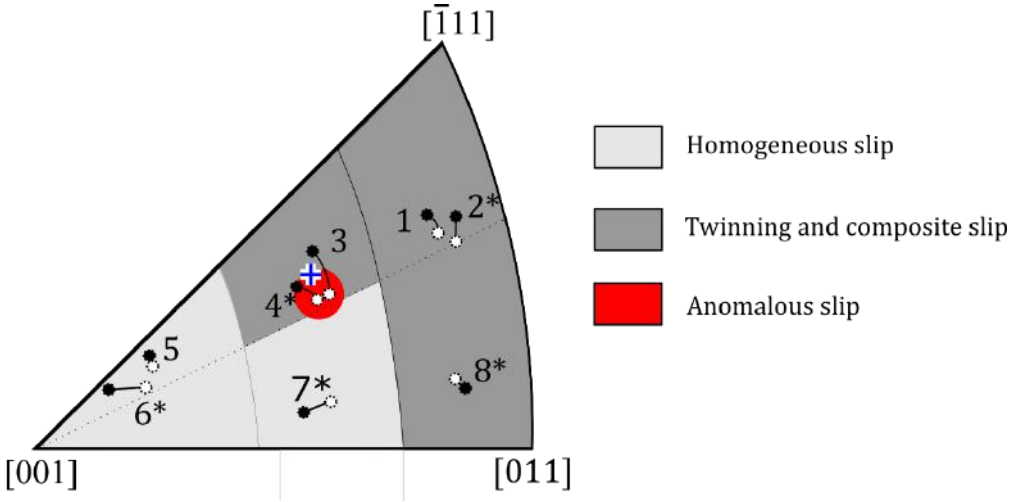

Figure 5.9: Deformation modes for different loading directions considered for uniaxial compression of Cr single crystals. The sample with center-triangle orientation deforms by anomalous slip. The direction [$\bar{2}$38], marked with a blue cross, was considered for the atomistic simulations of intersecting 1/2⟨111⟩ screw dislocation under compression in Section 5.2.2. The part of the stereographic triangle that contains these samples is colored dark gray only because of the observation of twinning on the specimen 3.

List of symbols

Symbol	Meaning
Latin symbols	
$\mathbf{b}$	Burgers vector
$\hat{\mathbf{n}}$	Unit normal of the viewing plane
$R_{p0.2}$	Yield stress
Greek symbols	
ϵ_{pl}	Plastic strain at 77 K
ϵ_{pl}^{pre}	Plastic strain during predefromation at RT

5.2 Junction formation and anomalous slip in Cr

Search for long straight ⟨111⟩ dislocations has so far been unsuccessful and we anticipate that these dislocations can only exist at junctions of intersecting ⟨111⟩ dislocations. This is consistent with dislocation reaction $1/2[111] + 1/2[1\bar{1}\bar{1}] \rightarrow [100]$, which is favorable even using simple linear elasticity. Understanding the mobility of this junction dislocation and the surrounding dislocation network is a pre-requisite to understanding the conditions that favor the anomalous slip in Cr.

5.2.1 TEM studies of dislocation networks

TEM JEOL JEM-2100F operating at 200 kV was used to characterize dislocation microstructures. The foils for analysis were prepared from the chromium specimen 4* (the only specimen that deformed by anomalous slip) by the process described in Section 3.3. The dislocations were characterized by the $\mathbf{g} \cdot \mathbf{b}$ analysis from a series of micrographs taken under the two-beam condition for six different diffraction conditions. Fig. 5.10(a) represents the detail of the observed dislocation junction between two intersecting 1/2 ⟨111⟩ screw dislocations and Fig. 5.10(b) shows designations of individual dislocations used in the $\mathbf{g} \cdot \mathbf{b}$ analysis.

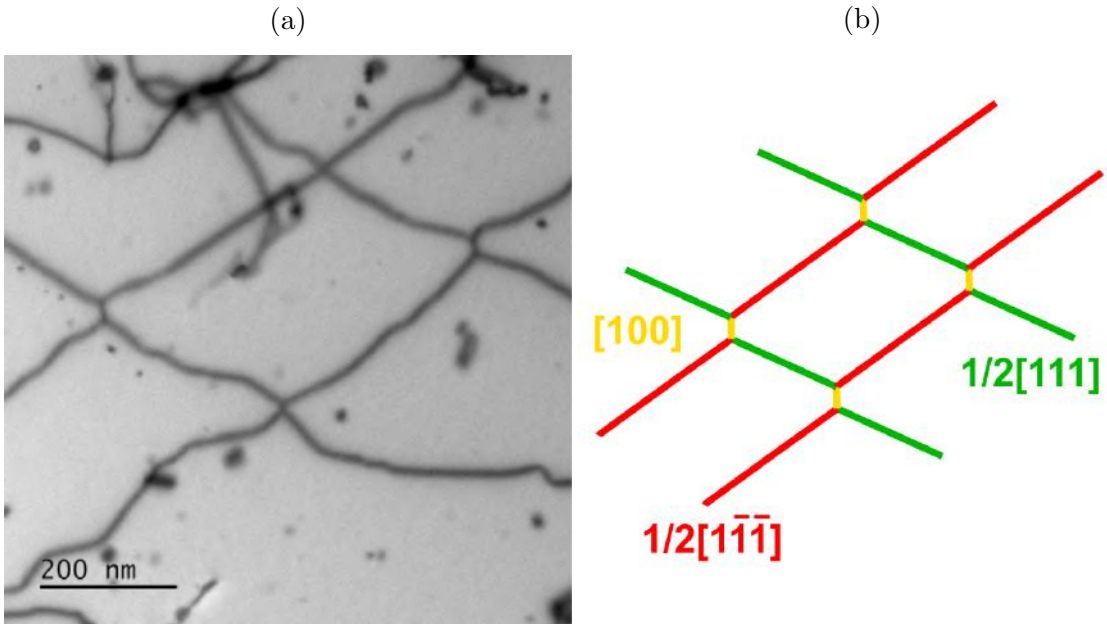

Figure 5.10: (a) Detail of a dislocation junction taken using the STEM mode in the [111] pole at 250 000 x magnification and the camera length of 40 cm. (b) Numbering of dislocations for the $\mathbf{g} \cdot \mathbf{b}$ analysis.

Fig. 5.11 shows a series of TEM micrographs taken and different diffraction conditions used for the $\mathbf{g} \cdot \mathbf{b}$ analysis, whose overview is presented in Table 5.6.

In the first diffraction condition, the dislocation labeled 3 is invisible, which suggests it can be one of the three dislocations with the dot product of its Burgers vector and diffraction condition equal to 0, i.e. $[11\bar{1}]$, $[1\bar{1}1]$ and [100]. However, if the

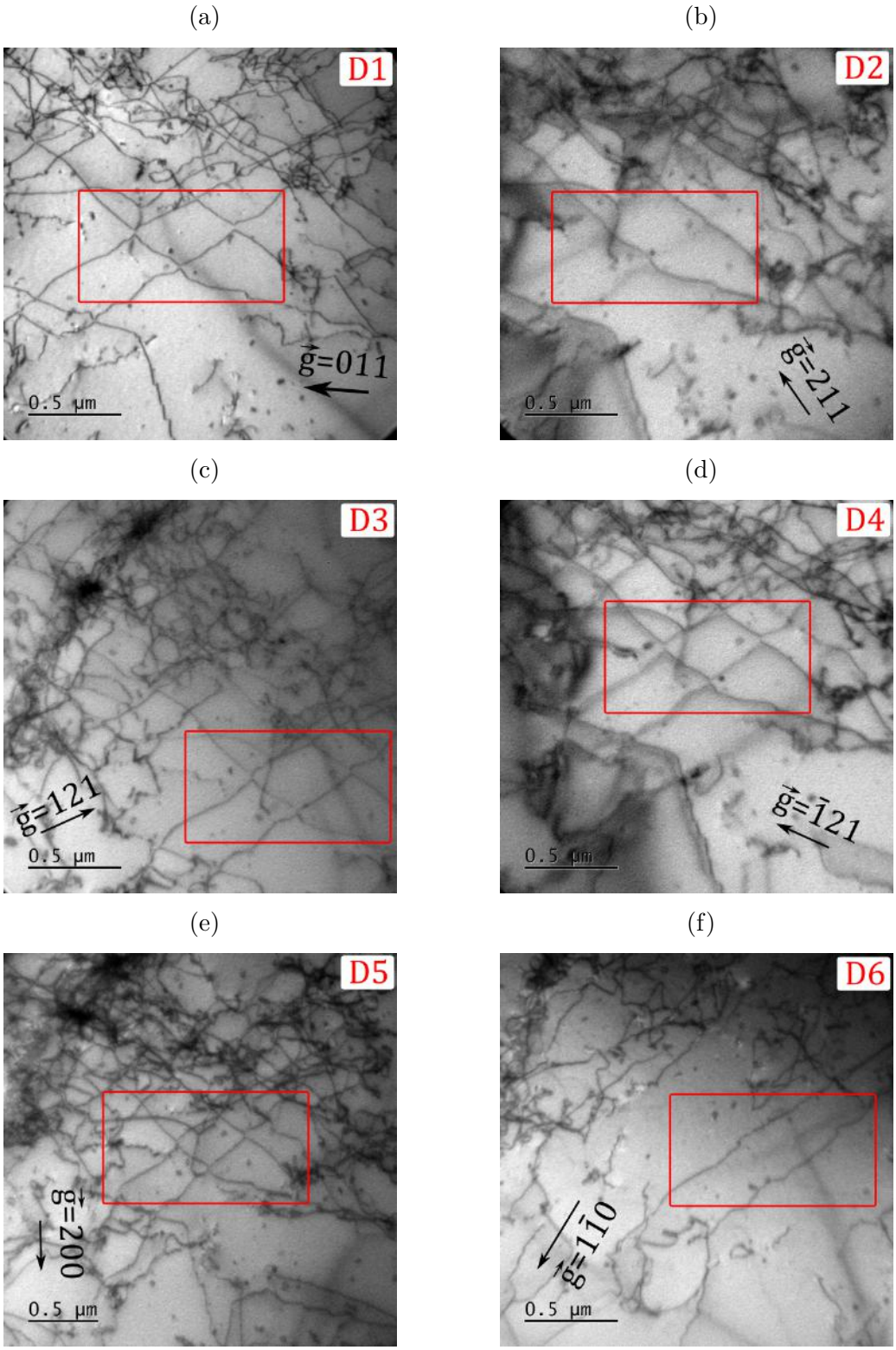

Figure 5.11: Series of TEM micrographs taken at different difraction condifions (D1-D6) at 40 000x magnification: (a) D1 : $\mathbf{g} = 011$, (a) D2 : $\mathbf{g} = 211$, (c) D3 : $\mathbf{g} = 121$, (d) D4 : $\mathbf{g} = \bar{1}21$, (e) D5 : $\mathbf{g} = 200$, (f) D6 : $\mathbf{g} = 1\bar{1}0$

$[11\bar{1}]$ dislocation was the solution, it would have to be invisible also in the diffraction conditions labeled as D4 or D6, which is not the case. The same applies to the $[1\bar{1}1]$ dislocation in the condition D3. However, in this case, the visibility is lower and the dislocation does not disappear completely. Additionally, two dislocations of the $\langle 111 \rangle$ type cannot produce another dislocation of the same type. Therefore, the [100] dislocation is the only remaining possibility. The dislocation labeled 1 is missing from the micrograph taken in the second diffraction (D2), leaving only $[1\bar{1}\bar{1}]$ possible. The dislocation labeled 2 disappears in micrograph taken in the condition D6, which suggests again three dislocations - [111], $[11\bar{1}]$ and [001]. The $[11\bar{1}]$ dislocation would have to be invisible also in the D1 condition, which is clearly not the case, and similarly, the [001] dislocation would have to be invisible in the D5 condition. The only dislocation that satisfies all criteria is [111].

Table 5.6: Summary of the diffraction conditions used to interpret Fig. 5.11 together with the dislocation visibility analysis for dislocations marked in Fig. 5.10(b). The last seven columns represent the result of the absolute value of the dot product between the diffraction vector and the Burgers vector of a suspected dislocation.

Diffraction condition		Dislocation visibility			Suspected dislocation						
					[111] $[\bar{1}\bar{1}\bar{1}]$	$[11\bar{1}]$ $[\bar{1}\bar{1}1]$	$[1\bar{1}\bar{1}]$ $[\bar{1}11]$	$[1\bar{1}1]$ $[\bar{1}11]$	[001] $[00\bar{1}]$	[010] $[0\bar{1}0]$	[100] $[\bar{1}00]$
		1	2	3	$\mathbf{g}\cdot\mathbf{b}$	$\mathbf{g}\cdot\mathbf{b}$	$\mathbf{g}\cdot\mathbf{b}$	$\mathbf{g}\cdot\mathbf{b}$	$\mathbf{g}\cdot\mathbf{b}$	$\mathbf{g}\cdot\mathbf{b}$	$\mathbf{g}\cdot\mathbf{b}$
D1	[011]	✓	✓	✗	2	0	2	0	1	1	0
D2	[211]	✗	✓	✓	4	2	0	2	1	1	2
D3	$[1\bar{2}1]$	✓	✓	✓	4	2	2	0	1	2	1
D4	$[12\bar{1}]$	✓	✓	✓	2	0	4	2	1	2	1
D5	[200]	✓	✓	✓	2	2	2	2	0	0	2
D6	$[1\bar{1}0]$	✓	✗	✓	0	0	2	2	0	1	1

The three dislocations in the network, i.e. $1/2[111]$, $1/2[1\bar{1}\bar{1}]$ and [100], lie on the same $(0\bar{1}1)$ plane. Two possibilities then follow from the behavior of this network under stress. If the junction breaks under stress, the two dislocations unzip from each other and may continue moving on planes favorable for individual dislocations. This would typically result in "normal" slip as predicted from the Schmid law. On the other hand, if the junction remains stable under stress, the three dislocations can only move on the plane common to all three, which is the $(0\bar{1}1)$ plane. In this case, the macroscopic plastic deformation would be governed by anomalous slip.

5.2.2 Simulation of anomalous slip in chromium

Computer atomistic simulations made in our group [227] were used to investigate the behavior of the junction in Fig. 5.10(a). A similar study was done by Bulatov and Cai [228] on molybdenum. They considered a uniaxial compression in the $[\bar{2}38]$ direction that is close to the center of the stereographic triangle. The simulation cell was constructed as two interpenetrating cylinders with their rotational axes parallel to [111] and $[1\bar{1}\bar{1}]$ directions, as shown in Fig. 5.12. The region inside

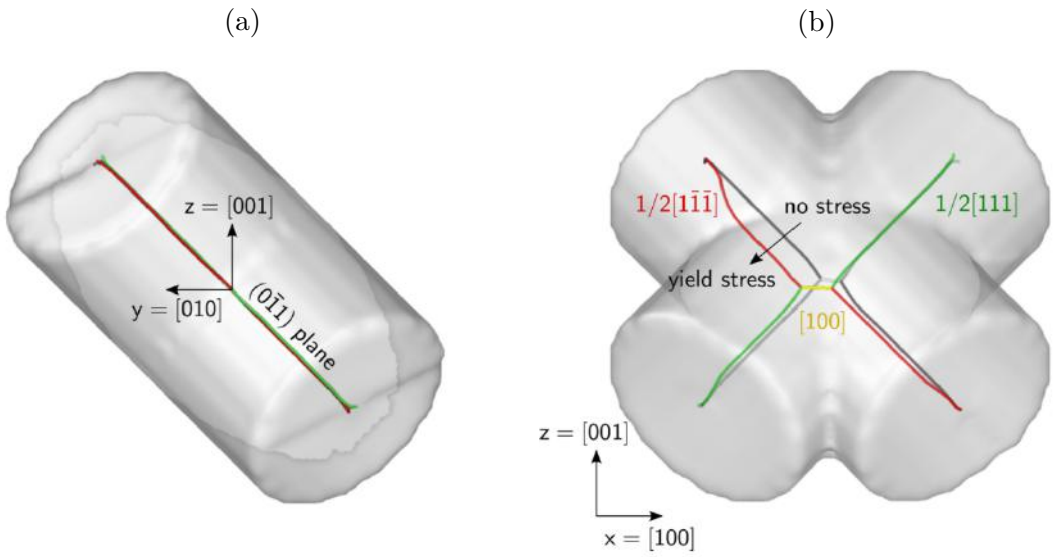

Figure 5.12: Simulation cell with the dislocation positions identified using the DXA algorithm. Gray lines: dislocations in the relaxed block at zero applied stress. Colored lines: displaced dislocations in the block subjected to large uniaxial compression in the [$\bar{2}$38] direction. (a) view in along the x negative, (b) view along the y direction.

the union of these cylinders was filled with atoms at the positions of the perfect bcc lattice that was oriented such that the x, y, and z axes were parallel to the three $\langle 100 \rangle$ directions. The 1/2[111] and 1/2[1$\bar{1}\bar{1}$] screw dislocations were inserted parallel to the rotational axes of the two cylinders using their anisotropic linear-elastic strain fields obtained from Stroh's theory [229]. The 25844 atoms whose distance from the surface of the simulation cell was smaller than the cut-off radius of atomic interactions (r_{cut}) were fixed at their displaced positions, whereas the remaining 26163 atoms inside the block were further relaxed at 0 K using the FIRE algorithm [230]. The structural relaxation was terminated when all forces on atoms dropped below 5 meV/Å. These boundary conditions ensure that the atoms in the interior of the two cylinders (i.e., farther from the surface than r_{cut}) experience bulk-like environments. The energy of the system of interacting atoms and the forces between them were described using the Bond Order Potential for Cr that was formulated recently by Lin, Vitek, and Mrovec [231]. This semi-empirical potential was developed partially using first principles calculations and correctly captures the mixed metallic and covalent character of bonds arising from partially filled d bands and the screening of d-d bonds by s electrons on neighboring atoms. However, this formulation does not consider magnetic spins as relevant degrees of freedom and thus treats Cr as an effectively non-magnetic bcc metal. Such simplification is acceptable for the triple-**Q** state of Cr that contains a large number of small magnetic domains with all three orientations of the wavevector **Q** (Fig. 1.7).

The dislocation substructure inside the relaxed simulation cell is shown in the right panel of Fig. 5.12 in gray. It was obtained by post-processing the relaxed atomic positions using the Dislocation Extraction Algorithm (DXA) [232] as implemented in the OVITO code [233]. The intersection of the 1/2[111] and 1/2[1$\bar{1}\bar{1}$] screw

dislocations produced a short [100] junction with the screw character, in agreement with experimental observation. The external uniaxial compression along the $[\bar{2}38]$ direction was then applied in the steps of $0.001C_{44}$ (about 100 MPa) by imposing the corresponding linear-elastic displacements to all atoms in the block. The atoms inside the block were relaxed for each stress state by the procedure described above.

The following two mechanisms may be operative when the applied stress reaches the yield stress. If the [100] junction is weak, the $1/2\langle 111\rangle$ dislocations would break from the junction and continue moving on the $\{110\}$ planes that are predicted by atomistic studies on isolated dislocations. In particular, the $1/2[111]$ dislocation would move on the $(\bar{1}01)$ plane, and the $1/2[\bar{1}11]$ dislocation on the (101) plane [78]. On the other hand, if the junction is strong, the two $1/2\langle 111\rangle$ dislocations and their [100] junction would remain tightly bound and move on the $(0\bar{1}1)$ plane that is common to all three. In this case, single-dislocation atomistic studies would be insufficient to explain the origin of the anomalous slip.

We observe in Fig. 5.12(b) that the application of stress moves the whole network on the $(0\bar{1}1)$ plane. A similar movement is observed also under uniaxial tension applied in the same direction. In this case, however, the network of the three dislocation moves on the $(0\bar{1}1)$ plane in the opposite direction.

These calculations were also done for α-Fe, where the two dislocations unzip from the junction under both uniaxial tension and compression. As a consequence, the macroscopic slip traces are determined by the slip system operative at the level of isolated dislocations. Using the terminology above, the two $1/2\langle 111\rangle$ screw dislocations in Cr form a strong [100] junction. Based on these results, we also conclude that the anomalous slip in Cr is not associated with the motion of isolated $1/2\langle 111\rangle$ screw dislocations but, instead, it is governed by the glide of intersecting $1/2\langle 111\rangle$ screw dislocations and their [100] junction on the $(0\bar{1}1)$ plane. This conclusion agrees with our STEM analysis made on deformed samples (Fig. 5.11). Furthermore, it confirms that the co-planar double slip model, proposed originally by Matsui & Kimura [70] and Louchet & Kubin [66] to explain the occurrence of the $(0\bar{1}1)$ slip in Mo, governs the anomalous slip in Cr at low homologous temperatures.

In principle, a thermodynamic model of dislocation glide should be considered to extend the results of molecular statics simulations to finite temperatures. However, the mechanism of plastic deformation of bcc metals at low homologous temperatures (i.e., below 10% of the melting temperature) is governed by long and nearly straight screw dislocations, whose behavior under stress is studied by molecular statics at 0 K. This justifies the use of molecular statics to explain the behavior of Cr at 77 K.

List of symbols

Symbol	Meaning	Equation
Latin symbols		
$\mathbf{b}$	Burgers vector	
C_{44}	Shear modulus	
$\mathbf{g}$	Diffraction vector	

6 Deformation mechanisms in α-Fe

6.1 Compression tests on polycrystalline α-Fe

The engineering stress-strain curve in Fig. 6.1 measured at 77 K shows various load drops that could be produced by twinning. Indeed, a closer look at the curve (inset in Fig. 6.1) reveals numerous load drops that are associated with the nucleation of twins in individual grains of the specimen.

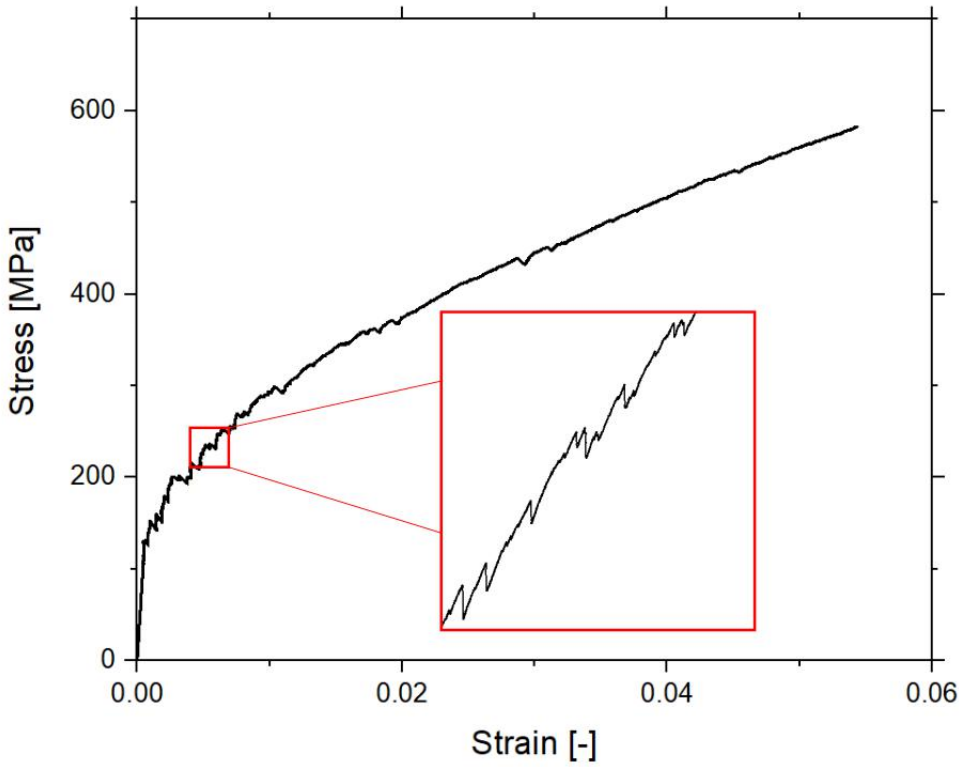

Figure 6.1: Engineering stress-strain relationship of the polycrystalline specimen tested in compression at 77 K. The consequences of load drops on the surface of the sample are shown in Fig. 6.2.

The grain structure represented by the IPF Z map before the deformation is shown in Fig. 6.2(a), and the deformed state represented by the same type of map is shown in Fig. 6.2(b). The loading axis is vertical. The black lines in Fig. 6.2(b) represent twins, where the deformation caused a change in topography resulting in either the incident electrons not being able to reach the twin or preventing the

diffracted electrons from reaching the detector due to the 70° tilt of the specimen. However, this is not the case for all twins, as demonstrated in the inset in Fig. 6.2(b).

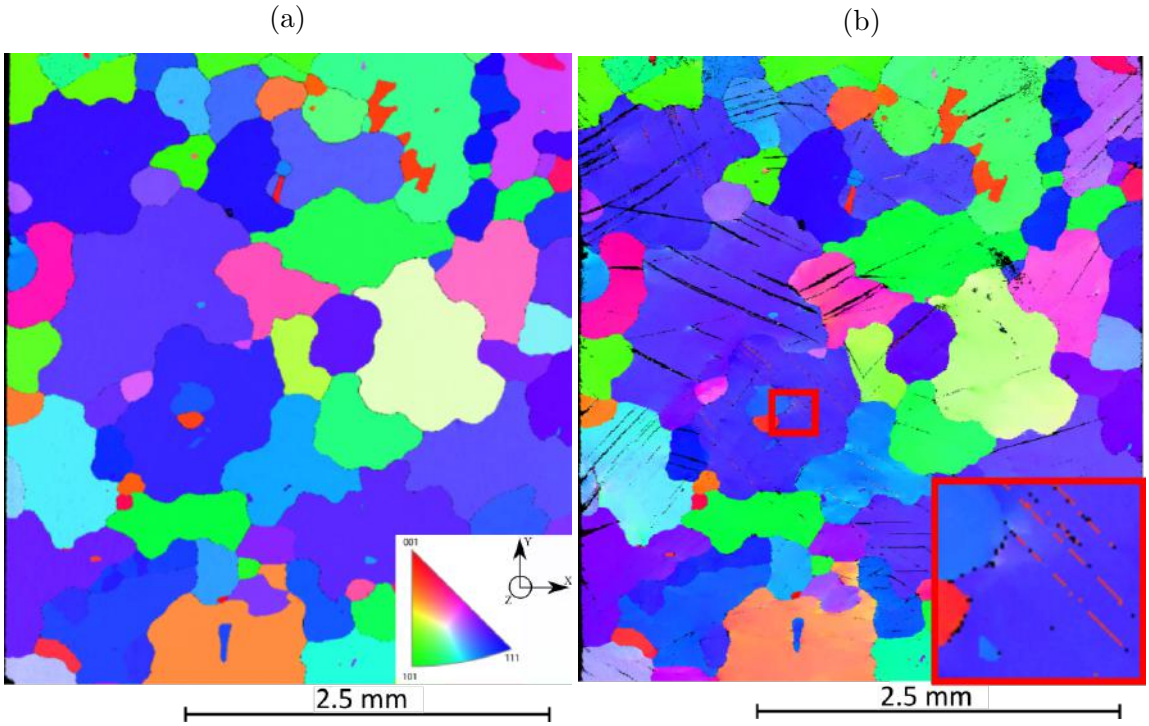

Figure 6.2: Example of the same area shown as EBSD IPF Z maps (a) before and (b) after deformation. The inset represents an enlargement of the marked region showing twins.

In this section, ten large grains were chosen with their initial orientations that cover the area of the stereographic triangle, as demonstrated in Fig. 6.3. In cases where the black lines appear in EBSD images the chosen grains, another EBSD mapping was performed on the specimen rotated by 90° to reveal any large misorientation and to decide if the deformation is caused by twinning or slip.

To demonstrate which slip or twinning systems were activated, the table with the five most stressed slip and twin systems is presented. The twinning systems are also marked with T or AT to distinguish the shear applied in the twinning and antitwinning sense, respectively. The grains were chosen based on their size, orientation of the loading axis, and the number of the active slip or twinning systems, which are always at least two. Fig. 6.4 shows the pattern quality maps of grains 1 and 3 and the tables below the five most stressed slip and twinning systems expected in these grains. If the twin could not be identified by EBSD due to geometrical constraints, another EBSD map with the specimen rotated by 90° was taken.

The twinning systems present in this grain 1 (Fig. 6.4(a)) are the $(\bar{2}11)[\bar{1}\bar{1}\bar{1}]$ and $(\bar{1}21)[11\bar{1}]$, which are both sheared in twinning sense and have SFs = 0.439 and 0.314, respectively. The five most stressed slip and twinning systems for grain 1 are summarized together with respective SFs in table on the bottom of Fig. 6.4(a).
The observed traces correspond to the most highly stressed twinning systems op-

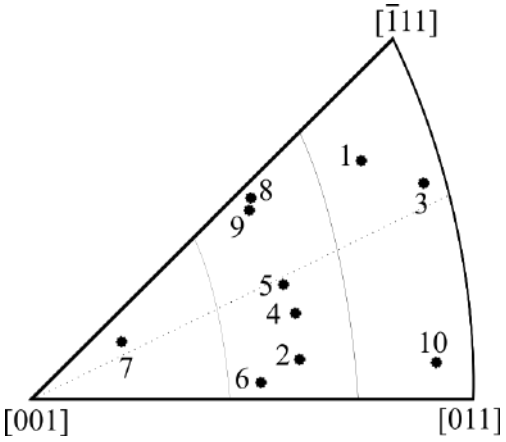

Figure 6.3: Stereographic triangle showing a loading axis direction of individual grains.

(a) (b)

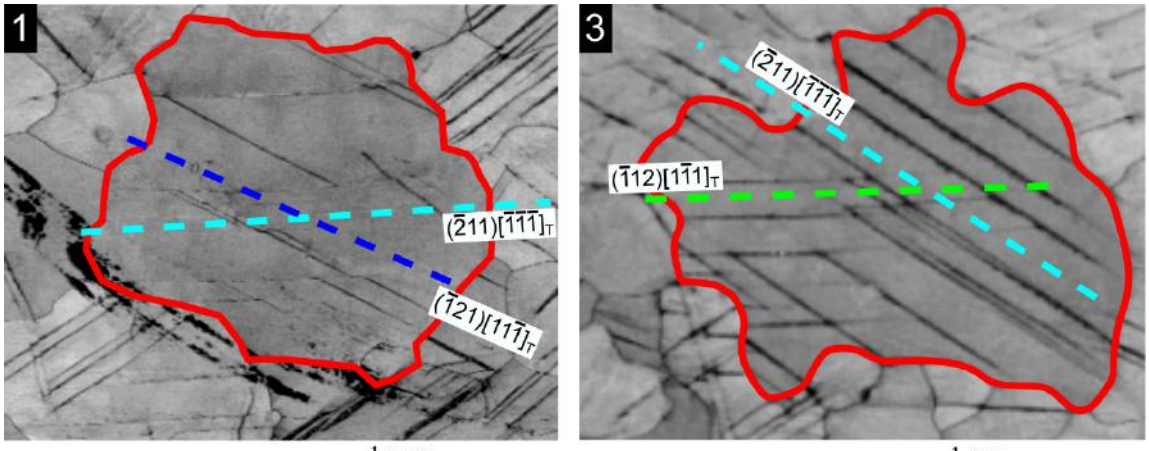

Slip sys.	SF	Twin sys.	SF
$(\bar{1}01)[\bar{1}\bar{1}\bar{1}]$	0.422	$\mathbf{(\bar{2}11)[\bar{1}\bar{1}\bar{1}]_T}$	0.439
$(1\bar{1}0)[111]$	0.338	$\mathbf{(\bar{1}21)[11\bar{1}]_T}$	0.314
$(0\bar{1}\bar{1})[\bar{1}\bar{1}1]$	0.319	$(\bar{1}\bar{1}2)[\bar{1}\bar{1}\bar{1}]_{AT}$	0.293
$(\bar{1}0\bar{1})[\bar{1}11]$	0.258	$(112)[11\bar{1}]_{AT}$	0.238
$(\bar{1}\bar{1}0)[11\bar{1}]$	0.225	$(1\bar{1}2)[1\bar{1}\bar{1}]_{AT}$	0.238

Slip sys.	SF	Twin sys.	SF
$(\bar{1}01)[\bar{1}\bar{1}\bar{1}]$	0.416	$\mathbf{(\bar{2}11)[\bar{1}\bar{1}\bar{1}]_T}$	0.465
$(1\bar{1}0)[111]$	0.388	$(\bar{1}\bar{1}2)[\bar{1}\bar{1}\bar{1}]_{AT}$	0.256
$(\bar{1}0\bar{1})[\bar{1}11]$	0.238	$(211)[1\bar{1}\bar{1}]_T$	0.247
$(0\bar{1}\bar{1})[\bar{1}\bar{1}1]$	0.226	$(\bar{1}21)[11\bar{1}]_T$	0.227
$(110)[1\bar{1}\bar{1}]$	0.190	$(1\bar{2}1)[111]_{AT}$	0.208

Figure 6.4: Pattern quality map of: (a) grain 1, and (b) grain 3 with highlighted twinning systems. The five most stressed slip and twinning systems in the grains 1 and 3 are shown in the tables under the maps. The orientations of these grains expressed in Bunge's notation are (214.3°, 27.6°, 87.4°) and (171°, 39.06°, 38.4°), respectively.

erating in this grain. Even though the most stressed slip system has greater SF than the second most highly stressed twinning system, no slip was observed. The

grain 3, shown in Fig. 6.4(b) has a loading axis oriented near the $[011] - [11\bar{1}]$ edge of the stereographic triangle. The $(\bar{2}11)[\bar{1}\bar{1}\bar{1}]$ twinning system with the highest Schmid factor of 0.465 is operative. However, the next twinning system $(\bar{1}12)[1\bar{1}1]$ sheared in the twinning sense with the SF = 0.156 is also visible, despite several more highly stressed systems sheared in both the twinning and the antitwinning sense being expected.

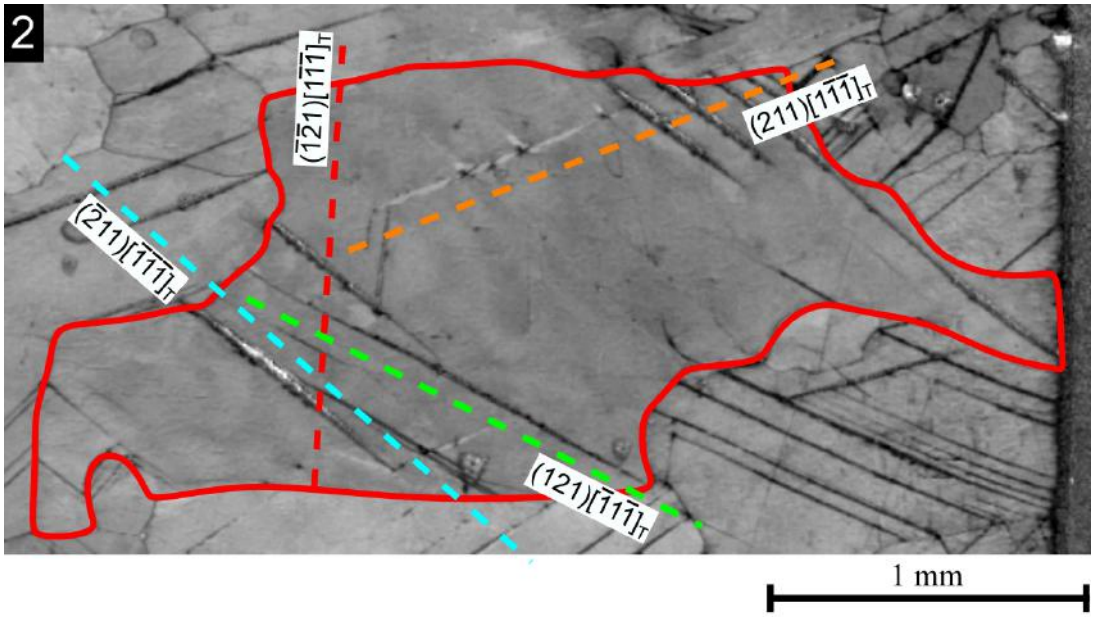

Slip sys.	SF	Twin sys.	SF
$(\bar{1}01)[\bar{1}\bar{1}\bar{1}]$	0.499	$(\bar{\mathbf{2}}\mathbf{11})[\bar{\mathbf{1}}\bar{\mathbf{1}}\bar{\mathbf{1}}]_\mathbf{T}$	0.435
$(\bar{1}0\bar{1})[\bar{1}11]$	0.476	$(1\bar{1}2)[1\bar{1}\bar{1}]_{AT}$	0.430
$(0\bar{1}\bar{1})[\bar{1}\bar{1}1]$	0.291	$(\bar{1}\bar{1}2)[\bar{1}\bar{1}\bar{1}]_{AT}$	0.429
$(1\bar{1}0)[1\bar{1}\bar{1}]$	0.269	$(\mathbf{211})[\mathbf{1}\bar{\mathbf{1}}\bar{\mathbf{1}}]_\mathbf{T}$	0.395
$(1\bar{1}0)[111]$	0.255	$(112)[11\bar{1}]_{AT}$	0.274

Figure 6.5: Pattern quality map with highlighted twinning systems of grain 2. The five most stressed slip and twinning systems of grain 2 are shown in table under the map. The orientation of the grain expressed in Bunge's notation is (278.4°, 25.8°, 18.1°).

The grain 2, oriented close to the $[001] - [011]$ edge of the stereographic triangle and shown in Fig. 6.5, contains four operative twinning systems, namely $(\bar{2}11)[\bar{1}\bar{1}\bar{1}]$, $(211)[1\bar{1}\bar{1}]$, $(121)[1\bar{1}1]$ and $(\bar{1}\bar{2}1)[1\bar{1}\bar{1}]$ with the SFs = 0.435, 0.395, 0.163 and 0.035, respectively. The twin formation may have been initiated at the grain boundary or at another twin. All of the observed systems are, however, sheared in the twinning sense, and none sheared in the antitwinning sense is present. The most stressed twinning system in grain 2 sheared in the antitwinning sense has more than 12 times larger Schmid factor compared to the twinning system sheared in twinning sense with the lowest SF that was observed. Similarly, no slip systems were observed as in the previous case.

The loading axis of grain 4, whose pattern quality map is shown in Fig. 6.6(a), is

(a)

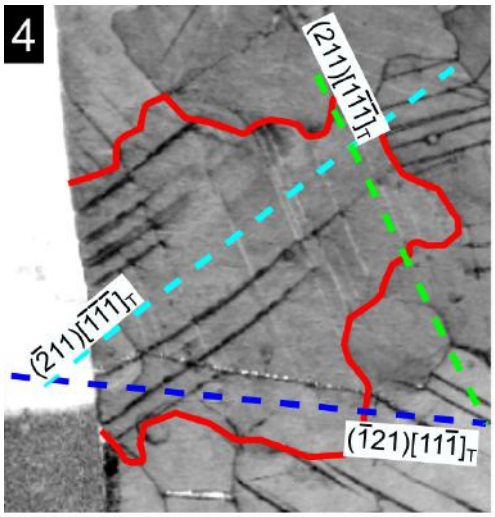

Slip sys.	SF	Twin sys.	SF
($\bar{1}$01)[$\bar{1}\bar{1}\bar{1}$]	0.497	($\bar{\mathbf{2}}$**11**)[$\bar{\mathbf{1}}\bar{\mathbf{1}}\bar{\mathbf{1}}$]$_\mathbf{T}$	0.446
($\bar{1}$0$\bar{1}$)[$\bar{1}$11]	0.443	(1$\bar{1}$2)[1$\bar{1}\bar{1}$]$_{AT}$	0.417
(0$\bar{1}\bar{1}$)[$\bar{1}\bar{1}$1]	0.333	($\bar{1}\bar{1}$2)[$\bar{1}\bar{1}\bar{1}$]$_{AT}$	0.414
(0$\bar{1}$1)[11$\bar{1}$]	0.280	(**211**)[**1**$\bar{\mathbf{1}}\bar{\mathbf{1}}$]$_\mathbf{T}$	0.350
(1$\bar{1}$0)[111]	0.276	(112)[11$\bar{1}$]$_{AT}$	0.300
		(**$\bar{1}$21**)[**11**$\bar{\mathbf{1}}$]$_\mathbf{T}$	0.277

(b)

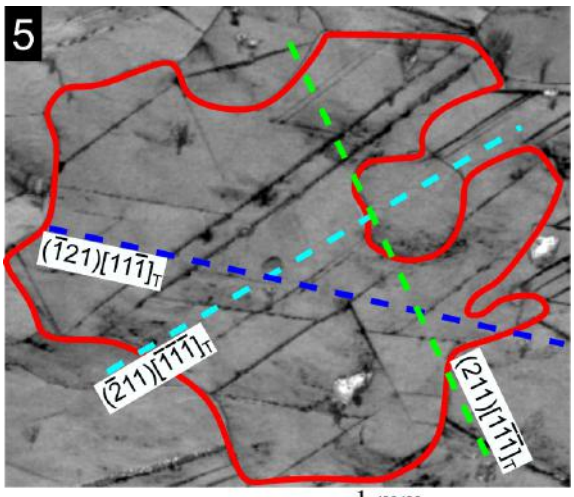

Slip sys.	SF	Twin sys.	SF
($\bar{1}$01)[$\bar{1}\bar{1}\bar{1}$]	0.439	($\bar{\mathbf{2}}$**11**)[$\bar{\mathbf{1}}\bar{\mathbf{1}}\bar{\mathbf{1}}$]$_\mathbf{T}$	0.439
($\bar{1}$0$\bar{1}$)[$\bar{1}$11]	0.434	(1$\bar{1}$2)[1$\bar{1}\bar{1}$]$_{AT}$	0.423
(0$\bar{1}\bar{1}$)[$\bar{1}\bar{1}$1]	0.375	($\bar{1}\bar{1}$2)[$\bar{1}\bar{1}\bar{1}$]$_{AT}$	0.415
(0$\bar{1}$1)[1$\bar{1}\bar{1}$]	0.298	(211)[1$\bar{1}\bar{1}$]$_{AT}$	0.329
(1$\bar{1}$0)[111]	0.267	(112)[11$\bar{1}$]$_{AT}$	0.320
		(**$\bar{1}$21**)[**11**$\bar{\mathbf{1}}$]$_\mathbf{T}$	0.299

Figure 6.6: Pattern quality map of: (a) grain 4, and (b) grain 5 with highlighted twinning systems. The five most stressed slip and six most stressed twinning systems in grains 4 and 5 are shown in tables under the maps. The orientations of the grains expressed in Bunge's notation are (308.4°, 42.7°, 50.1°) and (122.3°, 49.7°, 56.7°), respectively.

located near the center of the stereographic triangle. This grain shows the operation of three different twinning systems, namely ($\bar{2}$11)[$\bar{1}\bar{1}\bar{1}$], (211)[1$\bar{1}\bar{1}$] and ($\bar{1}$21)[11$\bar{1}$] with Schmid factors of 0.446, 0.350 and 0.277, respectively. These are the three most stressed twinning systems sheared in the twinning sense, skipping over the systems sheared in the antitwinning sense with higher Schmid factors. The loading axis of grain 5 is closer to the center of the stereographic triangle, slightly closer than that of grain 4. The grain 5, shown in Fig. 6.6(b), is located on a different side of the specimen, yet the operative twinning systems are identical. Therefore, even though twins can be initiated at grain boundaries by external factors, the most stressed twinning systems sheared in the twinning sense are always operational.

The loading axis of grain 6, whose pattern quality map is shown in Fig. 6.7(a), is located closest to the $[001]-[011]$ edge of the stereographic triangle. Unfortunately, only the ($\bar{2}$11)[$\bar{1}\bar{1}\bar{1}$] twinning system can be identified without ambiguity. The other three misorientations in this grain cannot be differentiated precisely because the surface markings are in very similar orientations. Going from the most stressed systems to the least, the orientation of the red twinning system ($\bar{1}\bar{1}$2)[$\bar{1}\bar{1}\bar{1}$] sheared in the

(a) (b)

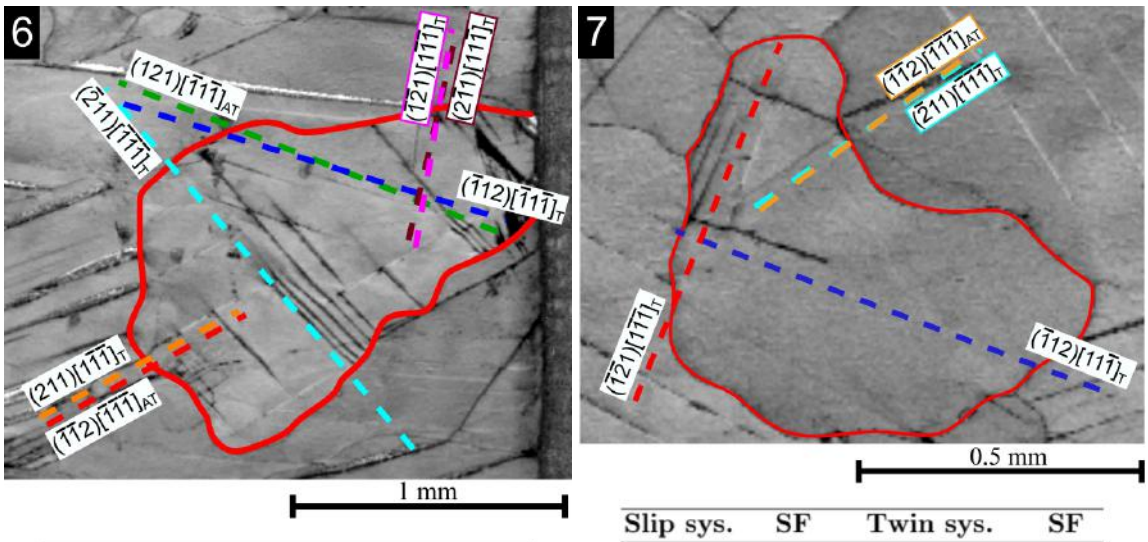

Slip sys.	SF	Twin sys.	SF
$(\bar{1}01)[\bar{1}\bar{1}\bar{1}]$	0.496	$(1\bar{1}2)[1\bar{1}\bar{1}]_{AT}$	0.457
$(\bar{1}0\bar{1})[\bar{1}11]$	0.488	$\mathbf{(\bar{1}\bar{1}2)[\bar{1}\bar{1}\bar{1}]_{AT}}$	0.455
$(0\bar{1}\bar{1})[\bar{1}\bar{1}1]$	0.311	$\mathbf{(\bar{2}11)[\bar{1}\bar{1}\bar{1}]_{T}}$	0.404
$(0\bar{1}1)[1\bar{1}\bar{1}]$	0.304	$\mathbf{(211)[1\bar{1}\bar{1}]_{T}}$	0.389
$(1\bar{1}0)[111]$	0.292	$(112)[11\bar{1}]_{AT}$	0.305

Slip sys.	SF	Twin sys.	SF
$(\bar{1}01)[\bar{1}\bar{1}\bar{1}]$	0.453	$(1\bar{1}2)[1\bar{1}\bar{1}]_{AT}$	0.499
$(\bar{1}0\bar{1})[\bar{1}11]$	0.444	$\mathbf{(\bar{1}\bar{1}2)[\bar{1}\bar{1}\bar{1}]_{AT}}$	0.469
$(0\bar{1}\bar{1})[\bar{1}\bar{1}1]$	0.431	$(112)[11\bar{1}]_{AT}$	0.448
$(0\bar{1}1)[1\bar{1}\bar{1}]$	0.421	$(\bar{1}12)[\bar{1}1\bar{1}]_{AT}$	0.395
$(1\bar{1}0)[111]$	0.359	$\mathbf{(\bar{2}11)[\bar{1}\bar{1}\bar{1}]_{T}}$	0.316
		$\mathbf{(\bar{1}21)[11\bar{1}]_{T}}$	0.299

Figure 6.7: Pattern quality map of: (a) grain 6, and (b) grain 7 with highlighted twinning systems. The most stressed slip and twinning systems of grain 6 and grain 7 are shown in the tables under the maps. The orientations of the grains expressed in Bunge's notation are (272.5°, 33.9°, 19.7°) and (281.2°, 40.8°, 76.2°), respectively.

antitwinning sense with the Schmid factor of 0.455 is very close to the orientation of the $(211)[1\bar{1}\bar{1}]$ system sheared in the twinning sense with the Schmid factor of 0.389. The difference between the theoretical orientations of these markings projected onto the surface is only 0.9°. The green twinning system $(\bar{1}12)[\bar{1}1\bar{1}]$ sheared in the antitwinning sense with the SF = 0.286 is only 4.6° from the dark blue $(121)[\bar{1}1\bar{1}]$ twinning system sheared in the twinning sense with the SF = 0.208. Lastly, the magenta twinning system $(2\bar{1}1)[11\bar{1}]$ with SF = 0.071 and the pink twinning system $(1\bar{2}1)[1\bar{1}\bar{1}]$ with the SF = 0.069 are both sheared in the twinning sense and have mutual misorientation of 1.5°.

If the surface markings of two twinning systems are only slightly misoriented,it is nearly impossible to decide which (or whether both) systems are active. However, if one of these is sheared in the twinning sense and the other in the antitwinning sense, it is safe to assume that the misoriented region is a twin resulting from twinning on the former system. The loading axis of grain 7, shown in Fig. 6.7(b) is closest to the [100] pole of the stereographic triangle. Therefore, several slip and twinning systems may be operative due to large Schmid factors. Similarly as the grain 6, the most strained twinning system in this grain cannot be accurately determined. The angular difference between traces of the orange $(\bar{1}\bar{1}2)[\bar{1}\bar{1}\bar{1}]$ system sheared in

the antitwinning sense with SF = 0.469 and teal $(\bar{2}11)[\bar{1}\bar{1}\bar{1}]$ sheared in the twinning sense with SF = 0.316 is only 1.8°. The other systems present are the blue $(\bar{1}21)[11\bar{1}]$ twinning system sheared in the twinning sense with the SF = 0.299 and the red $(\bar{1}\bar{2}1)[1\bar{1}\bar{1}]$ system sheared in twinning sense with SF = 0.230. The grain 8 lies close to the $[100] - [11\bar{1}]$ edge of the stereographic triangle and is the smallest grain in this study. The observed systems are the teal $(\bar{2}11)[\bar{1}\bar{1}\bar{1}]$ twinning system sheared in the twinning sense with SF = 0.400, blue $(\bar{1}21)[11\bar{1}]$ twinning system sheared in the twinning sense with SF = 0.382, and the red $(\bar{1}\bar{2}1)[1\bar{1}\bar{1}]$ twinning system sheared also in twinning sense with SF = 0.185. The corresponding pattern quality map with the highlighted operative systems is shown in Fig. 6.8(a). The twinning systems sheared in the antitwinning sense are not present in this grain even though their Schmid factors are equal or higher than those of the systems sheared in the twinning sense.

(a) (b)

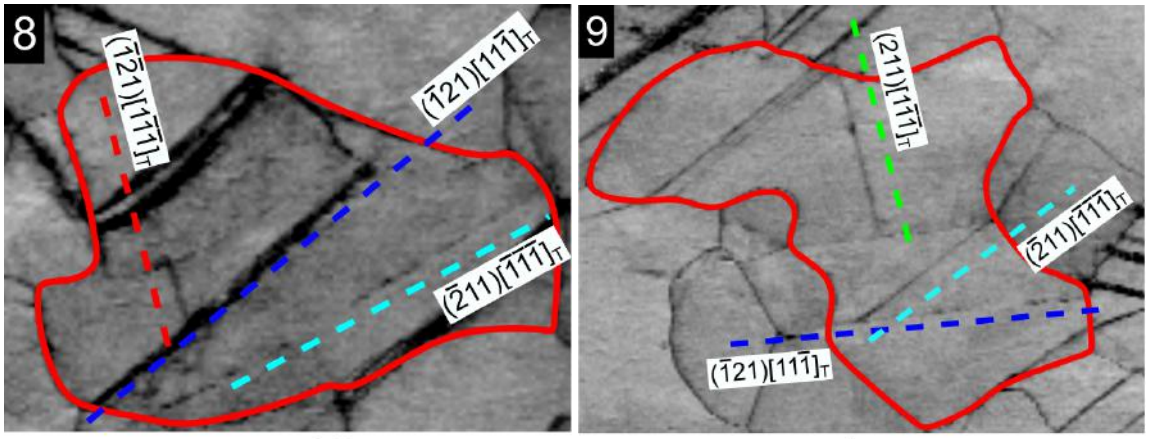

Slip sys.	SF	Twin sys.	SF
$(\bar{1}01)[\bar{1}\bar{1}\bar{1}]$	0.475	$(\bar{\mathbf{2}}\mathbf{11})[\bar{\mathbf{1}}\bar{\mathbf{1}}\mathbf{1}]_{\mathbf{T}}$	0.400
$(\bar{1}0\bar{1})[\bar{1}11]$	0.389	$(1\bar{1}2)[1\bar{1}\bar{1}]_{AT}$	0.400
$(0\bar{1}\bar{1})[\bar{1}\bar{1}1]$	0.378	$(\bar{\mathbf{1}}\mathbf{21})[\mathbf{11}\bar{\mathbf{1}}]_{\mathbf{T}}$	0.382
$(0\bar{1}1)[1\bar{1}\bar{1}]$	0.292	$(\bar{1}\bar{1}2)[\bar{1}\bar{1}\bar{1}]_{AT}$	0.372
$(1\bar{1}0)[111]$	0.281	$(112)[11\bar{1}]_{AT}$	0.360

Slip sys.	SF	Twin sys.	SF
$(\bar{1}01)[\bar{1}\bar{1}\bar{1}]$	0.451	$(1\bar{1}2)[1\bar{1}\bar{1}]_{AT}$	0.406
$(0\bar{1}\bar{1})[\bar{1}\bar{1}1]$	0.426	$(\bar{\mathbf{2}}\mathbf{11})[\bar{\mathbf{1}}\bar{\mathbf{1}}\mathbf{1}]_{\mathbf{T}}$	0.403
$(\bar{1}0\bar{1})[\bar{1}11]$	0.363	$(\bar{1}\bar{1}2)[\bar{1}\bar{1}\bar{1}]_{AT}$	0.378
$(0\bar{1}1)[1\bar{1}\bar{1}]$	0.339	$(\bar{\mathbf{1}}\mathbf{21})[\mathbf{11}\bar{\mathbf{1}}]_{\mathbf{T}}$	0.377
$(1\bar{1}0)[111]$	0.247	$(112)[11\bar{1}]_{AT}$	0.362

Figure 6.8: Pattern quality map of: (a) grain 8, and (b) grain 9 with highlighted twinning systems. The five most stressed slip twinning systems of these grains are shown in the tables under the maps. The orientations of the grains expressed in Bunge's notation are (213.5°, 22.8°, 33.2°) and (141.5°, 26.1°, 22°), respectively.

The loading axis of grain 9, shown in Fig. 6.8(b), lies on the $[001] - [\bar{1}11]$ edge of the stereographic triangle in close proximity to the loading axis of the grain 8. While the loading axes of both grains are very close to each other, the crystal lattice is rotated around the loading axis, hence the different orientation of the surface traces. The teal $(\bar{2}11)[\bar{1}\bar{1}\bar{1}]$ twinning system is present as well as the blue $(\bar{1}21)[11\bar{1}]$

twinning system, both sheared in the twinning sense with SF = 0.403 and 0.377, respectively. The last surface markings match green $(211)[1\bar{1}\bar{1}]$ twinning system (sheared in the twinning sense, SF = 0.224). However, no misorientation was found on the EBSD maps. The closest slip systems that could correspond to this trace (angular difference of approx. 6°) are the $(110)[1\bar{1}\bar{1}]$ and $(\bar{1}\bar{1}0)[1\bar{1}1]$ systems with SFs = 0.028 and 0.004, respectively. The reason for not resolving this misorientation might be caused by low resolution of the EBSD map. Analogously to the grain 8, operation of the twinning systems sheared in the twinning sense are observed, while traces of the systems sheared in the antitwinning sense are not visible, despite them having higher Schmid factors. The loading axis of grain 10, whose pattern quality map is shown in Fig. 6.9, lies closest to the [011] pole of the stereographic triangle than that of any other sample. The only two operative twinning systems, both sheared in the twinning sense are the teal $(\bar{2}11)[\bar{1}\bar{1}\bar{1}]$ and green $(211)[1\bar{1}\bar{1}]$ systems with SF = 0.484 and 0.447, respectively. In this case, no systems sheared in the antitwinning sense are operational, because they have lower Schmid factors.

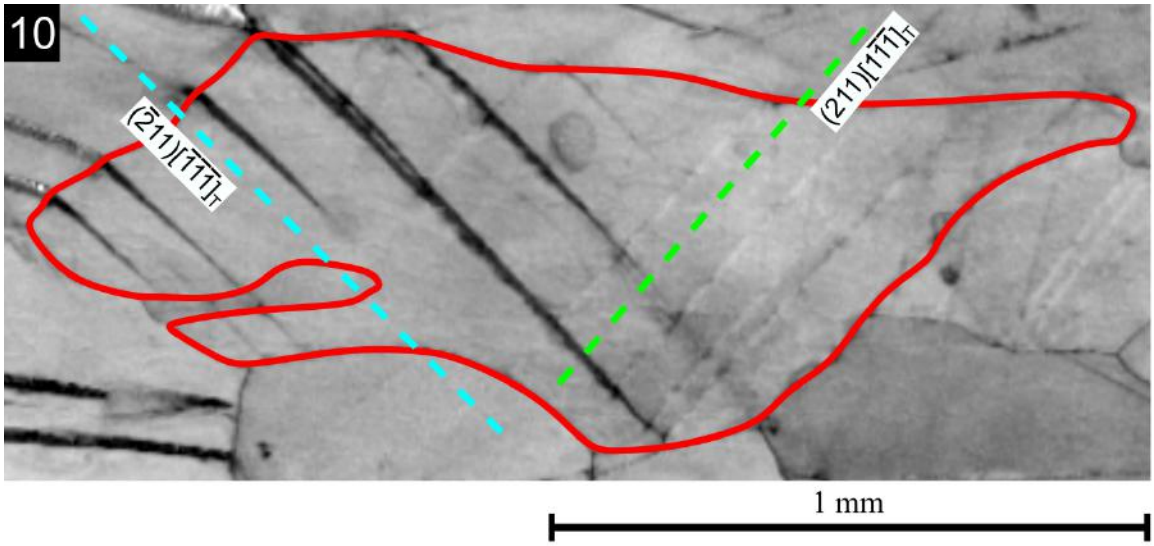

Slip sys.	SF	Twin sys.	SF
$(\bar{1}01)[\bar{1}\bar{1}\bar{1}]$	0.450	$(\mathbf{\bar{2}11})[\mathbf{\bar{1}\bar{1}\bar{1}}]_{\mathbf{T}}$	0.484
$(\bar{1}0\bar{1})[\bar{1}11]$	0.421	$(\mathbf{211})[\mathbf{1\bar{1}\bar{1}}]_{\mathbf{T}}$	0.447
$(1\bar{1}0)[111]$	0.388	$(\bar{1}\bar{1}2)[\bar{1}\bar{1}\bar{1}]_{AT}$	0.296
$(110)[1\bar{1}\bar{1}]$	0.353	$(1\bar{1}2)[1\bar{1}\bar{1}]_{AT}$	0.286
$(0\bar{1}\bar{1})[\bar{1}11]$	0.097	$(1\bar{2}1)[111]_{AT}$	0.188

Figure 6.9: Pattern quality map with highlighted twinning systems of grain 10. The five most stressed slip and twinning systems of grain 10 are shown in table under the map. The orientation of the grain expressed in Bunge's notation is (274.3°, 48.9°, 38°).

Cracks in the vicinity of twin boundaries were occasionally found in the deformed specimen. These cracks were found to propagate either along twin boundaries as shown in Fig. 6.10(a) and marked by the arrows, or at the irregularities of the twins, shown in Fig. 6.10(b). The twins in Fig. 6.10(a) are visible as the slightly darker bands below the cracks. Such behavior is usually observed in response to fatigue loading of fcc metals [234–236] and explained by the accumulation of dislocations at twin boundaries, because the latter allow dislocation storage to accommodate high plastic strain [237]. This process leads to generation of vacancies close to the twin boundary which subsequently coalesce to form a crack. Indeed, similar cracks have been reported before [238].

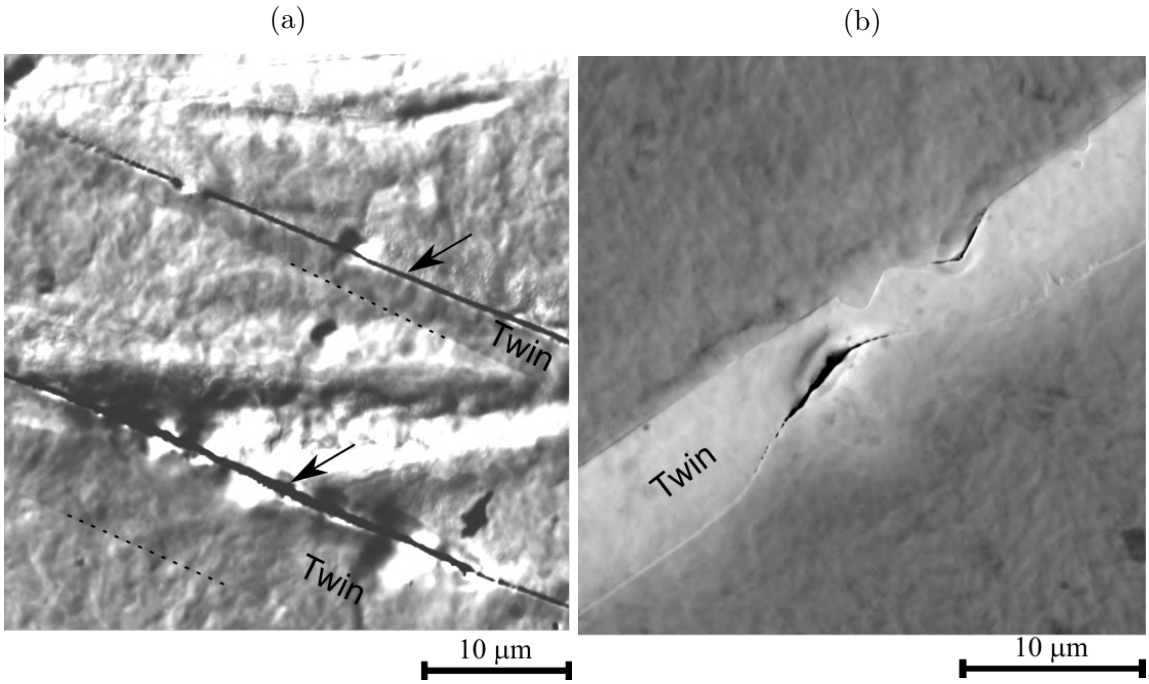

Figure 6.10: Example of twin boundary cracking in α-Fe polycrystal deformed in compression at 77 K: (a) cracking along the twin boundary, (b) cracks at irregularities inside twins.

Two more polycrystalline specimens were prepared by the same method and compressed, one in prestrained state to $\epsilon_{pl} = 0.9\%$, the second time without prestrain. The amount of plastic deformation at 77 K was 2.4 % and 2.5 % for the prestrained and unprestrained specimen, respectively. The prestrained specimen showed fewer smaller grains that deformed by twinning, however no slip traces were found. Furthermore, the stress-strain curves (not shown) do not exhibit large differences between each other.

We have previously shown in Fig. 4.7(a) an EBSD IPF Z map on the deformed polycrystalline specimen that was predeformed at RT to 0.9% and subsequently deformed at 77 K to 2.4 %. The loading axis on this figure is horizontal. This EBSD map reveals three sets of twins. In particular $(\bar{2}11)[\bar{1}\bar{1}1]$ system with SF = 0.452 and $(\bar{1}12)[11\bar{1}]$ with SF = 0.213 both sheared in the twinning sense. These are

the first and third most stressed slip systems in twinning sense. The last slip system corresponds to $(321)[1\bar{1}\bar{1}]$ with SF = 0.353 also sheared in the twinning sense. This is the only {123} system found during the investigation. In many cases, surface markings may match more twinning systems and it is thus possible that some of the twinning systems have been erroneously attributed to {112} twins. However, we find this unlikely. In this particular case, however, the identification of the twinning system is unambiguous as the closest slip markings of {112} systems are rotated by approx. 20° in both directions. Table 6.1 shows the Euler angles expressed in the Bunge notation for the structures shows in Fig. 4.7(a).

Table 6.1: Euler angles of yhe matrix and three twin types shown in Fig. 4.7(a). The angles are expressed in the Bunge notation.

Structure	**Euler angle**
Matrix	(108.5°, 6.4°, 9.3°)
$(\bar{1}12)[11\bar{1}]$	(327.5°, 43.1°, 21.7°)
$(\bar{2}11)[\bar{1}\bar{1}\bar{1}]$	(6.8°, 46.4°, 55.2°)
$(321)[1\bar{1}\bar{1}]$	(269°, 42°, 67.1°)

From the Euler angles, we can estimate the misorientation of any two structures. First, the rotation matrix $\mathbf{g}$ is computed for each structure [221, p. 21], that brings the twin into coincidence with the matrix. Secondly, we compute the misorientation matrix as:

$$\Delta\mathbf{g}_{mt} = \mathbf{g}_m\mathbf{g}_t^{-1} \tag{6.1}$$

where $\Delta\mathbf{g}_{mt}$ is misorientation matrix, $\mathbf{g}_m$ rotation matrix of matrix and g_t rotation matrix of twin. From the misorintation matrix $\Delta\mathbf{g}_{mt}$ we can further compute angular misorientation [239]. The angular misorientation gives the angle by which we rotate about a particular axis to arrive from orientation represented by the rotation matrix $\mathbf{g}_m$ to orientation represented by the rotation matrix $\mathbf{g}_t$. If we use this metric on the Euler angles in Table 6.1 and compute the misorientations between the matrix and twins, we obtain the following misorientations of the three twins with the surrounding matrix:

- 131.9° around [012] for the $(\bar{1}12)[11\bar{1}]$ twin,
- 70.4° around [011] for the $(\bar{2}11)[\bar{1}\bar{1}\bar{1}]$ twin,
- 145.9° around [113] for the $(321)[1\bar{1}\bar{1}]$ twin.

All of these misorientations are different. However due to the symmetry of the bcc lattice, they are all equivalent symmetry operations for $\Sigma 3$ twins. In practice, smallest angle of the equivalent angle/axis misorientations is shown. In this case, it would be 60° rotation around [111]. To find the smallest angle, one would have to multiply the the $\mathbf{g}_m$ and $\mathbf{g}_t$ matrices by all the 24 symmetry operators for bcc lattice before the misorientation matrix in Eq. (6.1) is computed and find the smallest angle among the results. These symmetry operators for cubic lattices can be found in Zhao

and Adams [240]. The second possibility is to compare the results with precomputed list of possible equivalent angle/axis misorientations for $\Sigma 3$ twins, which is the case here. The results thus show that all of the twins are of the same type. Twinning on {123} planes in further discussed in Chapter 7.

List of symbols

Symbol	Meaning	Equation
Latin symbols		
$\mathbf{g}_m$	Rotation matrix of crystal matrix	(6.1)
$\mathbf{g}_t$	Rotation matrix of twin	(6.1)
Greek symbols		
$\Delta\mathbf{g}_{mt}$	Misorientation matrix	(6.1)

6.2 Compression tests on α-Fe single crystals

Two iron single crystal specimens were prepared from the source crystal provided by Prof. Lejček (Institute of Physics of the Czech Academy of Sciences). The chemical composition of the specimen was shown previously in Table 3.4. Fe-mono-1 specimen was strained at RT to approx. 6% and Fe-mono-2 specimen was prestrained to 1.7% at RT and subsequently deformed at 77 K to another 2.5%. The orientation of the loading axes of the specimen, measured by the EBSD, lies in the center of the stereographic triangle, shown in Fig. 6.11. The right part of Fig. 6.11 presents a detail of the red-bounded area in the stereographic triangle. The empty circles show the initial position of the loading axis, while the filled circles mark the final orientation of the loading axis after deformation. The loading axis of Fe-mono-1 specimen rotates towards the [012] pole, which suggests operation of multiple slip systems. In cases where multiple slip systems are operational, the loading axis rotates towards the pole that is a weighted vector sum of the slip plane normals. At RT, where operation of many slip systems is possible, the rotation can be also canceled out to a certain extent by operation of systems on the planes with opposite indices. The measured misorintations of the axes are 0.6°, 0.9°, and 0.7° for the x, y, z axis respectively. It should be noted, that such small misorientations are below the angular resolution of the EBSD technique. This specimen was deformed at room temperature with the strain rate of 30 µm/min. The yield stress was only approximately 50 MPa and subsequent deformation resembles room temperature creep, as shown in Fig. 6.12.

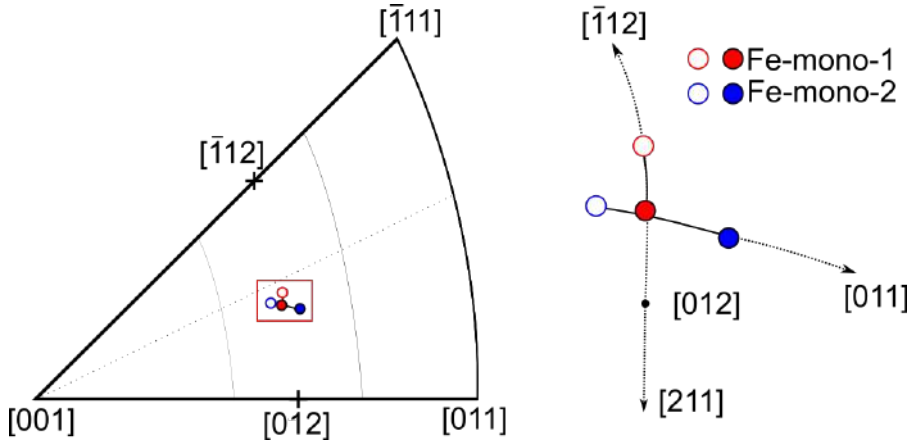

Figure 6.11: Rotation of loading axes of single-crystalline α-iron specimens. Empty circles mark the initial orientation of the loading axis and filled circles show the final orientation after deformation. The right part of the figure shown enlargement of the area bounded by the red rectangle.

The loading axis of specimen Fe-mono-2 that was deformed at 77 K, rotates strongly towards the [011] direction, see Fig. 6.11. This suggests that the most operative slip happens on (011) atomic planes. The misorientations of the axes for the Fe-mono-2 specimen are 2.2°, 2.6°, and 1.5° for the x, y, z axis respectively. The stress-strain curve of Fe-mono-2, shown in Fig. 6.12, exhibits the yield stress

$R_{p0.2}$ of approximately 460 MPa, almost ten times larger that the yield stress of the Fe-mono-1 specimen. The strain rate is identical to the one used to deform the Fe-mono-1 specimen. Furthermore, the stress-strain curves of both specimens do not exhibit a sharp yield point, but rather a gradual transition. The six most stressed slip systems for this orientation are $(\bar{1}01)[\bar{1}\bar{1}\bar{1}]$ with SF = 0.497, $(\bar{1}0\bar{1})[\bar{1}11]$ with SF = 0.453, $(0\bar{1}\bar{1})[\bar{1}\bar{1}1]$ with SF = 0.353, $(0\bar{1}1)[1\bar{1}\bar{1}]$ with SF = 0.309, $(01\bar{1})[111]$ and $(1\bar{1}0)[111]$, both with SF = 0.249. The combination of the first five systems would rotate the loading axis towards [211] pole. The operations of the third to the fifth most higly stressed slip systems would cause rotation of the loading axis towards the [011] pole.

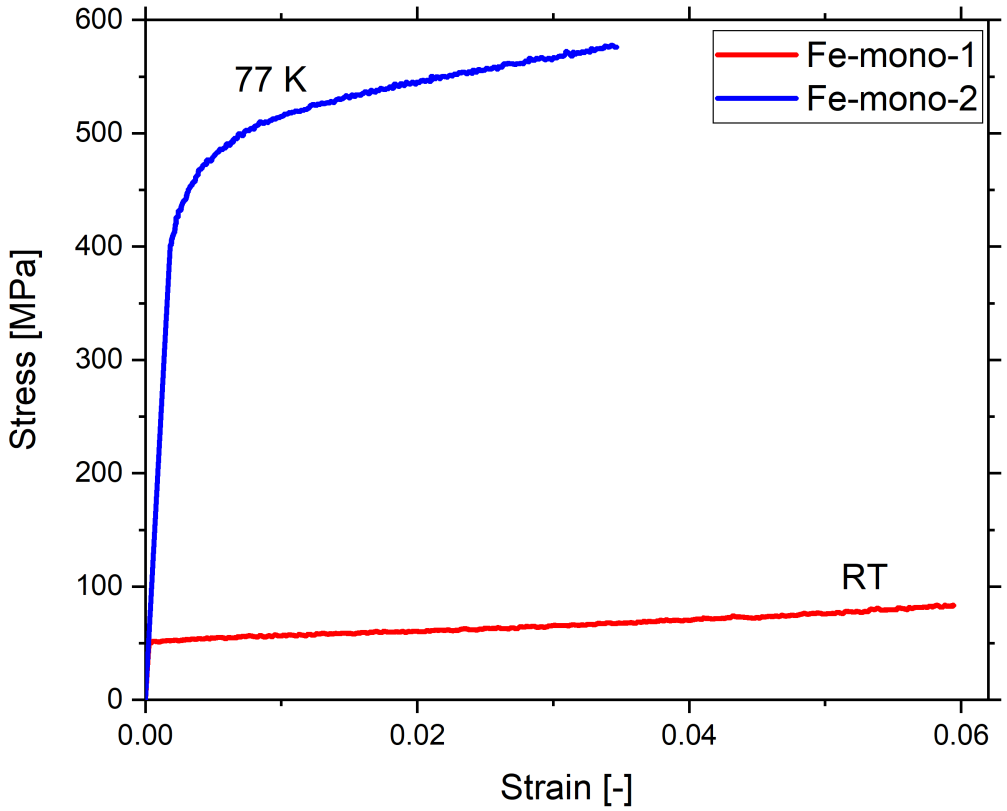

Figure 6.12: The engineering stress-strain curves of the single-crystalline specimens Fe-mono-1 and Fe-mono-2 deformed at RT and 77 K, respectively.

7 Twinning in Cr and α-Fe

A majority of twins in chromium specimens were found on {112} planes sheared in the twinning sense. However, some misoriented regions were also observed on {112} planes sheared in the antitwinning sense, although they were much less prominent (Fig. 5.7). These misoriented regions agree with traces of the $(\bar{1}\bar{1}2)[\bar{1}\bar{1}\bar{1}]$ system, which is sheared in the antitwinning sense with the Schmid factor of 0.293 and traces of the $(211)[1\bar{1}\bar{1}]$ system sheared in the twinning sense with the Schmid factor of 0.288. The angular difference between these two systems is only 7°, and we cannot unambiguously identify the operative systems. The individual misoriented islands agree well with the system sheared in the antitwinning sense, while the overall direction of these islands matches closer the system sheared in the twinning sense. In order to investigate the structure of these thin misoriented regions sheared in the antitwinning sense, we have extracted a lamella from the area marked as LLP (Lamella lift-out position) in Fig. 5.7(a).

The TEM micrograph of the lamella is shown in Fig. 7.1(a). The AT region corresponds to the $(\bar{1}\bar{1}2)[\bar{1}\bar{1}\bar{1}]$ traces marked by the orange dashed line in Fig. 5.7(a), and M represents matrix. The red circles mark the areas from which the Selected Area Electron Diffraction (SAED) patterns were taken. The SAED pattern from the red circles is shown in Fig. 7.1(b). We show them as one picture since they are the same in all red-circled areas. Fig. 7.1(c) and 7.1(d) show simulated SAED patterns for a structure with a twin and a high-energy stacking fault created by shearing in the opposite sense with the same magnitude of applied shear (the simulation cell is shown as an inset in the upper right corner). The green circles in Fig. 7.1(b), 7.1(c) and 7.1(d) mark the same positions in the reciprocal space. The simulation suggests that if the region was sheared in the antitwinning sense and the high-energy fault was stable, the SAED pattern would change to that in Fig. 7.1(c). However, this is not the case and the diffraction spots in Fig. 7.1(b) correspond to a regular twin. The same observation was done on niobium single crystal with twins caused by antitwinning shear [241].

To reconcile these TEM observation, atomistic simulation in our group were made to investigate in detail the stability of multilayer stacking fault produced by uniform shear. Even though dislocations in bcc metals generally do not dissociate into partial dislocations [242], there is evidence that the dissociated dislocations in multilayer stacking faults may be stable under stress [243–245]. The $1/2\langle 111\rangle$ screw dislocation in bcc metals can dissociate into three $1/6\langle 111\rangle$ partial dislocations [246–248] on three parallel neighboring {112} planes. Nowadays, it is generally accepted that shearing the crystal in the twinning direction leads to easy glide of the screw segments of the dislocations and nucleation of twin embryos. In contrast, the

shear in the antitwinning direction requires larger shear stress to form the multilayer stacking fault [249].

In Fig. 7.2 the black dots represent the atoms in ideal lattice positions, the orange line the $(\bar{2}11)$ twinning plane, grey circles the original position of atoms in the region to be twinned and the orange dots the positions of these atoms after twinning. The twinning shear is applied by displacing atoms in successive $(\bar{2}11)$ planes by the 1/6[111] Burgers vector relative to the atoms in the previous adjacent plane. This is represented by the red-filled region and red arrows. After the 1/6[111] partial dislocations pass under the twinning plane, the orange twinned region is created. We call this direction of shear the twinning direction. However, the same twin can be obtained if the region below the twinning plane is sheared in the opposite direction by a series of $-1/3$[111] partial dislocations, which is depicted as the blue region. In this case, the elementary displacements are twice as large compared to those corresponding to the shear applied in the twinning direction. Atomistic simulations show that the displacement in the antitwinning direction is less energetically favorable than displacement in the twinning direction, it could potentially explain the misoriented lamellae along the traces of $(\bar{1}\bar{1}2)$ plane in Fig. 5.7(a).

In order to investigate under which conditions the twin can be formed by uniformly applied shear stress, we use atomistic simulations to determine the energy barrier that is necessary to shear a bcc crystal in the twinning or antitwinning direction. These studies are made for one and more stacking faults generated on adjacent planes. Molecular statics was employed with the latest formulation of the Bond Order Potentials for Cr and α-Fe developed by Lin et al. [36,37]. The orthogonal simulation cell had periodic boundary conditions in x and z direction. In the remaining y direction, the simulation block was divided into outer region containing seven atomic planes on each side and inner region with 32 atomic planes. A planar stacking fault was placed in the middle of the inner block and every above-lying plane was sheared by a fault vector with varied magnitude in the 1/2[111] direction. In this way, a uniform shear was utilized to create stacking faults, followed by conjugate gradient minimization of the energy. In this calculation, the atoms in the inner region were relaxed in the perpendicular direction to a fault plane, while the atoms in the outer region were fixed. For further details, see Ref. [241]. The magnetic ground state in Cr, as described in Section 1.3, is not properly described by empirical potentials, or DFT [250]. However, even the BOP for Cr is non-magnetic. The internal magnetic order in α-Fe is treated correctly as a collinear ferromagnet [37], but overestimates the magnitudes of magnetic moments ($2.89\mu_B$ instead of $2.22\mu_B$ [251]). First, the minimum number of layers with metastable stacking fault corresponding to the twin was identified. This was found to be 2 for Cr and 3 for α-Fe for faults on {112} planes. The fault on {123} plane in α-Fe was found to be stable only for 2 layer configuration[1]. This stability was confirmed by full relaxation of atomic positions in the region surrounding the created stacking fault. Shearing the crystal in the $(\bar{2}11)$ plane in the [111] direction is consistent with the twinning shear as shown by the arrow in Fig. 7.3. Similarly, shearing the crystal on the $(\bar{2}\bar{1}3)$ plane in the [111] direction is consistent with the twinning shear. This shear causes the crystal to undergo a series of states from A, through B $\rightarrow$ C $\rightarrow$ D $\rightarrow$ E $\rightarrow$ F to

[1]Only configurations with 1 to 4 layers were tested.

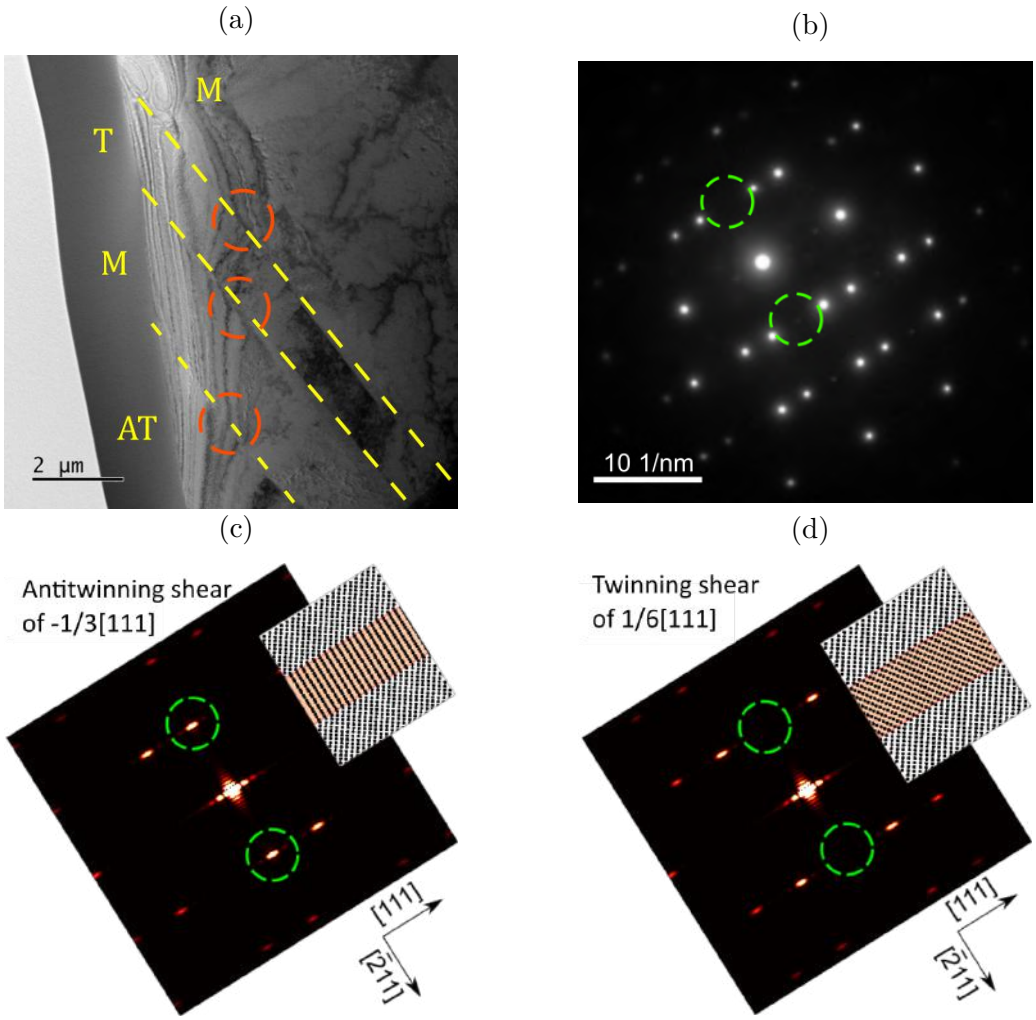

Figure 7.1: Comparison of diffraction contrast images taken from the misoriented region shown in Fig. 5.7(a), measured diffraction spot patterns and simulated spot patterns: (a) TEM micrograph from the lamella lifted-out from the misoriented region on Fig. 5.7(a) marked as LLP. Yellow dashed lines separate the differently oriented regions. AT denotes the region with traces of {112} planes sheared in the antitwinning sense, T denotes the region with traces of {112} planes sheared in the twinning direction, M marks the matrix. Orange circles represent the regions from which the SAED patterns were taken. (b) representative SAED pattern from TEM representing all regions inside orange circles (camera length 40 cm, [110] zone). (c) and (d) are simulated SAED patterns of the cells sheared locally in the antitwinning and twinning sense, respectively. Green circles in (b), (c), and (d) mark the same positions in all three images.

A', where the states A and A' represent the perfect lattice. The opposite sense of shearing the crystal in the $[\bar{1}\bar{1}\bar{1}]$ direction constitutes the antitwinning shear. This transforms the crystal through the states in the opposite order (A' $\rightarrow$ F $\rightarrow$ E $\rightarrow$ D $\rightarrow$ C $\rightarrow$ B $\rightarrow$ A). Here, the position C represents the twin, while B, D, E, F are intermediate states of the deformation. Clearly, the Generalized Stacking Fault Energy (GSFE) profile in Fig. 7.3(a) is asymmetric with the shear direction, which

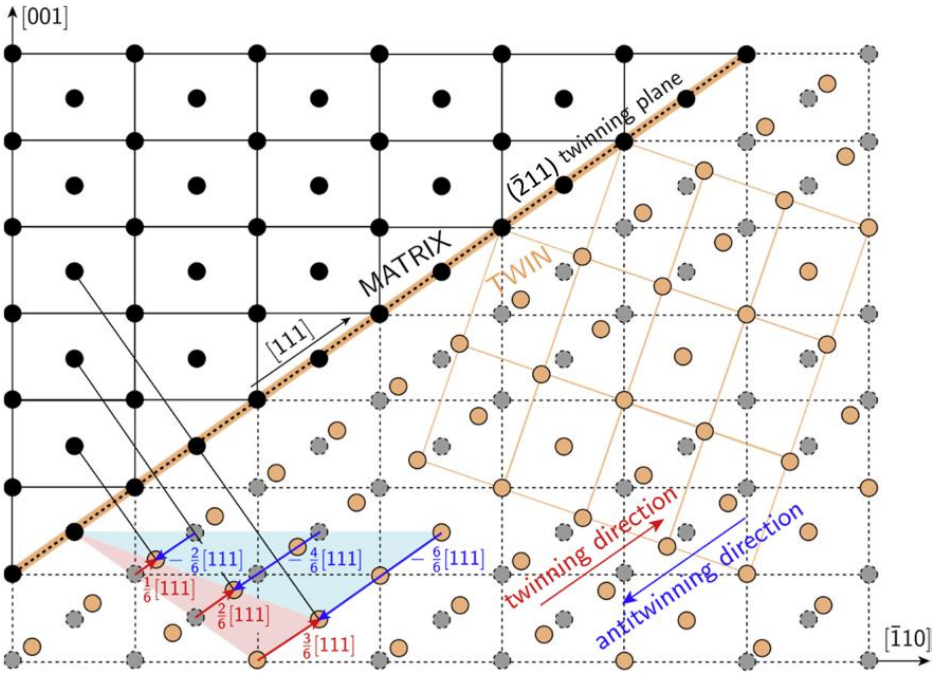

Figure 7.2: Schematic illustration of twin formation in the lower part of the crystal by the application of positive (twinning) shear with the relative atomic displacements of 1/6[111] (red region), and by negative (antitwinning) shear with the relative displacements of −1/3[111] (blue region).

constitutes the twinning-antitwinning asymmetry. If the crystal in the state C is relaxed, a minimum is found[2] and this minimum corresponds to a metastable twin boundary. This state is reached by applying twinning shear in the [111] direction with magnitude of $\lambda = 1/6$ or oppositely by applying the antitwinning shear in the $[\bar{1}\bar{1}\bar{1}]$ direction with magnitude of $\lambda = 1/3$ (as shown in Fig. 7.3(a) and illustrated in Fig. 7.2 by the red and blue arrows). Clearly, reaching the C state by the twinning shear requires overcoming a lower energy barrier than by the antitwinning shear.

In order to compute the twinning stress necessary to reach the state C, we define the twinning stress as the maximal slope computed in the twinning direction as

$$\sigma_T = \max\left(\frac{\partial \gamma_{A\to A'}}{\partial \boldsymbol{t}}\right), \tag{7.1}$$

where the $\boldsymbol{t} = \lambda a/2[111]$ is the fault vector displacement, and a is the lattice parameter. Similarly to the Eq. (7.1), the antitwinning stress σ_{AT} is defined as maximum slope in the opposite direction (A' → A), i.e. $\sigma_{AT} = \max(\partial\gamma_{A'\to A}/\partial\mathbf{t})$. These stresses are very large, which agrees with the fact that twins are very unlikely to nucleate homogeneously. In fact, they are formed at preexisting defects acting as stress concentrators, such as immobile dislocations [252]. According to Harding [112,253], the experimental twinning stress in α-Fe at 77 K is 0.39 GPa. This is further confirmed by Biggs et al. [113] and Edmonton [254] who report similar results. A similar study

[2]For faults on {112} plane in Cr with two and more stacking faults, for faults on {112} plane in α-Fe with three and more stacking faults and for 2 stacking faults on {123} planes in α-Fe.

about creation of multilayer faults in bcc metals is presented by Ojha et al. in [255] and α-Fe in [256]. Ogata et al. [257] studied the profile of unrelaxed stacking fault energy in fcc and bcc metals by the DFT.

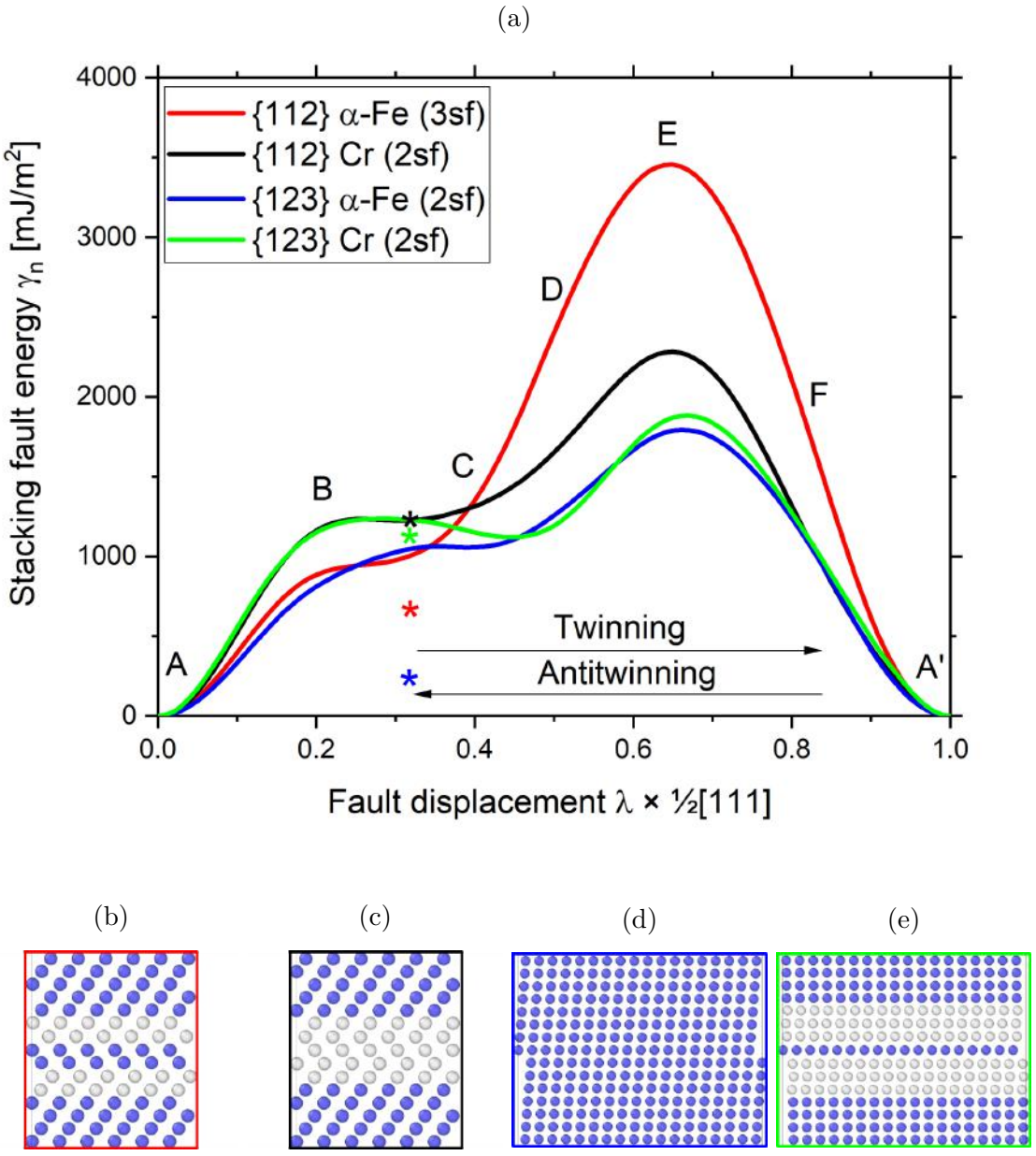

Figure 7.3: (a) GSFE energy profiles of for multilayer stacking faults created in the twinning and antitwinning sense on the {112} plane in α-Fe (red curve), {112} plane in Cr (black curve),{123} plane in α-Fe (blue curve), and {123} plane in Cr (green curve). The asterisks represent the energies of twin boundaries obtained by full atomic relaxations. Relaxed atomic structure of: (b) three-layer stacking fault on the {112} plane in α-Fe, (c) two-layer stacking fault on the {112} plane in Cr, (d) two-layer stacking fault on the {123} plane in α-Fe, (e) two-layer stacking fault on the {123} plane in Cr.

Since the nucleation of twins is a thermally activated process, we argue that the likeliness of nucleation of twins in the antitwinning sense can be expressed as a ratio of antitwinning to twinning stress σ_{AT}/σ_T. Due to the inherent twinning-antitwinning symmetry, this ratio can be computed for all bcc metals and is always larger than one. Low σ_{AT}/σ_T ratio suggests that nucleating twins by the antitwinning shear is likely (albeit most twins will be created by shear applied in the twinning sense). On the other hand, large ratio of σ_{AT}/σ_T suggests that the creation of twins by the antitwinning shear is improbable. Based on the calculations, the twinning and antitwinning stress necessary for the creation of {112} two-layer stacking fault in chromium by homogeneous shear is 33.7 and 40.0 GPa ($\sigma_{AT}/\sigma_T = 1.19$), respectively and the stresses for the {112} three-layer stacking fault in α-Fe are 25.8 and 63.2 GPa ($\sigma_{AT}/\sigma_T = 2.45$). The resulting atomic structure for {112} twins in α-Fe and Cr are shown in Fig. 7.3(b) and 7.3(b), respectively. The GSFE profiles of creating a stacking fault on {123} planes in α-Fe and Cr suggest that it is easier to create such fault. However, atomic structure of the relaxed stacking fault in α-Fe and Cr does not constitute a twin, as shown in Fig. 7.3(d) and 7.3(e), respectively. The relaxed structure of two-layer stacking fault in α-Fe shown in Fig. 7.3(d) is reminiscent of slightly sheared bcc structure and energy of such structure is also very low (asterisk in Fig. 7.3(a)). The same two-layer stacking fault in Cr (Fig. 7.3(e)) after relaxation represents a high-energy structure which also does not constitute a twin.

The ratios suggest that chromium is likely to form twins on {112} planes by antitwinning shear, while such twins on {112} in α-Fe are almost impossible to nucleate. These results agree very well with experiments in Sections 5.1 and 6.1. The shear stress required to produce twins on {123} planes and the σ_{AT}/σ_T ratio in α-Fe are smaller compared to the stress and ratio required to produced a twin on {112} planes. However, the process of growth of such twins may be different and more difficult that that of {112} twins. More in-depth analysis of {112} stacking faults created by twinning and antitwinning shear also in other bcc metals is available in our publication Gröger et al. [241].

List of symbols

Symbol	Meaning	Equation
Latin symbols		
$\boldsymbol{t}$	Fault vector	(7.1)
Greek symbols		
γ	Shear strain	(7.1)
μ_B	Bohr magneton	
σ_{AT}	Antitwinning stress	
σ_T	Twinning stress	(7.1)

8 Magnetic states of Cr after plastic deformation

Magnetism in chromium single crystals was investigated by the means of vibrating sample magnetometry and neutron scattering. The results show that the single-**Q** state, where the magnetic ordering can be characterized by a single wavevector, can be prepared by the field cooling method described by Golovkin et al. [174], Werner et al. [175] and others [172, 258, 259]. The single-**Q** state can be characterized to a certain extent by measuring the magnetic susceptibility along the three ⟨100⟩ directions of which one is parallel to the wavevector and two perpendicular to it. This was demonstrated in Section 4.3. The magnetic susceptibility, a measure of how easily a material can be magnetized in an external magnetic field, will be lower when measured parallel to the spins. Furthermore, in the single-**Q** state, the change of magnetic susceptibility across the spin-flip temperature T_{SF} is readily observable. The preparation of the single-**Q** state was also verified by the magnetic neutron scattering, which shows that a majority of specimens were in the single-**Q** state. However, less intense reflections corresponding to other spin density waves were observed. The presence of other SDWs, albeit much weaker in the intensity, suggests that the field cooling process did not fully transform the magnetic order in the specimen. The magnetic state of the field-cooled specimens that were predeformed at room temperature tend to favor the $(1 \pm \delta, 0, 0)$ spin density wave. However, the magnetic state is largely inconsistent between the specimens.

The magnetic neutron scattering of the specimens deformed at 77 K reveals that the magnetic state corresponds to the single-**Q** state described by the $(0, 1 \pm \delta, 0)$ SDW, which would be created by field cooling in the [010] direction. All three specimens deformed at 77 K were field-cooled in different ⟨100⟩ directions, and we would expect their initial state to be similar to the predeformed specimens. One could expect the final magnetic state after the plastic deformation at 77 K to be similar to the stress-cooled state, as elastic deformation precedes and is present during the plastic deformation. All of these assumptions are, however, wrong, as the final state is the perfect single-**Q** state. To the best of our knowledge, this behavior has not been reported in the literature, and unfortunately remains poorly understood.

8.1 Prediction of magnetically dead regions in Cr

We have made further magnetic neutron scattering experiments to test the hypothesis of Bienvenu et al. [11], that the glide of the 1/2[111] screw dislocations on {110},

{112} and {123} atomic planes creates magnetic faults. This is the result of the magnetic frustration, which is due to the fact that the 1/2[111] vector does not connect identical spins (is not the translation vector from the point of view of the magnetic structure). The fault region is characterized by a negligible magnitude of the atomic magnetic moment. Furthermore, a dislocation creating such magnetic fault would have to be followed by another dislocation of the same type to close the magnetic fault, making it effectively a superdislocation with ⟨111⟩ Burgers vector. We have simulated the expected magnetic neutron diffraction patterns by calculations described in Section 8.2, based on the DFT results obtained by Bienvenu et al. [11]. The infinite magnetic fault is shown Fig. 8.1, where antiferromagnetic order sets in away from the fault. Fig. 8.1(a) shows an infinite magnetic fault in chromium along the {110} plane, where the differently sized circles represent a different magnitude of magnetic moment. The touching circles have value of magnetic moment of $1.1\mu_B$, while the smallest ones have value of $0.2\mu_B$. Similarly, Fig. 8.1(b) shows an infinite magnetic fault on the {112} plane, but in this case, the smallest circles represent a zero magnetic moment.

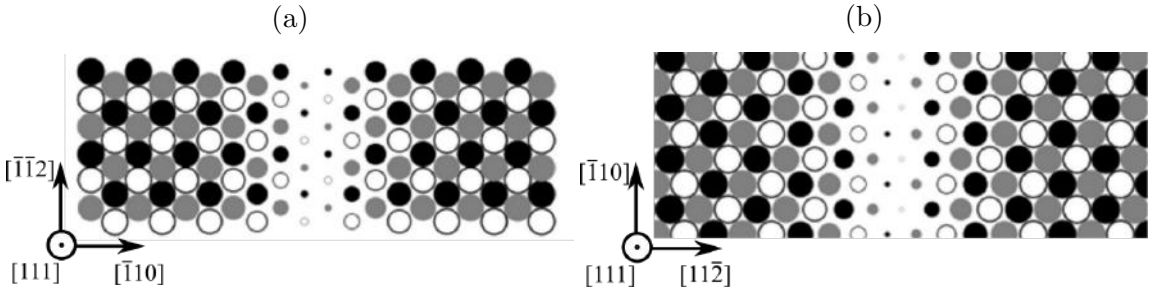

Figure 8.1: Magnitude of the magnetic moments in an infinite magnetic fault in a form of differently sized circles. Magnetic fault on: (a) {110} plane, (b) {112} plane. The touching circles represent the magnetic moment of $1.1\mu_B$, whereas the smallest circles represent valus of $0.2\mu_B$ and zero in (a) and (b), respectively. Figures adapted from Bienvenu et al. [11].

8.2 Simulation of neutron diffraction patterns

The following section describes the simulation of magnetic neutron scattering used in this thesis. The neutron scattering is a type of Bragg scattering, which is the coherent elastic scattering of waves by the crystal. For an ideal infinite crystal with the basis vectors $\mathbf{a}_1$, $\mathbf{a}_2$ and $\mathbf{a}_3$, the scattering with constructive interference can only occur at the diffraction vectors of the reciprocal lattice:

$$\mathbf{q} = h\mathbf{a}_1^* + k\mathbf{a}_2^* + l\mathbf{a}_3^* \tag{8.1}$$

where h, k and l are integers, and $\mathbf{a}_1^*$, $\mathbf{a}_2^*$ and $\mathbf{a}_3^*$ the reciprocal lattice vectors[1]. The approximation of the nuclear neutron scattering assumes that the magnitude of the

[1]The reciprocal lattice vectors are defined in terms of the Kronecker delta: δ_{ij} as $\mathbf{a}_i^* \cdot \mathbf{a}_j^* = \delta_{ij}$

incoming wave is the same throughout the specimen. The attenuation of the neutron beam and multiple scattering is neglected, therefore the specimen should be fairly small.

The structure factor $F(\mathbf{q})$ describes how a material scatters the incident wave. It provides the distribution of the scattered density by all waves with the wavevector $\mathbf{q}$ that are scattered by the atoms of the unit cell, summed over all atoms j in the simulation box. The nuclear structure factor is given by the complex-valued function:

$$F_n(\mathbf{q}) = \sum_{j=1}^{N} b_j e^{2\pi i(\mathbf{q}\cdot\mathbf{r}_j)} \cdot W_j(\mathbf{q}), \tag{8.2}$$

where b_j is the scattering length, a constant dependent on the material and an isotope describing the interference of the nuclei of the material with the passing neutron. The $\mathbf{r}_j$ represents a vector of atom position in the simulation box. The W_j is the Debye-Waller factor describing the attenuation of the coherent neutron scattering by the thermal motion and is expressed as [260, 261]:

$$W_j(\mathbf{q}) = e^{-2B_j s^2}. \tag{8.3}$$

Here the B_j is an experimentally measured constant, and s is described as

$$s = \frac{\sqrt{q_1^2 + q_2^2 + q_3^2}}{4\pi}, \tag{8.4}$$

where q_1, q_2 and q_3 are the Cartesian components of the diffraction vector $\mathbf{q}$. The intensity of the nuclear scattering at diffraction vector $\mathbf{q}$ can be calculated as $A|F_n(\mathbf{q})|^2$, where A is an absorption correction that depends on the measurement geometry and on the linear absorption coefficient of the sample [262]. If the above-mentioned conditions are met, the intensity of the diffracted beam $I_n(\mathbf{q})$ is proportional to the amplitude of the diffracted wave squared (more precisely squared modulus, since the amplitude is a complex number) for the individual reflections [263]:

$$I_n(\mathbf{q}) \propto |F_n(\mathbf{q})|^2. \tag{8.5}$$

The intensity of magnetic scattering can be calculated similarly to the nuclear neutron scattering described above. The magnetic structure factor takes the form of:

$$F_m(\mathbf{q}) = N_e^2 \sum_{j=1}^{N} A_{Mj}(\mathbf{q}) e^{2\pi i(\mathbf{q}\cdot\mathbf{r}_j)} \cdot W_j(\mathbf{q}) \tag{8.6}$$

where N_e is the neutron-electron coupling constant, that is expressed as $\mu_B e^2/2m_e c^2$ where μ_B is the nuclear Bohr magneton, e is electron charge, m_e electron mass, and c the speed of light[2]. This constant is negative due to the negative value of nuclear Bohr magneton, however after raising to the second power in Eq. (8.6) it becomes

[2]This is the most common description in the literature, but others exist as well. For reference, see [264–267] or [268, p. 59]

positive. The magnetic Bragg scattering amplitude $A_{Mj}(\mathbf{q})$ is further described as [269]:

$$A_{Mj}(\mathbf{q}) = f_{Mj}(\mathbf{q})\boldsymbol{\sigma} m_{\perp j}(\mathbf{q}), \tag{8.7}$$

where $\boldsymbol{\sigma}$ is the neutron spin operator expressed as a simple 2×2 Pauli matrix, and $m_{\perp j}(\mathbf{q})$ a projection of the magnetic moment onto the plane of scattering. The magnetic form factor $f_{Mj}(\mathbf{q})$ is the Fourier transform of the magnetization $M_j(\mathbf{r})$ of a single atom, where $\mathbf{r}$ is the atomic position in the simulation box and can be expressed as the volume integral [270]:

$$f_{Mj}(\mathbf{q}) = \int R^2(\mathrm{r}) j_l(\mathbf{q} \cdot \mathbf{r}) 4\pi r^2 dr. \tag{8.8}$$

The computation of the magnetic form factor requires expressing the radial part of an electron wave function in an atom $R(\mathbf{r})$ and the Bessel function j_l. Instead of calculating the integral in Eq. (8.8), it can be analytically approximated using the dipole approximation[3] as [271]:

$$f_{Mj}(\mathbf{q}) \simeq \langle j_0(s) \rangle + \frac{2 - g_J}{g_J} \langle j_2(s) \rangle, \tag{8.9}$$

where g_J is the Landé splitting factor. The expectation (average) values of the Bessel functions j_0 and j_2 are expressed as [272, 273]:

$$\langle j_0(s) \rangle = A_0 e^{-a_0 s^2} + B_0 e^{-b_0 s^2} + C_0 e^{-c_0 s^2} + D_0 \tag{8.10}$$

and

$$\langle j_2(s) \rangle = A_2 s^2 e^{-a_2 s^2} + B_2 s^2 e^{-b_2 s^2} + C_2 s^2 e^{-c_2 s^2} + D_2 s^2. \tag{8.11}$$

In these equations, s is described by Eq. (8.4) and the coefficients in Eq. (8.10) and (8.11) can be found for various materials in [271, pp. 454–456]. The values for Cr and α-Fe are summarized in Table 8.1.

Similarly to Eq. 8.5, the intensity of neutron magnetic scattering, $I_m(\mathbf{q})$, can be calculated as [262, 274]:

$$I_m(\mathbf{q}) \propto \langle 1 - (\hat{\mathbf{q}} \cdot \hat{\boldsymbol{\eta}}) \rangle^2 |F_m(\mathbf{q})|^2, \tag{8.12}$$

where $\hat{\boldsymbol{\eta}}$ represents the direction of the spins (fixed on all atoms here). The prefactor retains only the contributions of the wavevectors $\hat{\mathbf{q}}$ which are perpendicular to spins. The parameters used in the simulation of neutron scattering are described in Table 8.2 with units and references.

[3] Neglecting a spatial variation of the electromagnetic field over an atom or ion and replacing it by a field.

Table 8.1: The list of values of the parameters in Eq. (8.10) and (8.11) taken from [271, pp. 454–456].

Parameter	Cr	Fe	Parameter	Cr	Fe
A_0 [−]	0.1135	0.0706	A_2 [Å^2]	3.4085	1.9405
a_0 [Å^2]	45.199	35.008	a_2 [Å^2]	20.127	18.473
B_0 [−]	0.3481	0.3589	B_2 [Å^2]	2.1006	1.9566
b_0 [Å^2]	19.493	15.358	b_2 [Å^2]	6.802	6.323
C_0 [−]	0.5477	0.5819	C_2 [Å^2]	0.4266	0.5166
c_0 [Å^2]	7.354	5.561	c_2 [Å^2]	2.394	2.161
D_0 [−]	-0.0092	-0.0114	D_2 [Å^2]	0.0019	0.0036

Table 8.2: Values of the parameters used in equations to simulate the neutron scattering.

Parameter	Cr	Fe	Unit	Eq.	Ref.
b_j	3.6357	9.452	fm	(8.2)	[271, p. 446]
B_j	0.26	0.35	Å^2	(8.3)	[260]
N_e	-0.27×10^{-12}	-0.27×10^{-12}	cm	(8.6)	[262, 274]
g_J	2	2.09	[-]	(8.9)	[266, 275]

8.3 Simulated neutron diffraction patterns of magnetically dead regions

The simulation assumes the spin direction along [010], which corresponds to the LSDW single-**Q** state characterized by the $(0, 1 \pm \delta, 0)$ fundamental spin density wave. Therefore, the simulation describes the final magnetic state of the specimen deformed at 77 K. The simulation cell with the magnetic fault on the {110} comprises of 120 atoms, which is replicated 16 × 16 × 2 times in the x, y, z direction, respectively. The total number of atoms is 61 440 atoms. Similarly, the simulation of the magnetic fault on the {112} plane comprises also of 120 atoms replicated 20 × 20 × 2 times along the three axes. The total number of atoms is then 96 000. The atomic positions and the magnitudes of magnetic moments were obtained from DFT simulation of Bienvenu et al. [11], kindly provided to us by E. Clouet. It is imperative to mention that both the DFT and the simulation of neutron diffraction patterns are calculated at 0 K, while the experimental data obtained at PSI are measured at higher temperatures. Although we compare the same SDW states, the temperature difference may play a role. Due to crystal symmetry, all {110} planes are equivalent. Therefore, we have considered all these six {110} planes to simulate the magnetic neutron diffraction patterns from the faulted atomic block. The simulated magnetic neutron scatterings from the {110} planes are shown in Fig. 8.2. Similarly, twelve {112} planes exist in bcc crystals that are all crystalographically equivalent. The simulations of magnetic neutron diffraction patterns were thus made

by assuming that the magnetic fault may occur on all these planes. The simulated magnetic scattering patterns from {112} planes are shown in Fig. 8.3.

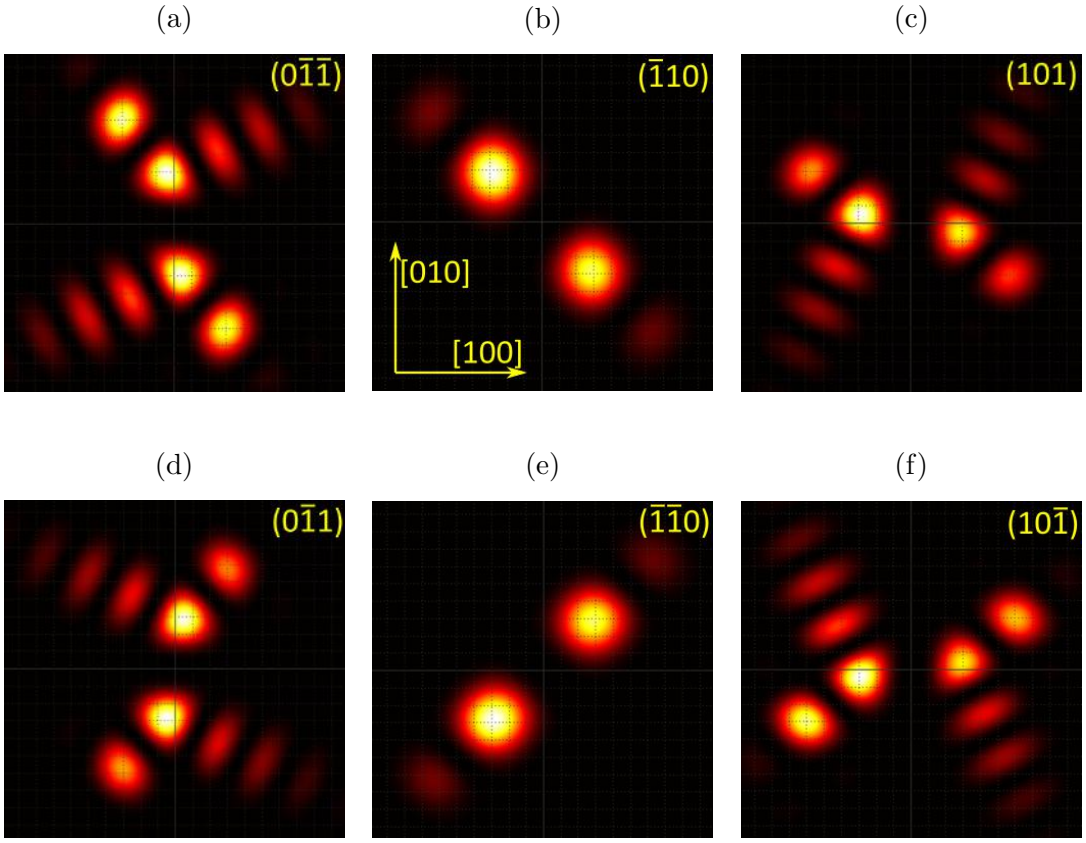

Figure 8.2: Simulations of symmetry-related diffraction patterns for {110} magnetic fault. Spin direction is $\mathbf{S} = [010]$, wavevector of SDW $\mathbf{Q} = [010]$ (i.e. LSDW state). Magnetic fault on: (a) $(0\bar{1}\bar{1})$ plane, (b) $(\bar{1}10)$ plane, (c) (101) plane, (d) $(0\bar{1}1)$ plane, (e) $(\bar{1}\bar{1}0)$ plane, (f) $(10\bar{1})$ plane.

Fig. 8.4(b) and 8.4(c) show superpositions of the neutron magnetic scattering of all {110} and {112} atomic planes, respectively, that were made with equal weights assigned to the individual diffractions from all {110} and {112} planes, as shown in Fig. 8.2 and 8.3, respectively. Fig. 8.4(a) shows the data from the neighborhood of [100] magnetic reflection that I have measured using magnetic neutron scattering at PSI at 10 K on the PSI 3 specimen. This measurement was done differently from those shown in Section 4.4. In this case, we used the so-called q-scans to resolve the reflections better. Q-scans are done with the 1D detector and acquired as line scans in the reciprocal space. This measurement is comprised of seventeen line scans from $0.96H$ to $1.04H$ ($H = [100]$), each line spanning from -0.14K to 0.14K ($K = [010]$) at $L = 0$ ($L = [001]$). The reflections in Fig. 8.4(a) belong to the $[1, \delta, 0]$ and $[1, -\delta, 0]$ on the top and bottom, respectively.

It is evident that the simulated diffraction patterns do not agree with the experimental measurements. The reason can be that not all symmetry-related faults are present with the same probability in the studied volume. In this case, different

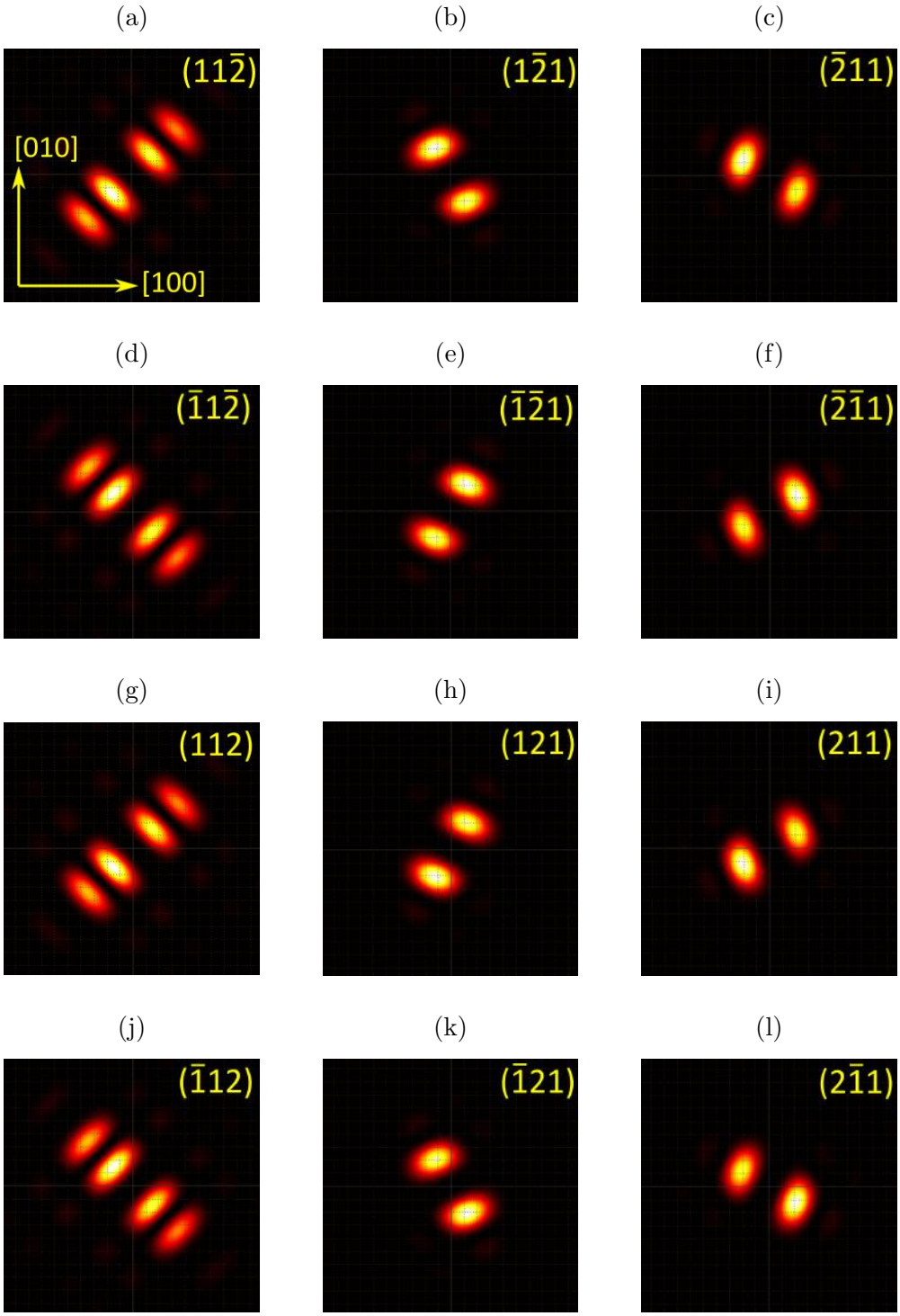

Figure 8.3: Simulation of symmetry-related diffraction patterns for {112} magnetic faults. Spin direction is $\mathbf{S} = [010]$, wavevector of SDW $\mathbf{Q} = [010]$ (i.e. LSDW state). Magnetic faults on: (a) (11$\bar{2}$) plane, (b) (1$\bar{2}$1) plane, (c) ($\bar{2}$11) plane, (d) ($\bar{1}$1$\bar{2}$) plane, (e) ($\bar{1}\bar{2}$1) plane, (f) ($\bar{2}\bar{1}$1) plane, (g) (112) plane, (h) (121) plane, (i) (211) plane, (j) ($\bar{1}$12) plane, (k) ($\bar{1}$21) plane, (l) (2$\bar{1}$1) plane.

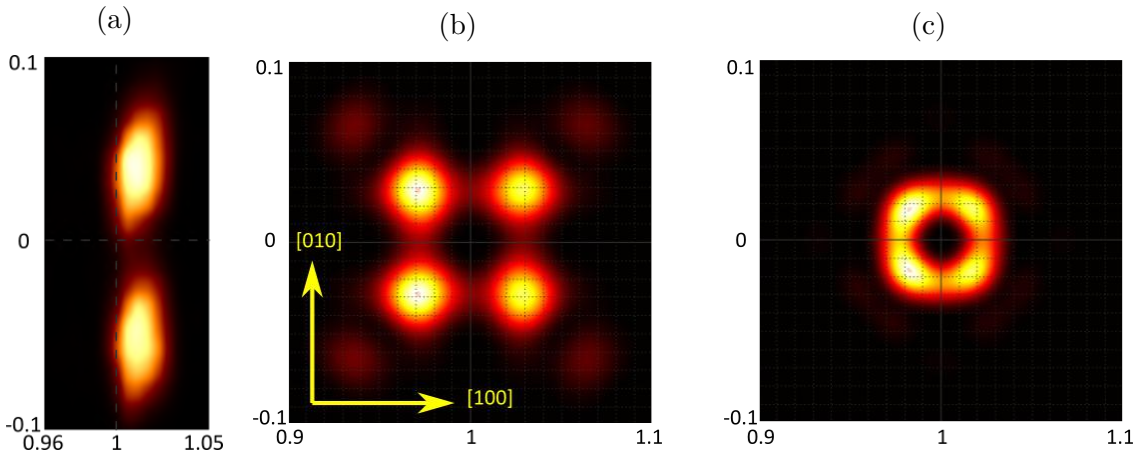

Figure 8.4: (a) Neighborhood of the [100] magnetic reflection obtained from neutron magnetic scattering. Visible reflections are $[1, \delta, 0]$ and $[1, -\delta, 0]$ on the top and bottom, respectively. Superposition of all simulated symmetry-related (b) {110} and (c) {112} magnetic diffraction patterns described in the text. Spin direction is $\mathbf{S} = [010]$, SDW wavevector $\mathbf{Q} = [010]$, i.e. LSDW state.

weights would have to be assigned to the patterns in Fig. 8.2 and 8.3. However, it is not clear how these weights could be determined from experiments. The volume fraction of the magnetic faults to the remaining material would likely be very small and difficult, if not impossible, to measure.

Furthermore, the TEM study of the anomalous slip in Cr deformed at 77 K in Section 5.2.2 did not present any evidence of superdislocations with ⟨111⟩ Burgers vectors as hypothesized by Bienvenu et al. [11]. So far, we have not found any evidence that would support their conclusion, that deformed Cr single crystals contain magnetically dead regions separating dislocations with the same Burgers vectors. The stresses around the dislocation affect the magnetic ordering, but they do not seem to be large enough to produce magnetic faults as predicted in their paper.

We have further shown that the spin-flip temperature T_{SF} is influenced by the level of deformation to which the specimen was subjected. T_{SF} can be also influenced by addition of substitutional elements. De Oliviera et al. [276] showed that addition of 0.4 wt. % of vanadium to chromium will lower T_{SF} to approx. 69 K and T_{SF} disappears completely at concentration of 0.69 wt. % of vanadium, leaving only the TSDW phase stable. Bacon and Cowlam [101] demonstrated that addition of 0.5 wt.% of Re stabilizes the simple antiferromagnetic structure between the TSDW and the paramagnetic phase. They further show on crushed chromium powder that deformation broadens T_{SF} to a temperature range in which both LSDW ant TSDW are stable. The deformation also introduces a simple antiferromagnetic structure, which is stable between the TSDW and the paramagnetic phase. The Néel temperature T_N also increases with increasing deformation, but according to Bacon and Cowlam, the transition is sharp. On the other hand, T_N decreases with increasing level of vanadium content [276]. The broadening of T_{SF} into a temperature range agrees with our results. However, as our deformation was not so severe compared Bacon and Cowlam, the changes to T_{SF} are less pronounced.

List of symbols

Symbol	Meaning	Equation
Latin symbols		
A	Absorption correction coefficient	
A_0, a_0	Parameter	(8.10)
A_2, a_2	Parameter	(8.11)
A_{Mj}	Magnetic Bragg scattering amplitude	(8.7,8.6)
$\mathbf{a}_1^*, \mathbf{a}_2^*, \mathbf{a}_3^*$	Reciprocal lattice vectors	(8.1)
B_0, b_0	Parameter	(8.10)
B_2, b_2	Parameter	(8.11)
b_j	Scattering length	(8.2)
B_j	Experimental constant	(8.3)
c	Speed of light in vacuum	
C_0, c_0	Parameter	(8.10)
C_2, c_2	Parameter	(8.11)
D_0	Parameter	(8.10)
D_2	Parameter	(8.11)
e	Electron charge	
F_n	Nuclear structure factor	(8.2)
F_m	Magnetic structure factor	(8.6, 8.12)
f_{Mj}	Magnetic form factor	(8.6, 8.8, 8.9)
g_J	Landé splitting factor	8.9
h, k, l	Plane indices	(8.1)
I_n	Intensity of nuclear neutron scattering	(8.5)
I_m	Intensity of magnetic neutron scattering	(8.12)
j_l	Bessel function	(8.8)
j_0, j_2	Expectation values of the Bessel functions	(8.9, 8.10, 8.11)
m_e	Electron mass	
$m_{\perp j}$	Projection of a magnetic moment onto scattering plane	(8.12)
N_e	Neutron-electron coupling constant	(8.6)
$\mathbf{Q}$	Wavevector	
$\mathbf{q}$	Scattering vector	(8.1)
q_1, q_2, q_3	Cartesian components of the scattering vector	(8.4)
$R(\mathrm{r})$	Radial part of electron wave function	(8.8)
$\mathbf{S}$	Spin direction	
T_{SF}	Spin-Flip temperature	
W_j	Debye-Waller factor	(8.2, 8.3)
Greek symbols		
δ_{ij}	Kronecker delta	
$\boldsymbol{\eta}$	Spin direction	(8.12)
λ	Wavelenght	
μ_B	Nuclear Bohr magneton	
$\boldsymbol{\sigma}$	Neutron spin operator	(8.7)

9 Discussion

9.1 Magnetic measurements on α-Fe

The hysteresis curves measured by VSM on polycrystalline α-Fe showed, as anticipated, that with more plastic deformation imposed on the material, the number of domain wall pinning sites increases. This effect is dominant when the probing magnetic field is parallel with the deformation axis and results in increasing slope of the hysteresis curve (larger susceptibility relative to unstressed specimens). When the direction of the probing field is perpendicular to the deformation axis, this effect is smaller and the slope of the hysteresis curve changes in the opposite direction (smaller susceptibility). Furthermore, if the step of the VSM measurement is fine enough, it is possible to observe the release of domain walls from the pinning sites.

The Kerr microscopy revealed that magnetic domains in single-crystalline specimens are larger compared to those in polycrystalline specimens. Interestingly, twins in the material create effective barriers for the domains in some cases, but they may also serve as nucleation sites for other magnetic domains, as shown in Fig. 4.7(b). Lai et al. found that twins in NiMnGa shape memory alloy transfer the magnetic domains through the twins according to the rotation of crystal lattice in the twin [277]. On the other hand, if the twins are very thin (tens to low hundreds of nm), the magnetic domain can pass through the domain structure [278]. Nonetheless, the effects observed here might appear only near the surface, since the depth resolution of Kerr microscopy is approximately 50 nm [279]. Bozorth [211] states that the maze-like domain structure in Fig. 4.4 is characteristic of a deformed material and the tree-like domain structure in Fig. 4.5 is characteristic of an undeformed material. Nonetheless, both specimens were strained, but at different temperatures and to different amounts. Fe-mono-1 specimen shown in Fig. 4.4 was strained at RT to approx. 6% and Fe-mono-2 specimen, shown in Fig. 4.5, was prestrained to 1.7% at RT and subsequently deformed at 77 K to further 2.5%. The results may indicate, that low-temperature slip have larger effect on magnetic domains than slip at RT.

9.2 Compression tests on Cr

The mechanism of low-temperature plastic deformation of UHV-annealed high-purity Cr single crystals depends on the orientation of the applied load as well as on whether the sample was predeformed at room temperature, thus creating mobile dislocation network. According to Fig. 5.9, the samples compressed close to the [001] direction exhibit homogeneous slip on slip systems with the highest Schmid

factors. In this region, predeformation does not alter the mechanism of plastic deformation. Similar behavior is observed for the specimen 7* predeformed at room temperature and subsequently compressed at 77 K in the center-triangle direction closer to the [001]-[011] edge. However, specimen 3, which was not predeformed at room temperature, exhibited a combination of composite slip and twinning.
The specimen 4* deformed in the direction corresponding to the center of the stereographic triangle showed anomalous slip on the $(0\bar{1}1)$ plane. For loading directions close to the [011]-[$\bar{1}$11] edge of the stereographic triangle, the specimens deformed predominantly by twinning on the $\{112\}\langle 111\rangle$ systems, irrespective of whether or not they were predeformed at room temperature. The specimens that fractured by cleavage also exhibited the formation of twins on {112} planes sheared in the antitwinning sense. The intersections of twins were found to lead to the nucleation of cracks and subsequent failure by cleavage. Our results agree with Marcinkovsky and Lipsitt [121], who state that twins in chromium are of the $\{112\}\langle 111\rangle$ type. Sameljuk et al. [124] states that cleavage is along {100} planes and delamination occurs along {112}, which is also in agreement with our observations.

The anomalous slip in the samples compressed in the direction corresponding to the center of the stereographic triangle was further reconciled using bright-field STEM imaging in the $[0\bar{1}1]$ zone combined with the $\mathbf{g}\cdot\mathbf{b}$ analysis in six different diffraction conditions. They reveal the presence of intersecting $1/2\langle 111\rangle$ screw dislocations. The stability of this junction at high stresses and low temperatures was further investigated by molecular statics simulations employing the recently developed BOP for Cr in the non-magnetic state. This state-of-the-art model that treats Cr as non-magnetic metal is applicable to the triple-$\mathbf{Q}$ state of our samples. It contains a large number of magnetic domains with all three $\langle 100\rangle$ orientations of the SDW wavevector $\mathbf{Q}$, which results in magnetically isotropic state above a certain length scale corresponding to the size of magnetic domains. The atomistic simulations show that the intersecting $1/2[111]$ and $1/2[1\bar{1}\bar{1}]$ screw dislocations spontaneously form the [100] screw junction, as expected from linear elasticity. More importantly, the application of external load in the [$\bar{2}$38] center-triangle direction shows that this junction remains stable up to very high stresses, where the stored energy is relaxed by moving the dislocation network on the common $(0\bar{1}1)$ plane. A different slip p;ane is predicted from atomistic simulations on single dislocations, an thus the simulations of dislocation junctions are necessary to understand the mechanism of anomalous slip. Instead, interactions between dislocations play an essential role and lead to the formation of strong $\langle 100\rangle$ junctions that cannot be easily broken by the external load. Our results thus provide evidence that the anomalous slip in Cr is governed by the co-planar double slip model proposed originally by Matsui and Kimura [70].

Similar experimental results were reported by Hsiung et al [64]. in molybdenum at room temperature with the high strain rate of 1 s^{-1} or by Louchet and Kubin [66] in niobium at 50 K. According to the literature, anomalous slip takes place only in pure metals and is suppressed by impurities. Bressers and Creten [61] investigated anomalous slip in vanadium single crystals with different levels of oxygen content (from 24 to 810 at. ppm). Their results shown that the morphology of surface markings belonging to anomalous slip change from finely distributed to coarse and

more separated surface markings.

We have also observed cracks along matrix/twin interfaces in Cr, but their morphology was different from those of α-Fe. The crack shown in Fig. 5.4(c) has a saw-like interface corresponding to the slip systems in the twinned region, whereas cracks in α-Fe appear to be straight. Transgranular cracks in the twinned region were also observed, as shown in Fig. 5.4(b). Cracks were also found to originate at the intersection of two twins as shown in Fig. 5.8(a).

9.3 Compression tests on α-Fe

The analysis of compression tests on the polycrystalline specimens with large grains reveals that the primary deformation mechanism at 77 K is twinning regardless of the orientation of the loading axis. Apart from SEM and EBSD analysis, the twinning is also evident from the stress-strain curve in Fig. 6.1 that displays many load drops caused by the nucleation of twins. No slip markings were observed in the polycrystalline specimens, that were deformed at 77 K with or without predeformation at room temperature.

Furthermore, all the analyzed twins were produced by twinning shear, even though, in many cases, the Schmid factor was larger for twinning systems sheared in the antitwinning shear. The reason for their non-existence is attributed to a large σ_{AT}/σ_T ratio that favors twin formation on the {112} planes subjected to twinning shear. No twins were observed to form on {112} planes sheared in the antitwinning sense. We have, however, found one $(321)[1\bar{1}\bar{1}]$ lamella sheared in the twinning sense.

Watanabe [280] focused on slip in α-Fe and computed that macroscopic slip on {123} planes requires significant energy. This might suggest that {123} twins are easier to nucleate, but their growth, which is mediated by the dislocation motion, is energetically more demanding. To the best of our knowledge, there is no literature documenting {123} twinning systems in α-iron. This phenomenon is discussed in-depth in Chapter 7.

The compression tests on the single-crystalline specimens did not reveal any slip traces on the surface, which suggests that the specimens deformed by homogeneous slip. This behavior is, however, different from what Aono et al. [5] reported on approx. 1 mm single crystals in compression. He reported a combination of cleavage and twinning, while our results suggest homogeneous slip. We attribute this difference to different purity of tested specimens. Allen et al. [111] reported macroscopic slip on $(\bar{3}12)[111]$ and $(\bar{1}01)[111]$ systems in tension at 77 K. Altshuler and Christian [114] report compression tests at 77 K in both polycrystalline and single-crystalline specimens. In case of polycrystalline specimens with the mean grain diameter of 0.013 mm, they report the yield stress of approximately 690 MPa. This is in disagreement with yield stress measured on our specimen, which is approx. 140 MPa. This discrepancy can be at least partially explained by their less pure material (194 wt. ppm of impurities in their specimen vs 66 wt. ppm in our specimen), smaller grain size and slightly faster strain rate, which would cause larger yield stress. Furthermore, the reported stress-strain curves of their polycrystalline specimen do not show load drops associated with twinning as seen of Fig. 6.1. The

loading axis of their single crystal specimens was [$\bar{1}$49], which is approx. 2.5° from [$\bar{4}$ 11 26] loading axis of our single crystal specimens. Single crystals reported in our work are also more pure than those used by Altshuler and Christian. Nevertheless, the reported yield stress of 50 MPa is almost identical for specimen deformed at RT. However, their specimen shows some strain hardening, whereas ours show almost continual room temperature creep. Comparing the specimens tested at 77 K, Altshuler and Christian report yield stress of approx. 540 MPa, whereas the yield stress of our specimen was approx. 460 MPa. This discrepancy can be again explained by chemical purity of the specimens, prestrain of our specimens at RT, and about twice slower strain rate used in our experiments.

9.4 Tensile tests on α-Fe and Cr

We have attempted to perform tensile tests on both α-Fe and Cr specimens, but the specimens failed by brittle fracture before reaching the elastic-plastic state in all cases. We have decided to use a dog-bone specimen instead of a normal tensile specimen with screw head because of the lack of material. The flat side of the specimen is also advantageous for EBSD measurements, and slip trace analysis. The geometry of the dog-bone specimens used is shown in Fig. 9.1.

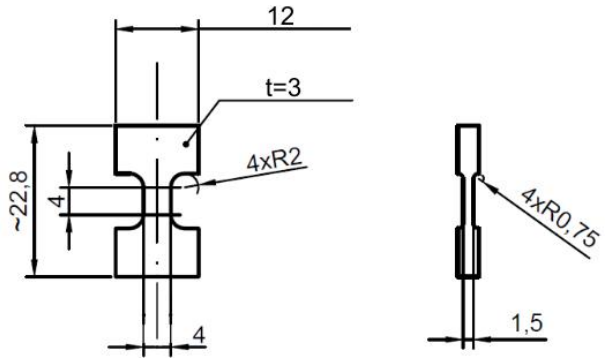

Figure 9.1: Schematic drawing of the tensile test specimen. All units are in mm.

The specimens were cut out of the source crystal by electro-erosive machining and carefully ground to remove any deformation and cracks caused by the electro-erosive machine. Subsequently, the specimens were electropolished in same way as described in Section 3.2. The chamber was filled with nitrogen vapor, thus the test temperature was slightly higher than in case of compression specimens (which were submerged in liquid nitrogen). The cross-head speed of the machine was 30 µm/min, which caused the plastic strain rate to be about 10^{-5} s^{-1}, similar to the compression specimens. The specimens' heads were clamped from two sides with clamps containing pyramidal protrusion to avoid sliding. Unfortunately, in the case of single-crystalline Cr specimen, the pyramidal protrusions acted as stress concentrators and the specimen failed by brittle fracture originating from one of these protrusions. The polycrystalline α-Fe specimen tested under the same conditions either failed in a same manner, or brittle fracture originated at a favorably oriented grain boundary. Tensile specimens from single-crystalline α-Fe were not made, as

they required too much material that is not available at the present. However, further growth experiments to produce large single crystals of iron are now under way at IPM.

10 Summary and future work

Following are the main achievements of this work that were discussed in detail in the previous chapters.

- Anomalous slip in chromium single crystals was demonstrated for the first time. The presence of $\langle 100 \rangle$ dislocation junctions was proven by the $\mathbf{g} \cdot \mathbf{b}$ analysis on micrographs acquired in TEM. Furthermore, the anomalous slip in Cr is confirmed by atomistic simulations done in our group, which show that it is governed by the co-planar double slip process of Matsui & Kimura [69] and Louchet & Kubin [66].

- The reason for the presence or absence of twins created by antitwinning shear in chromium and α-iron was elucidated. The presence of twins created by antitwinning shear depends on the ratio of stresses necessary to create multi-layer stacking faults in the antitwinning and twinning direction by uniform shear. This ratio is approximately twice as large for α-Fe compared to chromium, which explains why twins in α-Fe only form by the twinning shear.

- Misoriented lamellae on $\{123\}$ planes were observed in α-iron. However, these are scarce due to higher stresses necessary to move dislocations on $\{123\}$ planes compared to dislocations on $\{112\}$ planes. Nonetheless, according to calculations, shear stress required to nucleate these faults on $\{123\}$ planes by the twinning shear is smaller compared to the shear stress necessary to create a $\{112\}$ twin by antitwinning shear.

- Plastic deformation of Cr single crystals at 77 K promotes a single-$\mathbf{Q}$ state with the spin density wave along closest $\langle 100 \rangle$ crystal direction. This phenomenon has not been reported in the literature so far.

- Our neutron diffraction results do not support the conclusion of Beinvenu et al. [11], that dislocations in chromium give rise to magnetic faults. However, neutron diffraction is a statistical method and thus magnetic faults may not be found in the interaction volume with sufficient density to be revealed in diffraction patterns. So far, we have not found any evidence that would support their hypothesis.

- Based on results presented in this thesis, the effect of internal magnetic order of Cr and α-Fe seems to have little effect on their deformation properties within the first 5% of their plastic deformation. The only result that would support the opposite is the inexplicable increase of the yield stress of chromium

specimen that had the spin density wave wavevector oriented close to the loading axis (Fig. 4.13). On the other hand, the effect of plastic deformation on internal magnetic structure of Cr and α-Fe is severe.

Different propensity to twin formation and its non-existence when the shear is applied in the antitwinning sense is sometimes regarded as a consequence of different elastic anisotropy. The Zener's anisotropy ratio of α-Fe at room temperature is approx. 2.4 [281], whereas that for alkali metals Li, Na and K are 8.8, 8.2 and 6.4 respectively [282–284]. Both α-Fe and alkali metals exhibit large anisotropy, while other bcc metals show rather small values of Zener's ratio. In particular, Cr, Ta, W, Mo, Nb and V have Zener's ratio of 0.69, 1.58, 1.00, 0.81, 0.51 and 0.79, respectively [285–287]. The anisotropy indices seem to correlate with σ_{AT}/σ_T ratios computed in Ref. [241]. However, twinning is governed by the glide of twin boundary dislocations, whose cores are not described by elasticity. From this point of view, anisotropic elasticity cannot govern the glide of these dislocations, albeit it may somewhat affect this mechanism.

This work suggests that magnetic ordering does not play a major role in the twinning of bcc metals. Future research should focus on elucidating the deformation mechanisms of alkali metals, since the 5^{th} and 6^{th} group bcc metals and iron have been studied quite extensively. The lack of data on alkali metals stem from their high reactivity and thus difficult handling and testing. The only recent study on alkali metals was published by Sedlatschek et al. [288] who studied Li in tension, but did not focus on operative slip systems. Despite the nucleation and growth of twins in bcc metals have been simulated a number of times, in-situ experimental studies of twin formation is still lacking. In particular, it is still unclear how twin embryos originate. Future research could also focus on Fe-Cr alloys and their properties, which are one of the candidate materials considered for the design of fusion reactors [289, 290].

11 Author's publications, talks, and other projects

This chapter briefly summarizes the author's outputs and achievements during the Ph.D. study.

Author's ORCID number: 0000-0001-8758-0746
Author's ResearchedID: GNM-8788-2022
Total citations and H-index as of 7/2022:

- Publons: 23 total citations and H-index 3
- Google Scholar: 23 total citations and H-index 3

Publications in impact journals

- H. A. Tinoco, **J. Holzer**, T. Pikálek, Z. Buchta, J. Lazar, A. Chlupová, T. Kruml and P. Hutař. Determination of elastic parameters of Si_3N_4 thin films by means of a numerical approach and bulge tests. *Thin Solid Films* 672 (2019) 66-74.
- Z. Que, H.P. Seifert, P. Spätig, A. Zhang, **J. Holzer**, G. S. Rao and S. Ritter. Effect of dynamic strain ageing on environmental degradation of fracture resistance of low-alloy RPV steels in high-temperature water environments. *Corr. Sci.* 152 (2019) 172-189.
- Z. Que, H. P. Seifert, P. Spätig, **J. Holzer**, A. Zhang, G. S. Rao and S. Ritter. Environmental degradation of fracture resistance in high-temperature water environments of low-alloy reactor pressure vessel steels with high sulphur or phosphorus contents. *Corr. Sci.* 154 (2019) 191-207.
- Z. Que, H. P. Seifert, P. Spätig, **J. Holzer**, A. Zhang and G. S. Rao. Degradation Effects of Hydrogen and High-Temperature Water Environments on the Fracture Resistance of Low-Alloy RPV Steels. *Nuclear Science and Engineering.* (2021).
- **J. Holzer**, Z. Chlup, T. Kruml, and R. Gröger. Plastic deformation of magnetically isotropic Cr single crystals compressed at 77 K. *Int. J. Plast.* 138 (2021) 102938.

- H. A. Tinoco, P. Hutař, T. Kruml and **J. Holzer**. Modeling of elastoplastic behavior of freestanding square thin films under bulge testing. *Acta Mech.* 232 (2021) 2715-2731.
- A. Marshall, **J. Holzer**, P. Stejskal, C. Stephens, T. Vystavěl and M. Whiting. The EBSD spatial resolution of a Timepix-based detector in a tilt-free geometry. *Ultramicroscopy* 226 (2021) 113294.
- **J. Holzer**, A. Marshall, P. Stejskal, C. Stephens and T. Vystavěl. Large area EBSD mapping using a tilt-free configuration and direct electron detection sensor. *Microsc. Microanal.* 27 (2021) 1832-1835.
- K. Vrchovecká, A. Weiser, J. Přibyl, J. Kuta, **J. Holzer**, M. Pávková-Goldbergová, D. Sobola and Dlouhý, A. A release of Ti-ions from nanostructured titanium oxide surfaces. *Surf. Interfaces* 29 (2022) 101699.
- **J. Holzer**, Š. Gamanov, N. Luptáková, A. Dlouhý and J. Svoboda. Coarsening Kinetics of Y_2O_3 Dispersoid in New Grade of Fe-Al-Cr-Based ODS Alloy. *Metals* 12 (2022) 210.
- J. Svoboda, P. Bořil, **J. Holzer**, N. Luptáková, M. Jarý, B. Mašek, and P. Dymáček. Substantial Improvement of High Temperature Strength of New-Generation Nano-Oxide-Strengthened Alloys by Addition of Metallic Yttrium. *Materials* 15 (2022) 504.
- Š. Gamanov, **J. Holzer**, P. Roupcová and J. Svoboda. High temperature oxidation kinetics of Fe-10Al-4Cr-Y_2O_3 ODS alloy at 1200-1400 °C. *Corr. Sci.* 206 (2022) 110498.

Submitted manuscripts

- R. Gröger, **J. Holzer** and T. Kruml. (2022, submitted manuscript). Twinning and antitwinning in body-centered cubic metals. *Comp. Mater. Sci.*
- **J. Holzer**, M. Husťák, J. Hegrová, and R. Gröger. (2022, submitted manuscript). Grain coarsening of columnar iron polycrystals by repetitive cold work and annealing. *Metall. Mater. Trans. A.*
- V. Jetela, J. Klement, **J. Holzer** and J. Kondás. (2022, submitted manuscript). Bonded and additively manufactures crack retarders: A comparative study of damage tolerance properties. *Int. J. Fatigue.*

Oral talks on conferences

- **Dislocations 2019, Haifa, Israel**

  J. Holzer, R. Gröger, Z. Chlup. Plastic deformation of chromium single crystals at 77 K

- **MSMF 9 2019, Brno, Czech Republic**

  J. Holzer, Z. Chlup, T. Kuběnová, R. Gröger. Slip Activity in High-purity Chromium Single Crystals Compressed at 77 K

- **(Virtual) M & M 2021, Pittsburgh, PA, USA**

  J. Holzer, A. Marshall, P. Stejskal, C. Stephens, T. Vystavěl. Large area EBSD mapping using a tilt-free configuration and direct electron detection sensor

- **(Invited speech, Virtual) ICSRS-7 Structural relaxation is solids 2021, Vinnytsia, Ukraine**

  J. Holzer, T. Kruml, Z. Chlup, R. Gröger. On the mechanism if twinning in body-centered cubic metals

- **(Virtual) Krakow EBSD meeting 2021, Krakow, Poland**

  J. Holzer, C. Stephens, T. Vystavěl. Advances in reflection Kikuchi diffraction (RKD) for large area mapping and high-resolution analysis

- **(Virtual) RMS Virtual EBSD 2021, Oxford, UK**

  A. Marshall, **J. Holzer**, P. Stejskal, C. Stephens, T. Vystavěl, M. Whiting. Furthering the Resolution Limit of EBSD

- **(Virtual) MAS EBSD 2022**

  J. Holzer, B. Straka, C. Stephens, T. Vystavěl. A signal strength, pattern quality, and signal to background ratio comparison of an RKD and standard geometry via direct electron detectors

- **ICSMA-19 2022, Metz, France**

  J. Holzer, Z. Chlup, T. Kruml, R. Gröger. On the low temperature deformation of α-iron

- **ICSMA-19 2022, Metz, France**

  J. Holzer, Š. Gamanov, B. Mašek, J. Svoboda. Development and characterization of advanced Fe-10Al-4Cr-4Y_2O_3 ODS alloy for applications up to 1300 °C

- **MSMF 2022, Brno, Czech Republic**

  J. Holzer, Š. Gamanov, P. Dymáček, O. Khalaj, J. Svoboda. Processing and characterization of advanced Fe-Al-Cr-Y_2O_3 nanocomposites for application at 1100-1300 °C

Awards

- Brno Ph.D. Talent 2019 Experimental studies of the interplay of plasticity and magnetism in α-iron and chromium

- Scholarship Award – Cena Sergio Marchionne 2019

Projects

- CEITEC Specific research 2019 (CEITEC VUT-J-19-5955): Investigation of Anomalous slip in BCC metals using Transmission Electron Microscopy

Mentorship

- Ing. Miroslav Husťák (BUT) - short-term work contract at IPM. Preparation of coarse-grained polycrystal of α-Fe by successive cold-work and annealing and joint publication [193].

Internship

- Paul Scherrer Institute, Villigen, Switzerland

  Supervisor: Dr. Oksana Zaharko

  Duration: 1st August 2020 to 31st October 2020

  Purpose: Neutron scattering experiment, pyZebra software development
- Paul Scherrer Institute, Villigen, Switzerland

  Supervisor: Dr. Oksana Zaharko

  Duration: 1st March 2021 to 23rd March 2021

  Purpose: Neutron scattering experiment on Cr samples
- Thermo Fisher Scientific, Brno, Czech Republic

  Duration: 1st November 2019 to the present

Bibliography

[1] M. J. Paul, V. M. Muthaiah, S. Mula, Yttria-reinforced Fe-Cr ferritic alloy-based nanocomposites for fusion reactor structural applications, *Metall. Mater. Trans. A* 52 (2021) 627–643.

[2] J. W. Christian, Some Surprising Features of the Plastic Deformation of Body-Centered Cubic Metals and Alloys, *Metall. Trans. A* 14 (1983) 1237–1256.

[3] E. S. Greiner, Slip Markings in Chromium, *JOM* 2 (1950) 891–892.

[4] C. N. Reid, A. Gilbert, G. Hahn, Dislocation and deformation modes in chromium single crystals, *Trans. Metall. Soc. AIME* 239 (1967) 467–473.

[5] Y. Aono, E. Kuramoto, K. Kitajima, Plastic Deformation of High-Purity Iron Single Crystals, *Rep. Res. Inst. Appl. Mech.* 29 (1981) 127–189.

[6] F. Louchet, L. P. Kubin, D. Vesely, In situ deformation of bcc crystals at low temperatures in a high-voltage electron microscope: Dislocation mechanisms and strain-rate equation, *Philos. Mag. A* 39 (1979) 433–454.

[7] E. Fawcett, Spin-Density-Wave Antiferromagnetism in Chromium, *Rev. Mod. Phys.* 60 (1988) 209–283.

[8] J. M. Makar, B. K. Tanner, The effect of plastic deformation and residual stress on the permeability and magnetostriction of steels, *J. Magn. Magn. Mater.* 222 (2000) 291–304.

[9] K. M. Krishnan, Magnetism and microstructure: the role of interfaces, *Acta Mater.* 47 (1999) 4233–4244.

[10] S. Takahashi, J.-I. Echigoya, Z. Motoki, Magnetization curves of plastically deformed Fe metals and alloys, *J. Appl. Phys.* 87 (2000) 805–813.

[11] B. Bienvenu, C. C. Fu, E. Clouet, Impact of magnetism on screw dislocations in body-centered cubic chromium, *Acta Mater.* 200 (2020) 570–580.

[12] V. Vitek, Core Structure of Screw Dislocations in Body-Centred Cubic Metals: Relation to Symmetry and Interatomic Bonding, *Philos. Mag.* 84 (2004) 415–428.

[13] G. I. Taylor, C. F. Elam, The distortion of iron crystals, *Proc. R. Soc. Lond. A* 112 (1926) 337–361.

[14] M. S. Duesbery, The dislocation core and plasticity, *Dislocations in Solids* 8 (1989) 67–173.

[15] M. S. Duesbery, V. Vítek, D. K. Bowen, P. B. Hirsch, The Effect of Shear Stress on the Screw Dislocation Core Structure in Body-Centred Cubic Lattices, *Proc. R. Soc. Lond. A* 332 (1973) 85–111.

[16] S. L. Frederiksen, K. W. Jacobsen, Density Functional Theory Studies of Screw Dislocation Core Structures in Bcc Metals, *Philos. Mag.* 83 (2003) 365–375.

[17] L. Ventelon, F. Willaime, Core Structure and Peierls Potential of Screw Dislocations in α-Fe from First Principles: Cluster versus Dipole Approaches, *J. Comput-aided. Mater.* 14 (2007) 85–94.

[18] V. Vitek, V. Paidar, Non-Planar Dislocation Cores: A Ubiquitous Phenomenon Affecting Mechanical Properties of Crystalline Materials, *Dislocations in Solids* 14 (2008) 441–514.

[19] D. Rodney, L. Ventelon, E. Clouet, L. Pizzagalli, F. Willaime, Ab initio modeling of dislocation core properties in metals and semiconductors, *Acta Mater.* 124 (2017) 633–659.

[20] R. Peierls, The size of a dislocation, *Proc. Phys. Soc.* 52 (1940) 34–37.

[21] F. R. N. Nabarro, Dislocations in a simple cubic lattice, *Proc. Phys. Soc.* 59 (1947) 256–272.

[22] J. D. Eshelby, Edge dislocations in anisotropic materials, *Phil. Mag.* 40 (1949) 903–912.

[23] M. S. Daw, M. I. Baskes, Embedded-atom method: Derivation and application to impurities, surfaces, and other defects in metals, *Phys. Rev. B* 29 (1984) 6443–6453.

[24] B. L. Holian, A. F. Voter, N. J. Wagner, R. J. Ravelo, S. P. Chen, W. G. Hoover, C. G. Hoover, J. E. Hammerberg, T. D. Dontje, Effects of pairwise versus many-body forces on high-stress plastic deformation, *Phys. Rev. A* 43 (1991) 2655–2661.

[25] M. I. Baskes, Many-body effects in fcc metals: a Lennard-Jones embedded-atom potential, *Phys. Tev. Let.* 83 (1999) 2592–2595.

[26] M. W. Finnis, J. E. Sinclair, A simple empirical N-body potential for transition metals, *Phil. Mag. A* 50 (1984) 45–55.

[27] Z. Bangwei, O. Yifang, L. Shuzhi, J. Zhanpeng, An analytic MEAM model for all BCC transition metals, *Phys. B: Conden. Matter* 262 (1999) 218–225.

[28] M. I. Baskes, M. S. Daw, S. M. Foiles, The embedded atom method: theory and application, *Mat. Sci. Rep.* 9 (1988) 251–310.

[29] J. Tersoff, New empirical approach for the structure and energy of covalent systems, *Phys. Rev. B* 37 (1988) 6991–7000.

[30] G. C. Abell, Empirical chemical pseudopotential theory of molecular and metallic bonding, *Phys. Rev. B* 31 (1985) 6184–6196.

[31] D. W. Brenner, Empirical potential for hydrocarbons for use in simulating the chemical vapor deposition of diamond films, *Phys. Rev. B* 42 (1990) 9458–9471.

[32] Ş. Erkoç, Empirical many-body potential energy functions used in computer simulations of condensed matter properties, *Phys. Rep.* 278 (1997) 79–105.

[33] M. Mrovec, D. Nguyen-Manh, D. G. Pettifor, V. Vitek, Bond-order potential for molybdenum: Application to dislocation behavior, *Phys. Rev. B* 69 (2004) 094115.

[34] M. Mrovec, R. Gröger, A. G. Bailey, D. Nguyen-Manh, C. Elsässer, V. Vitek, Bond-order potential for simulations of extended defects in tungsten, *Phys. Rev. B* 75 (2007) 104119.

[35] M. Mrovec, D. Nguyen-Manh, C. Elsässer, P. Gumbsch, Magnetic bond-order potential for iron, *Phys. Rev. Let.* 106 (2011) 246402.

[36] Y.-S. Lin, M. Mrovec, V. Vitek, Bond-order potential for magnetic body-centered-cubic iron and its transferability, *Phys. Rev. B* 93 (2016) 214107.

[37] Y.-S. Lin, M. Mrovec, V. Vitek, Importance of inclusion of the effect of s electrons into bond-order potentials for transition bcc metals with d-band mediated bonding, *Model. Simul. Mater. Sci. Eng.* 24 (2016) 085001.

[38] J. A. Moriarty, Density-functional formulation of the generalized pseudopotential theory. III. Transition-metal interatomic potentials, *Phys. Rev. B* 38 (1988) 3199–3231.

[39] D. R. Trinkle, M. D. Jones, R. G. Hennig, S. P. Rudin, R. C. Albers, J. W. Wilkins, Empirical tight-binding model for titanium phase transformations, *Phys. Rev. B* 73 (2006) 094123.

[40] P. Hohenberg, W. Kohn, Inhomogeneous electron gas, *Phys. Rev.* 136 (1964) B864–B871.

[41] W. Kohn, L. J. Sham, Self-consistent equations including exchange and correlation effects, *Phys. Rev.* 140 (1965) A1133–A1138.

[42] R. J. Bartlett, Adventures in DFT by a Wavefunction Theorist, *J. Chem. Phys.* 151 (2019) 160901.

[43] J. C. Slater, A simplification of the Hartree-Fock method, *Phys. Rev.* 81 (1951) 385–390.

[44] L. Ventelon, F. Willaime, E. Clouet, D. Rodney, Ab initio investigation of the Peierls potential of screw dislocations in bcc Fe and W, *Acta Mater.* 61 (2013) 3973–3985.

[45] L. Ventelon, F. Willaime, Generalized stacking-faults and screw-dislocation core-structure in bcc iron: a comparison between ab initio calculations and empirical potentials, *Philos. Mag.* 90 (2010) 1063–1074.

[46] L. Dezerald, D. Rodney, E. Clouet, L. Ventelon, F. Willaime, Plastic anisotropy and dislocation trajectory in BCC metals, *Nature Comm.* 7 (2016) 1–7.

[47] L. Dezerald, L. Proville, L. Ventelon, F. Willaime, D. Rodney, First-principles prediction of kink-pair activation enthalpy on screw dislocations in bcc transition metals: V, Nb, Ta, Mo, W, and Fe, *Phys. Rev. B* 91 (2015) 094105.

[48] L. Casillas-Trujillo, D. Gambino, L. Ventelon, B. Alling, Screw dislocation core structure in the paramagnetic state of bcc iron from first-principles calculations, *Phys. Rev. B* 102 (2020) 094420.

[49] H. Cosrad, Effect of temperature on yield and flow stress of BCC metals, *Philos. Mag.* 5 (1960) 745–751.

[50] T. Suzuki, H. Koizumi, H. Kirchner, Plastic flow stress of bcc transition metals and the Peierls potential, *Acta Metall. Mater.* 43 (1995) 2177–2187.

[51] T. Suzudo, T. Onitsuka, K. Fukumoto, Analyzing the Cross Slip Motion of Screw Dislocations at Finite Temperatures in Body-Centered-Cubic Metals: Molecular Statics and Dynamics Studies, *Model. Simul. Mater. Sci. Eng.* 27 (2019) 064001.

[52] V. Vitek, R. C. Perrin, D. K. Bowen, The core structure of 1/2 (111) screw dislocations in bcc crystals, *Philos. Mag.* 21 (1970) 1049–1073.

[53] P. D. Bristowe, A. G. Crocker, A computer simulation study of the structures of twin boundaries in body-centred cubic crystals, *Philos. Mag. A* 31 (1975) 503–517.

[54] J. Wang, Z. Zeng, M. Wen, Q. Wang, D. Chen, Y. Zhang, P. Wang, H. Wang, Z. Zhang, S. X. Mao, Anti-twinning in nanoscale tungsten, *Sci. Adv.* 6 (2020) 1–8.

[55] M. S. Duesbery, V. Vitek, Plastic anisotropy in bcc transition metals, *Acta Mater.* 46 (1998) 1481–1492.

[56] K. Ito, V. Vitek, Atomistic Study of Non-Schmid Effects in the Plastic Yielding of Bcc Metals, *Phil. Mag. A* 81 (2001) 1387–1407.

[57] E. Schmid, W. Boas, Plasticity of crystals: With special reference to metals, Chapman & Hall, 1968.

[58] R. Gröger, A. G. Bailey, V. Vitek, Multiscale Modeling of Plastic Deformation of Molybdenum and Tungsten: I. Atomistic Studies of the Core Structure and Glide of $1/2\langle 111\rangle$ Screw Dislocations at 0 K, *Acta Mater.* 56 (2008) 5401–5411.

[59] Q. Qin, J. L. Bassani, Non-Schmid yield behavior in single crystals, *J. Mech. Phys. Solids* 40 (1992) 813–833.

[60] Y. Aono, E. Kuramoto, K. Kitajima, Fundamental Plastic Behaviors in High-Purity BCC Metals (Nb, Mo and Fe), in: R. C. Gifkins (Ed.), Strength of Metals and Alloys (ICSMA 6), Pergamon, 1982, 9–14.

[61] J. Bressers, R. Creten, Suppression of Anomalous Slip by Oxygen Interstitials in Vanadium, *Scr. Mater.* 11 (1977) 33–36.

[62] A. J. Garratt-Reed, G. Taylor, Stress-Strain Curves for Niobium Crystals Deformed at Temperatures below Ambient, *Philos. Mag.* 33 (1976) 577–590.

[63] R. Gröger, Z. Chlup, T. Kuběnová, Deformation Twinning in Vanadium Single Crystals Tested in Compression at 77 K, *Mater. Sci. Eng. A* 737 (2018) 413–421.

[64] L. L. Hsiung, On the Mechanism of Anomalous Slip in Bcc Metals, *Mater. Sci. Eng. A* 528 (2010) 329–337.

[65] P. J. Jeffcoat, B. L. Mordike, K. D. Rogausch, Anomalous Slip in Mo-5 at.% Nb and Mo-5 at.% Re Alloy Single Crystals, *Phil. Mag. A* 34 (1976) 583–592.

[66] F. Louchet, L. P. Kubin, Dislocation Substructures in the Anomalous Slip Plane of Single Crystal Niobium Strained at 50 K, *Acta Metall.* 23 (1975) 17–21.

[67] F. Louchet, L. P. Kubin, A Possible Explanation for the Anomalous Slip of B.C.C. Metals from in Situ Experiments, *Scr. Metall.* 9 (1975) 911–916.

[68] C. Marichal, K. Srivastava, D. Weygand, S. Van Petegem, D. Grolimund, P. Gumbsch, H. Van Swygenhoven, Origin of Anomalous Slip in Tungsten, *Phys. Rev. Lett.* 113 (2014) 025501.

[69] H. Matsui, H. Kimura, Anomalous {110} Slip and the Role of Co-Planar Double Slip in BCC Metals, *Scr. Metall.* 9 (1975) 971–978.

[70] H. Matsui, H. Kimura, Anomalous {110} Slip in High-Purity Molybdenum Single Crystals and Its Comparison with That in V(a) Metals, *Mater. Sci. Eng.* 24 (1976) 247–256.

[71] H. Matsui, H. Saka, K. Noda, H. Kimura, T. Imura, Direct Observation of Active Unexpected Slip in Molybdenum by HVEM, *Scr. Metall.* 8 (1974) 467–474.

[72] B. L. Mordike, Anomalous Slip and Discontinuous Yielding, *Phys. Status Solidi A* 34 (1976) K59–K61.

[73] M. H. A. Nawaz, B. L. Mordike, Anomalous Slip in Tantalum, *Z. Metallk.* 66 (1975) 644–647.

[74] W. Wasserbäch, Anomalous Slip in High-Purity Niobium and Tantalum Single Crystals, *Phys. Status Solidi A* 147 (1995) 417–446.

[75] H. Cho, C. A. Bronkhorst, H. M. Mourad, J. R. Mayeur, D. J. Luscher, Anomalous plasticity of body-centered-cubic crystals with non-Schmid effect, *Int. J. Solids Struct.* 139 (2018) 138–149.

[76] Z. Chen, Modelling the plastic deformation of iron, KIT Scientific Publishing, 2013.

[77] R. Gröger, V. Racherla, J. L. Bassani, V. Vitek, Multiscale Modeling of Plastic Deformation of Molybdenum and Tungsten: II. Yield Criterion for Single Crystals Based on Atomistic Studies of Glide of $1/2\langle 111\rangle$ Screw Dislocations, *Acta Mater.* 56 (2008) 5412–5425.

[78] R. Gröger, V. Vitek, Single Crystal Yield Criterion for Chromium Based on Atomistic Studies of Isolated 1/2[111] Screw Dislocations, *Int. J. Plast.*102733.

[79] T. E. Buchheit, C. C. Battaile, C. R. Weinberger, E. A. Holm, Multi-scale modeling of low-temperature deformation in bcc metals, *JOM* 63 (2011) 33–36.

[80] D. Cereceda, M. Diehl, F. Roters, D. Raabe, J. M. Perlado, J. Marian, Unraveling the temperature dependence of the yield strength in single-crystal tungsten using atomistically-informed crystal plasticity calculations, *Int. J. Plast.* 78 (2016) 242–265.

[81] Y. Lou, J. W. Yoon, Anisotropic yield function based on stress invariants for BCC and FCC metals and its extension to ductile fracture criterion, *Int. J. Plast.* 101 (2018) 125–155.

[82] O. Cazacu, B. Plunkett, F. Barlat, Orthotropic yield criterion for hexagonal closed packed metals, *Int. J. Plast.* 22 (2006) 1171–1194.

[83] N. Vajragupta, S. Ahmed, M. Boeff, A. Ma, A. Hartmaier, Micromechanical modeling approach to derive the yield surface for BCC and FCC steels using statistically informed microstructure models and nonlocal crystal plasticity, *Phys. Mesomech.* 20 (2017) 343–352.

[84] X.-K. Zhu, B. N. Leis, Average shear stress yield criterion and its application to plastic collapse analysis of pipelines, *Int. J. Press. Vessel. Pip.* 83 (2006) 663–671.

[85] L. Kubin, Dislocations, mesoscale simulations and plastic flow, Vol. 5, Oxford University Press, 2013.

[86] T. Oku, J. M. Galligan, Quantum mechanical tunneling of dislocations, *Phys. Rev. Lett.* 22 (1969) 596–597.

[87] N. Mott, Creep in metal crystals at very low temperatures, *Philos. Mag.* 1 (1956) 568–572.

[88] J. Weertman, Dislocation Model of Low-Temperature Creep, *J. Appl. Phys.* 29 (1958) 1685–1689.

[89] S. Takeuchi, T. Hashimoto, K. Maeda, Plastic Deformation of Bcc Metal Single Crystals at Very Low Temperatures, *Trans. JIM* 23 (1982) 60–69.

[90] J. J. Gilman, Flow of covalent solids at low temperatures, *J. Appl. Phys.* 46 (1975) 5110–5113.

[91] M. I. Kaganov, Y. V. Kravchenko, V. D. Natsik, Dislocation dragging by electrons in metals, *Sov. Phys. Uspekhi* 16 (1974) 878–891.

[92] B. V. Petukhov, Tunneling nucleation of kink pairs on dislocations in the Peierls potential relief with random distortions, *Low Temp. Phys.* 44 (2018) 912–917.

[93] L. Proville, D. Rodney, M.-C. Marinica, Quantum effect on thermally activated glide of dislocations, *Nat. Mater.* 11 (2012) 845–849.

[94] C. Marichal, H. Van Swygenhoven, S. Van Petegem, C. Borca, {110} Slip with {112} slip traces in bcc Tungsten, *Sci. Rep.* 3 (2013) 1–7.

[95] M. B. Stearns, Why is iron magnetic?, *Phys. Today* 31 (1978) 34–39.

[96] C. Graham Jr, Magnetocrystalline anisotropy constants of iron at room temperature and below, *Phys. Rev.* 112 (1958) 1117–1120.

[97] B. Westerstrand, P. Nordblad, L. Nordborg, The magnetocrystalline anisotropy constants of iron and iron-silicon alloys, *Phys. Scr.* 11 (1975) 383.

[98] B. D. Cullity, C. D. Graham, Introduction to magnetic materials, John Wiley & Sons, 2011.

[99] G. Shirane, W. J. Takei, Neutron Diffraction Study of Chromium Single Crystals, *J. Phys. Soc. Japan* 17 (1962) 123–141.

[100] A. W. Overhauser, Spin Density Waves in an Electron Gas, *Phys. Rev.* 128 (1962) 1437–1452.

[101] G. Bacon, N. Cowlam, Magnetic studies of annealed and alloyed chromium by neutron diffraction, *J. Phys. Condens. Matter.* 2 (1969) 238–251.

[102] R. Griessen, E. Fawcett, Mixed State in Antiferromagnetic Chromium, *J. Phys. F.* 7 (1977) 2141–2152.

[103] V. Golovkin, V. Bykov, V. Levdik, Anomalies on the Magnetic Structure of Chromium, *J. Exp. Theor. Phys.* 22 (1965) 1083–1090.

[104] U. Köbler, S. M. Dubiel, On the Magnetic Anisotropy of Chromium, *Z. Physik B* 61 (1985) 257–262.

[105] W. C. Muir, J. M. Perz, E. Fawcett, Elastic Constants of Antiferromagnetic Chromium, *J. Phys. F* 17 (1987) 2431–2445.

[106] H. J. van Rijn, H. L. Alberts, Elastic Constants of Chromium in the Single Q-Domain State, *J. Phys. F* 13 (1983) 1559–1570.

[107] V. L. R. Jacques, D. Le Bolloc'h, S. Ravy, Density Wave Defects in Chromium Probed by Coherent X-Rays, *Physica B Condens. Matter* 404 (2009) 573–575.

[108] G. E. Bacon, A Neutron-Diffraction Study of Very Pure Chromium, *Acta. Cryst.* 14 (1961) 823–829.

[109] M. Kleiber, M. Bode, R. Ravlić, R. Wiesendanger, Topology-Induced Spin Frustrations at the Cr (001) Surface Studied by Spin-Polarized Scanning Tunneling Spectroscopy, *Phys. Rev. Lett.* 85 (2000) 4606–4609.

[110] R. P. Steijn, R. M. Brick, Flow and fracture of single crystals of high purity ferrite, *T. Am. Soc. Metal.* 46 (1954) 1406–1448.

[111] N. Allen, B. Hopkins, J. McLennan, The Tensile Properties of Single Crystals of High-Purity Iron at Temperatures from 100 to −253 °C, *Proc. Roy. Soc. A.* 234 (1956) 221–246.

[112] J. Harding, The yield and fracture behaviour of high-purity iron single crystals at high rates of strain, *Proc. R. Soc. A: Math. Phys. Eng. Sci.* 299 (1967) 464–490.

[113] W. D. Biggs, P. L. Pratt, The deformation and fracture of alpha-iron at low temperatures, *Acta Metall.* 6 (1958) 694–703.

[114] T. L. Altshuler, J. W. Christian, The mechanical properties of pure iron tested in compression over the temperature range 2 to 293 K, *Philos. Trans. R. Soc. A* 261 (1967) 253–287.

[115] A. S. Keh, Work hardening and deformation sub-structure in iron single crystals deformed in tension at 298 K, *Philos. Mag.* 12 (1965) 9–30.

[116] P. Franciosi, L. T. Le, G. Monnet, C. Kahloun, M. H. Chavanne, Investigation of Slip System Activity in Iron at Room Temperature by SEM and AFM In-Situ Tensile and Compression Tests of Iron Single Crystals, *Int. J. Plast.* 65 (2015) 226–249.

[117] H. Kimura, Low temperature mechanical properties of high purity iron and effects of small amounts of solutes on them, *Trans. Jpn. Inst. Met.* 26 (1985) 527–541.

[118] H. H. Kranzlein, M. S. Burton, G. V. Smith, Preparation and properties of iron single crystals, *Mem. Sci. Rev. Met.* 65 (1968) 361–368.

[119] S. Yabe, M. Terano, N. Yoshino, Plane Strain Compression Test and Simple Shear Test of Single Crystal Pure Iron, *Procedia Eng.* 81 (2014) 1342–1347.

[120] E. W. Lee, M. A. Asgar, Magnetostriction and Anomalous Thermal Expansion of Chromium, *Phys. Rev. Lett.* 22 (1969) 1436–1439.

[121] M. J. Marcinkowski, H. A. Lipsitt, The plastic deformation of chromium at low temperatures, *Acta Metall.* 10 (1962) 95–111.

[122] C. N. Reid, A. Gilbert, Dislocation Structure in Chromium, Chromium-Rhenium, and Chromium-Iron Alloys, *J. Less-common metals* 10 (1966) 77–90.

[123] A. Gilbert, B. Allen, C. N. Reid, An Investigation of Mechanical Properties of Chromium, Chromium-Rhenium, and Derived Alloys, *NASA contractor report 118*.

[124] A. V. Sameljuk, A. D. Vasilev, S. A. Firstov, Low Temperature Deformation and Fracture Behaviour of [100] and [110] Chromium Single Crystals, *Int. J. Refract. Met. H.* 14 (1996) 249–255.

[125] D. Wu, T. G. Nieh, Incipient Plasticity and Dislocation Nucleation in Body-Centered Cubic Chromium, *Mater. Sci. Eng. A* 609 (2014) 110–115.

[126] I. Choi, C. Brandl, R. Schwaiger, Thermally Activated Dislocation Plasticity in Body-Centered Cubic Chromium Studied by High-Temperature Nanoindentation, *Acta Mater.* 140 (2017) 107–115.

[127] C. L. Briant, K. S. Kumar, N. Rosenberg, H. Tomioka, The Mechanical Properties of High Purity Chromium, *Int. J. Refract. Met. H.* 18 (2000) 9–11.

[128] P. J. Grundy, R. S. Tebble, Lorentz electron microscopy, *Adv. Phys.* 17 (1968) 153–242.

[129] M. Ohkoshi, T. Kusuda, Magnetic domain structures in CoCr films studied by Lorentz microscopy, *Jpn. J. Appl. Phys.* 22 (1983) L130–L132.

[130] K. Koike, Spin-polarized scanning electron microscopy, *Microscopy* 62 (2013) 177–191.

[131] D. T. Pierce, Spin-polarized electron microscopy, *Phys. Scr.* 38 (1988) 291–296.

[132] W. G. Stirling, M. J. Cooper, X-ray magnetic scattering, *J. Magn. Magn. Mater.* 200 (1999) 755–773.

[133] E. Balcar, S. W. Lovesey, F. A. Wedgwood, Theory of thermal neutron scattering from crystals containing ions with impaired f electrons, *J. Phys. C* 3 (1970) 1292–1302.

[134] B. Blau, K. N. Clausen, S. Gvasaliya, M. Janoschek, S. Janssen, L. Keller, B. Roessli, J. Schefer, P. Tregenna-Piggott, W. Wagner, O. Zaharko, The Swiss Spallation Neutron Source SINQ at Paul Scherrer Institut, *Neutron News* 20 (2009) 5–8.

[135] E. Lehmann, H. Pleinert, L. Wiezel, Design of a neutron radiography facility at the spallation source SINQ, *Nucl. Instrum. Methods. A* 377 (1996) 11–15.

[136] G. S. Bauer, Physics and technology of spallation neutron sources, *Nucl. Instrum. Methods. A* 463 (2001) 505–543.

[137] J. T. Cremer, M. A. Piestrup, H. Park, C. K. Gary, R. H. Pantell, C. J. Glinka, J. G. Barker, Imaging hydrogenous materials with a neutron microscope, *Appl. Phys. Lett.* 87 (2005) 161913.

[138] M. Furusaka, KENS neutron scattering facility, *Neutron News* 3 (1992) 8–14.

[139] M. Arai, F. Maekawa, Japan spallation neutron source (JSNS) of J-PARC, *Nuclear Physics News* 19 (2009) 34–39.

[140] Y. Yamada, N. Watanabe, N. Niimura, Y. Morii, S. Katano, K. Aizawa, J. Suzuki, S. Koizumi, T. Osakabe, M. Teshigawara, et al., Next generation neutron source project in Japan Atomic Energy Research Institute (JAERI), *Phys. B: Condens. Matter* 241 (1997) 42–45.

[141] C. H. Pyeon, Y. Hirano, T. Misawa, H. Unesaki, C. Ichihara, T. Iwasaki, S. Shiroya, Preliminary experiments on accelerator-driven subcritical reactor with pulsed neutron generator in Kyoto University Critical Assembly, *J. Nucl. Sci. Technol.* 44 (2007) 1368–1378.

[142] K. Kakurai, Y. Morii, Neutron scattering activities at JRR-3M, *Neutron News* 9 (1998) 15–22.

[143] S. C. Yoon, S. Y. Chang, J. S. Kim, J. L. Kim, Determination of neutron room scattering corrections in RCL's calibration facility at KAERI, *Radiat. Prot. Dosim.* 70 (1997) 349–351.

[144] S. J. Kennedy, Construction of the neutron beam facility at Australia's OPAL research reactor, *Phys. B: Condens. Matter* 385 (2006) 949–954.

[145] E. Lelievre-Berna, E. Bourgeat-Lami, Y. Gibert, N. Kernavanois, J. Locatelli, T. Mary, G. Pastrello, A. Petukhov, S. Pujol, R. Rouques, et al., ILL polarised hot-neutron beam facility D3, *Phys. B: Condens. Matter* 356 (2005) 141–145.

[146] A. Taylor, A second target station for ISIS, *Phys. B: Condens. Matter* 276 (2000) 36–37.

[147] R. Kampmann, R. Wagner, Elastic neutron-scattering experiments at the Geesthacht Neutron Facility (GeNF), *Phys. B: Condens. Matter* 241 (1997) 36–38.

[148] M. Meissner, P. Smeibidl, Neutron scattering at BENSC under extreme conditions: Up to 17 Tesla and down to 25mK, *Neutron News* 12 (2001) 12–18.

[149] W. Gläser, W. Petry, The new neutron source FRM II, *Phys. B: Condens. Matter* 276 (2000) 30–32.

[150] L. Van Eijck, L. D. Cussen, G. J. Sykora, E. M. Schooneveld, N. J. Rhodes, A. A. Van Well, C. Pappas, Design and performance of a novel neutron powder diffractometer: PEARL at TU Delft, *J. Appl. Crystallogr.* 49 (2016) 1398–1401.

[151] P. Fischer, L. Keller, J. Schefer, J. Kohlbrecher, Neutron diffraction at SINQ, *Neutron News* 11 (2000) 19–21.

[152] L. Rosta, Cold neutron research facility at the Budapest Neutron Centre, *Appl. Phys. A* 74 (2002) s52–s54.

[153] V. N. Shvetsov, Neutron sources at the Frank Laboratory of Neutron Physics of the Joint Institute for Nuclear Research, *Quantum Beam Sci.* 1 (2017) 1–9.

[154] M. Rogante, V. T. Lebedev, Y. Kulvelis, A. Y. Vul, V. S. Kozlov, K. A. Konoplev, The 20-Year Russian-Italian Scientific Collaboration in Industrial Applications of Neutrons and Prospects on High Flux Reactor "PIK" of Russian National Centre Kurchatov Institut, *Neutron News* 32 (2021) 9–15.

[155] P. Lukáš, M. Vrána, P. Mikula, A. Brožová, M. Ernestová, New facility for neutron diffraction studies of residual stresses in highly radioactive materials in NPI Řež, *Phys. B: Condens. Matter* 385 (2006) 670–672.

[156] B. C. Hauback, H. Fjellvåg, O. Steinsvoll, K. Johansson, O. T. Buset, J. Jørgensen, The high resolution Powder Neutron Diffractometer PUS at the JEEP II reactor at Kjeller in Norway, *J. Neutron Res.* 8 (2000) 215–232.

[157] W. C. Koehler, R. W. Hendricks, The United States national small-angle neutron scattering facility, *J. Appl. Phys.* 50 (1979) 1951–1951.

[158] W. T. Heller, M. Cuneo, L. Debeer-Schmitt, C. Do, L. He, L. Heroux, K. Littrell, S. V. Pingali, S. Qian, C. Stanley, et al., The suite of small-angle neutron scattering instruments at Oak Ridge National Laboratory, *J. Appl. Crystallogr.* 51 (2018) 242–248.

[159] J. A. Roberts, The Los Alamos Neutron Science Center (LANSCE), *Neutron News* 10 (1999) 11–14.

[160] H. Prask, J. Rowe, J. Rush, I. Schroeder, The NIST cold neutron research facility, *J. Res. Natl. Inst.* 98 (1993) 1–13.

[161] B. M. Powell, Neutron scattering at Chalk river, *Neutron News* 1 (1990) 16–20.

[162] C. Gou, D. F. Chen, K. Sun, C. T. Ye, Present status of neutron scattering and CARR neutron scattering project in CIAE, *Phys. B: Condens. Matter* 311 (2002) 40–43.

[163] G. Sun, C. Zhang, B. Chen, J. Gong, S. Peng, A new operating neutron scattering facility CMRR in China, *Neutron News* 27 (2016) 21–26.

[164] ZEBRA: Thermal Single Crystal Diffractometer, https://www.psi.ch/en/sinq/zebra, accessed: 23.03.2022.

[165] D. B. Williams, C. B. Carter, Transmission electron microscopy: A textbook for material science, Springer, 2009.

[166] M. K. Wilkinson, C. G. Shull, Neutron diffraction studies on iron at high temperatures, *Phys. Rev.* 103 (1956) 516–524.

[167] C. G. Shull, J. S. Smart, Detection of antiferromagnetism by neutron diffraction, *Phys. Rev.* 76 (1949) 1256–1257.

[168] C. G. Shull, W. A. Strauser, E. O. Wollan, Neutron diffraction by paramagnetic and antiferromagnetic substances, *Phys. Rev.* 83 (1951) 333–345.

[169] R. Feynman, R. B. Leighton, M. Sands, The Feynman lectures on physics, Addison-Wesley Boston, MA, USA, 1965.

[170] H. J. Williams, R. M. Bozorth, W. J. P. R. Shockley, Magnetic domain patterns on single crystals of silicon iron, *Phys. Rev.* 75 (1949) 155.

[171] R. D. James, M. Wuttig, Magnetostriction of martensite, *Philos. Mag. A* 77 (1998) 1273–1299.

[172] T. J. Bastow, R. Street, Magnetic Structures of Field-Cooled and Stress-Cooled Chromium, *Phys. Rev.* 141 (1966) 510–516.

[173] J. M. Cowley, Diffraction physics, Elsevier, 1995.

[174] V. Golovkin, V. Bykov, V. Levdik, Obtaining the "Single-Q" State of Chromium by Action of Low Temperatures in the Presence of a Magnetic Field, *ZhETF Pis. Red.* 14 (1971) 382–385.

[175] S. A. Werner, A. Arrott, H. Kendrick, Temperature and magnetic-field dependence of the antiferromagnetism in pure chromium, *Phy. Rev.* 155 (1967) 528–539.

[176] M. Ando, S. Hosoya, Size and behavior of antiferromagnetic domains in Cr directly observed with x-ray and neutron topography, *J. Appl. Phys.* 49 (1978) 6045–6051.

[177] S. A. Werner, A. Arrott, M. Atoji, Effects of pressure and a magnetic field on chromium studied by neutron diffraction, *J. Appl. Phys.* 39 (1968) 671–673.

[178] J. Kerr, On rotation of the plane of polarization by reflection from the pole of a magnet, *Lond. Edinb. Dublin Philos. Mag. J. Sci.* 3 (1877) 321–343.

[179] A. Hubert, R. Schäfer, Magnetic domains: the analysis of magnetic microstructures, Springer Science & Business Media, 2008.

[180] I. V. Soldatov, R. Schäfer, Selective sensitivity in Kerr microscopy, *Rev. Sci. Instrum.* 88 (2017) 073701.

[181] J. McCord, Progress in magnetic domain observation by advanced magneto-optical microscopy, *J. Phys. D: Appl. Phys.* 48 (2015) 333001.

[182] T. Fujii, I. Morimoto, Residual Resistivity of High Purity Iron, *Jpn. J. Appl. Phys.* 8 (1969) 1154–1158.

[183] D. Schaible, M. Hirscher, H. Kronmuller, Residual resistivity ratio and plasticity of high-purity NiAl single crystals, *Philos. Mag. Lett.* 78 (1998) 121–125.

[184] L. Ponto, D. Landolt, Electropolishing of Chromium in Phosphoric Acid-Sulphuric Acid Electrolytes, *J. Appl. Electrochem.* 17 (1987) 205–214.

[185] N. Wiser, Electrical Resistivity of the Simple Metals, *Contemp. Phys.* 25 (1984) 211–249.

[186] T. F. Connolly, Groups IV, V, and VI Transition Metals and Compounds: Preparation and Properties, Springer Science & Business Media, 2012.

[187] P. C. Camargo, J. A. Ehlert, F. R. Brotzen, Growth of chromium-vanadium single crystals by floating-zone technique, *J. Cryst. Growth* 57 (1982) 241–244.

[188] P. W. Bridgman, Certain Physical Properties of Single Crystals of Tungsten, Antimony, Bismuth, Tellurium, Cadmium, Zinc, and Tin, *Proc. Am. Acad. Arts Sci.* 60 (1925) 305–383.

[189] D. C. Stockbarger, The production of large single crystals of lithium fluoride, *Rev. Sci. Instrum.* 7 (1936) 133–136.

[190] S. Kimura, I. Shindo, Single crystal growth of YIG by the floating zone method, *J. Cryst. Growth* 41 (1977) 192–198.

[191] S. Kadečková, B. Šesták, Growth of High-Purity Iron Single Crystals, *Krist. Tech.* 2 (1967) 191–203.

[192] C. S. Smith, L. Guttman, Measurement of internal boundaries in three-dimensional structures by random sectioning, *JOM* 5 (1953) 81–87.

[193] J. Holzer, M. Husťák, J. Hegrová, R. Gröger, Grain coarsening of columnar iron polycrystals by repetitive cold work and annealing (submitted manuscript), *Metall. Mater. Trans. A*.

[194] J. M. D. Coey, Magnetism and magnetic materials, Cambridge university press, 2010.

[195] M. Sato, Y. Ishii, Simple and approximate expressions of demagnetizing factors of uniformly magnetized rectangular rod and cylinder, *J. Appl. Phys.* 66 (1989) 983–985.

[196] M. Beleggia, M. De Graef, Y. T. Millev, D. A. Goode, G. Rowlands, Demagnetization factors for elliptic cylinders, *J. Phys. D: Appl. Phys* 38 (2005) 3333–3342.

[197] R. I. Joseph, Ballistic demagnetizing factor in uniformly magnetized cylinders, *J. Appl. Phys.* 37 (1966) 4639–4643.

[198] D.-X. Chen, E. Pardo, A. Sanchez, Demagnetizing factors for rectangular prisms, *IEEE Trans. Magn.* 41 (2005) 2077–2088.

[199] A. Aharoni, Demagnetizing factors for rectangular ferromagnetic prisms, *J. Appl. Phys.* 83 (1998) 3432–3434.

[200] D. C. Jiles, Dynamics of domain magnetization and the Barkhausen effect, *Czechoslov. J. Phys.* 50 (2000) 893–924.

[201] D. C. Jiles, D. L. Atherton, Theory of ferromagnetic hysteresis, *J. Magn. Magn. Mater.* 61 (1986) 48–60.

[202] R. Szewczyk, Validation of the anhysteretic magnetization model for soft magnetic materials with perpendicular anisotropy, *Materials* 7 (2014) 5109–5116.

[203] A. Ramesh, D. C. Jiles, J. M. Roderick, A model of anisotropic anhysteretic magnetization, *IEEE Trans. Magn.* 32 (1996) 4234–4236.

[204] W. M. Kiarie, E. J. Barron, A. P. S. Baghel, I. C. Nlebedim, M. D. Bartlett, D. C. Jiles, Modeling of Magnetic Properties of Magnetorheological Elastomers Using JA Hysteresis Model, *IEEE Trans. Magn.* 57 (2020) 1–5.

[205] A. Raghunathan, Y. Melikhov, J. E. Snyder, D. C. Jiles, Generalized form of anhysteretic magnetization function for Jiles–Atherton theory of hysteresis, *Appl. Phys. Lett.* 95 (2009) 172510.

[206] A. Ramesh, D. C. Jiles, Y. Bi, Generalization of hysteresis modeling to anisotropic materials, *J. Appl. Phys.* 81 (1997) 5585–5587.

[207] D. C. Jiles, Theory of the magnetomechanical effect, *J. Phys. D: Appl. Phys.* 28 (1995) 1537–1546.

[208] R. Szewczyk, Computational problems connected with Jiles–Atherton model of magnetic hysteresis, in: Recent Advances in Automation, Robotics and Measuring Techniques, Springer, 2014, 275–283.

[209] K. M. Chwastek, J. M. Szczygłowski, An alternative method to estimate the parameters of Jiles–Atherton model, *J. Magn. Magn. Mater.* 314 (2007) 47–51.

[210] Jiles–Atherton model library for OCTAVE/MATLAB, https://github.com/romanszewczyk/JAmodel/, accessed: 11.04.2022.

[211] R. M. Bozorth, Magnetic domain patterns, *J. Phys. Radium.* 12 (1951) 308–321.

[212] L. W. McKeehan, W. C. Elmore, Surface magnetization in ferromagnetic crystals, *Phys. Rev.* 46 (1934) 226–229.

[213] R. Street, E. O. Hall, Magnetic Domain Structure in Twinned Crystals of Silicon Iron, *Proc. Phys. Soc. B* 68 (1955) 1033–1037.

[214] E. Hug, Evolution of the magnetic domain structure of oriented 3% SiFe sheets with plastic strains, *J. Mater. Sci.* 30 (1995) 4417–4424.

[215] A. R. Pepper, R. Street, The effect of field-cooling on the magnetic susceptibility of chromium, *Proc. Phys. Soc.* 87 (1966) 971–973.

[216] A. Maurya, A. Thamizhavel, S. K. Dhar, P. Bonville, Magnetic anisotropy, unusual hysteresis and putative "up-up-down" magnetic structure in $EuTAl_4Si_2$ (T = Rh and Ir), *Sci. Rep.* 5 (2015) 1–10.

[217] M. Griffel, J. W. Stout, The magnetic anisotropy of manganous fluoride between 12 and 295 K, *J. Chem. Phys.* 18 (1950) 1455–1458.

[218] J. R. Tessman, The Parallel Susceptibility of an Antiferromagnet at Low Temperatures, *Phys. Rev.* 88 (1952) 1132–1137.

[219] A. C. Botterman, Magnetization and susceptibility studies on some antiferromagnetic linear chains, Technische Hogeschool Eindhoven, 1976.

[220] C. Kittel, Introduction to Solid State Physics, Wiley, 1996.

[221] H. J. Bunge, Texture analysis in materials science: mathematical methods, Butterworth-Heinemann, 2013.

[222] W. R. Busing, H. A. Levy, Angle calculations for 3-and 4-circle X-ray and neutron diffractometers, *Acta Crystallogr.* 22 (1967) 457–464.

[223] S. A. Werner, Choice of scans in neutron diffraction, *Acta Crystallogr. A* 27 (1971) 665–669.

[224] C. J. McHargue, Twinning in Columbium, *Trans. Met. Soc. AIME* 224 (1962) 334–339.

[225] R. Gröger, Z. Chlup, T. Kuběnová, I. Kuběna, Interplay of Slip and Twinning in Niobium Single Crystals Compressed at 77 K, *J. Mater. Re,* 34 (2019) 261–270.

[226] C. J. Hamelin, B. J. Diak, A. K. Pilkey, Multiscale modelling of the induced plastic anisotropy in bcc metals, *Int. J. of Plast.* 27 (2011) 1185–1202.

[227] R. Gröger, Origin of variable propensity for anomalous slip in body-centered cubic metals (submitted manuscript), *Acta Mater.*

[228] V. V. Bulatov, W. Cai, Nodal effects in dislocation mobility, *Phys. Rev. Let.* 89 (2002) 115501.

[229] A. N. Stroh, Steady State Problems in Anisotropic Elasticity, *J. Math. Phys.* 41 (1962) 77–103.

[230] E. Bitzek, P. Koskinen, F. Gähler, M. Moseler, P. Gumbsch, Structural Relaxation Made Simple, *Phys. Rev. Lett.* 97 (2006) 170201.

[231] Y.-S. Lin, M. Mrovec, V. Vitek, A New Method for Development of Bond-Order Potentials for Transition Bcc Metals, *Model. Simul. Mater. Sci. Eng.* 22 (2014) 034002.

[232] A. Stukowski, V. Bulatov, A. Arsenlis, Automated Identification and Indexing of Dislocations in Crystal Interfaces, *Model. Simul. Mater. Sci. Eng.* 20 (2012) 085007.

[233] A. Stukowski, Visualization and Analysis of Atomistic Simulation Data with OVITO –the Open Visualization Tool, *Model. Simul. Mater. Sci. Eng.* 18 (2009) 015012.

[234] A. F. Knorr, M. Marx, F. Schaefer, Crack initiation at twin boundaries due to slip system mismatch, *Scr. Mater.* 94 (2015) 48–51.

[235] C. Blochwitz, W. Tirschler, Twin boundaries as crack nucleation sites, *Cryst. Res. Technol.* 40 (2005) 32–41.

[236] Z. F. Zhang, Z. G. Wang, Grain boundary effects on cyclic deformation and fatigue damage, *Prog. Mater. Sci.* 53 (2008) 1025–1099.

[237] L. L. Li, Z. J. Zhang, P. Zhang, Z. G. Wang, Z. F. Zhang, Controllable fatigue cracking mechanisms of copper bicrystals with a coherent twin boundary, *Nat. Commun.* 5 (2014) 1–7.

[238] C. N. Reid, The association of twinning and fracture in bcc metals, *Metall. Trans. A* 12 (1981) 371–377.

[239] G. E. Lloyd, A. B. Farmer, D. Mainprice, Misorientation analysis and the formation and orientation of subgrain and grain boundaries, *Tectonophysics* 279 (1997) 55–78.

[240] J. Zhao, B. L. Adams, Definition of an asymmetric domain for intercrystalline misorientation in cubic materials in the space of Euler angles, *Acta Crystallogr. A* 44 (1988) 326–336.

[241] R. Gröger, J. Holzer, T. Kruml, Twinning and antitwinning in body-centered cubic metals (submitted manuscript), *Comp. Mater. Sci.*

[242] C. R. Weinberger, B. L. Boyce, C. C. Battaile, Slip planes in bcc transition metals, *Int. Mater. Rev.* 58 (2013) 296–314.

[243] A. W. Sleeswyk, $1/2\langle 111\rangle$ screw dislocations and the nucleation of $\{112\}\langle 111\rangle$ twins in the bcc lattice, *Philos. Mag.* 8 (1963) 1467–1486.

[244] V. Vitek, Thermally activated motion of screw dislocations in BCC metals, *Phys. Stat. Sol. B* 18 (1966) 687–701.

[245] A. J. Bogers, W. G. Burgers, Partial dislocations on the {110} planes in the BCC lattice and the transition of the FCC into the BCC lattice, *Acta Metall.* 12 (1964) 255–261.

[246] K. P. D. Lagerlöf, On Deformation Twinning in b.c.c. Metals, *Acta Metall. Mater.* 41 (1993) 2143–2151.

[247] X. Zhao, C. Lu, A. K. Tieu, L. Zhan, M. Huang, L. Su, L. Pei, L. Zhang, Deformation twinning and dislocation processes in nanotwinned copper by molecular dynamics simulations, *Comput. Mater. Sci.* 142 (2018) 59–71.

[248] Y. T. Zhu, X. L. Wu, X. Z. Liao, J. Narayan, L. J. Kecskés, S. N. Mathaudhu, Dislocation–twin interactions in nanocrystalline fcc metals, *Acta Mater.* 59 (2011) 812–821.

[249] A. Paxton, Theoretical strength, twinning, antitwinning and pseudotwinning - a quantum mechanical approach, TMS, 1994, 27–41, symposium on Twinning in Advanced Materials, as part of the 1993 Materials Week; Conference date: 18-10-1993 Through 20-10-1993.

[250] R. Hafner, D. Spisak, R. Lorenz, J. Hafner, Does density-functional theory predict a spin-density-wave ground state for Cr?, *J. Phys. Condens. Matter.* 13 (2001) L239–L247.

[251] J. Crangle, G. M. Goodman, The magnetization of pure iron and nickel, *Proc. Roy. Soc. Lond. A* 321 (1971) 477–491.

[252] S. Mahajan, Accommodation at deformation twins in bcc crystals, *Metall. Trans. A* 12 (1981) 379–386.

[253] J. Harding, The yield and fracture of high-purity iron single crystals under repeated tensile impact loading, *Mem. Sci. Rev. Met.* 65 (1968) 245–254.

[254] B. Edmondson, The effect of composition and structure on the tensile properties of high-purity iron single crystals, with particular reference to the question of brittle fracture, *Proc. R. Soc. A: Math. Phys. Eng. Sci.* 264 (1961) 176–197.

[255] A. Ojha, H. Sehitoglu, Twinning stress prediction in bcc metals and alloys, *Philos. Mag. Lett.* 94 (2014) 647–657.

[256] A. Ojha, H. Sehitoglu, L. Patriarca, H. J. Maier, Twin nucleation in Fe-based bcc alloys—modeling and experiments, *Model. Simul. Mater. Sci. Eng.* 22 (2014) 075010.

[257] S. Ogata, J. Li, S. Yip, Energy landscape of deformation twinning in bcc and fcc metals, *Phys. Rev. B* 71 (2005) 224102.

[258] B. C. Munday, A. R. Pepper, R. Street, Properties of chromium cooled in a magnetic field, *Braz. J. Appl. Phys.* 15 (1964) 611–612.

[259] M. O. Steinitz, Physical properties of chromium, *J. Magn. Magn. Mater.* 60 (1986) 137–144.

[260] V. F. Sears, S. A. Shelley, Debye–Waller factor for elemental crystals, *Acta Crystallogr. A* 47 (1991) 441–446.

[261] L.-M. Peng, G. Ren, S. L. Dudarev, M. J. Whelan, Debye–Waller factors and absorptive scattering factors of elemental crystals, *Acta Crystallogr. A* 52 (1996) 456–470.

[262] J. W. Lynn, Magnetic neutron scattering, *J. Appl. Phys.* 75 (1994) 6806–6810.

[263] A. Furrer, Introduction to Neutron Scattering, Vol. 96-01, PSI-Proceedings, 1996.

[264] W. Ratcliff, D. Kan, W. Chen, S. Watson, S. Chi, R. Erwin, G. J. McIntyre, S. C. Capelli, I. Takeuchi, Neutron diffraction investigations of magnetism in $BiFeO_3$ epitaxial films, *Adv. Funct. Mater.* 21 (2011) 1567–1574.

[265] H. J. Kang, Neutron scattering studies on magnetism and phonon in the electron-doped neodymium-cerium cuprate and praseodymium-lanthanide-cerium cuprate, Ph.D. thesis, The University of Tennessee (2005).

[266] Z. Yamani, Z. Tun, D. H. Ryan, Neutron scattering study of the classical antiferromagnet MnF_2: A perfect hands-on neutron scattering teaching course, *Can. J. Phys.* 88 (2010) 771–797.

[267] Y. Zhao, D. Parshall, W. Ratcliff, J. Lynn, Magnetic Phase Transition and Spin Wave Excitations in the Colossal Magnetoresistive Manganites: An Experiment Using the BT7 Triple-Axis SpectrometerNIST Center for Neutron Research.

[268] R. Comès, B. Dorner, J. M. Loveluck, R. D. Mountain, H. G. Smith, N. Wakabayashi, J. W. White, Dynamics of solids and liquids by neutron scattering, Vol. 3, Springer Science & Business Media, 2012.

[269] G. E. Bacon, Neutron Diffraction, Clarendon Press, 1975.

[270] M. Blume, A. J. Freeman, R. E. Watson, Neutron Magnetic Form Factors and X-Ray Atomic Scattering Factors for Rare-Earth Ions, *J. Chem. Phys.* 37 (1962) 1245–1253.

[271] P. J. Brown, International Tables for Crystallography, Volume C: Mathematical, physical and chemical tables, Springer Science & Business Media, 1992.

[272] E. J. Lisher, J. B. Forsyth, Analytic approximations to form factors, *Acta Crystallogr. A* 27 (1971) 545–549.

[273] G. H. Lander, T. O. Brun, Calculation of Neutron Magnetic Form Factors for Rare-Earth Ions, *J. Chem. Phys.* 53 (1970) 1387–1391.

[274] W. Ratcliff, P. Kienzle, J. W. Lynn, S. Li, P. Dai, G. F. Chen, N. L. Wang, Magnetic form factor of $SrFe_2As_2$ Neutron diffraction measurements, *Phys. Rev. B* 81 (2010) 140502.

[275] A. J. P. Meyer, G. Asch, Experimental g' and g values of Fe, Co, Ni, and their alloys, *J. App. Phys.* 32 (1961) S330–S333.

[276] A. J. A. De Oliveira, O. F. De Lima, W. A. Ortiz, P. C. De Camargo, Spin-flip transition and magnetic phase diagram of Cr-V alloys, *Solid State Commun.* 96 (1995) 383–386.

[277] Y. W. Lai, N. Scheerbaum, D. Hinz, O. Gutfleisch, R. Schäfer, L. Schultz, J. McCord, Absence of magnetic domain wall motion during magnetic field induced twin boundary motion in bulk magnetic shape memory alloys, *Appl. Phys. Lett.* 90 (2007) 192504.

[278] B. Zhang, W. A. Soffa, Magnetic domains and coercivity in polytwinned ferromagnets, *Phys. Status Solidi A* 131 (1992) 707–725.

[279] K. Postava, J. F. Bobo, M. D. Ortega, B. Raquet, H. Jaffres, E. Snoeck, M. Goiran, A. R. Fert, J. P. Redoules, J. Pištora, J. C. Ousset, Magneto-optical measurements of magnetization reversal in nanometer scale sputtered Fe thin films, *J. Magn. Magn. Mater.* 163 (1996) 8–20.

[280] R. Watanabe, Possible Slip Systems in Body Centered Cubic Iron, *Mater. Trans.* 47 (2006) 1886–1889.

[281] H. M. Ledbetter, R. P. Reed, Elastic properties of metals and alloys, I. Iron, nickel, and iron-nickel alloys, *J. Phys. Chem. Ref. Data* 2 (1973) 531–618.

[282] H. C. Nash, C. S. Smith, Single-crystal elastic constants of lithium, *J. Phys. Chem. Solids* 9 (1959) 113–118.

[283] M. E. Diederich, J. Trivisonno, Temperature dependence of the elastic constants of sodium, *J. Phys. Chem. Solids* 27 (1966) 637–642.

[284] P. A. Smith, C. S. Smith, Pressure derivatives of the elastic constants of potassium, *J. Phys. Chem. Solids* 26 (1965) 279–289.

[285] F. H. Featherston, J. R. Neighbours, Elastic constants of tantalum, tungsten, and molybdenum, *Phys. Rev.* 130 (1963) 1324–1333.

[286] K. J. Carroll, Elastic Constants of Niobium from 4.2 to 300 K, *J. App. Phys.* 36 (1965) 3689–3690.

[287] D. I. Bolef, R. E. Smith, J. G. Miller, Elastic properties of vanadium. I. Temperature dependence of the elastic constants and the thermal expansion, *Phys. Rev. B* 3 (1971) 4100–4108.

[288] T. Sedlatschek, J. Lian, W. Li, M. Jiang, T. Wierzbicki, M. Z. Bazant, J. Zhu, Large-deformation plasticity and fracture behavior of pure lithium under various stress states, *Acta Mater.* 208 (2021) 116730.

[289] S. Küchler, V. Vojtech, S. S. A. Gerstl, R. E. Schäublin, J. F. Löffler, Thermally Decomposed Binary Fe–Cr Alloys: Toward a Quantitative Relationship Between Strength and Structure, *Adv. Eng. Mater.* 24 (2022) 2100909.

[290] W.-Y. Chen, Y. Miao, J. Gan, M. A. Okuniewski, S. A. Maloy, J. F. Stubbins, Neutron irradiation effects in Fe and Fe–Cr at 300 °C, *Acta Mater.* 111 (2016) 407–416.

List of abbreviations

Abbreviation	Meaning
ASTM	American Society for Testing and Materials
BCC	Body Centered Cubic
BOP	Bond Order Potential
CEITEC	Central European Institute of Technology
CL	Camera Length
CRSS	Critical Resolved Shear Stress
CT	Computed Tomography
DFT	Density Functional Theory
DXA	Dislocation Extraction Algorithm
EAM	Embedded Atom Model
EBSD	Electron Back-Scattered Diffraction
FCC	Face Centered Cubic
FEAR	Fitted Ellipse Aspect Ratio
FIB	Focused Ion Beam
FWHM	Full Width at Half Maximum
GIS	Gas Injection System
GSFE	Generalized Stacking Fault Energy
ICP-MS	Inductively Coupled Plasma Mass Spectroscopy
IPF	Inverse Pole Figure
IPM	Institute of Physics of Materials
LLP	Lamella Lift-Out Position
LSDW	Longitudinal Spin Density Wave
MGPT	Model Generalized Pseudopotential Theory
MOKE	Magneto-Optical Kerr Effect
MRSSP	Maximum Resolved Shear Stress Plane
P-N	Peierls-Nabarro (model)
PPB	Parts Per Billion
PPM	Parts Per Million
PPMS	Physical Property Measurement System
PTFE	Polytetrafluoroethylene
RRR	Residual Resistivity Ratio
RT	Room Temperature
SEM	Scanning Electron Microscopy
SF	Schmid Factor
SINQ	The Swiss spallation Neutron Source
SDW	Spin Density Wave
STEM	Scanning Transmission Electron Microscopy

Abbreviation	Meaning
TEM	Transmission Electron Microscopy
TSDW	Transversal Spin Density Wave
UHV	Ultra High Vacuum
VSM	Vibrating Sample Magnetometry